

A systematic empirical study on the synthesis of turbostratic nanoscale
graphene produced via chamber detonation of gaseous hydrocarbon
precursors

by

Justin P. Wright

B.S., Shippensburg University of Pennsylvania, 2015

AN ABSTRACT OF A DISSERTATION

submitted in partial fulfillment of the
requirements for the degree

DOCTOR OF PHILOSOPHY

Department of Physics
College of Arts and Sciences

KANSAS STATE UNIVERSITY
Manhattan, Kansas

2022

Abstract

A systematic study on the formation and characterization of detonation carbon using various hydrocarbon precursors is presented. All precursors share similar trends in product yields with the requirement of oxygen/carbon ratio (O/C) ≤ 1.0 to produce solid carbon, and the detonation data indicating that a minimum temperature and pressure of 2300 ± 150 K and 13 ± 1 atm, respectively, are both required to produce solid carbon with graphene morphology. These two results form a theoretical model that can be used to predict whether the reaction will form a soot or a graphene before the experiment takes place. Characterizations such as Raman, XRD, TEM, etc. are used to systematically distinguish the solid carbon produced between soot, graphene, and graphite. The resulting graphene product is a turbostratic nanoscale graphene with 5-30 layers depending on the O/C ratio and precursor, and can be industrially scaled up to produce kg/day quantities at low cost. Differing O/C ratios produce graphenes with different properties that we call low O/C and high O/C graphene. Syngas is also produced as a byproduct for O/C mixtures ≤ 1.0 , and there are low-to-zero solid carbon yields for O/C mixtures > 1.0 which instead produce carbon monoxide and hydrogen, an appealing industry reaction in the process of being scaled up.

A systematic empirical study on the synthesis of turbostratic nanoscale
graphene produced via chamber detonation of gaseous hydrocarbon
precursors

by

Justin P. Wright

B.S., Shippensburg University of Pennsylvania, 2015

A DISSERTATION

submitted in partial fulfillment of the
requirements for the degree

DOCTOR OF PHILOSOPHY

Department of Physics
College of Arts and Sciences

KANSAS STATE UNIVERSITY
Manhattan, Kansas

2022

Approved by:

Major Professor
Christopher Sorensen

Copyright

© Justin P. Wright 2022.

Abstract

A systematic study on the formation and characterization of detonation carbon using various hydrocarbon precursors is presented. All precursors share similar trends in product yields with the requirement of oxygen/carbon ratio (O/C) ≤ 1.0 to produce solid carbon, and the detonation data indicating that a minimum temperature and pressure of 2300 ± 150 K and 13 ± 1 atm, respectively, are both required to produce solid carbon with graphene morphology. These two results form a theoretical model that can be used to predict whether the reaction will form a soot or a graphene before the experiment takes place. Characterizations such as Raman, XRD, TEM, etc. are used to systematically distinguish the solid carbon produced between soot, graphene, and graphite. The resulting graphene product is a turbostratic nanoscale graphene with 5-30 layers depending on the O/C ratio and precursor, and can be industrially scaled up to produce kg/day quantities at low cost. Differing O/C ratios produce graphenes with different properties that we call low O/C and high O/C graphene. Syngas is also produced as a byproduct for O/C mixtures ≤ 1.0 , and there are low-to-zero solid carbon yields for O/C mixtures > 1.0 which instead produce carbon monoxide and hydrogen, an appealing industry reaction in the process of being scaled up.

Table of Contents

List of Figures	x
List of Tables	xix
Acknowledgements	xx
Dedication	xxi
1 Introduction	1
2 Experimental Methods	3
2.1 Safety and procedure	3
2.1.1 Description of precursors	3
2.1.2 Laboratory safety protocols	6
2.1.3 Overview of apparatus and characterization tools	8
2.1.4 Detonation procedure	12
2.2 Instrumentation	14
2.2.1 Raman spectroscopy	14
2.2.2 Powder X-ray diffraction	15
2.2.3 Transmission electron microscopy	16
2.2.4 Specific surface area measurements	16
2.2.5 Scanning electron microscopy	17
2.2.6 Gas chromatography	18
2.2.7 Fourier-transform infrared spectroscopy	18
2.2.8 Zeta potential	19

2.2.9	Atomic force microscopy	19
2.2.10	Elemental analysis	19
2.2.11	Thermogravimetric analysis	20
2.2.12	Sonication, exfoliation, and solvent dispersion	20
3	Acetylene-oxygen fill mixtures	21
3.1	Synthesis of turbostratic nanoscale graphene via chamber detonation of oxygen/acetylene mixtures	21
3.2	Continued acetylene-oxygen fill mixture analysis	37
3.2.1	Spectra blackbody detail	37
3.2.2	Pressure and temperature rise time	38
3.2.3	Spectrometer light intensity and further temperature data	41
3.2.4	Turbidity	44
3.2.5	Sample appearance	46
3.2.6	AFM	47
3.2.7	TGA	48
3.2.8	All O/C compared to the 0.3 O/C sample	49
3.2.9	Solvent dispersion	50
4	Construction of a pilot-scale plant to produce 10 kg of graphene in 5.5 days	53
4.1	Description of pilot-scale plant apparatus	53
4.2	Pilot-scale plant procedure	55
4.3	Engineering details	56
4.3.1	Custom spark plugs	56
4.3.2	Electrode clean cycle	58
4.3.3	Sample collection	59
4.3.4	Reactor operating conditions and failures	62
4.4	Bulk sample comparison to single-shot sample	64

4.4.1	Appearance and density	64
4.4.2	Raman	65
4.4.3	XRD	65
4.4.4	BET	66
4.4.5	TEM	66
4.4.6	SEM	67
5	Various precursor fill-mixtures	69
5.1	Methane-oxygen	69
5.1.1	Detonation data	69
5.1.2	Post-detonation analysis	71
5.2	Ethylene-oxygen	72
5.2.1	Pressure	73
5.2.2	Temperature	75
5.2.3	Mass and yield	76
5.2.4	Chemical equation	77
5.2.5	BET	78
5.2.6	Raman	79
5.2.7	XRD	81
5.2.8	TEM	83
5.2.9	SEM	84
5.3	Acetylene-oxygen + Argon	85
5.3.1	Pressure, rise time, temperature, mass, density, and SSA	86
5.3.2	Raman	88
5.3.3	XRD	90
5.3.4	TEM	92
5.4	Acetylene-oxygen + nitrogen	93
5.4.1	Detonation details	93

5.4.2	Raman	93
5.5	Propane-oxygen	94
5.5.1	Detonation details	94
5.5.2	Raman	95
5.6	Acetylene-oxygen via different methods	96
5.6.1	Skinny tube experiment	98
5.6.2	Shock tube experiment	99
5.7	Benzene, toluene, and xylenes	100
5.7.1	Detonation data	101
5.7.2	Raman	104
5.7.3	XRD	105
5.7.4	TGA	107
6	Overall trends	109
6.1	Product yields	109
6.2	Raman and XRD	112
6.3	Soot, graphene, and graphite	116
6.4	Temperature and Pressure	120
6.5	The graphene model	123
6.5.1	The thermodynamic argument of graphene formation	124
6.5.2	Aerosol gelation revisited	126
6.6	Conclusion	127
	Bibliography	128

List of Figures

2.1	The SDS and labeled drawer in which it is kept in the hibay lab.	6
2.2	On the left, the steel curtain protecting the passthrough for the gas tubes (shown passing under the curtain) and the entrance to the ducts on the east wall is shown. The middle depicts the snorkel device set up adjacent to the reactor vessel, and the right depicts the steel wall and make-up air vents on the west wall.	8
2.3	White labels with red text and red arrows depict the reactor vessel details. .	9
2.4	From left to right: temperature probe, photodiode, spectrometer with fiber optic, and piezocrystal.	10
2.5	From left to right: screenshot of the custom LabVIEW program, gas manifold, and control box developed by Stephen Corkill.	11
2.6	Left: old manual flowmeters; right: new electronic MFCs.	11
2.7	A step by step description of the detonation process is included alongside a diagram. A red box outlines a picture of the spark generated by the 10 kV step-up transformer.	13
3.1	Linearized blackbody of a 0.45 O/C spectrum between two Planck blackbody temperatures (dashed lines).	37
3.2	Pressure data is plotted as black circles, and temperature data is plotted as red empty squares.	38
3.3	Peak temperature is plotted versus spectrometer integration time.	40
3.4	The detonation flash captured with an iPhone 11 camera in slow motion for each O/C mixture. Each frame represents 33.3ms.	41

3.5	Spectrometer light intensity at 300 nm (top) and the resulting temperature calculated (bottom). 300 nm is presented due to the relatively higher signal-to-noise ratio compared to higher wavelengths. Each detonation is labeled as its integration time in milliseconds, right, and assigned a different color. Horizontal error bars represent length of integration time in milliseconds. There is a 1.8 ms buffer time between each data point regardless of the integration time. Data is a result of several years of detonations with the spectrometer positioned differently with respect to the chamber window, thus the light intensity in a.u. cannot be directly intercompared.	43
3.6	Spectrometer light intensity at 300 nm (left) and calculated temperature (right). 300 nm is presented due to the relatively higher signal-to-noise ratio compared to higher wavelengths. Intensity and temperature are averaged across all data for each O/C in 2 ms increments and normalized to peak at 1 a.u. for light spectra. Temperature data follows the same color-labeling as the intensity data.	44
3.7	Turbidity captured from HeNe laser focused on photodiode through the chamber windows.	45
3.8	The 1/e point of all turbidity measurements.	46
3.9	iPhone SE picture of graphene samples. The top picture is captured in normal room lighting, and the bottom picture has altered contrast for visibility purposes. A thin red line is drawn between the pictures for clarity. The four samples in the top row are the 0.25, 0.3, 0.35, and 0.4 O/C, and in the bottom row 0.45, 0.5, 0.6, and 0.75 O/C.	47

3.10	AFM pictures of 0.3 O/C (top) and 0.75 O/C (bottom). The left and right 0.3 O/C pictures have x-y scales of 10x10 nm and 1x1 nm, respectively, and z-scale colormaps from 0-200 nm and 0-5 nm, respectively. The left and right 0.75 O/C pictures have x-y scales of 10x10 nm and 1x1 nm, respectively, and z-scale colormaps from 0-75 nm and 0-8 nm, respectively.	48
3.11	TGA of 0.3 O/C sample.	49
3.12	Y-axis shows the log of the ratio between all O/C and the 0.3 sample plotted on a log scale. All 0.3 values are equal to unity as a result.	50
3.13	TEM images of 10 mg of 0.4 O/C graphene in, from left to right: 10 mL of acetone sonicated for 60 min at room temperature; 10 mL of acetone sonicated for 60 min at 50 °C; and 10 mL of chloroform sonicated for 60 min at room temperature.	51
4.1	Pilot-scale plant on the left and a basic schematic on the right.	54
4.2	Top left: bag filter after collecting 1 kg of graphene. Bottom left: graphene-coated Kevlar on the inside of the cut-open bag filter after collecting 1 kg of graphene. Right: close-up picture with altered contrast of the Kevlar and cut-open bag filter.	55
4.3	Top left: custom electrode; top right: cubical feature with ports for electrodes; bottom left: ceramic-coated spark plugs; bottom right: view of the spark in the cube.	57
4.4	Collected mass is plotted versus bag number, with each bag capable holding ~1 kg. The estimated mass is plotted in black circles and the measured mass is plotted in red circles, each with a 2% error bar. Mass was measured by weighing the entire collection system before and after the graphene was produced to ensure graphene lost during container transfer would not impact the result. Bags 1-3 were mixtures of various O/C ratios.	60

4.5	Top left: bag filter cut open to reveal graphene inside and picture of HEPA filter; bottom left: 10 kg of graphene collected and stored with a closeup image of the sample; right: single shot graphene sample from the 17 L chamber for comparison.	61
4.6	Picture of holes burned through the top half of silicon bag filter. The face of Dr. Arjun Nepal is seen in the background.	62
4.7	Image of the gas fill user interface. The long arrows overlap to monitor the flow rate as the gases fill the chamber.	63
4.8	Left: a fan directed at the valve that connects the chamber to the collection system; right: a small crack in the valve gasket responsible for leaking production gas into the blast room.	64
4.9	Raman of single shot 0.3 O/C sample in blue and bulk 0.3 O/C sample in yellow.	65
4.10	XRD of single shot 0.3 O/C sample in blue and bulk 0.3 O/C sample in yellow. The (002) peak intensity is scaled to unity for both samples.	66
4.11	Left: single shot 0.3 O/C sample; right: bulk 0.3 O/C sample.	67
4.12	Left: single shot 0.3 O/C sample; right: bulk 0.3 O/C sample.	68
5.1	Peak pressure plotted in black circles on left axis and rise time to peak pressure plotted in red squares on right axis.	70
5.2	Chart shows the fill pressure, measured overpressure, and relative overpressure adjusted for fill pressure for each O/C.	70
5.3	GC measurements showing the full chromatogram and closeups up the three detected peaks for O/C = 1.6, 1.8, and 2.0.	71
5.4	The methane-oxygen fill mixture chemical equation for all O/C.	71
5.5	Molar hydrogen (red) and carbon monoxide (blue) products with respect to methane-fill is plotted as a function of the ratio of over pressure to fill pressure.	72

5.6	Peak pressure in black circles on the left axis and rise time to peak pressure in red pluses and triangles on the right axis are plotted versus O/C. Open circles and open triangles represent 2 atm fill data that was taken for 0.7 O/C.	74
5.7	After-detonation overpressure plotted as a function of O/C. 1 atm fill pressures are plotted as blue closed circles, and 2 atm fill pressures are plotted as red open circles. All data is taken relative to fill pressure.	75
5.8	Temperature in black circles on the left axis and duration of light intensity in red pluses and triangles on the right axis are plotted versus O/C. Open circles and open triangles represent 2 atm fill data that was taken for 0.7 O/C. The 1.0 O/C mixture is omitted due to a lack of blackbody radiation.	76
5.9	Mass in black circles on the left axis and yield in red pluses and triangles on the right axis are plotted versus O/C. Open circles and open triangles represent 2 atm fill data that was taken for 0.7 O/C.	77
5.10	The chemical equation in moles for ethylene-oxygen fill mixtures for all O/C. 2 atm fill pressures for 0.7 O/C are equivalent for 1 atm fill pressures when adjust for initial pressure and thus are represented by the 1 atm equation.	78
5.11	SSA plotted versus O/C. The 2 atm and 1 atm fill pressures for 0.7 O/C are labeled.	79
5.12	Raman spectra of ethylene samples in comparison to graphite and the 0.3 O/C acetylene sample, and spectra of the 0.825 and 0.9 O/C ethylene samples plotted on a log scale	80
5.13	All (002) peaks are scaled to equal unity. a) XRD of ethylene-oxygen (blue) samples in comparison to the 0.3 O/C acetylene-oxygen sample (yellow) and graphite (red). The 0.9 O/C ethylene-oxygen sample is plotted in green. b) XRD spectrum of 0.825 O/C ethylene-oxygen sample. c) XRD spectrum of 0.825 O/C ethylene-oxygen sample.	82
5.14	TEM images of ethylene-oxygen samples.	84

5.15 SEM images of ethylene-oxygen samples.	85
5.16 Comparison of samples with added argon to the original samples. The open circles represent the 0.5 O/C, and the squares represent the 0.3 O/C. Rise time to peak pressure is plotted in blue, the peak pressure is plotted in purple, the temperature is plotted in orange, the density is plotted in red, the mass is plotted in green, and the SSA is plotted in magenta.	87
5.17 Raman comparison of samples with added argon to the original samples. The original low and high O/C are plotted in blue and green, respectively. Added argon to low and high O/C are plotted in purple and yellow, respectively. Graphite plotted in red is added for comparison. All samples are scaled such that $I_G = 1$. Three dashed blue lines are centered on the three prominent peaks of the 0.3 sample, and one dashed red line is centered on the 2D peak of the graphite sample.	89
5.18 XRD of acetylene-oxygen + argon samples in comparison to acetylene-oxygen and graphite. Low and high O/C of acetylene samples are plotted in blue and green, respectively. The argon added samples of low and high O/C are plotted in purple and yellow, respectively. Graphite is plotted in red and is a different graphite powder than used previously.	91
5.19 TEM images of 0% argon samples were taken at KU, and TEM images of added argon samples were taken a k-state, described in section 2.2.3.	92
5.20 Raman spectra plotted on normal axis and log scale. The G peak intensity is scaled to unity.	94
5.21 Chemical equation of propane samples. An extra 0.0159 mol of oxygen was included in equation due to residual air left after vacuum.	95
5.22 Raman spectra of the 0.9 O/C propane sample. The G peak intensity is scaled to unity.	96
5.23 Newly constructed 17 L skinny detonation chamber.	97

5.24	Raman spectra (left) and XRD (right) of the 0.3 O/C acetylene sample made in the new chamber (bottom) compared to the original chamber (top). The G peak intensity and (002) peak are scaled to unity.	99
5.25	Raman spectra of the 0.13 O/C acetylene sample. The G peak intensity is scaled to unity.	100
5.26	Picture showcasing the alternate setup for liquid precursors. Left shows the heating tape to bring the chamber up to temperature, and right shows the insulation required. Figure reproduced with permission from Shusil Sigdel. .	101
5.27	Picture of the samples. Figure reproduced with permission from Shusil Sigdel.	103
5.28	Chemical equations of the liquid precursors verified by overpressure, GC, and FTIR analysis. A thin red line separates each liquid precursor dataset. . . .	104
5.29	Raman spectra of all liquid precursors (top) and Raman plotted on log scale of the 1.0 O/C benzene and 0.9 O/C toluene samples (bottom).	105
5.30	XRD spectra of benzene (blue), toluene (green), and xylene (magenta) in comparison to graphite (red). Figure reproduced with permission from Shusil Sigdel.	106
5.31	TGA of the toluene 0.6 (red) and 0.9 (green) O/C samples. Figure reproduced with permission from Shusil Sigdel.	108
6.1	The yield of each product relative to the hydrocarbon precursor is plotted versus O/C for all precursors. Each symbol represents a different product, and each color represents a different precursor. Squares represent hydrogen, empty squares represent water, circles represent carbon, lightly-filled circles represent carbon dioxide, and empty circles represent carbon monoxide. Black represents methane, blue represents acetylene, green represents ethylene, red represents propane, pink represents benzene, gold represents toluene, and cyan represents xylenes.	110

6.2	Stoichiometric chemical equation for each hydrocarbon precursor used, and a general equation for balancing the equation.	111
6.3	Qualitative plot summarizing the trends seen in Figure 6.1. Carbon monoxide is tracked in green, solid carbon is tracked in black, hydrogen is tracked in gold, water is tracked in blue, and carbon dioxide is tracked in red. The stoichiometric label is placed ~ 2.5 O/C, though all precursors are expected to follow this trend relative to their stoichiometric O/C.	112
6.4	SSA is plotted versus the D-G peak overlap height relative to the G peak from the Raman. Soot has a wide variety of reported SSA and D-G peak overlap height values from the literature [1–4]. An arrow signifies the trend from low O/C to high O/C for each precursor.	113
6.5	Raman 2D peak FWHM is plotted versus the Raman I_{2D}/I_G peak ratio. Samples with wide or zero 2D peaks have an indiscernible FWHM. Soot has a known absence of a 2D peak [2–4].	114
6.6	Raman G peak FWHM is plotted versus the Raman I_D/I_G peak ratio. Samples with D-G peak overlaps of ≥ 0.5 have an indiscernible FWHM but measurable I_D/I_G . Soot has a known high D-G peak overlap and broad range of possible I_D/I_G peak ratios [2–4].	115
6.7	XRD (002) FWHM is plotted versus the XRD d.spacing. Soot has wide range of possible FWHM and d.spacings [2, 5].	116
6.8	$\Gamma(y)$ is plotted versus $\phi(x)$ for all samples, literature values of SLG, BLG, soot, and measured graphite. The large error bar on soot signifies the large range of accepted soot values in the literature.	119

6.9	Temperature is plotted versus pressure for all precursors. Solid points represent graphene characterization and empty points represent soot characterization. Circle points have known values of both temperature and pressure, and square points have known values of temperature but calculated pressure via ideal gas law. A larger x-axis error-bar is given for square points for this reason. The dashed circles labeled "special case" are the graphenes from the argon samples whose temperature and pressure values are considered incorrect. A square is drawn in dashed lines to indicate a likely boundary between the soot samples and the graphene samples.	121
6.10	Temperature is plotted versus pressure with a boundary between graphene and soot drawn.	122

List of Tables

2.1	Shows the MFC recorded values for trials 1 and 2, and the corresponding O/C ratios obtained.	12
5.1	Tabulated data of Raman spectra for the ethylene samples.	81
5.2	Tabulated data of XRD FWHM, location, d-spacing, Scherrer equation, and predicted number of layers.	83
5.3	Tabulated data of rise time to peak pressure, peak pressure, temperature, mass, powder density, and SSA of the acetylene+argon samples.	88
5.4	Tabulated data of Raman spectra for the argon samples.	90
5.5	Tabulated data of XRD FWHM, location, d-spacing, Scherrer equation, and predicted number of layers.	92
5.6	Tabulated data of the precursor, O/C, yield, temperature, and SSA. “no bb” for temperature means no blackbody was recorded, and n/a for SSA means the measurement could not be done due to a lack of mass produced by the sample.	102
5.7	Tabulated data of Raman spectra for the liquid precursor samples. “n/a” is written for samples where data doesn’t apply.	104
5.8	Tabulated data of XRD FWHM, location, d-spacing, Scherrer equation, and predicted number of layers.	107

Acknowledgments

First I must give my acknowledgements to my team, through which I owe all of my experience and growth to. Head honcho Chris Sorensen deserves the first of my appreciation for his continued guidance and wisdom throughout the years. He is a wonderful educator and I am truly grateful to have worked underneath his supervision. Stefan Bossmann has been like a second PI to me, never failing to respond to my inexhaustible supply of questions. Stephen Corkill - engineer extraordinaire - also deserves significant recognition for his companionship and advice on both the project and life in general. Shusil Sigdel has been a vital partner in the field and together we have spearheaded many achievements, even though he is a Manchester United fan (who says people can't set aside their differences!). Finally, Arjun Nepal has mentored me in my early years to develop me into the scientist that I have become today.

I would like to thank Hydrograph for continued funding and support of my graduate career. I would like to thank the faculty of K-State for their lessons and education, and I would like to thank all of my fellow students here at K-State for developing a strong community of support and love. We have all helped each other through difficult classes (with a healthy dose of competition) and celebrated each other's achievements as if they were our own.

Last but not least, I would like to thank my friends and family for their loyalty and support of my journey along the prairie.

Dedication

I dedicate this dissertation to all of my loved ones, and even some of my liked ones.

Chapter 1

Introduction

Graphene is a 2D hexagonal lattice of sp^2 bonded carbon that has unique and interesting properties including great material strength [6]¹, electrical conductivity [6–8], and novel optical properties [9]. Given graphene’s remarkable qualities, it has great promise for a variety of future applications; and given this promise, there is strong motive to develop synthetic methods that are scalable and will lead to the manufacture of graphene.

Graphene was first produced by mechanical exfoliation [10], which is not amenable to scale up. Bulk quantities can be obtained via methods such as Hummers’ method [11–14] and chemical vapor deposition [15, 16]. All these leading graphene-producing techniques are expensive (\$70-200/kg), require large amounts of energy, contain impurities, and often produce undesirable byproducts such as benzene derivatives [17]. Thus, there is a market need to produce high quality and green graphene at low cost.

We have discovered a controlled detonation process for the synthesis of multilayer graphene nanosheets [18, 19]. The process is a novel, cost-effective and eco-friendly, one-step method that involves detonation of a gas-phase hydrocarbon (typically C_2H_2) with oxygen (O_2) in a multiliter chamber. Detonation synthesis has several advantages such as simplicity, high productivity, economic viability, and short synthesis time. This synthesis method is catalyst-free and generates syngas as useful by-products during synthesis. Recent work by

¹References 1-5 appear in the table of contents as a result of how this document is auto-generated in Latex.

Gaur et al. has shown that detonation synthesis of graphene aerosol gels can be used to make micro-supercapacitors [20].

The premise of detonation synthesis is that the high temperature conditions of the shock wave are important to the formation of graphene. Earlier work from our group [18, 19] found high temperature (3000 K) to be a key component of graphene synthesis. Choi et al. [21] also demonstrated shell soot, a unique graphene-like carbon generated from a laser augmented acetylene diffusion flame reaching 3200 K. More recently, rapid joule heating [22] has followed these two discoveries to achieve high temperature conditions that yield graphene.

This work begins in Chapter 2 discussing the gaseous precursors that will be explored to make graphene samples and the scientific tools necessary to characterize the results. Chapter 3 covers the extensive detail of the work done on acetylene-oxygen mixtures, starting with a publication in journal Nano Select and introducing further work done that was left out of the journal submission. Then Chapter 4 discusses the feasibility and successes of scaling up the graphene product into industrial quantities, and various other precursors are tested for their viability in Chapter 5. Finally, Chapter 6 summarizes the results and reveals a theoretical model derived from the empirical data.

Chapter 2

Experimental Methods

The goal of this chapter is to outline the instrumentation involved in the entire detonation procedure – from making a sample to analyzing it. It will cover information about the precursors used, safety protocols of the lab, the procedure of the detonation process, and details on the instrumentation used during the detonation as well as used after the detonation in characterizing the material.

2.1 Safety and procedure

This section will provide an overview on lab safety, detonation procedure, details about the reactor chamber, and details on the data collection instrumentation accompanying the reactor chamber. Analysis of the data will take place in the following chapters.

2.1.1 Description of precursors

These experiments use explosive precursors to generate high temperature and pressure conditions in a constant volume environment. Dealing with these explosive precursors requires attention to safety protocols and is discussed below. The gaseous precursors used in this work are acetylene (C_2H_2), ethylene (C_2H_4), methane (CH_4), propane (C_3H_8), oxygen (O_2), argon (Ar), and nitrogen (N_2). Of mention in this work will also be liquid precursors: ben-

zene (C_6H_6), toluene (C_7H_8), and xylenes (C_8H_{10}). These liquid precursors' data are the work of Shusil Sigdel under collaboration with the author, and are necessary to complete this dissertation. A brief description of these chemicals will be provided.

All the gaseous precursors can deprive their storage room of breathable oxygen content resulting in asphyxiation, unconsciousness, and death. In the event gaseous precursors are stored inside of a contained room, a breathable oxygen detector should be present and working at all times. Ventilation is also recommended. Acetylene, ethylene, methane, and propane are flammable and thus must be stored separately from an oxidizer and kept away from heat sources [23, 24].

Acetylene consists of two carbons, triple bonded to each other, and bound to a hydrogen each. Due to its instability, the acetylene gas is dissolved in acetone and absorbed onto a porous material within the cylinder. At flow pressures greater than 15 psi (1 atm) gauge pressures, acetylene may decompose and explode, a problem exacerbated by heat. A distinct smell is applied to the acetylene in the cannister so that gas leaks can be quickly identified [23].

Ethylene consists of two carbons, doubled bonded to each other, and bonded to two hydrogens each. It is considered hazardous upon inhalation and has a faintly sweet smell [23].

Methane consists of a single carbon saturated by four hydrogens, and is the main component of natural gas. An odorant is added to identify gas leaks as it is naturally odorless [23].

Propane consists of three carbons singly bound to each other and saturated by eight hydrogens. It is a byproduct of natural gas processing and petroleum. Like methane it is naturally odorless and thus an odorant is added to identify gas leaks [23].

Oxygen is a diatomic molecule of two oxygen atoms doubled bonded to each other. It is an oxidizer and must be stored separately from flammable gases and other sources of heat. Breathing in large amounts of pure oxygen can cause various symptoms such as loss of consciousness [23].

Argon is a stable noble gas consisting of a single argon atom. It is nontoxic and inert

[23].

Nitrogen is a diatomic molecule of two nitrogen atoms triple bonded to each other. Although nontoxic and inert, it is often considered deadly in industry due to its common usage and that it can cause immediate unconsciousness and gradual asphyxiation when enough gas leaks to deprive the room of breathable oxygen [23].

Benzene, toluene, and xylenes are all highly flammable and thus must also be kept away from heat sources. Handling of these chemicals must be performed wearing lab gloves and utilization of either respiratory protection or a fumehood [23].

Benzene consists of six carbons forming an aromatic ring, with alternating double bonds, and a single hydrogen bound to each carbon atom. It is liquid at room temperature and toxic upon skin contact exposure, classified as a carcinogen. Benzene evaporates quickly in air and has a boiling point near 80 °C [23].

Toluene consists of six carbons forming an aromatic ring, with alternating double bonds, a single hydrogen bound to five of these carbons, and a single carbon with three hydrogens bound to one of the carbons. It is liquid at room temperature, evaporates quickly in air, and has a boiling point near 110 °C. The toxicity of toluene compared to benzene is reduced, though still understudied and not yet proven carcinogenic. Inhalation can cause disorientation and many other side effects [23].

Xylene consists of six carbons forming an aromatic ring with alternating double bonds, a single hydrogen bound to four of these carbons, and two carbons with three hydrogen bonds each bound two of these carbons. The location of the two carbons attached to the ring may vary, forming three isomers. Distinction of these isomers is difficult, resulting in commercially available xylene to be called mixed xylene or xylenes due to the chemical being a mixture of all three isomers. Xylenes are liquid at room temperature, evaporate quickly, and have a boiling point near 140 °C. It has reduced toxicity from that of benzene, though it is still slightly toxic as a skin irritant and inhalation hazard [23].

2.1.2 Laboratory safety protocols

Here, a brief description of laboratory safety protocols is presented.

The gaseous precursors must be stored in a location protected from the blast. A room is walled off by 0.476 cm thick steel isolating our detonation chamber from the rest of the laboratory. This room will be referred to from here on as the blast room. Gases are connected to the detonation chamber in the blast room by a passthrough in the steel wall, which is covered by a steel curtain on the interior of the blast room to prevent debris from accessing the passthrough in the event of a reactor breach (2.2). The gas tanks must also be secured to the wall and separated based on flammability and oxidizer content. A safety data sheet (SDS) detailing all gases and chemicals in the laboratory must be up to date and accounted for (2.1). In compliance with OSHA standards, an emergency number of the primary investigator must be posted on all entrances to the laboratory, as well as the location of the SDS [24, 25].

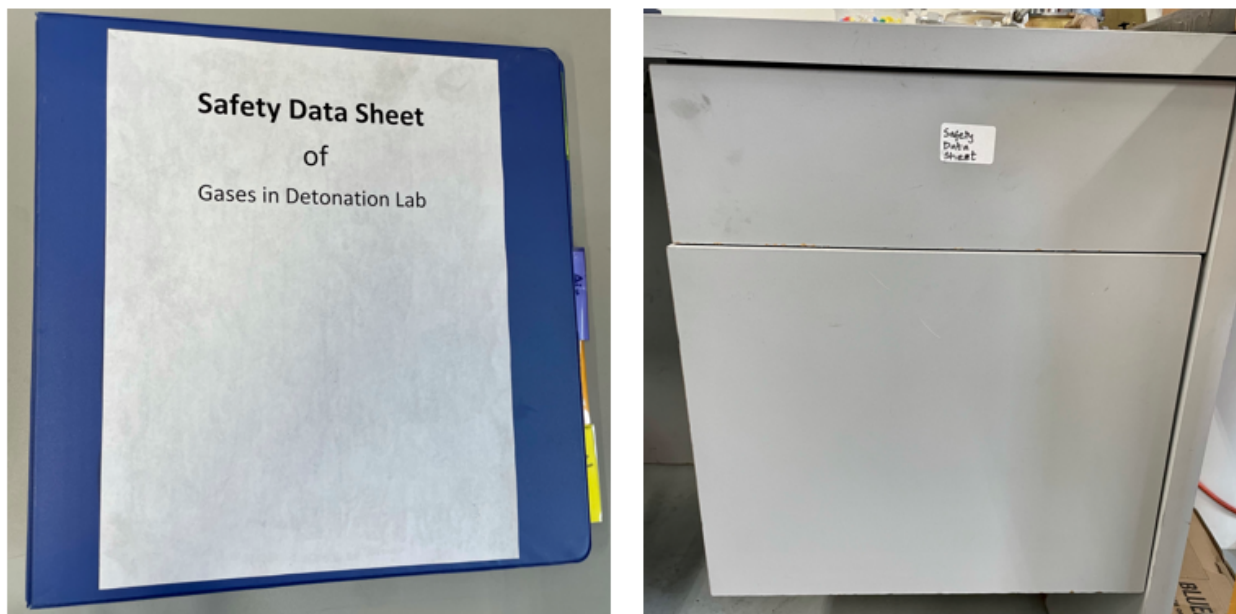


Figure 2.1: *The SDS and labeled drawer in which it is kept in the hibay lab.*

Before the detonation process begins, all occupants in the laboratory space must be notified in advance, and vacate the blast room. A WERMA LED signal tower will sound at the start of the gas-fill phase, during the middle of the gas-fill phase, and during the end of

the gas-fill phase, where a 3-second countdown will signal the onset of the explosion. After the detonation process has been completed, entry into the blast room is permitted.

Proper safety equipment must be worn by all who enter the blast room after a detonation. Though there are mixed results as to whether or not graphene is toxic to humans [26–29], nanoparticles still present health risks [30, 31]. Respiratory protection in the form of N95 masks or half facepiece masks have been approved as sufficient respiratory protection, after passing a fit test, by local safety officers. Gloves, lab coats, and safety goggles must be worn to protect the body from exposure to carbon nanoparticles [24]. Hats are also recommended by local staff.

The density of air is well known at 1.2 mg/mL; the density of the graphene material will be shown in chapter 3 to be as light as 3-5 mg/mL depending on the mixture. Graphene nanoparticles thus pose an airborne risk, and all work with it must be contained within the blast room or within access to a fume hood. The blast room contains two ducts behind the steel walls on the east side, with their entrance at the bottom of the wall protected by steel curtains that pull at a rate of ~ 23 cfm. This cfm is enough to fully evacuate the air inside the blast room at a rate of 1 blast room volume emptied every 90 seconds, or 40 room volumes every hour. Four vents drilled into the top of the steel wall on the western side provide make-up air for the blast room. The door to the blast room may also be opened to provide additional make up air. Finally, there is a dust collector model UFO-101 placed outside of the blast room that pulls at 1224 cfm and is connected to a movable fume hood called a snorkel. This snorkel can be adjusted within the blast room to further protect staff from exposure to airborne carbon nanoparticles.



Figure 2.2: *On the left, the steel curtain protecting the passthrough for the gas tubes (shown passing under the curtain) and the entrance to the ducts on the east wall is shown. The middle depicts the snorkel device set up adjacent to the reactor vessel, and the right depicts the steel wall and make-up air vents on the west wall.*

2.1.3 Overview of apparatus and characterization tools

Here, a description of the detonation chamber and data collection system is presented. This section is largely similar to the description in our paper published in Nano Select provided in chapter 3.

Figure 2.3 shows a picture of the reactor, which is a 16.7 L cylinder with internal height 37 cm and diameter 24 cm made of 2.54 cm thick aluminum, with a mass of 45 kg. The chamber is connected to a gas manifold operated by a control box which automates our system via a LabVIEW program. In the manifold immediately above the chamber is a cubical feature that contains electrodes to conduct a spark and ignite the mixture. This cubical feature will be further described in chapter 4. There is a valved port on top of the chamber to collect gas after detonation. Around the circumference of the chamber are three thick fused quartz windows to afford optical access to the interior. On the top of the chamber is a plugin for a piezoelectric crystal to collect pressure impulse data. A HeNe laser (632 nm, 10 mW) shines through two diametrically opposed quartz glass windows into a photodiode placed behind a

color filter ($632 \text{ nm} \pm 5 \text{ nm}$).

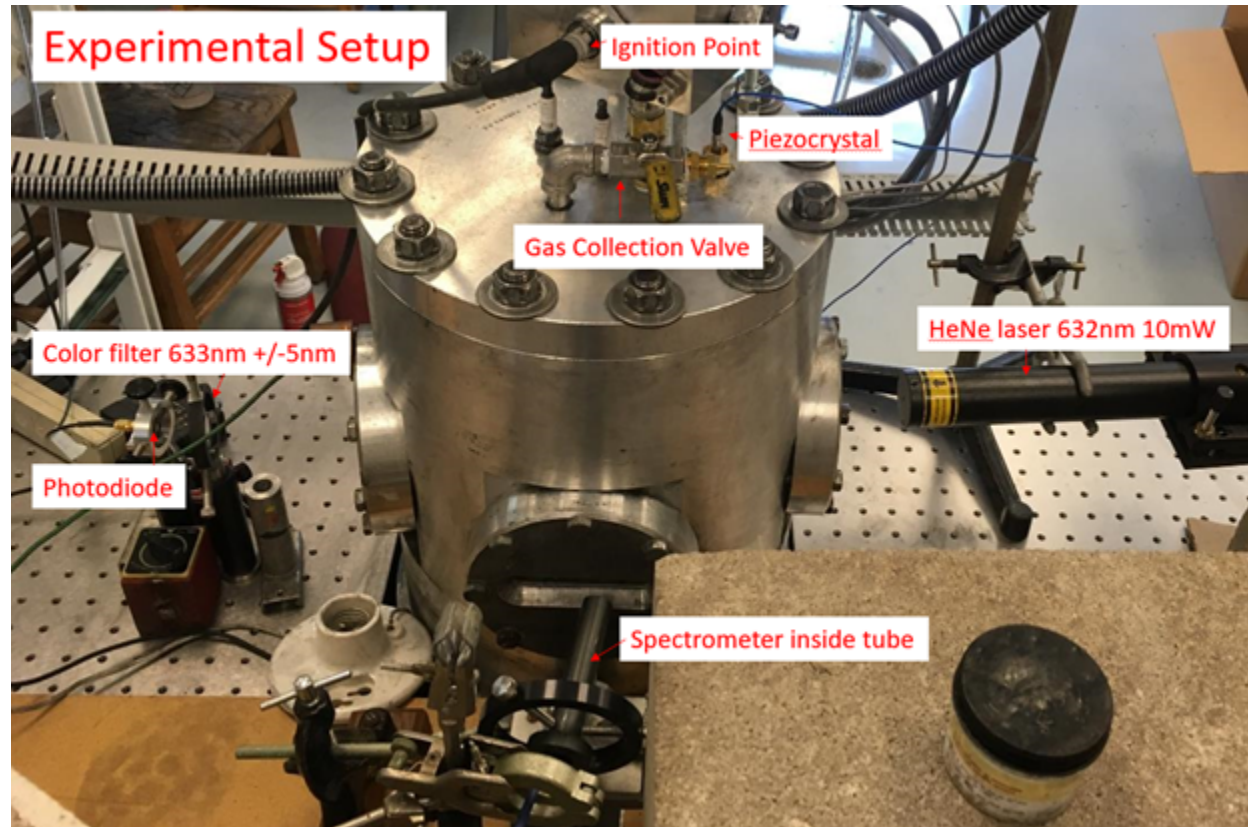


Figure 2.3: *White labels with red text and red arrows depict the reactor vessel details.*

A fiber optic at one quartz window collects light from the detonation flash and transmits that to an Ocean Optics Ocean FX spectrometer (range 200-1050 nm) triggered to collect data 20 ms before the spark is thrown. The light collection integration time can be varied from 20 μs – 10 ms, with a 1.8 ms buffer time between each shuttered integration time. This means a minimum of 1.82 ms occurs between each measurement. From these spectra, temperature can be calculated (see 3.1).

A PCB 113B26 piezocrystal is plugged into the top of the chamber. This records an impulse data in psi at a resolution of 2 mpsi.

The HeNe lasers emits a constant signal that is collected by a Thorlabs' SM05PD3A photodiode. When the reaction begins, blackbody radiation and the graphene that forms will affect the signal response. From this data we can infer turbidity.

Two Automation direct THMK-D08L10 temperature probes are equipped diametrically

opposed above the height of the quartz glass windows with Automation direct PCA-500 clamps. These probes record the external temperature of the chamber before and after the reaction.



Figure 2.4: *From left to right: temperature probe, photodiode, spectrometer with fiber optic, and piezocrystal.*

The process by which the reaction occurs is controlled automatically based on a custom LabVIEW program, electronic control box, and gas manifold designed by engineer Stephen Corkill. This program controls each step of the procedure outlined in section 2.1.4, and triggers the data collection of the piezocrystal, spectrometer, and photodiode on the order of tens of milliseconds before the initiation of the detonation blast. Gas flow and vacuum withdrawal are connected to the chamber by the manifold placed atop the detonation chamber, which consists of electronic valves operated via air pressure from an air compressor.

The reaction is initiated by a 10 kV industrial step-up transformer that sparks between two custom-made spark plugs. A more detailed description of the design and necessity of these custom spark plugs will occur in chapter 4.

Historically, our group used a pair of old manual flowmeters to control the reaction mixture [18, 19, 32, 33]. These flowmeters have leaks and are not calibrated for each individual hydrocarbon precursor. For this work, a set of new Alicat MCW-10SLPM mass flow controllers (MFCs) have been purchased and are electronically operated and calibrated for each precursor. Thus, the past descriptions of oxygen to hydrocarbon mixture, presented as O/C

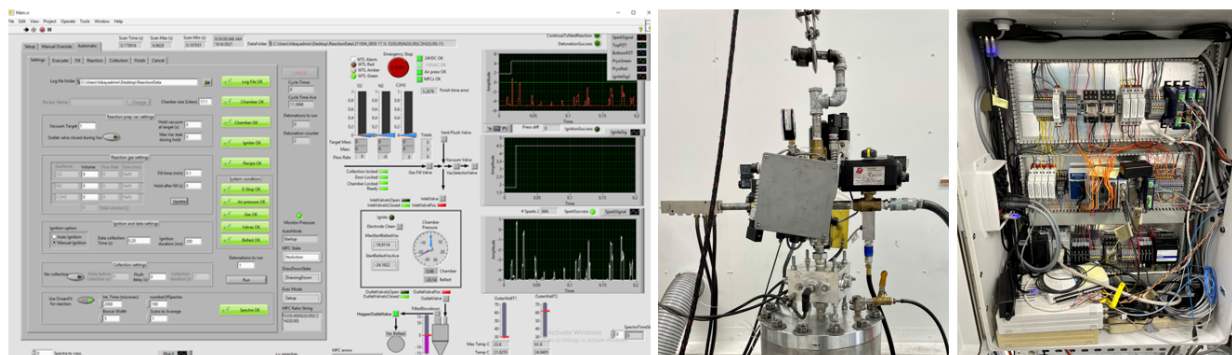


Figure 2.5: From left to right: screenshot of the custom LabVIEW program, gas manifold, and control box developed by Stephen Corkill.

ratio, is uncalibrated relative to this dissertation [18, 19, 32, 33].

An experiment was conducted to correlate the old manual flowmeters to the new MFCs. Table 2.1 shows the experiment to fill the 17 L chamber via adjusting the manual flowmeters while being measured by the MFCs. With this, we were able to find what the manual ratios were dispensing relative to the correct molar values as measured by the MFCs. The masses are measured in standard L. In addition, this was a blind experiment: the old manual flowmeters were adjusted without knowledge of the MFC recorded values until the experiment was completed in its entirety, and the gas dispensed was determined by monitoring a pressure gauge equipped to the chamber drawn down to a -29 “Hg vacuum. The experiment was performed twice to demonstrate repeatability.

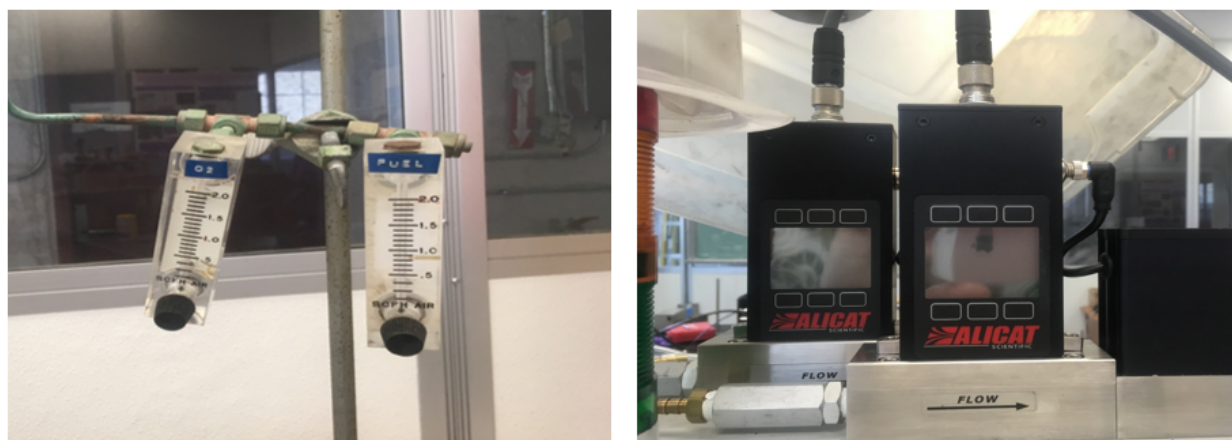


Figure 2.6: Left: old manual flowmeters; right: new electronic MFCs.

Manual O/C Ratio	Trial 1 O ₂	Trial 2 O ₂	Trial 1 C ₂ H ₂	Trial 2 C ₂ H ₂	Trial 1 MFC O/C	Trial 2 MFC O/C
0.3	3.54	3.58	12.58	12.56	0.28	0.29
0.4	3.89	4.00	11.83	11.80	0.33	0.34
0.5	4.48	4.47	10.95	10.98	0.41	0.41
0.6	5.38	5.19	10.48	10.80	0.51	0.48
0.7	5.94	5.74	10.65	10.48	0.56	0.55
0.8	5.79	5.85	9.91	9.98	0.58	0.59

Table 2.1: Shows the MFC recorded values for trials 1 and 2, and the corresponding O/C ratios obtained.

Column 1, titled manual O/C ratio, shows the O/C ratio being metered in by the old manual flowmeters. Columns 2 and 3 show the amount of oxygen that was actually metered in as measured by the MFCs across two trial runs. Columns 4 and 5 show the amount of acetylene that was actually metered in as measured by the MFCs across two trial runs. The precision of trial 1 compared to trial 2 indicate the repeatability of this experiment. Columns 6 and 7 show the MFC oxygen/acetylene ratios of trial 1 and 2, respectively. Thus, a discrepancy between the calibrated MFC ratio (columns 6 and 7) compared to the old manual flowmeters ratio (column 1) is seen.

The data was plotted to determine an equation to convert manual ratios to electronic ratios:

$$\text{Electronic ratio}[x] = -0.32x^2 + 0.999x \quad (2.1)$$

where x = manual ratio of O/C. This formula shows an average of 2.5% error converting the known values. Thus, the O/C described in this dissertation can be correlated to earlier work published by our group predating 2021 [18, 19, 32, 33].

2.1.4 Detonation procedure

Here, a description of the detonation procedure is presented and summarized by Figure 2.7.

The procedure is controlled through the automated program with operator-input settings. First, the chamber is pumped down to 0.15 to 0.03 atm (absolute pressure). This causes

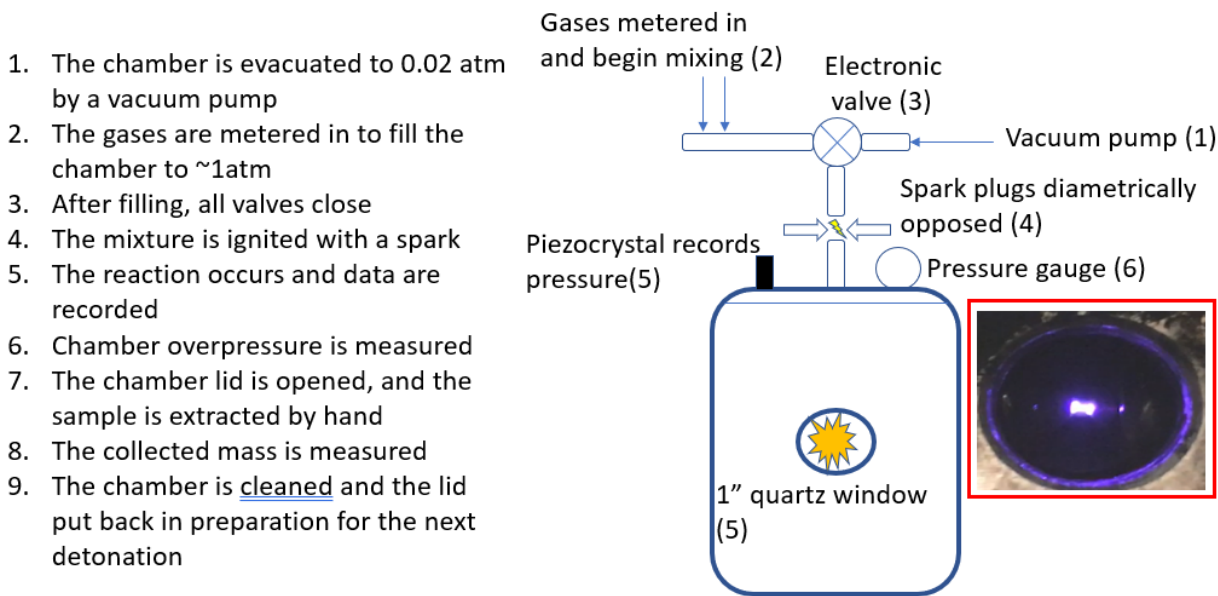


Figure 2.7: A step by step description of the detonation process is included alongside a diagram. A red box outlines a picture of the spark generated by the 10 kV step-up transformer.

a \pm 3% uncertainty in the mixture O/C ratio. A stronger vacuum is ideal but not always realized due to laboratory conditions. Second, the MFCs meter in the gaseous precursors in a fixed molar ratio of our choosing. The chamber is filled to zero-gauge pressure (1 atm absolute pressure). There is a one-second delay in the system as all valves close. About 20 ms before ignition, the spectrometer, photodiode, and piezocrystal are triggered to record data. Finally, the spark is generated and the mixture detonates.

After the detonation cycle is completed, we wait \sim 30 seconds to begin removing the graphene product from the chamber. First, chamber overpressure is measured. Then we use the valve on top of the chamber to fill a Tedlar sample bag for gas analysis. The remaining gas is vented into the snorkel. Next the manifold and chamber lid are removed and the sample is scooped into a tared container. The sample mass and approximate volume are measured. Finally, the chamber is cleaned with acetone and prepped for another detonation.

2.2 Instrumentation

This section presents a description of the instrumentation used to characterize the detonation material. Proper understanding of these instruments' operation, calibration, uses, and interpretation are critical to developing a full depiction of the sample properties.

2.2.1 Raman spectroscopy

Raman spectroscopy (raman) is a spectroscopy technique that measures vibrational modes of atoms. A laser, with wavelengths typically in the visible light or infrared range, excites the atoms in the material causing the energy phonons in the laser to shift, which are then scattered and measured by a detector. Three types of scattering result from this excitation: Rayleigh scattering, Stokes Raman scattering, and Anti-Stokes Raman scattering [34].

Rayleigh scattering is the elastic scattering that is a result of the energy being unchanged after interacting with the molecule. It is the predominant type of scattering, but it is not measured due to the lack of excitation. Stokes Raman scattering occurs during inelastic scattering when the molecule gains energy and causes the scattered photon to lose energy and increase wavelength. Anti-Stokes Raman scattering is the opposite process, where the molecule loses energy in the inelastic collision and the scattered photon gains energy and decreases wavelength. Due to most molecules being in the ground vibrational level, Stokes Raman scattering is the more probable of the two inelastic collisions, and thus is the type of intensity that is measured during Raman spectroscopy [34].

Raman is typically plotted as arbitrary units (a.u.) versus wavenumber, a quantity with units of inverse length that is directly proportional to energy. Though the incident laser wavelength is constant, the energy shift described above will increase a specific amount based on the chemical bonds of the molecule. Every molecule has a unique vibrational frequency fingerprint that can be identified by Raman [34]. For example, the differences between graphite and graphene, both six-membered hexagonal lattice carbon rings, can even be detected, making Raman one of the most important measurements when trying to characterize materials [35–38]. Furthermore, Raman can distinguish different types of soots,

graphites, graphenes, and etc., such as providing details about the layering of the material, the interaction between those layers, the defect/disorder of the material, and the crystallinity of the material [35–38].

Raman spectroscopy analyses were conducted using an Invia Reflex Renishaw microspectrometer equipped with an argon laser ($\lambda_0 = 532$ nm, source power 20 mW). We used a 100X objective (NA = 0.90) to focus the laser beam with a power of about 1 mW at the sample surface. The measurements using this instrument were performed by the author.

2.2.2 Powder X-ray diffraction

Powder X-ray diffraction (XRD) is a scattering technique that uses X-rays to measure the crystallographic structure of a powder material. X-rays cause elastic scattering by exciting the atoms to emit spherical waves in both constructive and destructive interference patterns [39]. Destructive waves cancel, whereas constructive waves add together to form what is known as Bragg's diffraction law,

$$2d\sin\theta = n\lambda \quad (2.2)$$

where d is the spacing between atomic layers, θ is the incidence angle of scattering, n is an integer, and λ is the wavelength of the X-ray. Constructive waves come from the crystalline lattice of the material, where the atoms are in a common structural arrangement. The more crystalline the material is results in more relative signal-to-noise ratio during the measurement. XRD is plotted as intensity of scattered X-rays versus the scattering angle, and characterization is performed by analyzing the peak location, intensity, and symmetry [39].

The d -spacing of materials are commonly on the order of magnitude of angstroms, which is similar to the wavelength of X-rays, and thus XRD can determine grain size of the material. Similar to Raman, XRD can also differentiate between soot, graphite, and graphenes, as well as different types of soots, graphites, and graphenes. All samples were measured with a D8 ADVANCE diffractometer (Bruker) with a $\text{Cu K}\alpha$ source of 0.15406 nm in wavelength. No instrument operations were performed by the author.

2.2.3 Transmission electron microscopy

Transmission electron microscopy (TEM) is a microscopy technique that allows imaging to occur on the scale of nanometers. The theoretical principles operate similarly to that of optical microscopes, except electrons are used instead of photons due to their smaller wavelength. An electron gun focuses beams of electrons through samples, where dark and light patterns show up due to the thickness of the material. Impenetrable (thick) samples will show up completely dark. TEM generally provides information on crystal structure, grain boundaries, layering, and can even produce diffraction patterns of the crystal. Like Raman and XRD, TEM can distinguish soot, graphene, and graphite, as well as different types of soots, graphenes, and graphites [40].

High resolution TEM characterization was performed at the Microscopy and Analytical Imaging Research Resource Laboratory (MAI) at the University of Kansas. The measurements were performed on a Hitachi H-8100 (200 keV) on copper grids. Measurements were also taken with a CM-100 (100 keV) TEM instrument here at K-State. No samples were measured by the author as an operator.

2.2.4 Specific surface area measurements

Brunauer–Emmett–Teller (BET) is an analysis technique to measure the specific surface area (SSA) of solid materials using physical adsorption of gas molecules to form a monolayer coating while saturating the sample’s pores. Inert adsorbent gas, such as nitrogen at 77 K, argon at 87 K, and carbon dioxide at 273 K, is flowed into the sample while monitoring the saturation pressure compared to equilibrium pressure, called P/P_0 . Before this takes place, sample preparation involves heating under a gentle vacuum to bake off surface volatiles and water, and then the dry weight must be measured to at least four significant figures of accuracy in the milligram range, such as 123.4 mg, to produce an accurate result. With the accurate dry mass of the sample known, the adsorption process takes place, and the adsorption equation from BET theory, $1/v(P_0/P - 1)$, where v is the volume of gas required to form a monolayer on the adsorbent per gram of adsorbent, is plotted versus P/P_0 [41, 42].

The linear region of the slope of the resulting graph, called an isotherm, is used to calculate the SSA by the machine. For most materials, the slope in the range $0.05 \leq P/P_0 \leq 0.3$ is sufficient to derive an accurate SSA. This is because most materials have pore sizes greater than 2 nm in size. Pore sizes of ≥ 50 nm, ≥ 2 nm, and ≤ 2 nm are referred to as macroporous, mesoporous, and microporous materials, respectively. BET theory was invented for macroporous and mesoporous materials, but struggles to accurately calculate the SSA of microporous materials because the often sub-nanometer pore size is the same order of magnitude as the gas molecules, preventing the gas from properly saturating the pores. The surface coating instead gives an “effective SSA”, which while not the true SSA, represents the accessible SSA during surface chemical and physical interactions. Exfoliation of nanoporous samples may increase the pore size [41, 42].

For carbon samples, using nitrogen as the adsorbate gas is often not recommended, especially for microporous samples, due to the quadrupolar moment that can cause electrical “sticking” to the surface of the sample, further preventing the gas from accessing the pores. Argon is now the standard for BET machines due to its lack of a quadrupole; carbon dioxide is most recommended for carbon samples, but requires a more expensive and elaborate machine setup [41, 42].

The BET machine used is a Quantachrome autosorb iQ with nitrogen at 77 K. The samples were measured by author or under his supervision. Argon has not yet been set up at k-state.

2.2.5 Scanning electron microscopy

Scanning electron microscopy (SEM) is an electron microscopy technique similar to that of TEM. Whereas TEM detects transmitted electrons that contain information about thin sample morphology, layering, and diffraction, SEM detects reflected electrons that contain information about surface morphology and crystalline structure. Often SEM instruments image at the microscale, but some capable instruments can resolve at the nanoscale [43].

The SEM for two samples was taken by Surface Science Western using a Hitachi SU8230

Regulus ultra-high resolution field emission scanning electron microscope (FESEM). The samples were coated with a thin layer of iridium to minimize sample charging during imaging. Further SEM images were taken by a Hitachi S-3400N, with the author as the instrument operator.

2.2.6 Gas chromatography

Gas chromatography (GC) is a chromatography technique in which the chemical components of a sample are separated and identified. Liquid samples may also be used with an instrument option to vaporize the sample into a gas phase during analysis. The thermal conductivity relative to helium is plotted versus time, in which chemicals may be identified by the time in seconds at which they peak. A molar representation of the entire sample may be obtained upon comparing the area underneath the curve of a each chemical peak with that of the area underneath the curve of the machine-specific calibration of that chemical [44].

A Gas Chromatograph model 310 configured with a traditional 4-filament thermal conductivity detector that can heat to 275 °C was used. 5-10 mL of gas were injected into the instrument, and the sample was analyzed at a column oven temperature ranging from 50 – 100 °C. No machine operations were performed by the author.

2.2.7 Fourier-transform infrared spectroscopy

Fourier-transform infrared spectroscopy (FTIR) is a spectroscopy technique in which infrared radiation is directed through a sample, producing an absorption spectrum unique to every molecule. Once the raw data on infrared spectroscopy is obtained, a Fourier transform is applied to the data in order to generate the graph, in which transmittance is plotted versus wavenumber. Gases, liquids, and solids can all be measured by FTIR [45].

The instrument used was a Agilent Cary 630 FTIR spectrometer, collected over range of 400 – 4000 cm^{-1} using the attenuated total reflectance (ATR) sampling accessory. Sample was loaded into the diamond sampling window, then the press tip lowered so that there was contact made between the sample and infrared energy emitting from the diamond window.

FTIR was not operated by the author.

2.2.8 Zeta potential

Zeta potential is the electrical potential difference between chemicals in a colloid. The strength of the charge is correlated with the stability in the system, with values below ± 30 mV considered to be susceptible to agglomeration and values higher considered to be stable suspensions due to electrical repulsion forces. Cationic samples have a (+) charge, whereas anionic samples have a (-) charge [46].

The zeta potentials for all samples were measured in water. DLS and zeta potential measurements were done using a ZetaPALS ζ potential analyzer purchased by Brookhaven Instruments Corporation. No instrument operations were performed by the author.

2.2.9 Atomic force microscopy

Atomic force microscopy (AFM) is a microscopy technique in which a silicon probe, connected to a piezocrystal and tracked by a laser, gently taps the surface of the sample as it moves around, generating a 3-dimensional image based on the topological differences in the deflection of the probe. This method allows sub-nanometer topographies to be measured. As there are no lenses involved, AFM does not have the common issues of optical and electron microscopy such as diffraction, aberration, and etc [47].

AFM images were taken by a Nanoscope AFM image system (Digital Instruments) utilizing TESPA-HAR probes in tapping mode. The images were then analyzed by Bruker's Nanoscope software. No measurements were performed by the author.

2.2.10 Elemental analysis

Elemental analysis, also known as CHNO (carbon, hydrogen, nitrogen, oxygen) analysis is a technique of heating a sample in an oxygen-rich atmosphere on a scale balance to determine the molar composition of the sample via GC [48]. The elementary analysis was performed by

ALS Environmental, Tucson, AZ. They went bankrupt in 2020. Graphene powders (0.05g each) were heated to 200 °C for 1h to remove adsorbed H₂O, N₂, etc. and then burned at > 1000 °C in pure O₂ atmosphere. C was measured as CO₂, and H as H₂O via gas chromatography. NO and NO₂ were reduced over a Ca/Al alloy. The resulting NH₃ was titrated with diluted H₂SO₄.

2.2.11 Thermogravimetric analysis

Thermogravimetric analysis (TGA) is a thermal analysis technique in which a furnace containing a precision balance continuously measures the sample mass while the temperature changes over time. Multiple background furnace environments are available such as a vacuum, oxidizing gas, reducing gas, inert gas, air, and more, which taken into account with the change in mass relative to temperature provides clues about various physical and chemical phenomena. The change in mass is plotted versus temperature [49].

The TGA machine used was a Shimadzu TGA-50 Analyzer, where 5 mg of sample was heated under a stream of nitrogen gas flow (10 mL/min) from 25 to 600 °C at a rate of 10 °C/min. TGA was not operated by the author.

2.2.12 Sonication, exfoliation, and solvent dispersion

Sonication is the use of high frequency, often ultrasonic (> 20 kHz) vibrations for applications such as exfoliating materials, degassing dissolved gases from liquids, stirring gases through a barrier, and dispersing nanoparticles in solvents. For our purposes, we are interested in exfoliation and solvent dispersion. Exfoliation is a post-processing treatment of a material in which layers are stripped apart, changing the properties of the material. Solvent dispersions are the mixing of two more or materials to obtain a colloid or solution [50].

Sonication was performed by a Branson Bransonic m1800 ultrasonic bath or shaking via hand. All measurements were taken by the author.

Chapter 3

Acetylene-oxygen fill mixtures

This chapter will focus on presenting the experiments with acetylene-oxygen mixtures and the resulting graphenes' characterization. It will cover a paper that was submitted to journal Nano Select as well as additional information that was omitted from the journal submission.

3.1 Synthesis of turbostratic nanoscale graphene via chamber detonation of oxygen/acetylene mixtures

Here the paper that was submitted to journal Nano Select is presented. Acetylene-oxygen fill mixtures, described as molar ratios of oxygen/carbon = O/C , are varied from $O/C = 0.25$ to 0.75 and their properties studied. This O/C notation will be maintained throughout this dissertation. Of importance is to note the result that by changing the oxygen content in the fill mixture the properties of the material also change to what we describe as “low O/C ” and “high O/C ” graphene.

The introduction in the journal submission is mirrored to the introduction of this dissertation.

RESEARCH ARTICLE

Synthesis of turbostratic nanoscale graphene via chamber detonation of oxygen/acetylene mixtures

Justin P. Wright¹  | Shusil Sigdel¹ | Stephen Corkill¹ | Jose Covarrubias² |
 Levon LeBan² | Arjun Nepal¹ | Jun Li² | Ranjith Divigalpitiya³ |
 Stefan H. Bossmann² | Christopher M. Sorensen¹ 

¹ Department of Physics, Kansas State University, Manhattan, Kansas, USA

² Department of Chemistry, Kansas State University, Manhattan, Kansas, USA

³ Department of Chemistry, Western University, London, Ontario, Canada

Correspondence

Christopher M. Sorensen, Department of Physics, Kansas State University, Manhattan, KS 66506, USA.

Email: sor@phys.ksu.edu

Funding information

Carbon-2D

Abstract

A study of the detonation synthesis method to make graphene and the properties of the resulting graphene is presented. The gaseous precursors are mixtures of oxygen and acetylene with oxygen/carbon molar ratios of $O/C = 0.25$ to 0.75 . Chamber pressure and temperature data indicate pressures ≤ 300 psi and temperatures of 2550 ± 100 K after initiation of the reaction mixture. The graphene material collected from the chamber after the detonation was characterized by Raman, XRD (X-ray diffraction), BET, SEM (scanning electron microscopy), TEM (transmission electron microscopy), and so on. The material properties divide into two groups: low O/C (≤ 0.45) and high O/C (≥ 0.5). Low O/C graphene appears as a low density, aerosol gel with ~ 8 weakly associated, disordered turbostratic layers with a lateral extent of 20 to 30 nm. High O/C graphene appears as a denser powder with ~ 30 weakly associated turbostratic layers, with a lateral extent of 100 to 200 nm. We conclude, as we have previously, that the high detonation temperature during the reaction is the primary reason that graphene is formed rather than soot. Differentiation into two types of graphene products is hypothesized to be a result of aggregation kinetics to form a static gel that pre-empts layering (stacking) when O/C is low.

KEYWORDS

aerosol gel, detonation synthesis, graphene, high temperature, O_2/C_2H_2 reactions, turbostratic

1 | INTRODUCTION

Graphene is a 2D hexagonal lattice of sp^2 bonded carbon that has unique and interesting properties including great material strength,^[1] electrical conductivity,^[1,2,3] and novel optical properties.^[4] Given graphene's remarkable qualities, it has great promise for a variety of future applications; and given this promise, there is strong motive to develop

synthetic methods that are scalable and will lead to the manufacture of graphene.

Graphene was first produced by mechanical exfoliation,^[5] which is not amenable to scale up. Bulk quantities can be obtained via methods such as Hummers' method^[6-9] and chemical vapor deposition.^[10,11] All these leading graphene-producing techniques are expensive ($\$70$ - 200 kg^{-1}), require large amounts of energy, contain

This is an open access article under the terms of the [Creative Commons Attribution](https://creativecommons.org/licenses/by/4.0/) License, which permits use, distribution and reproduction in any medium, provided the original work is properly cited.

© 2021 The Authors. *Nano Select* published by Wiley-VCH GmbH

impurities, and often produce undesirable byproducts such as benzene derivatives.^[12] Thus, there is a market need to produce high quality and green graphene at low cost.

We have discovered a controlled detonation process for the synthesis of multilayer graphene nanosheets.^[13,14] The process is a novel, cost-effective and eco-friendly, one-step method that involves detonation of a gas-phase hydrocarbon (typically C_2H_2) with oxygen (O_2) in a multiliter chamber. Detonation synthesis has several advantages such as simplicity, high productivity, economic viability, and short synthesis time. This synthesis method is catalyst-free and generates syngas as useful by-products during synthesis. Recent work by Gaur et al. has shown that detonation synthesis of graphene aerosol gels can be used to make micro-supercapacitors.^[15]

The premise of detonation synthesis is that the high temperature conditions of the shock wave are important to the formation of graphene. Earlier work from our group^[13,14] found high temperature (3000 K) to be a key component of graphene synthesis. Kim et al.^[16] also demonstrated shell soot, a unique graphene-like carbon generated from a laser augmented acetylene diffusion flame reaching 3200 K. More recently, rapid joule heating^[17] has followed these two discoveries to achieve high temperature conditions that yield graphene.

We have demonstrated a scaled-up version of the detonation graphene process that yielded approximately 2 kg per day of inexpensive graphene. With further optimization of the pilot scale plant, producing more mass in a shorter time is possible. Thus, detonation synthesis of graphene is a unique, economical and industrially scalable method that will enable graphene to enter the materials marketplace.

The present embodiment of the controlled detonation method uses oxygen and acetylene as precursors. This paper will focus on different precursor fill ratios for the production of graphene with the objective to compare the characterizations of the graphenes subsequently produced. We describe these ratios as molar ratios $O_2/C_2H_2 = O/C$. The mixtures we will discuss are $O/C = 0.25, 0.3, 0.35, 0.4, 0.45, 0.5, 0.6, \text{ and } 0.75$. We will refer to 0.25–0.45 samples as low O/C , and 0.5–0.75 samples as high O/C for reasons that will become apparent.

2 | MATERIALS AND METHODS

2.1 | Description of the detonation chamber

The detonation chamber is a 16.7 L cylinder with internal height 37 cm and diameter 24 cm made of 2.54 cm thick

aluminum. The chamber is connected to a gas manifold operated by a control box which automates our system via a LabVIEW program. In the manifold immediately above the chamber is a cubical feature that contains electrodes to conduct a spark and ignite the mixture. There is a valved port on top of the chamber to collect gas after detonation. Around the circumference of the chamber are three thick fused quartz windows to afford optical access to the interior. On the top of the chamber is a plugin for a piezoelectric crystal to collect pressure impulse data.

2.2 | Detonation procedure

Figure 1 describes the apparatus setup and detonation procedure. The procedure is controlled through an automated program with operator-input settings. First, the chamber is pumped down to 0.15 to 0.03 atm (absolute pressure). This causes a $\pm 3\%$ uncertainty in the mixture O/C ratio. Second, electronic valves meter in the oxygen (O_2) and acetylene (C_2H_2) in a fixed molar ratio of our choosing. The chamber is filled to zero-gauge pressure (1 atm absolute pressure). There is a one-second delay in the system as all valves close. Next, a spark of 10,000 V is generated from an industrial step-up transformer and the mixture detonates.

2.3 | How data are collected

Temperature: A fiber optic at one quartz window collects light from the detonation flash and transmits that to an Ocean Optics Ocean FX spectrometer (range 200–1050 nm) triggered to collect data 20 ms before the spark is thrown. The light collection integration time can be varied from 20 μs –10 ms, with a 1.8 ms buffer time between each shuttered integration time. This means a minimum of 1.82 ms occurs between each measurement.

Pressure: A piezocrystal is plugged into the top of the chamber. This records an impulse data in psi at a response time of 19.5 μs .

2.4 | Collecting the sample and cleaning the chamber

After the detonation cycle is completed, we wait ~ 30 seconds to begin removing the graphene product from the chamber. First, chamber overpressure is measured. Then we use the valve on top of the chamber to fill a Tedlar sample bag for gas analysis. The remaining gas is vented into a fume hood. Next the manifold and chamber lid are removed and the sample is scooped into a tared container. The sample mass and approximate volume are measured.

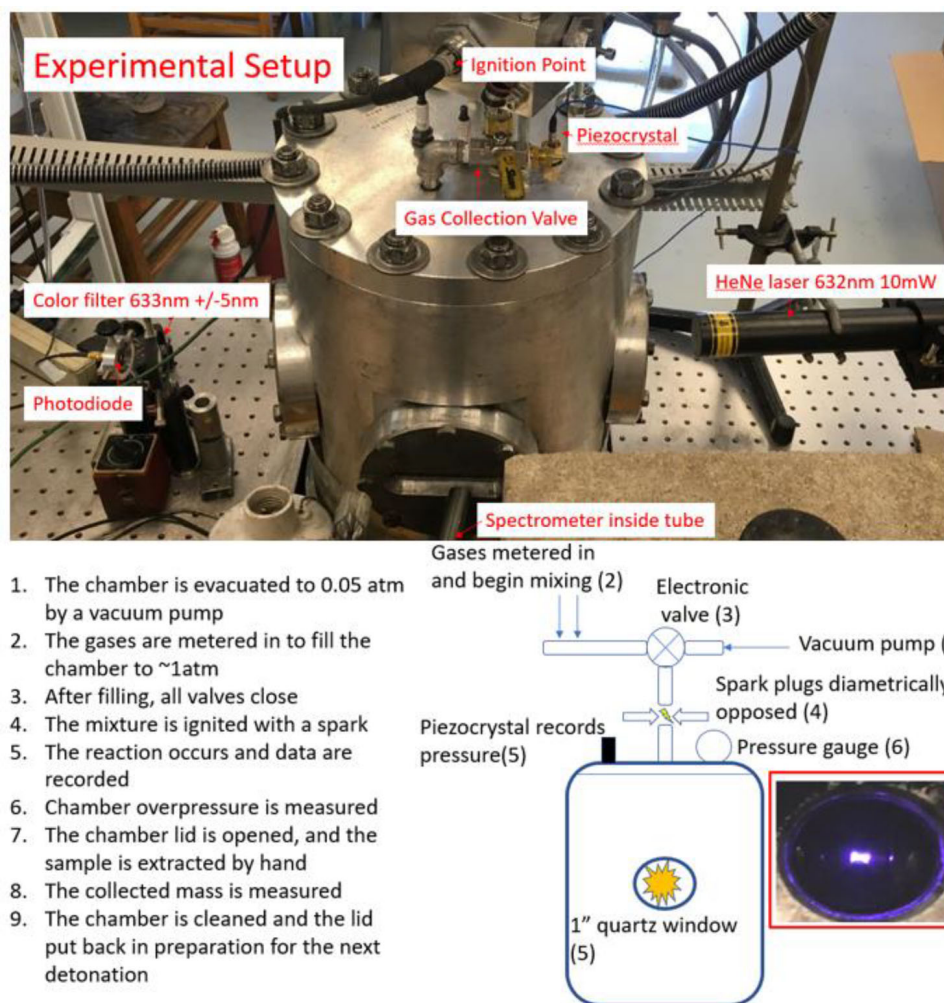


FIGURE 1 Top: White labels with red text and red arrows depict the reactor vessel details. Bottom: A step by step description of the detonation process is included alongside a diagram. A red box outlines a picture of the spark generated by the 10 kV step-up transformer

Finally, the chamber is cleaned with acetone and prepped for another detonation.

3 | MEASUREMENTS MADE DURING DETONATION

3.1 | Detonation pressure

Figure 2A depicts a representative pressure curve from each O/C ratio (not averaged data). The piezocrystal only records impulse pressure and is not a continuous pressure monitoring device. We describe our method as a detonation because high pressures are reached. A pressure wave is considered a detonation as it exceeds ~100 psi (6.6 atm).^[18] The wave is supersonic as it compresses the reactants, causing chemical reactions that release energy and continue to propagate the wave.^[18]

There is a linear increase in peak pressure with O/C, starting around 192 psi (13 atm) at O/C = 0.25 to nearly

315 psi (25 atm) at O/C = 0.75. Figure 2B shows that the rise time it takes to reach peak pressure varies with O/C.

We interpret the quick pressure rise times to imply detonations formed from the impulse shock of the spark, a process referred to as direct ignition.^[18] Slower rise times imply deflagrations that transition to detonations (thermal initiation) that take time and turbulence to form a detonation wave, a process referred to as self-ignition.^[18] Light is being emitted during this whole process for both reactions as indicated by the spectrometer (see Section 3.2, below).

3.2 | Radiation temperature via the spectrometer

Figure 3A shows a typical example of the spectrum of the light emitted as a function of time during a detonation. The spectrum is continuous with no emission lines and could be fit to Planck's black body law^[14] as shown below. At higher wavelengths, the spectrometer gets noisier making

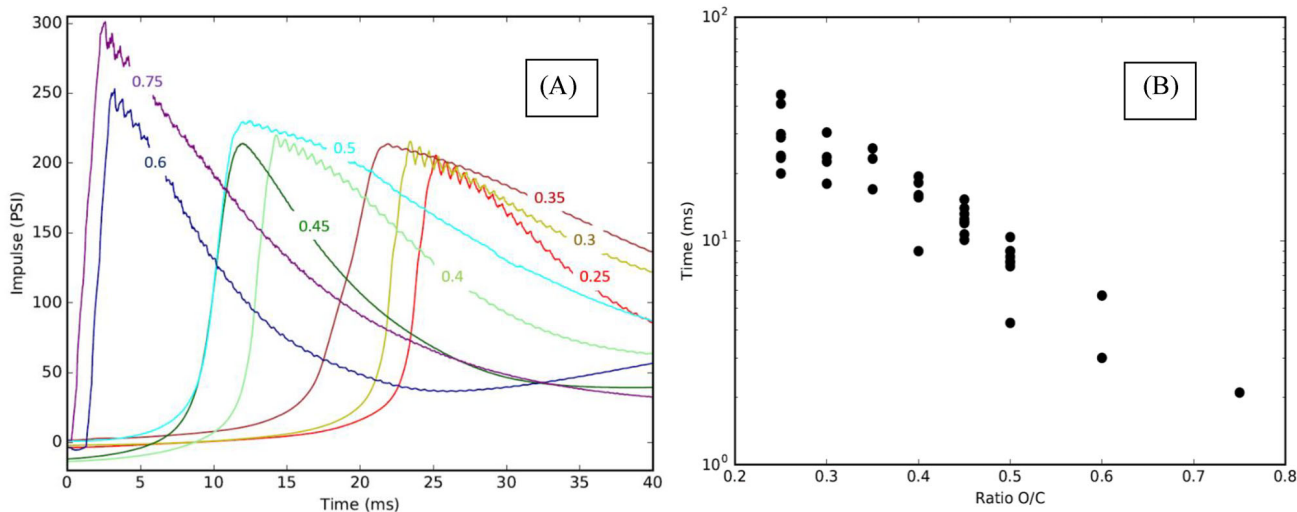


FIGURE 2 A, Chamber pressure versus time for different O/C ratios. Each detonation begins at 0 ms, taking 1–30 ms to reach peak pressure dependent on O/C. B, Pressure rise time versus O/C ratio. Rise time is plotted on a log axis

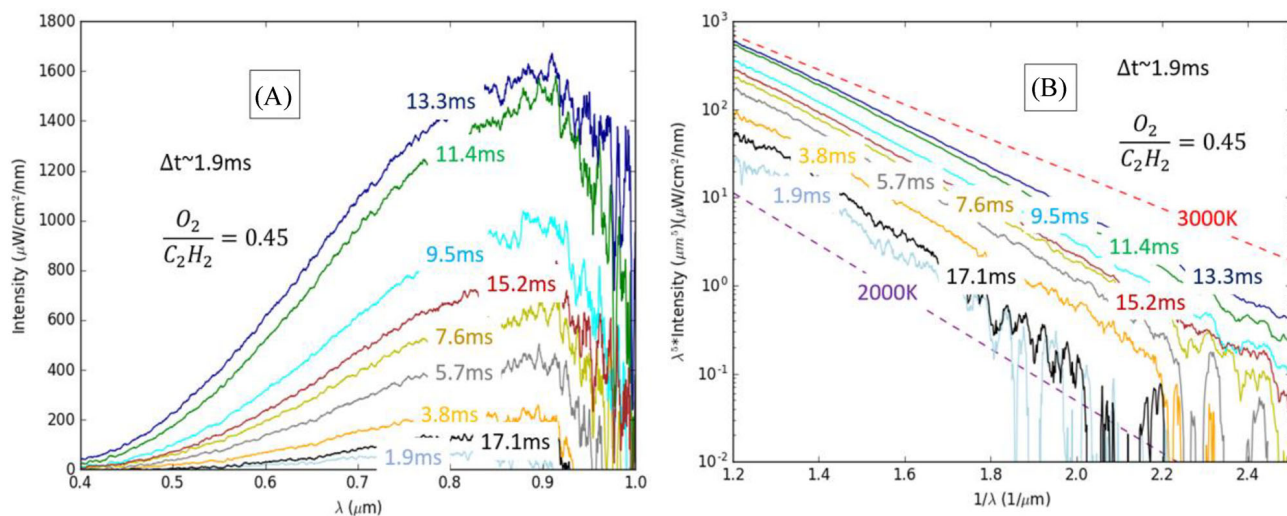


FIGURE 3 Blackbody spectra from a detonation of a sample O/C = 0.45 mixture collected via the spectrometer. The nine spectra lines increase in time with $\Delta t \sim 1.9$ ms between each line. A, Blackbody spectrum and (B) linearized blackbody between two Planck blackbody temperatures (dashed lines)

analysis above $\lambda = 0.9 \mu\text{m}$ difficult. The time at which the intensity peaks is 13 ms in Figure 3A.

The Planck thermal radiation law for a body at temperature T , gives the spectral energy density $B(\lambda, T)$ as a function of the emitted wavelength λ . Wien's approximation to the Planck radiation law, Equation (1), assumes $hc \gg \lambda k_B T$, where h is the Planck constant, c the speed of light, and k_B is the Boltzmann constant. This condition holds for optical wavelengths and the temperatures we observe. Thus

$$B(\lambda, T) \cong \frac{2hc^2}{\lambda^5} \left(e^{\frac{-hc}{\lambda k_B T}} \right) \quad (1)$$

Rearranging terms and applying a logarithm yields

$$\text{Log}(\lambda^5 * B(\lambda, T)) \cong \text{Log}(2hc^2) - \left(0.434 \frac{hc}{k_B T} \right) \left(\frac{1}{\lambda} \right) \quad (2)$$

With this, a Wien plot can be made by plotting $\text{Log}(\lambda^5 * B(\lambda, T))$ versus inverse wavelength. Such a plot is linear if it obeys the Planck law and if the emissivity of the radiating material is wavelength independent. Figure 2B shows the data plotted as prescribed by Equation (2). The results are linear implying Planck thermal radiation and a constant emissivity. The temperatures clearly lie between 2000 and 3000 K for this example.

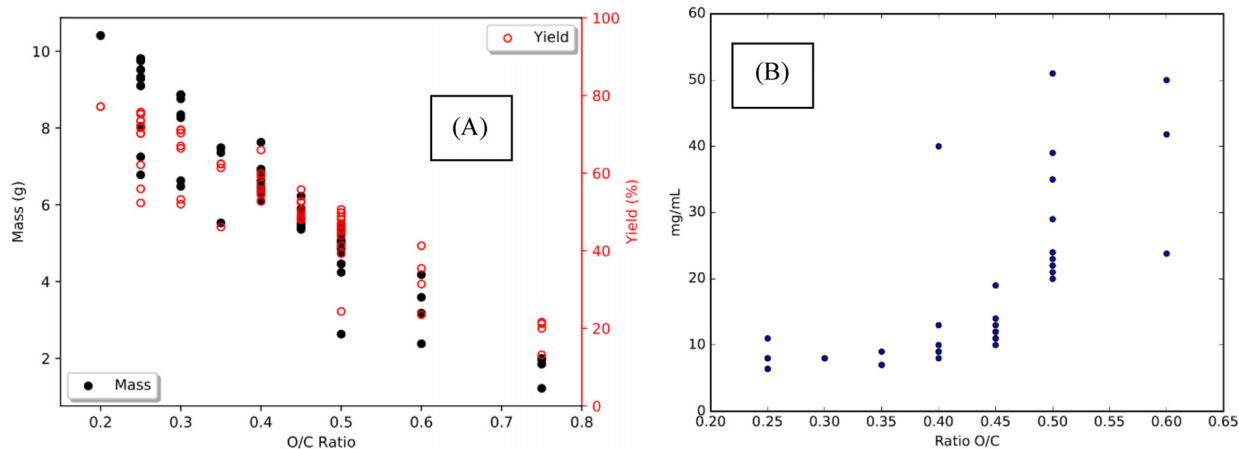


FIGURE 4 A, Graphene mass and yield versus O/C ratio. Yield is calculated as amount of carbon collected after detonation compared with the total carbon put into the chamber in the form of acetylene (C_2H_2). Yield is plotted in open circles; mass is plotted in closed circles. B, Graphene powder mass density versus O/C ratio

From these data, time resolved temperature measurements can be made. These measurements come with the caveat of long integration and buffer times between each snapshot described earlier. Therefore, each intensity and temperature measurement are the average of the rapidly changing temperatures in the chamber. A total of 40 temperature measurements were made. We find the peak temperatures to be $T = 2550 \pm 100$ K independent of O/C in the range O/C = 0.25 to 0.60. One measurement was made at O/C = 0.75 to find $T = 4200$ K. We did not attempt to reproduce this measurement. These quoted peak temperatures are very likely averages of a high temperature peak followed by the rapid cooling known to follow in this detonation method^[14] and not time resolved by our spectrometer, and thus the reported values here might be lower than the actual peak.

4 | MEASUREMENTS COLLECTED AFTER DETONATION

4.1 | Mass, yield, density

Visual inspection of the graphene samples removed from the chamber after detonation showed gray powdery samples for high O/C ratios and black fluffy samples for lower O/C ratios. The mass and density are acquired as described above. Yield is calculated as the total amount of available carbon from the acetylene that turns into graphene. Figure 4A shows the total mass and the percent graphene yield as a function of O/C.

The mass is expected to decrease with higher O/C as the total amount of carbon available in the form of C_2H_2 decreases. The yield is expected to decrease as well because more carbon can burn to carbon oxides.^[19]

TABLE 1 Elemental analysis of O/C samples with graphite^[21] and soot^[22] as a reference

Sample [O_2/C_2H_2]	C [%]	H [%]	N [%]	O [%]
Graphene: 0.25	99.8	0.15	0	0.05
Graphene: 0.30	99.8	0.15	0	0.05
Graphene: 0.35	99.7	0.12	0	0.18
Graphene: 0.40	98.9	0.08	0	1.02
Graphene: 0.45	99.0	0.05	0	0.95
Graphene: 0.50	98.6	0.05	0	1.35
Graphene: 0.60	98.7	0.01	0	1.29
Graphene: 0.75	98.0	0	0	2
Graphite ^[19]	98.6	0	0	1.4
Soot ^[20]	96	3.6	0	0.4

Figure 4B shows that the mass density of the produced graphene increases as O/C increases. Previous work with this system^[20] showed that gelation of the aerosol occurs, especially at higher volume fractions of the graphene carbon aerosol that forms immediately after the detonation. Higher volume fractions occur at lower O/C ratios due to shorter gel times, which is further explored in section 5.3. The result is an aerosol gel with densities as low as 3 mg cc^{-1} . This material is fragile and inadvertent crushing occurs while collecting the samples.^[20]

4.2 | Elemental analysis

Table 1 shows CHNO analyses of our graphene product was performed by Desert Analytics, Tucson, AZ 85714 and in the core chemical laboratory of the University of Kansas Medical Center via method of organic elemental analysis. The results indicate exceptionally high carbon purity.

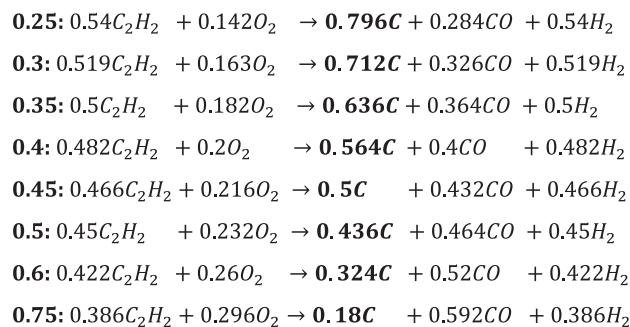


FIGURE 5 Predicted chemical reactions based on the average measured yield of each O/C ratio and the GC and FTIR gas analyses of the product. The carbon collected from the chamber is in bold black. An additional 0.016 mol of O_2 was present in each oxygen term from the small amount of air remaining after vacuum

The composition becomes more similar to graphite as O/C increases with increased oxygenation in the sample. There is negligible hydrogenation for all samples, unlike typical soot.

4.3 | Gas analysis

Gas chromatography (GC) and Fourier Transform Infrared Spectroscopy (FTIR) analysis indicate the only detectable gases formed are hydrogen and carbon monoxide, a mixture commonly known as syngas. There is also an unquantifiable and insignificant amount of water.^[23]

Figure 5 shows the hypothesized chemical reaction that are consistent with GC and FTIR analysis. Our analyses gave no indication of polycyclic aromatic hydrocarbons (PAHs), unburned acetylene, carbon dioxide, or other hydrocarbon formations in the sample.

4.4 | Specific surface area

Figure 6 shows that the Brunauer-Emmett-Teller (BET) measured specific surface area (SSA) decreases with increasing O/C. The 0.3 ratio was measured using three different protocols at two different facilities: 77 K with N_2 ; 87 K with Ar; and 273 K with CO_2 . Here at K-State we only did a N_2 measurement, and all three were measured by Quantichrome Anton Paar. All three methods produce the same results. The average half-pore size distribution of the 0.3 sample was determined to be around 0.4 nm.

4.5 | Raman spectroscopy

Raman spectroscopy analyses were conducted using an Invia Reflex Renishaw microspectrometer equipped with

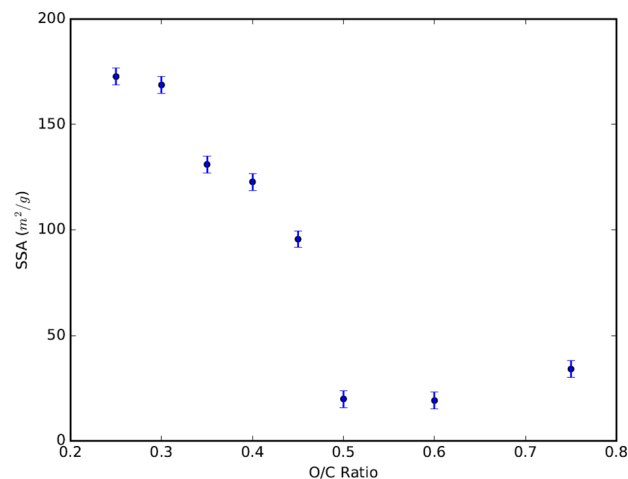


FIGURE 6 Specific surface area versus O/C ratio

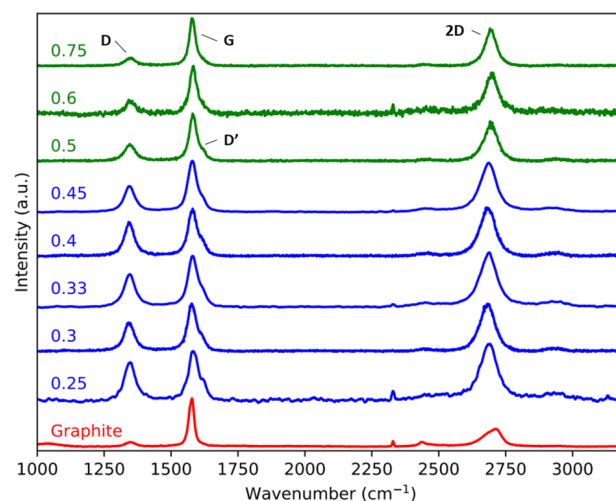


FIGURE 7 Raman spectra of samples prepared at low O/C ratios in blue, high O/C ratios in green, and in comparison to graphite crystals in red. All spectra are normalized to have the same G peak intensity. Not every peak is labeled

an argon laser ($\lambda_0 = 532$ nm, source power 20 mW). We used a 100X objective (NA = 0.90) to focus the laser beam with a power of about 1 mW at the sample surface.

The Raman spectra of our material in Figure 7 show all the features characteristic of graphene with *D*, *G* and *2D* bands. The *D*, *G*, and *2D* peaks of the low O/C are centered at 1345, 1579, and 2683 cm^{-1} , respectively. The *D*, *G*, and *2D* peaks of the high O/C are centered at 1349, 1580, and 2696 cm^{-1} , respectively. The *D*, *G*, and *2D* peaks of the graphite are centered at 1349, 1578, and 2715 cm^{-1} , respectively. For reference, the positions of the *G* and *2D* bands of a single layer graphene at 532 nm are 1585 and 2676 cm^{-1} , respectively, in literature.^[24–27]

Figure 7 also shows a significant *D* peak for the low O/C samples. This peak implies disorder in the material. This conclusion is corroborated by the appearance of a *D'* peak,

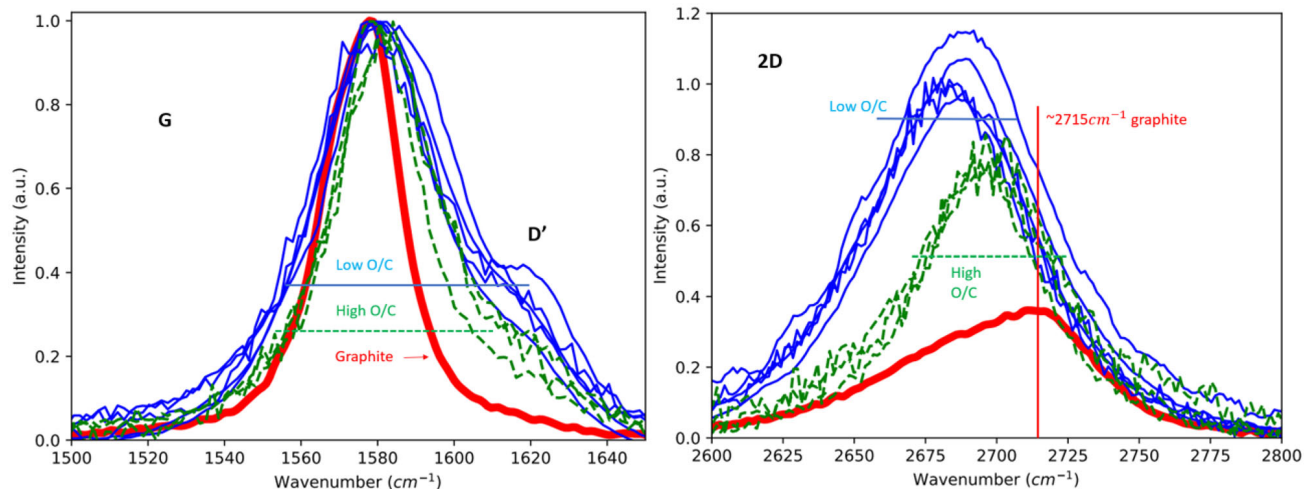


FIGURE 8 Raman G peaks (left) and $2D$ peaks (right) for samples prepared at all O/C ratios, low O/C in blue line, high O/C in green, dashed line, and graphite crystals in red, thick line. All spectra are normalized to have the same G peak intensity of 1.0 as in Figure 7. D' band shoulder near 1600 cm^{-1} is indicated. Vertical line at 2715 cm^{-1} is the center $2D$ peak position for graphite

seen as a shoulder on the high frequency side of the G peak. Significant disorder causes the G peak to shift to lower frequencies, and, indeed, the G peak of our material is at lower frequency than single layer graphene (SLG).

Figure 8 shows a comparison of the Raman $2D$ peak to that of the literature.^[25–28] SLG lies within the range of $2660\text{--}2680\text{ cm}^{-1}$ at the excitation wavelength of 532 nm .^[27] Notably, the literature has shown there is a shift in peak position to higher frequency as the layering increases^[24–27]; for example, bi-layer graphene is about 20 cm^{-1} higher. The peak location of our samples shift to higher wavenumbers with higher O/C, indicating more layers.

Figure 8 also examines the G peak of our material compared to graphite. It is known that the G peak of SLG is at $\sim 1585\text{ cm}^{-1}$,^[27] and the peak moves to lower wave numbers as the layers increase approaching that of graphite at 1579 cm^{-1} . Our material's G peak are comparable the location of graphite, indicating the presence of layers. However, further exploration of Raman (Figure 10) will show that our graphene is in fact turbostratic. In addition, our XRD results, to be discussed in a later section (Section 4.6), show a larger interlayer spacing than graphite (0.346 to 0.351 nm vs. 0.337 nm) and the asymmetry of peaks (100), (004), and (110) due to the Warren effect, also indicating that our materials are turbostratic in nature. It is known that many factors, such as defects, configuration of interlayer stacking, doping, strain, stress, and temperature, may perturb the Raman spectra of SLGs and cause the G peak to downshift.^[27]

Figure 9 plots the two intensity ratios I_{2D}/I_G and I_D/I_G versus the O/C ratio. An intensity ratio of $I_{2D}/I_G > 0.5$ is consistent with bilayer graphene, and an intensity ratio of

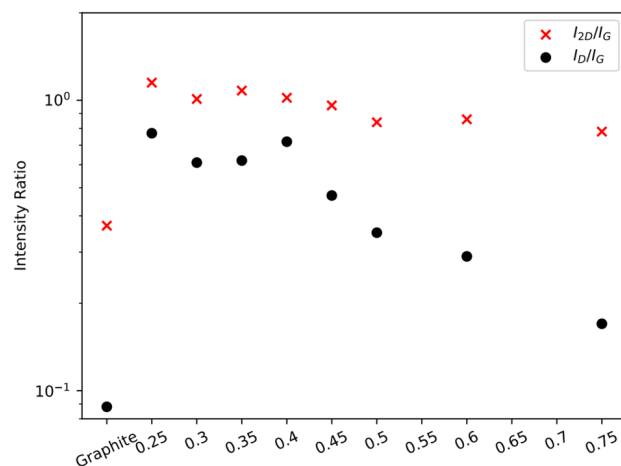


FIGURE 9 Intensity ratio of I_{2D}/I_G (red crosses) and I_D/I_G (black dots) plotted on a log scale versus O/C

$I_{2D}/I_G > 2$ is consistent with SLG.^[24] Our low O/C samples have $I_{2D}/I_G > 1$, our high O/C samples have $I_{2D}/I_G > 0.75$, and graphite has $I_{2D}/I_G \sim 0.4$. The ratio $I_D/I_G \approx 0.75$ for low O/C, but falls abruptly near O/C = 0.5 to values of ~ 0.2 . As discussed above, higher I_D/I_G indicates higher degrees of disorder for low O/C samples compared to high O/C samples, and both have higher I_D/I_G compared to the graphite crystals, which, due to its high degree of order, is expectedly low.

Figure 10 shows Raman measured from Surface Science Western (Renishaw InVia Raman Spectrometer, wavelength = 514 nm , 2.41 eV) with a better signal to noise ratio examining O/C = 0.3 and 0.5 samples. These samples were chosen as representatives of low O/C and high O/C. Turbostratic peaks can be seen for both samples. The D peak,

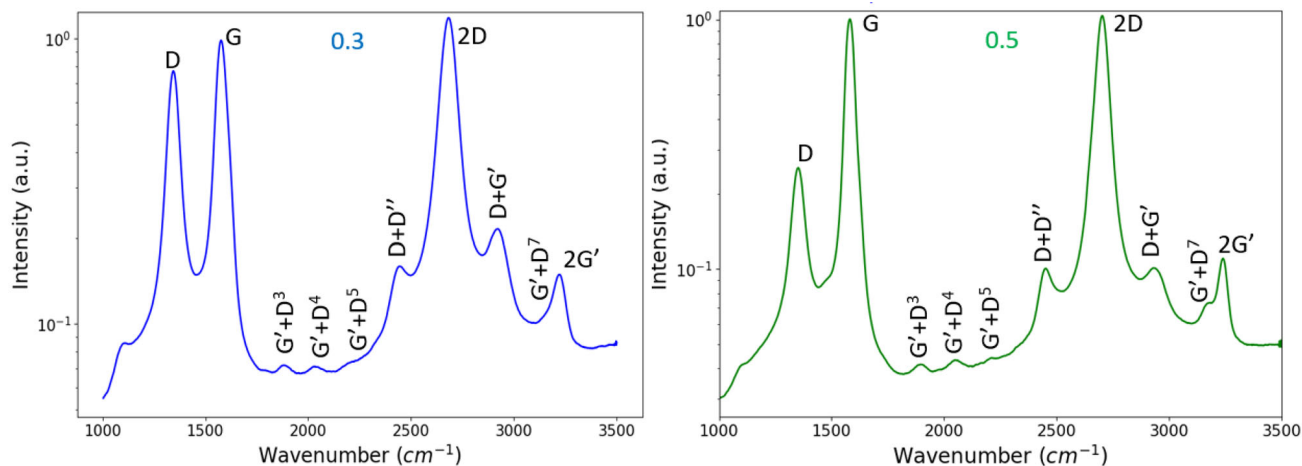


FIGURE 10 Log plots of low O/C (0.3, blue) and high O/C (0.5, green). Figure is the result of 10 runs and a running average to reduce noise and scaled such that $I_G = 1.0$

G peak, and $2D$ peak of the 0.3 sample are located at 1345, 1577, and 2675 cm^{-1} respectively when adjusting from a 514 nm to a 532 nm excitation wavelength.^[27] The D peak, G peak, and $2D$ peak of the 0.5 sample are located at 1352, 1582, and 2695 cm^{-1} respectively when adjusting from a 514 nm to a 532 nm excitation wavelength.^[27] These results are comparable to the first Raman measurements with slight differences in peak locations attributed to instrument noise clearly seen in the Figure 7 and Figure 8 Raman spectra.

The peaks $G'+D^3$ and $G'+D^4$ at positions 1885 and 2035 cm^{-1} in the low O/C and 1897 and 2052 cm^{-1} ^[30,31] in the high O/C materials indicate that our material has a turbostratic nature. Turbostratic graphene has random relative rotation between adjacent layers which causes the π -orbital hybridization between adjacent graphene layers found in graphite to dissipate. Consequently, multilayer graphene such as ours will have an electronic structure very similar to that of CVD SLG.^[27,31] Regarding the magnitude of these peaks, for the 0.3 sample, $\frac{I_G}{I_{G'+D^3}} \cong 16$ and $\frac{I_G}{I_{G'+D^4}} \cong 15$; whereas for the 0.5 sample, $\frac{I_G}{I_{G'+D^3}} \cong 32$ and $\frac{I_G}{I_{G'+D^4}} \cong 30$. The $G'+D^3$ and $G'+D^4$ are also referred to as TS_1 and TS_2 in the literature respectively.^[30,31]

Baldan et al.^[32] shows that at the excitation laser wavelength of 514 nm, La , the extent of the lateral crystallite size, can be calculated using

$$La = 4.4 \left(\frac{I_G}{I_D} \right) \quad (3)$$

From Equation (3) we calculate a $La = 5.6$ nm for low O/C, and a $La = 17.4$ nm for high O/C. The full width at half maximum ($FWHM$) of the low O/C D , G , and $2D$ peaks are 76, 71, and 96, respectively. The ($FWHM$) of the

high O/C D , G , and $2D$ peaks are 71, 51, and 66, respectively. The low O/C material has broader peaks indicating a shorter range crystallinity whereas the high O/C material has sharper peaks indicating longer range crystallinity. Finally, we observe multiple peaks in addition to the standard D , G , and $2D$ peaks analogous to that of single layer CVD graphene.^[31]

In summary, the Raman data, for the most part, have some consistency with single or few layer graphene with defects especially for the low O/C ratio materials. We shall see below in this paper that our material is multilayered. This combined with the Raman inference suggests that the individual graphene layers of our material are weakly interacting. Furthermore, the two small Raman peaks between wavenumbers 1800–2200 cm^{-1} are another strong evidence to suggest a turbostratic graphene. We shall also see below in this paper that our material is nanoscale, not micron sized, as are all other graphenes of which we are aware. Nanoscale leads to a greater ratio of edge sites and their inherent defect nature. Whatever the effects of nanoscale dimensions have on the Raman, the Raman clearly indicate our material is not graphite and not an amorphous soot.

4.6 | XRD

Figure 11 shows X-Ray Powder Diffraction data (XRD). All samples were measured with a D8 ADVANCE diffractometer (Bruker,) with a Cu $K\alpha$ source of 0.15406 nm in wavelength. The samples match well with the known literature for graphene.^[33,34] The diffraction peaks can be indexed to a hexagonal unit cell similar to that of the AB-stacked Highly Ordered Pyrolytic Graphite (HOPG) structure. Graphite (HOPG) powder (from Acros Organics) has

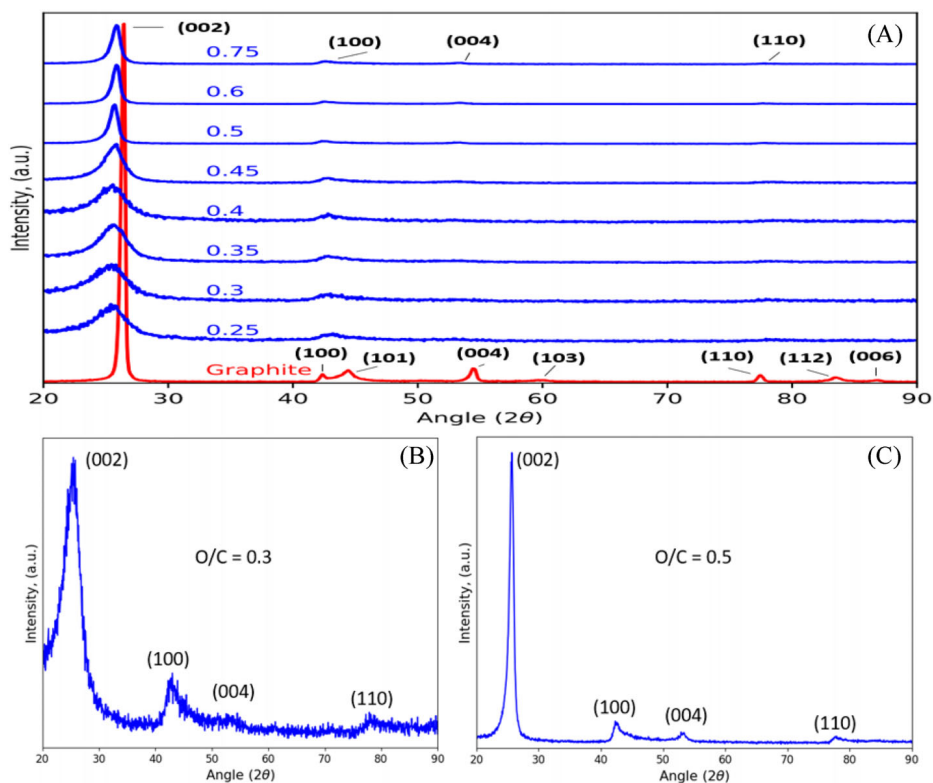


FIGURE 11 XRD of samples prepared at different O/C ratios compared with the graphite crystals. The graphene spectra are normalized to have (002) peak intensity = 1. A, shows all samples; (B) shows just detail the O/C = 0.3 sample; and (C) shows just detail the O/C = 0.5 sample

traditional symmetric delta function peaks seen with 3D crystalline materials.

All graphene samples have peaks (002), (100), (004), and (110) (referring to hexagonal unit cell) but shift to lower angle from that of graphite. (002), (100), (101), (004), (103), (110), (112), and (006) reflections are clearly present in the HOPG sample.^[35] The presence of a strong (002) peak and (004) peak, along with the indication that there is strong ordering of graphene platelets in the c-direction or a high correlation between the graphene layers. The absence of “mixed” reflections (101) and (103) in our samples indicates randomly rotated graphene platelets with respect to each other. The (004) and (110) peaks are visible, with greater signal-to-noise ratio in high O/C samples indicating the higher degrees of crystallinity in high O/C samples compared to low O/C samples.^[36]

The graphene planes (002) are centered near $2\theta = 25.33^\circ$ for O/C = 0.3 representing the low O/C and $2\theta = 25.74^\circ$ for O/C = 0.5 representing high O/C to imply an interplanar spacing of $d = 0.351$ nm and $d = 0.346$ nm respectively, both of which are larger than $d = 0.337$ nm for our graphite sample at $2\theta = 26.4^\circ$. These values are in good agreement with known graphene and graphite spacings, respectively.^[37,38] The full width at half maximum (FWHM) of the low O/C and high O/C are 3.07° and 0.79° respectively.

The Scherrer equation is given as follows

$$\tau = \frac{K * \lambda}{\beta * \cos(\theta)} \quad (4)$$

where τ is the mean size of the ordered (crystalline) domains, κ is a dimensionless shape factor = 0.89, λ is the x-ray wavelength = 0.15406 nm for our instrument, β is the line broadening at half the maximum intensity (FWHM) after subtracting the instrumental line broadening in radians, and θ is the Bragg angle. Application of Equation (4) for plane (002) gives domain size $\tau = 2.6$ nm for the low O/C samples, and $\tau = 10.2$ nm for the high O/C samples. Interpreting this as a thickness in which we use our d -spacing as the interlayer spacing indicates ~ 8 layers for the low O/C samples and ~ 30 layers for the high O/C samples. In addition, all detonation-produced samples show the (100) peak near $2\theta = 42.7^\circ$ which gives the in-plane lattice of $a = 0.246$ nm, in good agreement with the HOPG structure.

The larger interlayer spacing and presence of asymmetric (100) peak which is a signature of a two-dimensional layer indicate that the graphene stacking in the detonation-produced sample is different from that of the graphite structure; both Raman and XRD data are consistent with

TABLE 2 Zeta potential in water of detonation graphene produced from different O/C ratios

O/C	Charge [mV]
0.25 sample	22
0.3 sample	60
0.4 sample	36
0.5 sample	33
0.75 sample	34

a turbostratic structure. Both the low O/C and high O/C graphene samples are unambiguously turbostratic in that we see the classic asymmetric line shape of in-plane reflections of peaks (100) and (110) due to the Warren effect (sharp increase at low angle side and gradual decrease in high angle side of a peak) of a classic two-dimensional material.^[39] Out of the two phases, the one we get with high O/C is unmistakably turbostratic; low O/C looks like a mix of two phases distorted (not hexagonal) but turbostratic nonetheless.

4.7 | Zeta potential

Table 2 shows the zeta potentials for all samples, which were measured in water. DLS and zeta potential measurements were done using a ZetaPALS ζ potential analyzer purchased by Brookhaven Instruments Corporation. The zeta potential is consistently above +30 mV for the samples but with O/C = 0.25 an exception at 22 mV. Samples with a potential greater than +30 mV tend to be stable suspensions (low agglomeration), whereas potentials less than +30 mV indicate low stability and agglomeration susceptibility.^[40]

A positive sign of the zeta potential, as found here, indicates the presence of positive charges at the interface between solvent (here: ultrapure water) and graphene. Since elementary analysis has indicated that - especially at low O/C ratios - our graphene samples consist of 99+ percent of carbon, the presence of charged heteroelements (oxygen and hydrogen) at the interface is not likely. In the absence of charged heteroelements, carbocations (defects in the graphene structure, consistent with the Raman spectra) are the only remaining explanation since the pH of water is very close to 7. The presence of positive charges at the graphene interface has been observed before by Rodgers et al.^[41] who studied few-layer graphene that was synthesized via exfoliation. They noted that no established models exist for the presence of positive charges at the pristine graphene interface. (All of the samples have been measured more than five times; hence the number for the anomalous 0.3 sample is accurate.)

TABLE 3 Table shows settling times of the graphene after being dispersed in a variety of solvents

Solvent	Settling time
Chloroform	>1 year
Acetone	<2 hours, sonication dependent
Ethylene glycol	3 hours
1-Butanol	2 hours
Water	20 minutes, sonication dependent
Cyclohexane	30 minutes
Toluene	30 minutes
Dimethylformamide	> 2 months

Note: From this compatibilities can be inferred

4.8 | Dispersions

Table 3 shows the dispersion of the graphene was tested in various solvents. The dispersions were prepared by hand-shaking the samples for 10 seconds and then introduced to a sonication bath if hand-shaking was unsuccessful. Only acetone and water needed a sonication bath. The graphene samples dispersed well in non-polar solvents. Dispersions in chloroform (CHCl_3) and dimethylformamide (DMF) were most complete and did not settle over month time scales.

4.9 | SEM and TEM

The SEM was taken by Surface Science Western using a Hitachi SU8230 Regulus ultra-high resolution field emission scanning electron microscope (FESEM). The samples were coated with a thin layer of iridium to minimize sample charging during imaging. Figure 12 shows the results of the 0.3 sample and the 0.5 sample. For the 0.3 sample, the aggregates range in size from approximately 50 nm up to 100 nm and appear to be randomly oriented. For the 0.5 sample, the particles range in size from approximately 75 nm to 500 nm. Some particles have a plate morphology, while others appear to have a three-dimensional morphology. Both samples look similar with the higher O/C appearing denser. All samples appear as balled aggregates, perhaps porous, with ramified surfaces, perhaps fractal.^[20]

Figure 13 shows higher magnification TEM pictures of the graphene. High resolution TEM characterization was performed at the Microscopy and Analytica Imaging Research Resource Laboratory (MAI) at the University of Kansas. Measurements were performed on a Hitachi H-8100 (200 keV) on copper grids. The pictures on the left are for O/C = 0.3. At both magnification scales, the particles are relatively transparent to the electron beam. The pictures on the right are for O/C = 0.75. Now, at both

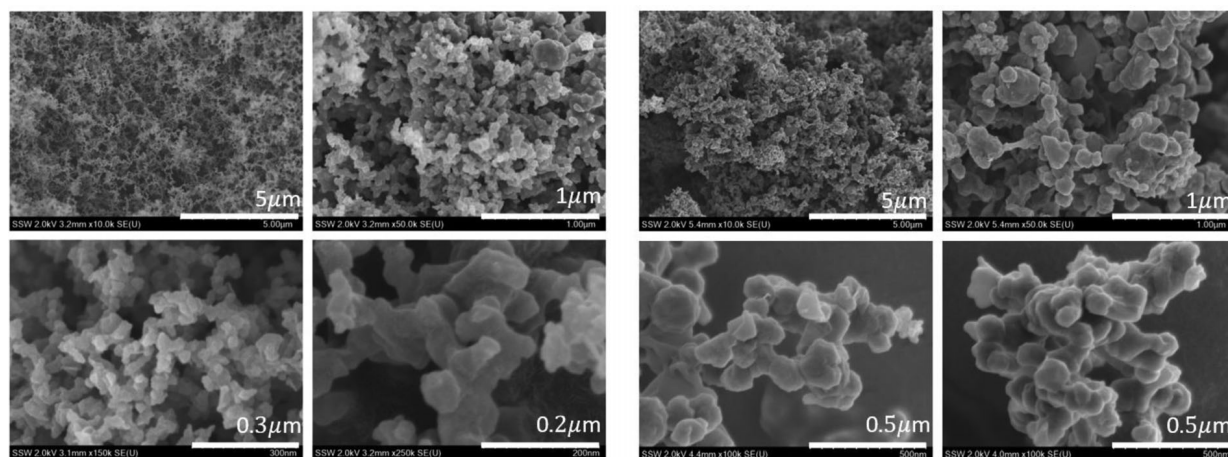


FIGURE 12 SEM pictures showing graphene produced from various $O/C = 0.3$ (left) and $O/C = 0.5$ (right)

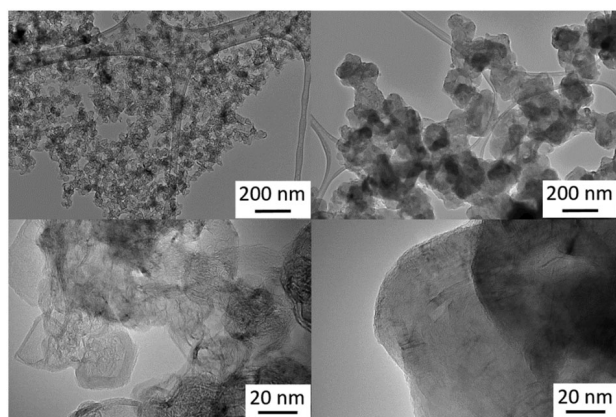


FIGURE 13 TEM pictures of $O/C = 0.3$ sample (left) and $O/C = 0.75$ sample (right). Lower pictures are a factor of ten more magnified than the upper

magnification scales, the particles are relatively darker for the electron beam, to imply particles that are thicker than those for $O/C = 0.3$. The particle lateral widths are on the order of 20 to 30 nm for the $O/C = 0.3$ sample and 100 to 200 nm for the $O/C = 0.75$ sample. This thin and thick and lateral size contrast holds for the other O/C ratios, $O/C \leq 0.45$ and $O/C \geq 0.5$, respectively.

Previous TEM at micron scales indicated a fractal aggregate morphology.^[20] Both the pore size (Section 4.4) and small platelets indicate that the graphene describe herein is a unique nano-scale graphene unlike micron scale graphenes described in the literature.

5 | DISCUSSION

5.1 | Correlations with O/C

Figure 14 shows the physical properties of bulk density, XRD d -spacing difference from graphite, XRD (002)

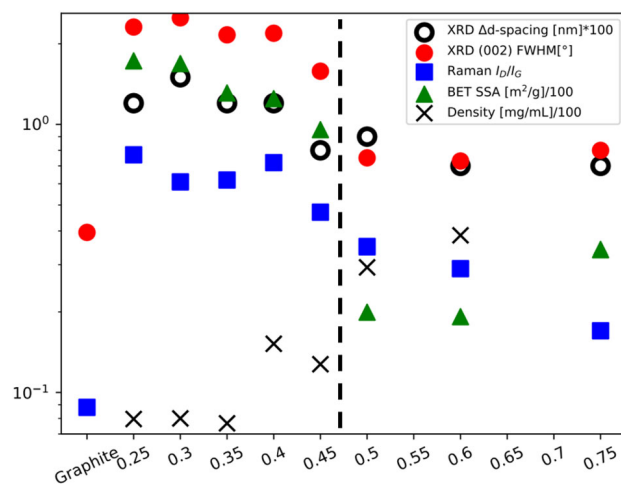


FIGURE 14 The d -spacings in black open circles, XRD (002) peak $FWHM$ in red solid circles, Raman I_D/I_G in blue squares, BET specific surface area (SSA) in green triangles, and bulk density as black X. The specific surface area, density, and d -spacings were scaled such that all these measurements can fit on one graph. The Delta in the d -spacing refers to the difference between the O/C ratio d -spacing with that of graphite. Graphite d -spacing is not shown due to this. Density of 0.75 sample was not measured as stated above. Graphite was not measured with the BET, thus graphite SSA also is not shown. There is a dashed line drawn just before 0.5 O/C to indicate the boundary between two regimes of properties

linewidth, Raman I_D/I_G intensity ratio, and specific surface area of the graphene products all as a function of the precursor O/C ratio. All the physical properties show an abrupt shift between $O/C = 0.45$ and 0.5 to imply our method has yielded two different graphene materials. We call these two materials “low O/C ” and “high O/C ” graphenes, terms we have been using throughout this paper. We now give an interpretation of this shift.

The shift in all these properties could be due to changes in the degree of disorder in the sample; the Raman

D-peak shows that high O/C samples show better layers and less imperfections. The specific surface area decreases as O/C increases, indicating larger stack size, that is, a greater number of layers. The XRD Scherrer domain size corroborates this showing varying degrees of multi-layer stacking – ~8 layers for low O/C samples and ~30 layers for high O/C samples, as well as higher degrees of crystallinity in higher O/C samples.

Despite the layering, much of the Raman implies both monolayer and bilayer graphene for both low O/C and high O/C, and a turbostratic structure. Nevertheless, SSA and visual inspection with TEM indicate multi-layering. As Raman is affected by the interaction between the layers, we propose that the multi-layering of the graphene involves weak interlayer coupling - not chemically bound AB-stacked layers, but single or bilayer flakes that rest on each other to form a multilayer stack. The 2D peak analysis of our Raman (section 4.5) indicating single or bilayer layer graphene in the context of the multi-layers also indicates turbostratic graphene. Turbostratic graphene has two weak peaks between 1800 to 2200 cm^{-1} , which is present in all O/C.

XRD analysis (section 4.6) similarly indicates turbostratic graphene. (001) reflections show ordering in *c*-direction; absence of mixed (*hkl*) lines and having asymmetric (100) and (110) reflection (in-plane reflections) are consistent with a turbostratic layered arrangement. The layers are stacked but there is no rotational order between them which is different from normal graphite samples.

The turbostratic properties of the graphene samples are consistent with successful dispersion experiments (section 4.7) which rely on the flakes to break apart and evenly disperse in solvents. This is further backed up by careful analysis of the BET measurement: the measured subnanometer average half-pore size (0.4 nm) means that the N_2 gas adsorption molecules have difficulty in accessing the pores, classifying our sample as a nanoporous material. The BET method is ideal for measuring large pores preferably above 2 nm in size. The 0.3 sample specific surface area (SSA) of $160 \text{ m}^2\text{g}^{-1}$ is merely the accessible SSA. Hence the inference that the average number of layers is the single-layer SSA divided by the sample, *viz.* $\sim 2700 \text{ m}^2\text{g}^{-1}$ divided by $160 \text{ m}^2\text{g}^{-1} \approx 17$ layers would only be applicable if the graphene samples were meso or macroporous materials.

In summary low O/C graphene appears in the bulk as a low density aerosol gel. The nanoparticles composing the gel have ~8 layers with a width of 20 to 30 nm based on TEM imaging. They are attached together in ramified, and very likely fractal, aggregates.^[20,43] The individual layers do not interact strongly with their neighbors. High O/C graphene appears in the bulk as a denser powder. Its microstructure is ~30 weakly associated but ordered lay-

ers with a lateral extent of 100 to 200 nm based on TEM imaging. Both samples show turbostratic properties hence retain many electrical properties similar to a CVD grown single layer as shown with Raman spectrum which reflects materials band structure.

5.2 | High temperature gas phase synthesis of graphene

At a most general level of description, the material we make via chamber detonation is a carbonaceous soot. The current understanding of the soot formation mechanism involves rapid molecular clustering reactions of resonance stabilized radical (RSR) species that lead to clusters of polycyclic aromatic hydrocarbon (PAH).^[44] Once formed, these PAH clusters grow at flame temperatures, ca. 2000 K, via chemisorption of numerous small hydrocarbons in the flame reacting with RSR moieties on the cluster surface. Eventually, the roughly spherically shaped clusters dehydrogenate to form solid, amorphous soot spherules.

The measured temperatures in our reactor are in excess of 2500 K, much greater than luminous sooting flames, and the “soot” we make has primary particles that are not amorphous spherules but multi-layer flakes of graphene. Hence, we conclude that the higher temperature causes a much different mechanism of formation than that of amorphous soot formation. The high temperature explanation was first proposed in our previous work^[13,14] and subsequently supported by a solid phase synthesis of graphene.^[17] It is also supported by the observation of “shell soot” with a layered structure similar to graphene seen in a laser augmented acetylene diffusion flame that reached temperatures in excess of 3000 K.^[14]

Lei et al.^[19] used “quantum chemical nanoreactor” computer simulations to model our detonation synthesis method.^[13,14] The study varied the O/C ratio from 0.0 to 1.0. The simulation indicated graphene formation begins by the breaking the acetylene into vinylidene ($\text{H}_2\text{C} = \text{C} \cdot$) and ethynyl ($\text{HC} \equiv \text{C} \cdot$) radicals, the former being the preferred route. These lead first to carbon chains and then to 2D ring structures. They found that trace oxygen could promote the formation of regular graphene with six-membered rings, but the addition of high oxygen oxidized the carbon and inhibited ring formation. Upon comparing their simulations to our previous work,^[13,14] they summarized that oxygen plays a “dual role”, in a two-stage route to graphene. It reacts with the C_2H_2 to make energy for high temperature and pressure, and then, when somewhat depleted, it guides the chains to form rings that are mostly six-membered.

Lei et al. find that graphene is not observed in their simulations when the $\text{O/C} > 0.2$ whereas our previous

work found graphene even when $O/C = 0.8$.^[19] In the present work we continue to find graphene, as indicated by Raman, for all O/C we studied up to 0.75. However, now we also find a distinct demarcation in graphene properties between $O/C = 0.45$ and 0.50. When $O/C \geq 0.50$ the product is much less graphene-like than what we obtain at smaller O/C ratios. Thus we can hypothesize that the division of our product into two types of graphene could be related to the ring formation inhabitation seen in the simulations ala Lei et al. With this hypothesis, we must remember the simulations represent the reaction only up to 500 picoseconds.

5.3 | Aerosol gelation and the two-phase nature of our product

Another explanation of the two-phase nature of our product rests in the aggregation kinetics of the graphene plates immediately after they are formed. We will make the simplifying assumption that graphene plate formation chemistry abruptly stops to create a dense aerosol of single layer plate, and then, just as abruptly, the aerosol begins to aggregate. This is consistent with the millisecond decrease of the flash of light from the detonation. Then at time equal zero, chemistry stops having formed a myriad of single graphene plates, and the graphene aerosol begins to aggregate via random Brownian motion. We have shown that a dense aerosol of nano-sized particles can form a gel,^[20] If the time to form a gel, the gel time, is long, the aggregates of the single graphene platelets can grow to be large. Usually, for an aerosol the gravitational settling time is faster than the gel time, and the aggregates fall to the bottom of the container or floor. On the other hand, if the gel time is short, only small aggregates of graphene plates can form before the aggregation stops due to formation of a gel which inhibits diffusion. For our product large aggregates form at high O/C ratio, and small aggregates form at low O/C ratio. And, in fact, the material we collect from the chamber is an aerosol gel when $O/C \leq 0.45$ and a powder on the chamber's bottom for $O/C \geq 0.5$.

The gel time can be calculated with a simple formula based on kinetic aggregation theory^[20,45]

$$t_{gel} = K^{-1} a^3 f_v^{-2.5} \quad (5)$$

In Equation (5) $K = 4kT/3\eta$ where k is Boltzmann's constant, η is the shear viscosity of the medium, a is the size of the aggregating particles, and f_v is the volume fraction of the particles. To use this formula, we assume the graphene plates are spheres of radius $a = 10$ to 25 nm, and they form both multilayer graphene and fractal aggregates with a fractal dimension of 1.8. The volume fraction is obtained

TABLE 4 Gel time estimates for various O/C ratios and two monomer sizes a

O/C	a	t_{gel}	a	t_{gel}
0.25	10 nm	1.4 seconds	25 nm	15 seconds
0.45	10 nm	11 seconds	25 nm	110 seconds
0.75	10 nm	84 seconds	25 nm	840 seconds

from the data for carbon mass produced, Figure 5. For the viscosity we also take the medium to be equal molar CO and H_2 , as indicated by analyses of the post detonation gases, and use $T = 300$ K because we find the gas cools quickly and $T/\eta(T) \sim T^{0.3}$, a very weak dependence. With all these assumptions and approximations, we find the gel times listed in Table 4.

The rapid functionality on volume fraction in Equation (5) leads to significantly different gel times for the different O/C ratios. We typically take ~ 30 seconds to open the chamber. Thus Table 4 suggests that $O/C = 0.25$ would have gelled and indeed those formulations do yield low density aerosol gels. Furthermore, the gelation would have stopped the random Brownian motion of the graphene plates and hence limited the number of plates in an aggregate. This is consistent with what we find. On the other hand, Table 4 also suggests that $O/C = 0.75$ would not have gelled before we opened the chamber or perhaps even before it settled via gravity to the bottom of the chamber. Indeed those formulations lead to powders on the bottom. Furthermore, there would be no gelation to stop the random Brownian motion of the graphene plates, and hence the multi-layering of the plates would have continued for a longer time until they fell to the bottom of the chamber. And, indeed, large O/C leads to large multi-layering. These rough numbers support the hypothesis, and although they by no means prove it, they do suggest future experiments.

6 | CONCLUSION

We have presented a study of the graphene detonation synthesis method with systematic variation of the O/C molar ratio of the precursor gases, oxygen/acetylene. We find in all cases a detonation temperature of $T = 2550 \pm 100$ K independent of O/C . This temperature is ca. 500–1000 K hotter than sooting oxygen/acetylene flames. Thus current theories of carbonaceous, amorphous soot formation do not apply. Hence, we ascribe graphene formation to this high temperature. Based on the characterization of the material properties of the resulting graphene with Raman, XRD, BET, SEM, TEM, Zeta potential, and so on, we find two distinct groups: low O/C (≤ 0.45) and high O/C (≥ 0.5). Low O/C graphene appears as a low density, aerosol gel with ~ 8 weakly associated, disordered turbostratic layers

with lateral sizes 20 to 30 nm in extent. High O/C graphene appears as a denser powder with ~30 weakly associated but ordered turbostratic layers with lateral sizes 100 to 200 nm in extent. To explain this differentiation, we hypothesize that when O/C is low, aggregation kinetics to form a static gel in the dense aerosol formed immediately after detonation and pre-empted layering (stacking). TEM shows that the lateral sizes of our graphene flakes are on the scale of 20 to 200 nm. Thus we would claim that we have made nanographene.

The detonation synthesis method is a simple, ecologically benign, and industrially scalable process that requires minimal energy input to yield an inexpensive, high-quality, turbostratic product. We believe these positive features will enable the unique properties of graphene to be applied throughout the marketplace. For the future, the detonation method is amenable to other precursor mixtures of gases, liquids, and powders. Future work will show more experiments of detonation synthesis done in the parameter space of combustible precursors that may form unique materials under the high temperature and rapid quench conditions.

ACKNOWLEDGMENT

The work was financially supported by Carbon-2D.

CONFLICT OF INTEREST

The authors declare no conflict of interest.

DATA AVAILABILITY STATEMENT

The data that support the findings of this study are available from the corresponding author upon reasonable request.

ORCID

Justin P. Wright  <https://orcid.org/0000-0002-7628-3866>

Christopher M. Sorensen  <https://orcid.org/0000-0002-1980-3394>

REFERENCES

1. A. K. Geim, *Science*. **2009**, 324, 1530. <https://doi.org/10.1126/science.1158877>
2. M. I. Katsnelson, *Mater. Today*. **2007**, 10, 20.
3. R. Ruoff, *Nat. Nanotechnol.* **2008**, 3, 517.
4. A. K. Geim, K. S. Novoselov, *Nat. Mater.* **2007**, 6, 183.
5. K. S. Novoselov, A. K. Geim, S. V. Morozov, D. Jiang, Y. Zhang, S. V. Dubonos, I. V. Grigorieva, A. A. Firsov, *Science*. **2004**, 306, 666.
6. S. Park, R. S. Ruoff, *Nat. Nanotechnol.* **2009**, 4, 217.
7. S. Park, J. An, I. Jung, R. D. Piner, S. J. An, X. Li, A. Velamakanni, R. S. Ruoff, *Nano Lett.* **2009**, 9, 1593.
8. C. Gomez-Navarro, R. T. Weitz, A. M. Bittner, M. Scolari, A. Mews, M. Burghard, K. Kern, *Nano Lett.* **2009**, 9, 2206.
9. A. A. Green, M. C. Hersam, *Nano Lett.* **2009**, 9, 4031.
10. A. Charrier, A. Coati, T. Argunova, Y. Garreau, R. Pinchaux, I. Forbeaux, J. Debever, M. Sauvage-simkin, J. Themlin, *J. Appl. Phys.* **2002**, 92, 2479.
11. C. Berger, Z. M. Song, X. B. Li, X. S. Wu, N. Brown, C. Naud, D. Mayou, T. Li, J. Hass, A. N. Marchenkov, E. H. Conrad, P. N. First, W. A. de Heer, *Science* **2006**, 312, 1191.
12. C. H. A. Wong, Z. Sofer, M. Kubešová, J. Kučera, S. Matějková, M. Pumera, *Proc. Natl. Acad. Sci.* **2014**, 111(38), 13774. <https://doi.org/10.1073/pnas.1413389111>
13. C. M. Sorensen, A. Nepal & G. P. Singh, Process for High-yield Production of Graphene via Detonation of Carbon Containing Material, C. M. Sorensen, A. Nepal, G. P. Singh, U.S. Patent No. 9,440,857; September 13, 2016.
14. A. Nepal, G. P. Singh, B. N. Flanders, C. M. Sorensen, *Nanotechnology*. **2013**, 24, 245.
15. A. P. S. Gaur, W. Xiang, A. Nepal, J. P. Wright, P. Chen, T. Nagaraja, S. Sigdel, B. LaCroix, C. M. Sorensen, S. R. Das, *ACS Appl. Energy Mater.* **2021**, 4(8), 7632. <https://doi.org/10.1021/acsaem.1c00919>
16. Y. J. Kim, S. Lee, P. Pikhitsa, M. Choi, *J. Mech. Sci. Technol.* **2008**, 22, 134. <https://doi.org/10.1007/s12206-007-1016-7>
17. D. X. Luong, K. V. Bets, W. A. Algozeeb, M. G. Stanford, C. Kittrell, W. Chen, R. V. Salvatierra, M. Ren, E. A. McHugh, P. A. Advincula, Z. Wang, M. Bhatt, H. Guo, V. Mancevski, R. Shahsavari, Y. BI, J. M. Tour. *Nature*. **2020**, 577, 647.
18. I. Glassman, R. A. Yetter, *Combustion*. Elsevier, Burlington, MA, **2008**
19. T. Lei, W. Guo, Q. Liu, H. Jiao, D.-B. Cao, B. Teng, Y.-W. Li, X. Liu, X.-D. Wen, *J. Chem. Theory Comput.* **2019**, 15, 3654.
20. R. Dhaubhadel, C. S. Gerving, A. Chakrabarti, C. M. Sorensen, *Aerosol Sci. Technol.* **2007**, 41(8), 804.
21. R. Al-Gaashani, A. Najjar, Y. Zakaria, S. Mansour, M. A. Atieh, *Ceram. Int.* **2019**, 45(11), 14439.
22. A. Santamaria, N. Yang, E. Eddings, F. Mondragon, *Combust. Flame* **2010**, 157(1), 33.
23. P. R. Pujado, B. V. Vora, In *A century of petrochemical advances*, American Institute of Chemical Engineers: Conference: 2008 AIChE Annual Meeting **2008**.
24. A. C. Ferrari, J. C. Meyer, V. Scardaci, C. Casiraghi, M. Lazzeri, F. Mauri, S. Piscanec, D. Jiang, K. S. Novoselov, S. Roth, A. K. Geim, *Phys. Rev. Lett.* **2006**, 97, 187401. <https://doi.org/10.1103/PhysRevLett.97.187401>
25. I. Calizo, A. A. Balandin, W. Bao, F. Miao, C. N. Lau, *Nano Lett.* **2007**, 7(9), 2645.
26. M. Wall, *Mater. Struct.* **2012**, 7, 35.
27. A. C. Ferrari, *Solid State Commun.* **2007**, 143(1-2), 47.
28. L. M. Malard, M. A. Pimenta, G. Dresshaus, M. S. Dresselhaus, *Phys. Rep.* **2009**, 473(5-6), 51.
29. J. - B. Wu, M. - L. Lin, X. Cong, H. - N. Liu, P. - H. Tan, *Chem. Soc. Rev.* **2018**, 47, 1822.
30. J. A. Garlow, L. K. Barrett, L. Wu, K. Kisslinger, Y. Zhu, J. F. Pulecio, *Sci Rep.* **2016**, 6, 19804. <https://doi.org/10.1038/srep19804>.
31. E. J. Heller, Y. Yang, L. Kocia, W. Chen, S. Fang, M. Borunda, E. Kaxiras, *ACS Nano*. **2016**, 10(2), 2803. <https://doi.org/10.1021/acsnano.5b07676>.
32. M. R. Baldan, E. C. Almeida, A. F. Azevedo, E. S. Goncalves, M. C. Rezende, N. G. Ferreira, *Appl. Surf. Sci.* **2007**, 254(2), 600. <https://doi.org/10.1016/j.susc.200706038>.

33. R. Siburian, H. Sihotang, S. Lumban Raja, M. Supeno, C. Simanjuntak, *Orient. J. Chem.* **2018**, *34*(1), 182.
34. M. S. Seehra, V. Narang, U. K. Geddam, A. B. Stefaniak, *Carbon N Y.* **2017**, *III*, 380.
35. R. W. G. Wyckoff, *Crys. Struc.* **1963**, *1*, 7.
36. C. F. Holder, R. E. Schaak, *ACS Nano.* **2019**, *13*(7), 7359.
37. G. Wang, J. Yang, J. Park, X. Gou, B. Wang, H. Liu, J. Yao, *J. Phys. Chem. C.* **2008**, *112*, 8192.
38. Z. H. Sheng, L. Shao, J. J. Chen, W. J. Bo, F. B. Wang, X. H. Xia, *ACS Nano* **2011**, *5*, 4350.
39. H. Fujimoto, *Carbon N Y* **2003**, *41*, 1585.
40. H. Wang, M. Kalubowilage, S. H. Bossmann, P. B. Amama, *RSC Adv.* **2019**, *9*(48), 27927.
41. A. N. J. Rodgers, M. Velicky, R. A. W. Dryfe, *Langmuir.* **2015**, *31*(48), 13068. <https://doi.org/10.1021/acs.langmuir.5b04219>
42. M. D. Stoller, S. J. Park, Y. W. Zhu, J. H. An, R. S. Ruoff, *Nano Lett.* **2008**, *8*, 3498.
43. R. Dhaubhadel, F. Pierce, A. Chakrabarti, C. M. Sorensen, *Phys. Rev. E.* **2006**, *73*, 011404.
44. K. O. Johansson, M. P. Head-Gordon, P. E. Schrader, K. R. Wilson, H. A. Michelsen, *Science.* **2018**, *361*(6406), 997. <https://doi.org/10.1126/science.aat3417>.
45. C. M. Sorensen, A. Chakrabarti, *Soft Matter.* **2011**, *7*, 2284. <https://doi.org/10.1039/c0sm00228c>

How to cite this article: J. P. Wright, S. Sigdel, S. Corkill, J. Covarrubias, L. LeBan, A. Nepal, J. Li, R. Divigalpitiya, S. H. Bossmann, C. M. Sorensen, *Nano Select.* **2021**, *1*.
<https://doi.org/10.1002/nano.202100305>

3.2 Continued acetylene-oxygen fill mixture analysis

Several details were left out of the paper in interest of being concise. Here we will explore these supplementary information.

3.2.1 Spectra blackbody detail

Figure 3.1 shows the blackbody spectra in Figure 3b from section 3.1 of the journal submission for a single spectrum plotted over a broader wavelength scale. While that Figure 3b was condensed for clarity, here the linearized slope of detonation spectra compared to two theoretical blackbody spectra of 2000 and 3000 K scaled to convene circa $1.1 \mu\text{m}^{-1}$ can be seen [51]. The intersection point of all three spectra clarify the difference in slopes.

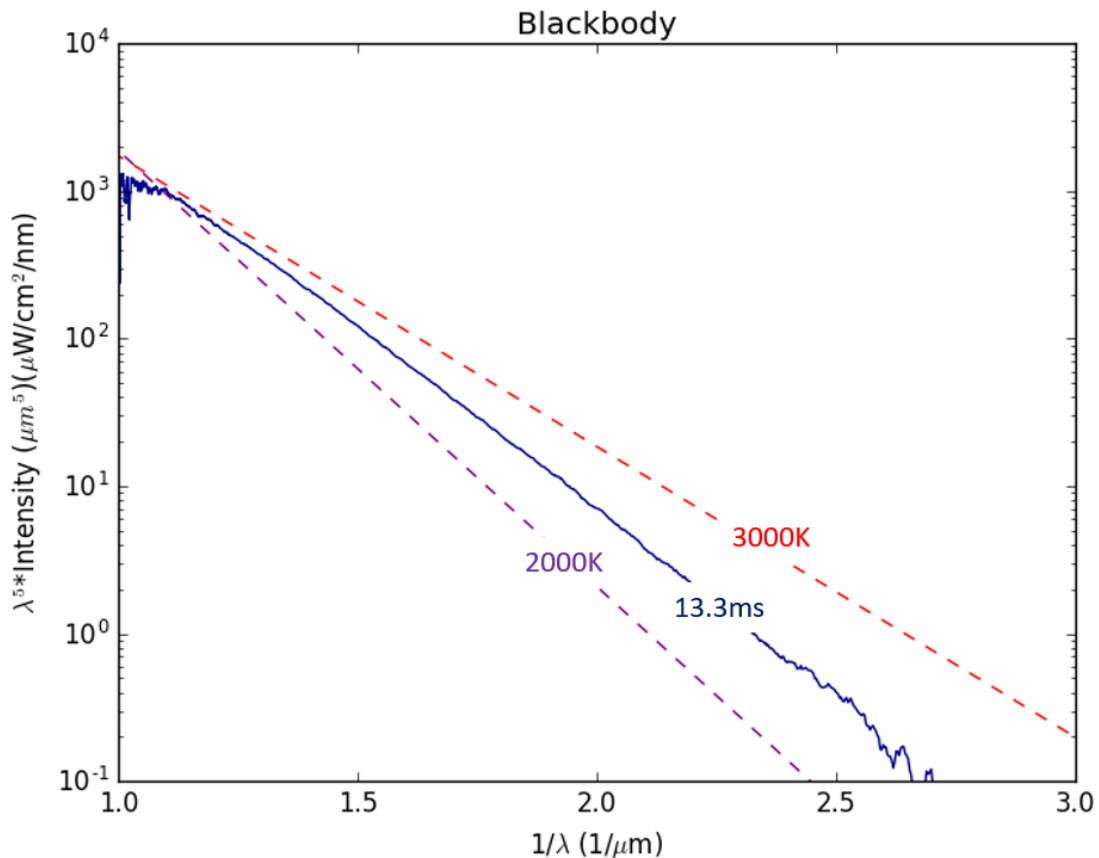


Figure 3.1: *Linearized blackbody of a 0.45 O/C spectrum between two Planck blackbody temperatures (dashed lines).*

3.2.2 Pressure and temperature rise time

Figure 3.2 plots the log of time in milliseconds it takes to reach peak pressure and peak temperature from the initiation of the reaction, called the rise time, versus O/C. While the pressure rise time shows a clear trend as discussed in section 3.1 (the journal submission), temperature rise time has no such clear trends. The ideal gas law states,

$$PV = nRT \quad (3.1)$$

with P, V, n, R, and T being the pressure, volume, number of moles, ideal gas constant, and

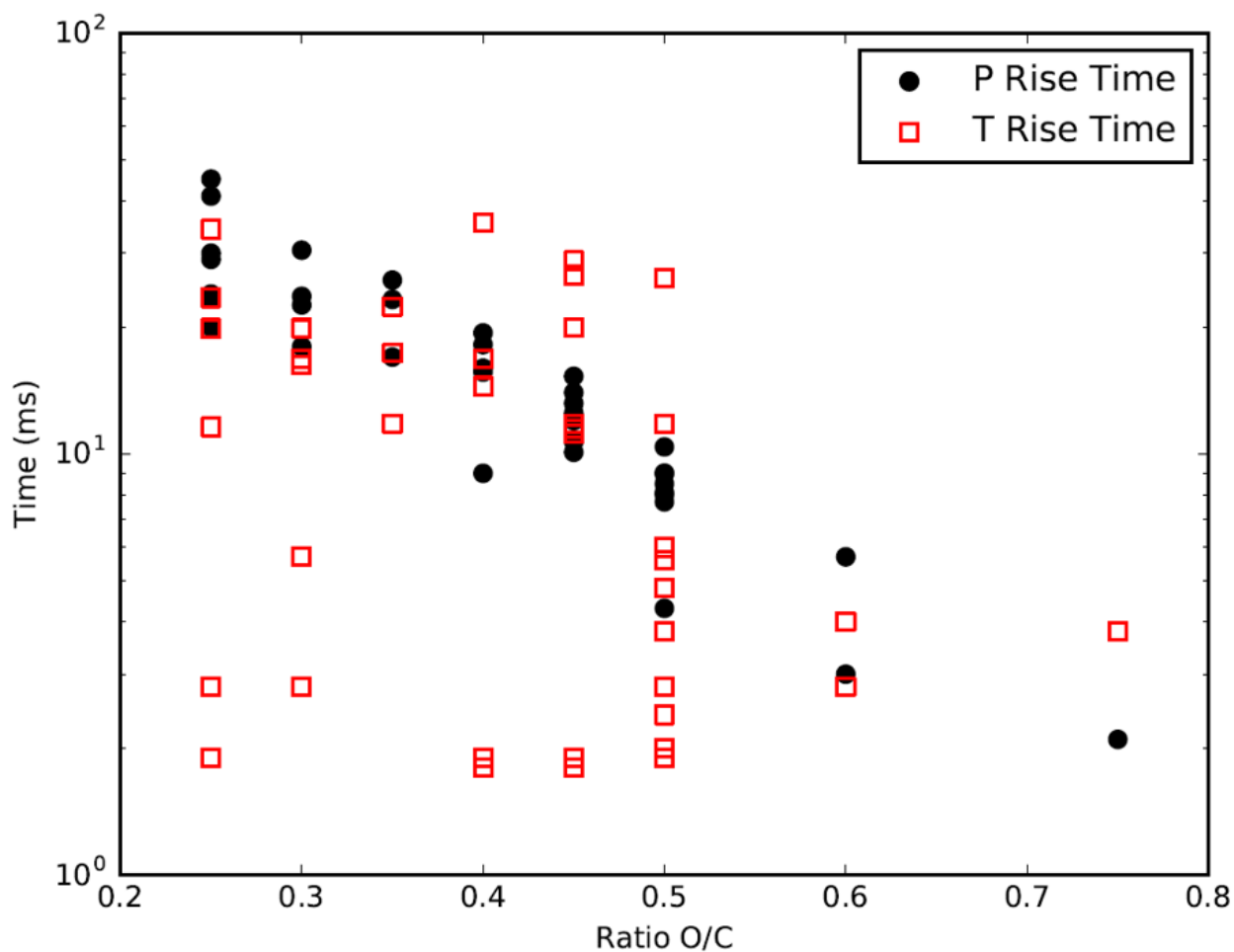


Figure 3.2: Pressure data is plotted as black circles, and temperature data is plotted as red empty squares.

temperature, respectively, showing that pressure and temperature have a linear relationship

with respect to each other [52]. However, the number of moles n also has a linear relationship with pressure, and as given by the chemical equations in section 3.1, the number of moles increase after the reaction indicating that pressure and temperature may not be linearly correlated. Thus the disparity between the rise times of T and P in Figure 3.2 may be due to the chaotic and inconsistent formation time of the products and the formation behavior of the moles based on chamber conditions.

There are perhaps alternate explanations as to the T and P rise time disparity. The pressure plots in section 3.1 indicate while there may be a slow burn or deflagration in some mixtures upon ignition as captured by long rise times [53–55], the eventual explosion and rise from low pressures to peak pressure occurs on the scale of a few milliseconds. Section 2.1.3 shows that the spectrometer has a buffer period of 1.8 ms where no data is recorded, which suggests that the spectrometer may be too slow to capture peak temperature. Furthermore, the apparatus setup shown in Figure 2.3 displays the piezocrystal capturing P and spectrometer capturing T in different locations. In the event of an inhomogeneous reaction, peak P and T would not be possible to be correlated. It is conceivable that the spectrometer is only able to record the radiating blackbody material directly on the window whereas the piezocrystal can record the shockwave reverberating in the chamber [56, 57].

Further work was done to address these concerns. Figure 3.3 shows that there is no dependence on spectrometer integration time in resolving peak T across all O/C, suggesting that the spectrometer may indeed be too slow and thus success is random. Random success results in a wide variety of measured temperatures, regardless of integration time. However, given that the peak pressures recorded are precise in the several millisecond framework indicates that there should still be a precise peak T time-frame that, calibrated for difference in location, is adjacent to the precise time-frame of peak P data.

This conclusion combined with Figure 3.4 convey that the detonation reaction is indeed inhomogeneous. The inhomogeneity is most clearly seen in the 0.25 O/C detonation picture frames, where the concentration of light shifts from the left to the right between frames two and three. Careful examination of the color of each frame also shows nonuniform patches of white light with other warm colors. Finally, the 33 ms per frame timescales generally

correlate to P rise times in Figure 3.2. Thus, the inhomogeneity of the detonation reaction combined with the difference in location may explain why temperature and pressure data do not follow the ideal gas law.

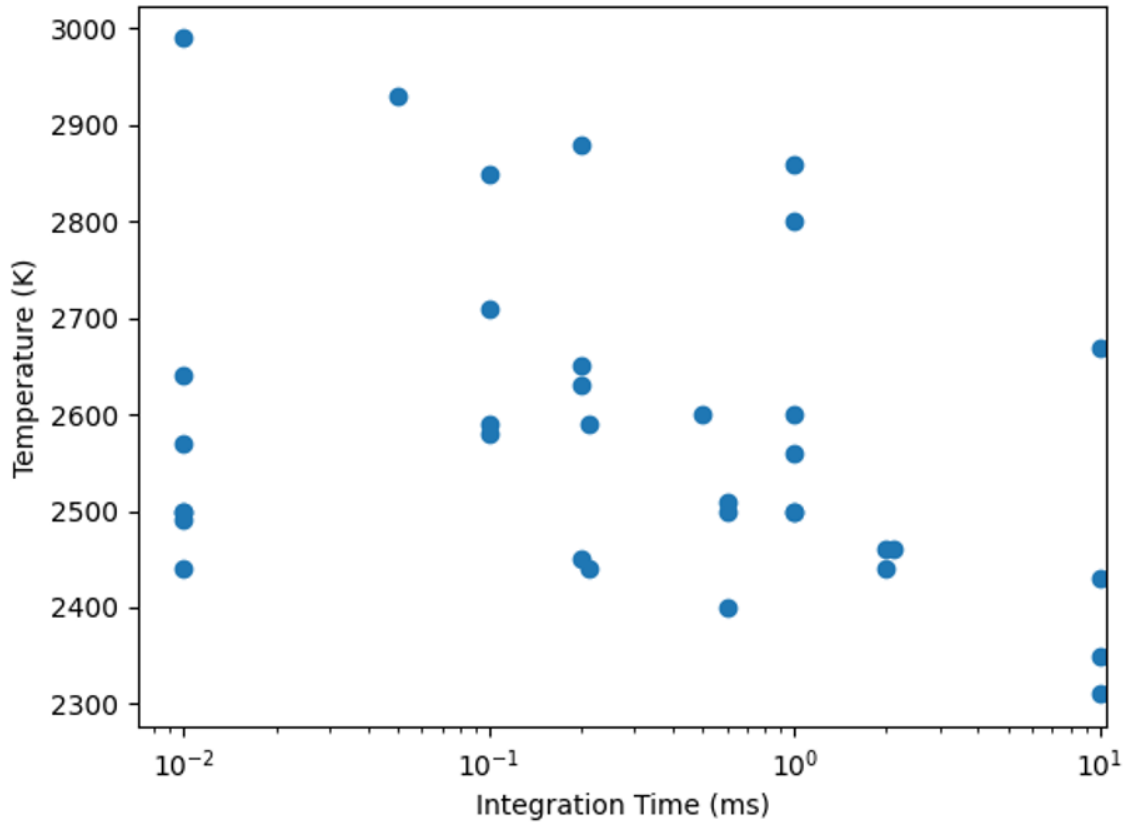


Figure 3.3: Peak temperature is plotted versus spectrometer integration time.

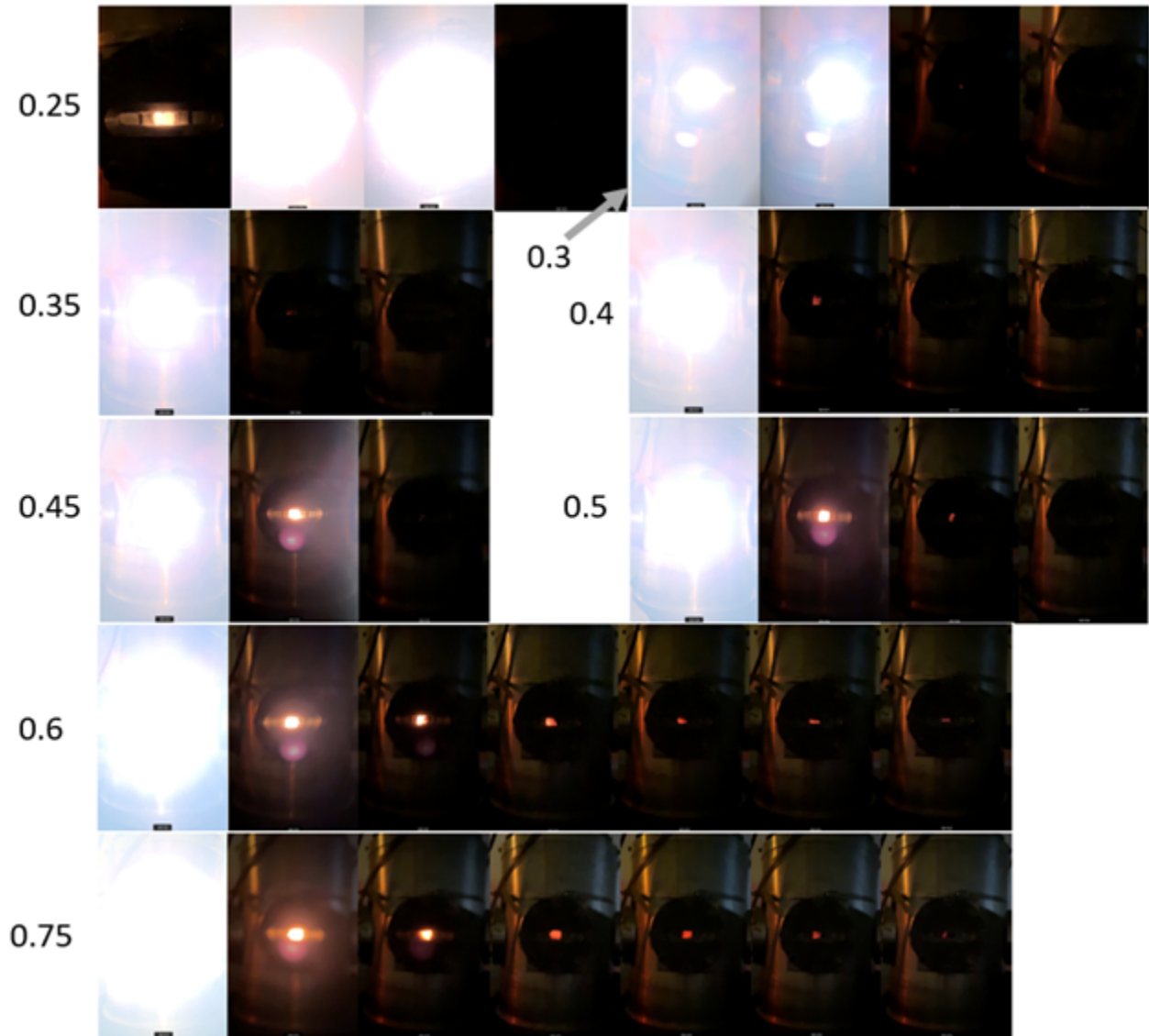


Figure 3.4: *The detonation flash captured with an iPhone 11 camera in slow motion for each O/C mixture. Each frame represents 33.3ms.*

3.2.3 Spectrometer light intensity and further temperature data

From section 3.1 we know that the spectra obtained from the detonation flash is a blackbody. As shown in section 3.3 the spectrometer temperature calculations have no apparent functionality with integration time, raising the question of how the spectrometer light intensity behaves. Figure 3.5 shows all of the available spectrometer data for $O/C = 0.45$, from which the light intensity at 300 nm can be compared to the resulting calculated temperature. The

light intensity monotonically increases and peaks at ~ 12 ms for all integrations times, and exponentially decreases until no more light is measured. Figure 2 from section 3.1 reveals an exponential rise to peak pressure at ~ 12 ms and a monotonic decrease, a trend opposite to that of the light intensity in Figure 3.5.

The relatively constant temperatures calculated from the light intensity have no apparent functionality with respect to each other. This relationship may be explained by already known physical laws: the Stefan-Boltzmann law describes blackbody radiance as

$$j^* = \sigma T^4 \tag{3.2}$$

where j^* is the emitted blackbody radiance, T is temperature, and σ is the Stefan-Boltzmann constant. The emitted blackbody radiance has units of watt/m^2 to signify that the light intensity emitted from the blackbody is dependent on the surface area of the hot emitting material [52]. Thus, the measured light intensity monotonic increase with time can be correlated with the formation of graphene as the hot emitting blackbody material, and the exponential decrease can be correlated by the continued growth of the graphene aerosol gel because graphene, a carbon allotrope, is black and absorptive (seen below in Figure 3.9). Furthermore, temperature may be relatively constant in this period as the number of moles change correlate to the light intensity, obeying the ideal gas law.

The same light intensity and temperature analysis can be performed for all O/C. Figure 3.6 shows the light spectra obtained for each O/C averaged across all measurements alongside the resulting temperature calculations. Temperature remains relatively constant, downward trending, and similar for all samples with the exception of a high initial temperature for the 0.75 sample. No apparent functionality between light intensity and temperature is seen. Light intensity spectra peaks at faster timescales for high O/C compared to that of low O/C. The time at which light intensity peaks not correlating linearly to decreasing O/C could be due to statistical error in the data; there is more data for some O/C than others (for example, >10 measurements for 0.5 but only one for 0.75), and as shown in Figure 3.5 there is an inconsistency in peak time. Each O/C curve is reminiscent to that of the

corresponding pressure curve in Figure 1 from 3.1 as discussed previously. All of this indicates that material forms quicker for higher O/C.

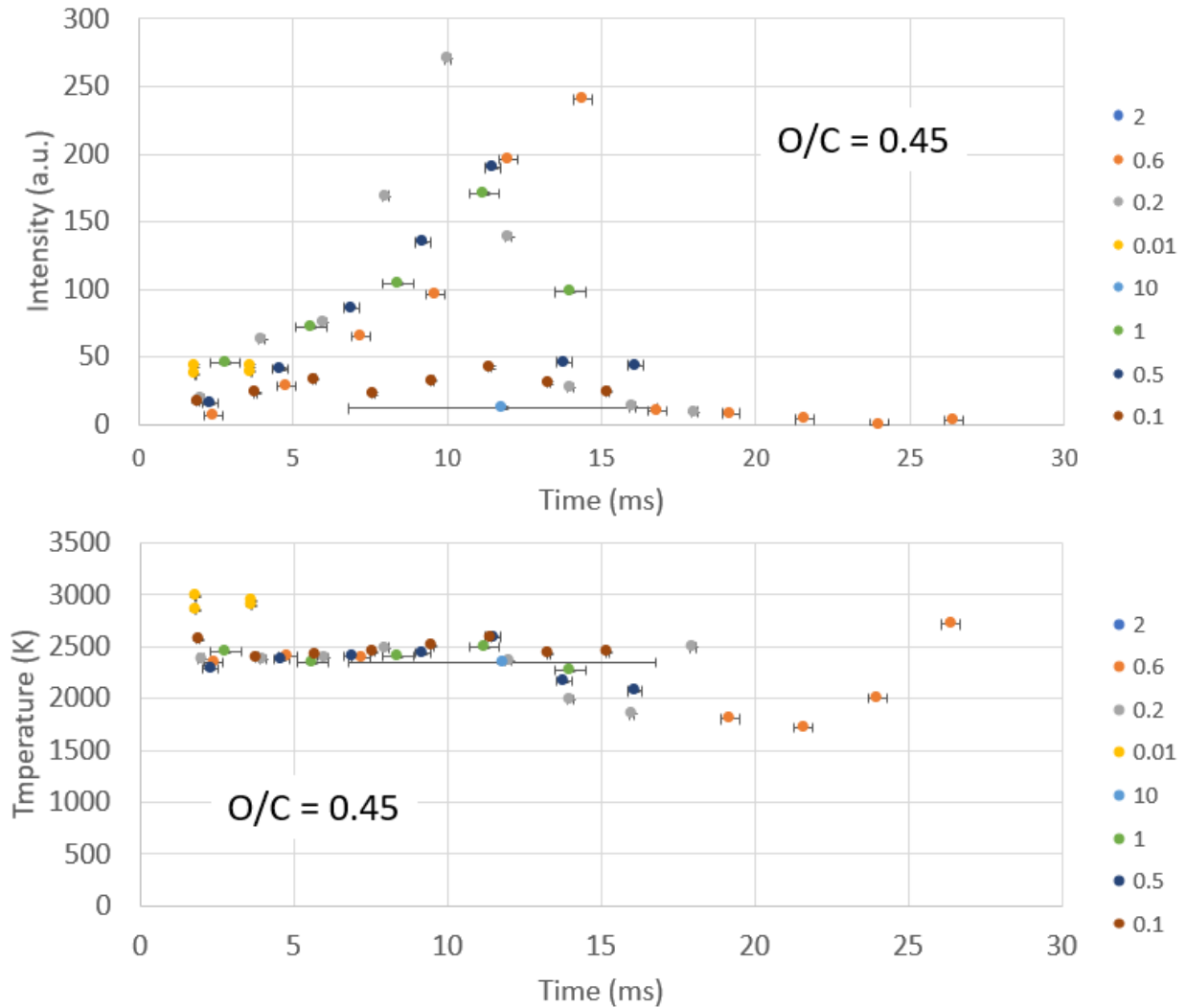


Figure 3.5: Spectrometer light intensity at 300 nm (top) and the resulting temperature calculated (bottom). 300 nm is presented due to the relatively higher signal-to-noise ratio compared to higher wavelengths. Each detonation is labeled as its integration time in milliseconds, right, and assigned a different color. Horizontal error bars represent length of integration time in milliseconds. There is a 1.8 ms buffer time between each data point regardless of the integration time. Data is a result of several years of detonations with the spectrometer positioned differently with respect to the chamber window, thus the light intensity in a.u. cannot be directly intercompared.

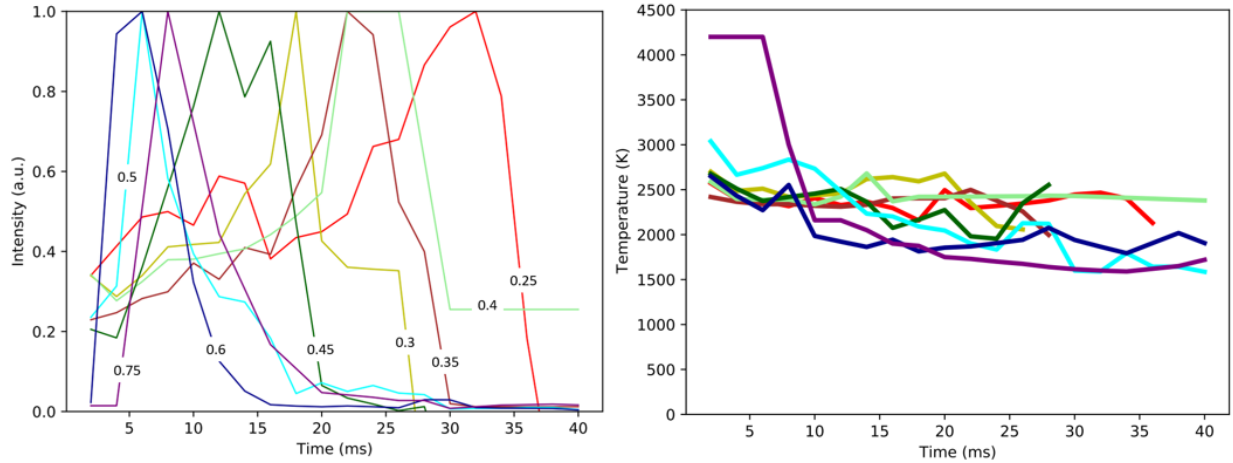


Figure 3.6: Spectrometer light intensity at 300 nm (left) and calculated temperature (right). 300 nm is presented due to the relatively higher signal-to-noise ratio compared to higher wavelengths. Intensity and temperature are averaged across all data for each O/C in 2 ms increments and normalized to peak at 1 a.u. for light spectra. Temperature data follows the same color-labeling as the intensity data.

3.2.4 Turbidity

The photodiode as shown in section 2.1.3 produces the data in Figure 3.7. No clear trend with O/C is seen. Figure 3.8 plots all data 1/e points indicating consistent timescales for all turbidity measurements with no dependence on O/C. Both Figure 3.6 and Figures 3.7 and 3.8 indicate spectral visibility range to last on the order of 20-30 ms for most measurements. The lack of O/C dependence conflicts with the results from section 3.2.3, suggesting that perhaps material formation time is independent of O/C.

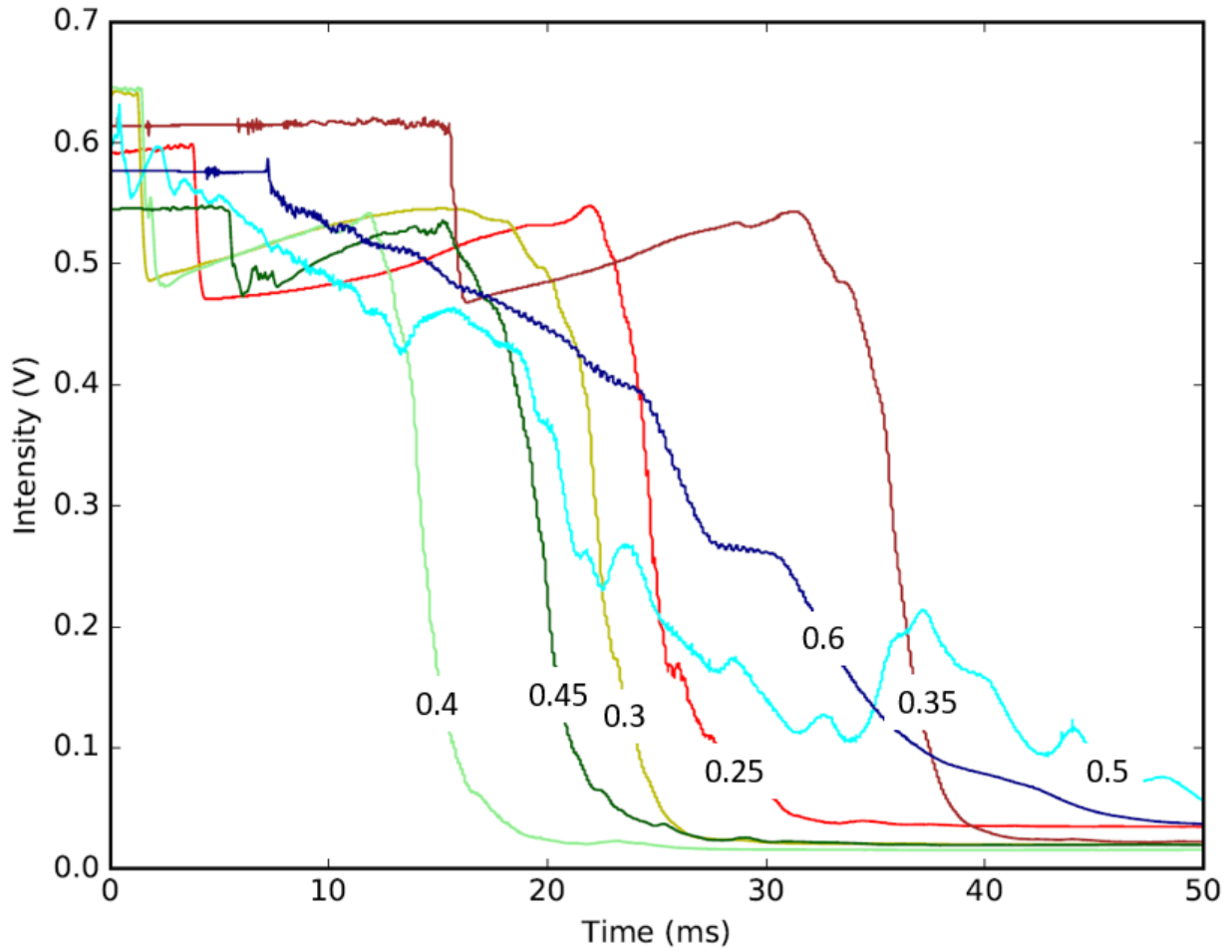


Figure 3.7: *Turbidity captured from HeNe laser focused on photodiode through the chamber windows.*

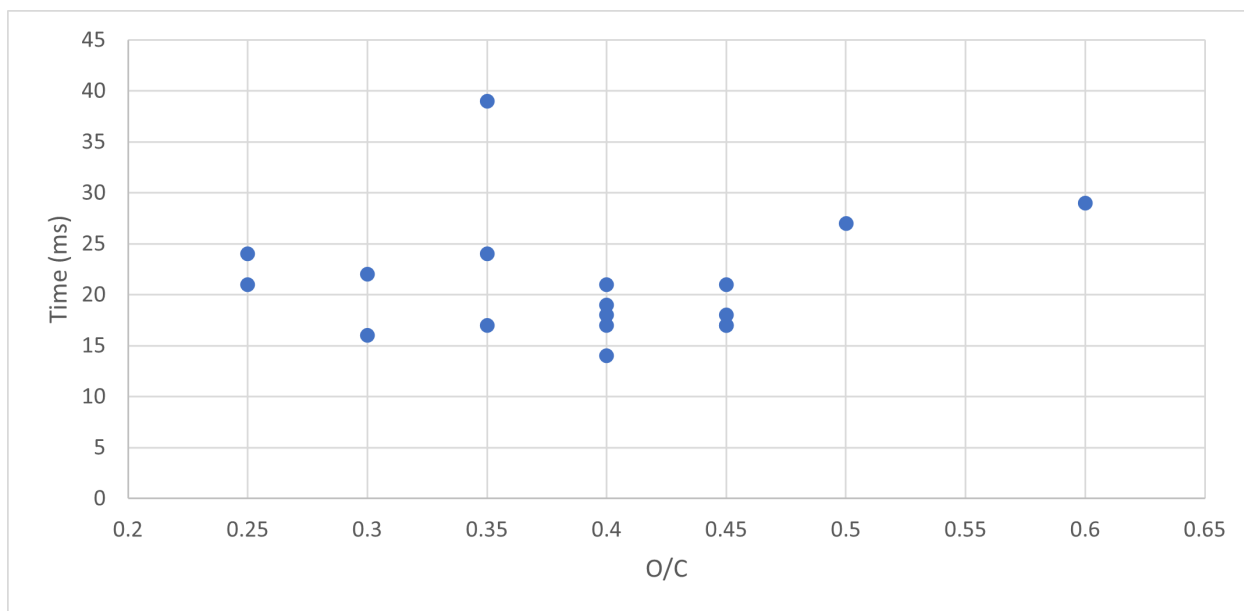


Figure 3.8: *The $1/e$ point of all turbidity measurements.*

3.2.5 Sample appearance

Figure 3.9 shows a picture of the graphene synthesized for all O/C in normal lighting and altered contrast. Normal lighting reveals a black material not well-captured by camera. Altered contrast shows low O/C samples appearing as large black chunks reminiscent of angel food cake and the high O/C appearing as dark grey powders. Sharp-edge outlines of the low O/C aerosol gels in the altered contrast photo are due to the contrast settings and is not reflective real world properties, which are fluffy and soft as mentioned above. To the naked eye, the high O/C samples appear slightly grey or less black than the low O/C samples to lesser degree than the altered contrast of Figure 3.9.



Figure 3.9: *iPhone SE picture of graphene samples. The top picture is captured in normal room lighting, and the bottom picture has altered contrast for visibility purposes. A thin red line is drawn between the pictures for clarity. The four samples in the top row are the 0.25, 0.3, 0.35, and 0.4 O/C, and in the bottom row 0.45, 0.5, 0.6, and 0.75 O/C.*

3.2.6 AFM

Figure 3.10 shows AFM images of 0.3 and 0.75 O/C measuring small scale flake thicknesses of approximately 5 nm and 8 nm, respectively, which corroborates the Scherrer equation calculation in 3.1. Larger particles are also visible on the scale of a few hundred nanometers. On both small and large scales, the high O/C particles are thicker in comparison to low O/C particles with lateral widths at least doubled in size.

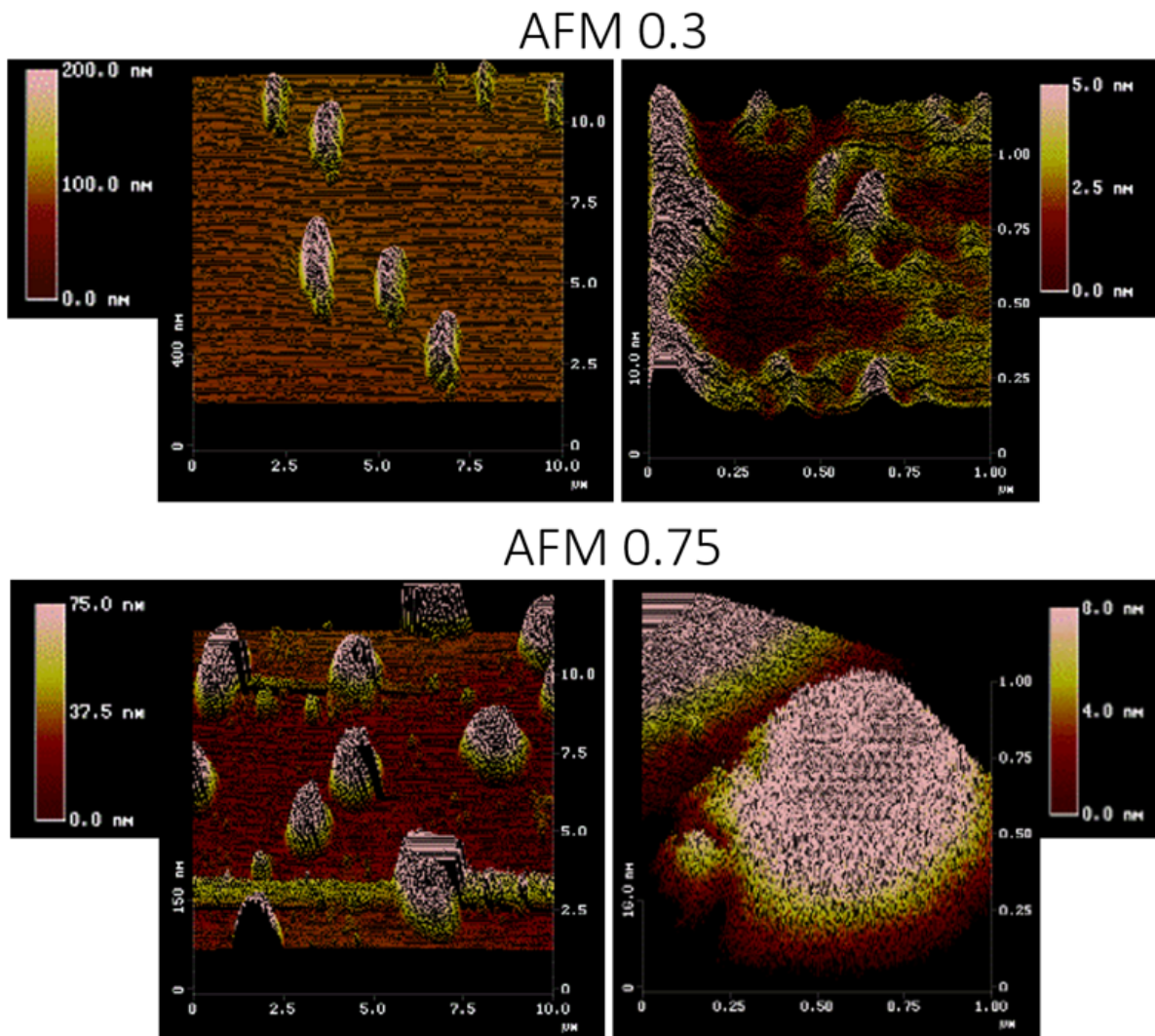


Figure 3.10: AFM pictures of 0.3 O/C (top) and 0.75 O/C (bottom). The left and right 0.3 O/C pictures have x-y scales of 10x10 nm and 1x1 nm, respectively, and z-scale colormaps from 0-200 nm and 0-5 nm, respectively. The left and right 0.75 O/C pictures have x-y scales of 10x10 nm and 1x1 nm, respectively, and z-scale colormaps from 0-75 nm and 0-8 nm, respectively.

3.2.7 TGA

Figure 3.11 plots TGA of low O/C graphene indicating thermal stability up to high temperatures. A decreasing sample mass would indicate the presence of organic volatiles such as polycyclic aromatic hydrocarbons (PAHs) [58–61], whereas an increase in mass indicates the presence of surface oxygen reactions [62]. The lack of organic volatiles and PAHs reflect

the purity of the sample.

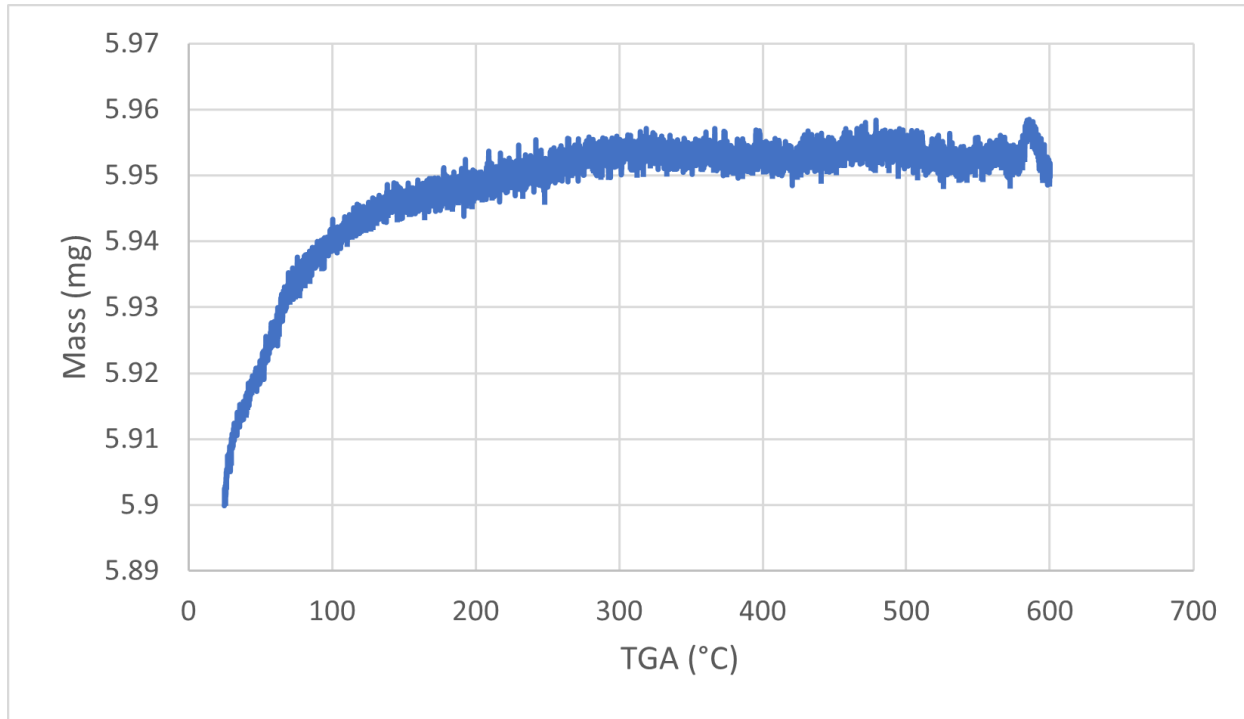


Figure 3.11: *TGA of 0.3 O/C sample.*

3.2.8 All O/C compared to the 0.3 O/C sample

Figure 3.12 shows various parameters relative to the 0.3 sample. The 0.3 O/C sample was chosen for comparison for reasons that will become apparent in chapter 4. With less moles of carbon and the presence of increased oxygen to form reactive carbon-oxides [63], high O/C samples expectedly decrease in %yield and mass compared to low O/C samples. Peak pressure, peak temperature, and final number of moles increase with O/C marginally whereas density shows the largest relative increase with increasing O/C. SSA decreases with increasing O/C precipitously relative to the other parameters and then slightly increases, a property discovered in 3.1 that we have not yet been able to explain. Mass and %yield showing the opposite trend to peak pressure, peak temperature, and final number of moles is likely correlated, as is density showing the opposite trend to that of the SSA.

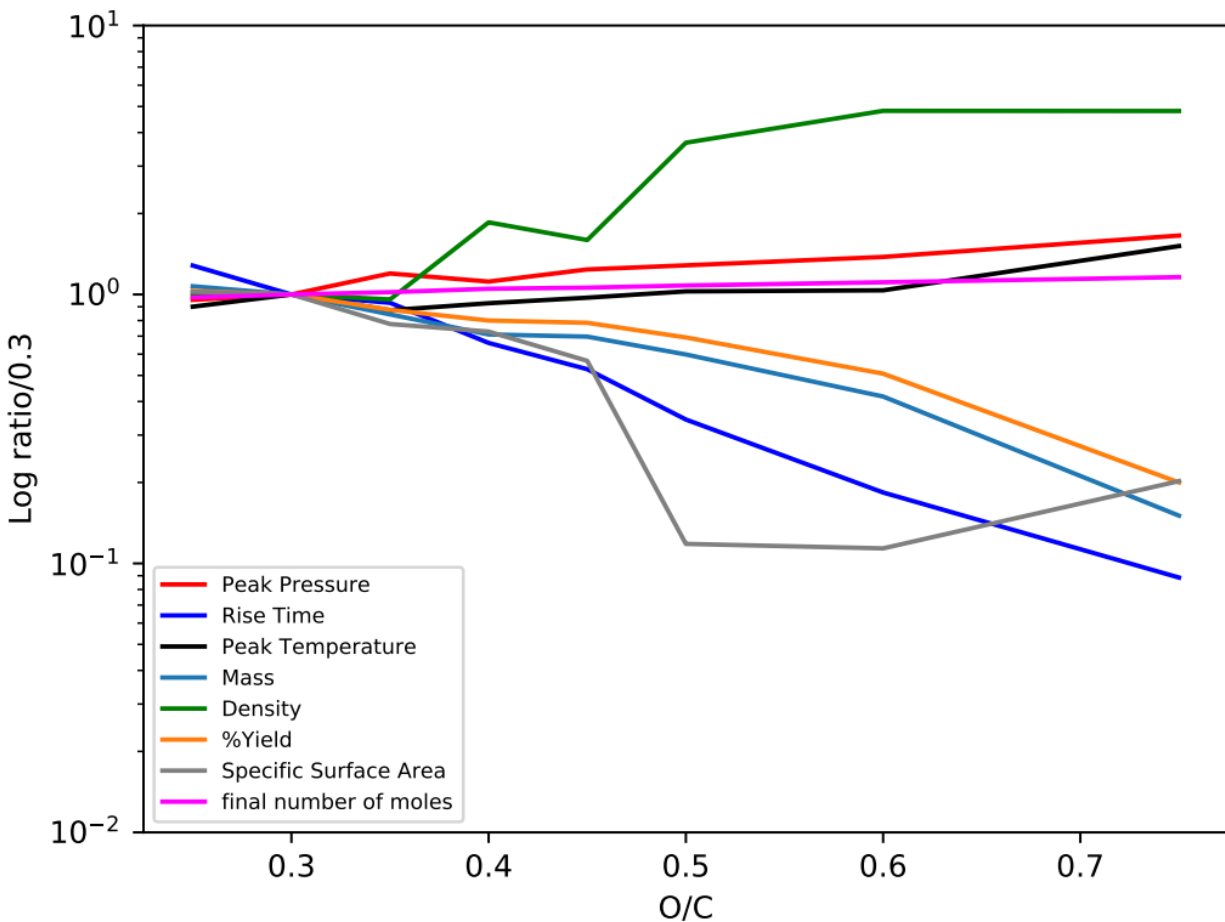


Figure 3.12: Y-axis shows the log of the ratio between all O/C and the 0.3 sample plotted on a log scale. All 0.3 values are equal to unity as a result.

3.2.9 Solvent dispersion

Here, more detail will be given to the solvent dispersion that has been briefly covered in 3.1.

Sonication experiments with chloroform (CHCl_3) and water (H_2O) mixtures were performed with 10 mg of the 0.4 O/C sample in each mixture. Sonicating samples beyond ten minutes (the minimum time tested) in the ultrasonic bath for these mixtures show no difference in suspension dispersibility or length. Mixture ratios of $\text{CHCl}_3/\text{H}_2\text{O} \geq 1$ largely obtain smooth suspensions with water bubbles, where higher relative water concentrations induce larger bubbles. At mixture ratios of $\text{H}_2\text{O}/\text{CHCl}_3 \geq 5$, CHCl_3 forms a bubble that traps graphene at the bottom of the container. A small amount of graphene floats on top of the water if there is not enough CHCl_3 . At concentrations of graphene/ $\text{CHCl}_3 \geq 1$ graphene

be well suspended. Flipping the container around does not pop the bubble.

In the case of mixtures whose suspensions precipitate such as acetone (C_3H_6O), hotter sonication temperatures allow suspensions to last longer before precipitation. Figure 3.13 shows TEM images of room temperature and 50 °C graphene dispersions in acetone and chloroform. The C_3H_6O images indicate significant aggregation at room temperature while somewhat less aggregation at 50 °C; in comparison, $CHCl_3$ shows very little aggregation. Rock salt bath temperatures at 0 °C can increase the sonication time required to evenly suspend graphene in C_3H_6O by several hours, whereas hot temperatures at 50 °C can reduce the required sonication time to evenly suspend by several tens of minutes. It is unclear if the long sonication times required for 0 °C temperatures to disperse is due to the ultrasonic bath's (section 2.2.10) low power necessitating longer time to disperse while cold, or if the ultrasonic bath is unable to disperse while cold and only succeeds after the solution warms up upon interacting with room temperature up over time.

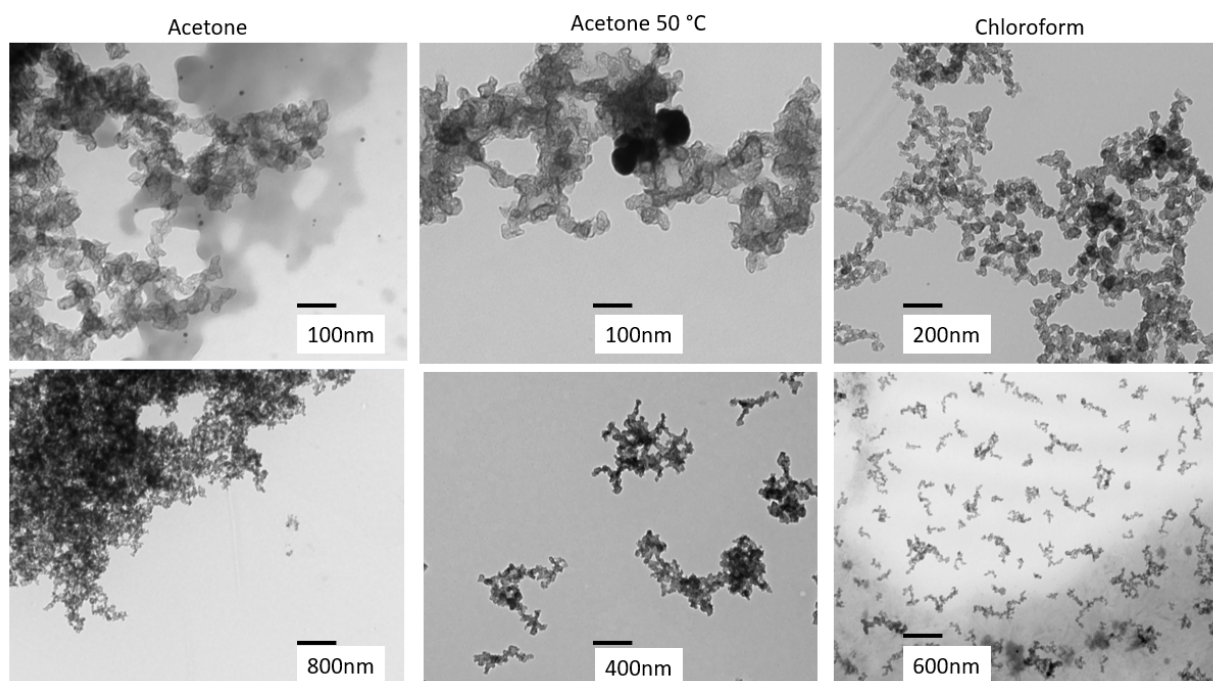


Figure 3.13: TEM images of 10 mg of 0.4 O/C graphene in, from left to right: 10 mL of acetone sonicated for 60 min at room temperature; 10 mL of acetone sonicated for 60 min at 50 °C; and 10 mL of chloroform sonicated for 60 min at room temperature.

In mixtures of $CHCl_3$ and C_3H_6O , graphene precipitates after several hours similar to

pure C_3H_6O suspensions described in section 3.1 even when $CHCl_3$ concentration is relatively large. Suspension appearance is indiscernible from that of pure C_3H_6O .

10 mL of cyclohexane (C_6H_{12}) has been sonicated with 10 mg of 0.4 O/C graphene for 5 min and 60 min, and 5 mL of carbon disulfide (CS_2) has been sonicated with 10 mg of 0.4 O/C graphene for 5 min and 60 min. Both CS_2 samples precipitated within 1 hr regardless of sonication time. With C_6H_{12} the 5 min sonicated sample was partially suspended for at least 18 hrs, and the 60 min sample was fully suspended for at least 18 hrs. No further data is available.

Chapter 4

Construction of a pilot-scale plant to produce 10 kg of graphene in 5.5 days

Characterization of acetylene-oxygen fill mixtures has revealed high quality turbostratic graphene with differing properties based on O/C ratio. The premise of bench-scale gaseous precursor detonations using technology reminiscent of engines incites the possibility of scaling up the graphene-making reaction process to a pilot-scale plant capable of mass producing graphene in kilograms per day. Here the successful scale-up is presented.

4.1 Description of pilot-scale plant apparatus

Figure 4.1 shows a picture of the pilot-scale plant machine with a basic diagram. The 3.9 L detonation chamber sits on top attached to the manifold as described in section 2.5 supported by an aluminum structure. PVC tubing of length x diameter = 169 x 23 cm is connected to the underside of the chamber via an electronic valve. Within the PVC tubing is a 3 micron silicon bag filter with Kevlar fabric shielding on the upper interior of said filter that can be seen in Figure 4.2. The PVC is connected to a vacuum ballast of ≥ 400 L held at -25" Hg. We call this PVC tubing enclosing the bag filter and Kevlar that is held under constant vacuum the "collection system".

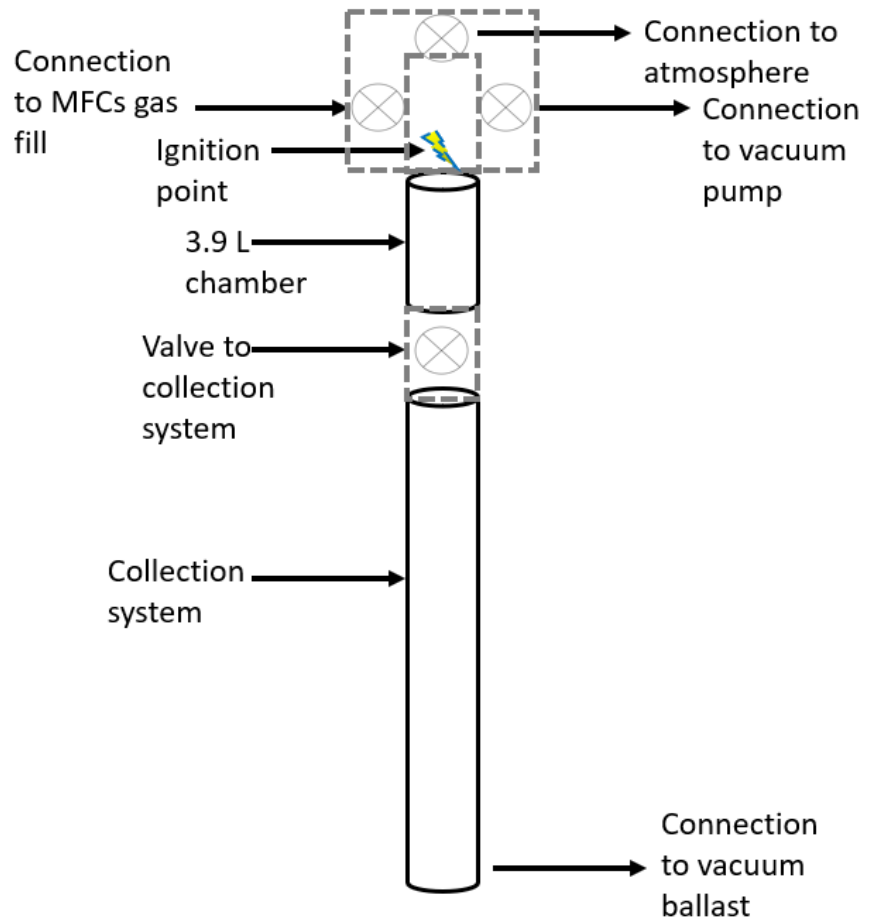
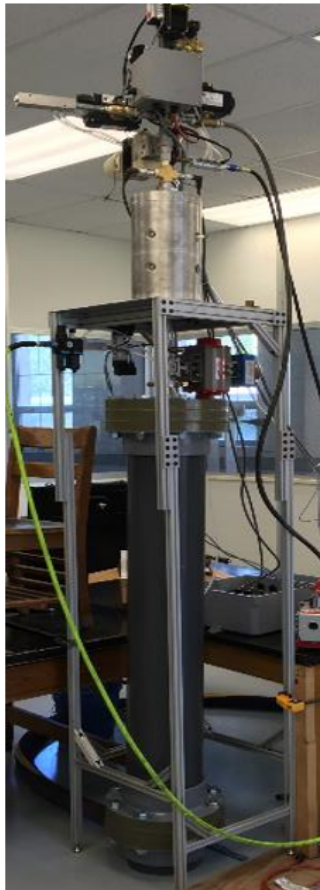


Figure 4.1: *Pilot-scale plant on the left and a basic schematic on the right.*



Figure 4.2: *Top left: bag filter after collecting 1 kg of graphene. Bottom left: graphene-coated Kevlar on the inside of the cut-open bag filter after collecting 1 kg of graphene. Right: close-up picture with altered contrast of the Kevlar and cut-open bag filter.*

4.2 Pilot-scale plant procedure

The pilot-scale plant operates as per the procedure presented in section 2.1.4 with a few additions. Two seconds after the spark is thrown in the automated program, the bottom valve opens the reactor to the collection system where the graphene and reaction gases are sucked down by the vacuum. The gases are exhausted while the graphene is collected by the bag filter (Note: product gases hydrogen and carbon monoxide are both valuable commodities [64–72] and collection designs for them are still in experiment). Simultaneously, the manifold connects the chamber to atmosphere which pulls air down through the chamber and manifold in a “clean cycle” that wipes graphene off of the spark plugs and motivates any graphene remaining in the chamber to enter the collection system. When the clean cycle finishes, the entire process repeats resulting in a cycle time of one detonation every 45 seconds producing 2.03 g of graphene, or a rate of 1 kg of graphene in 6.2 hrs for $O/C =$

0.3. The production cycle time is dependent on the fill speed of the MFCs, the evacuation rate of the vacuum pumps, and the clean cycle of the electrodes; better equipment will allow faster cycle times.

This presented machine and procedure was successful in creating 10 kg of graphene in 5.5 days at a rate of 1 kg of graphene per bag filter every 6.2 hrs resulting in a patent application [73]. The 0.3 O/C sample was chosen to make up the majority of the 10 kg bulk sample due to its high yield per detonation (Figure 4a in 3.1) and its cleanability in the clean cycle discussed below (section 4.3.2).

4.3 Engineering details

Despite the brilliance and best efforts of all persons involved, the pilot-scale plant did not work the first time it was built and turned on. Here the empirical engineering observations necessary to make the machine operable are presented.

4.3.1 Custom spark plugs

Initial work was performed using automotive spark plugs as the source of ignition [18, 19, 32, 33]. However, the spark plugs would coat in graphene after each detonation causing the spark plug to short upon further ignition attempts. Hence, designing an apparatus that would minimize the contact between graphene and the electrodes while providing a source of cleaning between detonations (section 4.3.2) became necessary.

Epoxying ceramic insulation around long-probe automotive spark plugs resulted in a system capable of firing 10-20 shots before failing. Graphene buildup over time on the ceramic would eventually require manual cleaning. Furthermore, various epoxies did not prove to have compatibility with the ceramic resulting in internal shorting anywhere between 5-500 shots, thus requiring a rebuild of the spark plug.

A custom spark plug was designed and built by engineer Stephen Corkill to circumvent the epoxy and shorting issues. Glass was chosen as the insulator due to its compatibility

with epoxy [74] and copper as the electrodes due to its high conductivity [75]. A series of compression-fit o-rings and gaskets are built to vacuum seal the ignition area and hide the attachment of the glass around the copper in order to reduce to risk of graphene infiltration. These electrodes are highly robust and can last thousands of shots before the glass is at risk of breaking; further improvements are in experiment despite their successful usage in making 10 kg of graphene in 5.5 days.

Acetylene as a precursor is highly reactive and known to decompose upon certain temperature and pressure conditions [23], implying the bare minimum energy to initiate the reaction would be sufficient in exploding the entire mixture. Thus the tips of the electrodes were made into sharp-points to produce a strong electric field [76, 77]. Surprisingly this resulted in difficulty in setting off the reaction. It then became apparent that not only is the strength of the field important but so is the energy density to increase the spark exposure to the reactive mixture. To maximize spark density, flat electrode tips were tested but this resulted in a weaker field that also had trouble detonating. Mushroom-head tips were tested and proven to be the most effective and subsequently became the primary design.

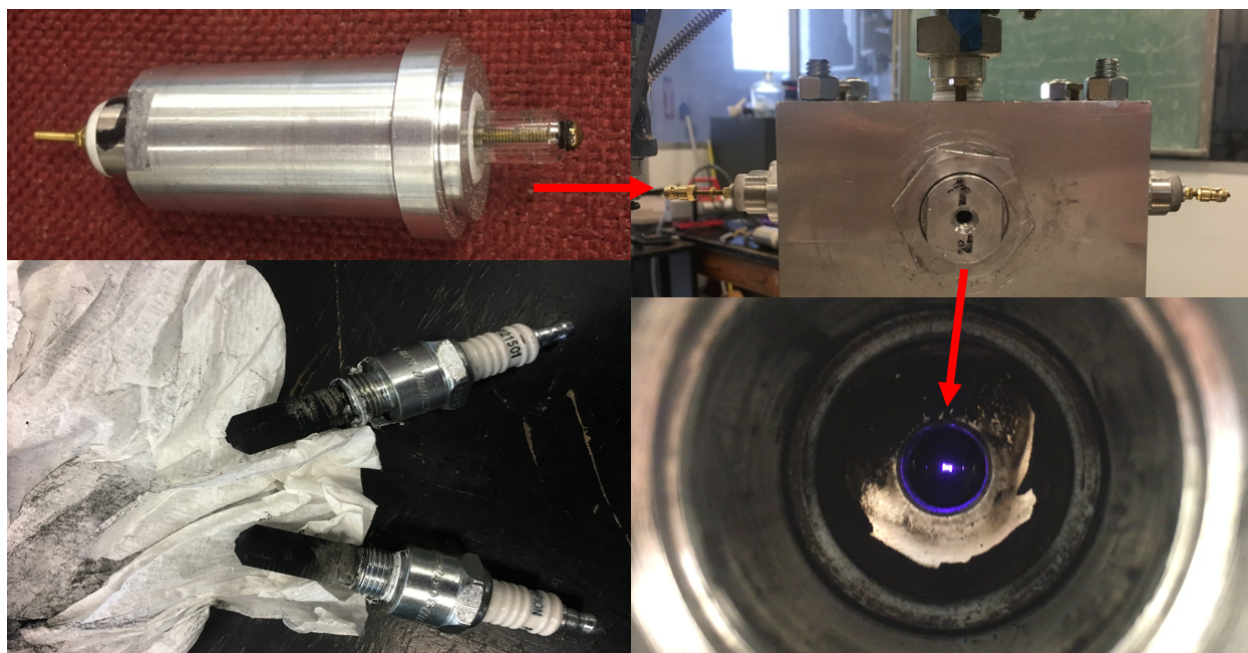


Figure 4.3: *Top left: custom electrode; top right: cubical feature with ports for electrodes; bottom left: ceramic-coated spark plugs; bottom right: view of the spark in the cube.*

4.3.2 Electrode clean cycle

An effective clean cycle is the most critical aspect of keeping the machine running back-to-back detonations. The custom designed electrodes (section 4.3.1) assist in reducing the risk of shorting but the tips still coat in graphene after each detonation. Vacuum withdrawal through the chamber's connection to the collection system is not enough to wipe all of the graphene off of the electrode tips, necessitating the air flush described in section 4.2. Two metallic scoops vitally placed underneath the electrode tips provide turbulence to the flush which clean the underside of the electrodes.

Subtracting even one second off of the clean cycle has an impact on the hourly production rate, but quick clean cycles run the risk of gradual graphene buildup resulting in eventual failure, which then halts production and requires manual cleaning of the electrodes. Though longer clean cycles are more efficient in maintaining production, cycle time, as just mentioned, is also an important parameter and so a balance must be established. Clean cycle lengths have been tested between 2-20 s and found to be most effective within the 8-15 s range depending on other parameters such as O/C ratio and freshness of the electrodes.

After many detonations the electrode glass becomes at risk of cracking and the tip surface roughens, but O/C ratio has perhaps the largest impact on clean cycle effectiveness and duration. Though the sample properties within the low O/C range are similar (3.1), the lower the O/C mixture results in the higher yield per shot. More graphene per shot also means more graphene to clean per shot, and O/C mixtures below 0.3 O/C have proven to be unable to consistently cleaned with the current apparatus, thus resulting in the 0.3 O/C sample as the flagship and comparison sample of our work. Increasing the O/C ratio is easier to clean and thus reduces clean cycle time by several seconds; 0.4 O/C is able to function with clean cycle times of 2-5 s.

During a vacuum pump failure resulting in 2 vacuum pumps instead of 3 maintaining the vacuum ballast (and thus a slower and weaker vacuum draw during the evacuation stage and clean cycle), it has been found that the clean cycle time was able to be effectively reduced by several seconds. This reduction in speed of the air flush providing increased

cleaning capabilities indicates the importance of fluid dynamics and turbulence in cleaning the electrode tips, topics which have not yet been explored for this project.

4.3.3 Sample collection

The mass of the graphene collected during the 10 kg run is compared to the predicted mass based on known yield in Figure 4.4 and found to be accurate with the 0.3 O/C sample but not the 0.4 sample, suggesting that earlier estimations of the 0.4 O/C yield was incomplete. Note that this project took place before much of the data in section 3.1 was produced and known.

Vacuum withdrawal is sufficient in removing most of the graphene from the reactor due to the near-air density of the material, while the air flush provides the final contribution. Once withdrawn, the nanoscale particle size of the graphene necessitates high quality filters to properly collect. Though the silicon bag filter is only rated for 3 microns, a majority of the sample is retained due to the agglomeration. A 0.5 μm HEPA filter placed in between the vacuum ballast and bag filter for protection of the vacuum pumps is shown in Figure 4.5 to have been carbonized, and a filter change is required every several kilograms.

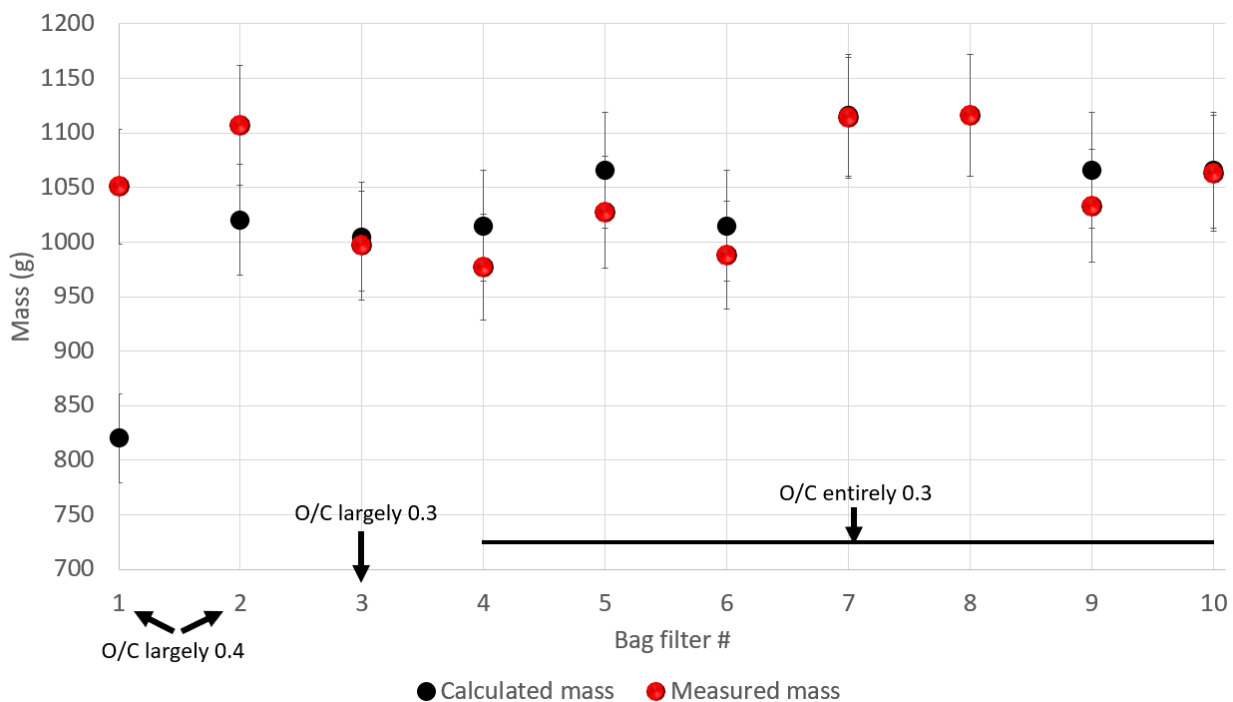


Figure 4.4: Collected mass is plotted versus bag number, with each bag capable holding ~ 1 kg. The estimated mass is plotted in black circles and the measured mass is plotted in red circles, each with a 2% error bar. Mass was measured by weighing the entire collection system before and after the graphene was produced to ensure graphene lost during container transfer would not impact the result. Bags 1-3 were mixtures of various O/C ratios.



Figure 4.5: *Top left: bag filter cut open to reveal graphene inside and picture of HEPA filter; bottom left: 10 kg of graphene collected and stored with a closeup image of the sample; right: single shot graphene sample from the 17 L chamber for comparison.*

The graphene sample and gases withdrawn from the chamber are hot immediately after the reaction. Initial experiments using only the silicon bag filter inside the collection system was found to have holes burned through the top half of the filter as shown in Figure 4.6, likely due to the uniform vacuum in the collection system to pull the reaction products in every direction after exiting the chamber. Thus Kevlar fabric was layered on the top half of the interior of the bag filter to provide high temperature protection [78].



Figure 4.6: *Picture of holes burned through the top half of silicon bag filter. The face of Dr. Arjun Nepal is seen in the background.*

4.3.4 Reactor operating conditions and failures

The machine is programmed to stop running in the event of a detonation failure in order to reduce the waste of resources. Detonations are detected by using a piezocrystal to measure the peak pressure and deemed successful if the pressure passes a minimum threshold.

The MFCs experience wear and flow at reduced rates over time resulting in one gas to finish filling before the other, filling the spark area with either pure oxygen or pure acetylene. Neither environment will produce a detonation [79], inspiring additional programming to stop the detonation process if a gas is not flowing at the required rate. This may also be visually tracked in the form of overlapping arrows on the UI screen depicted in Figure 4.7.

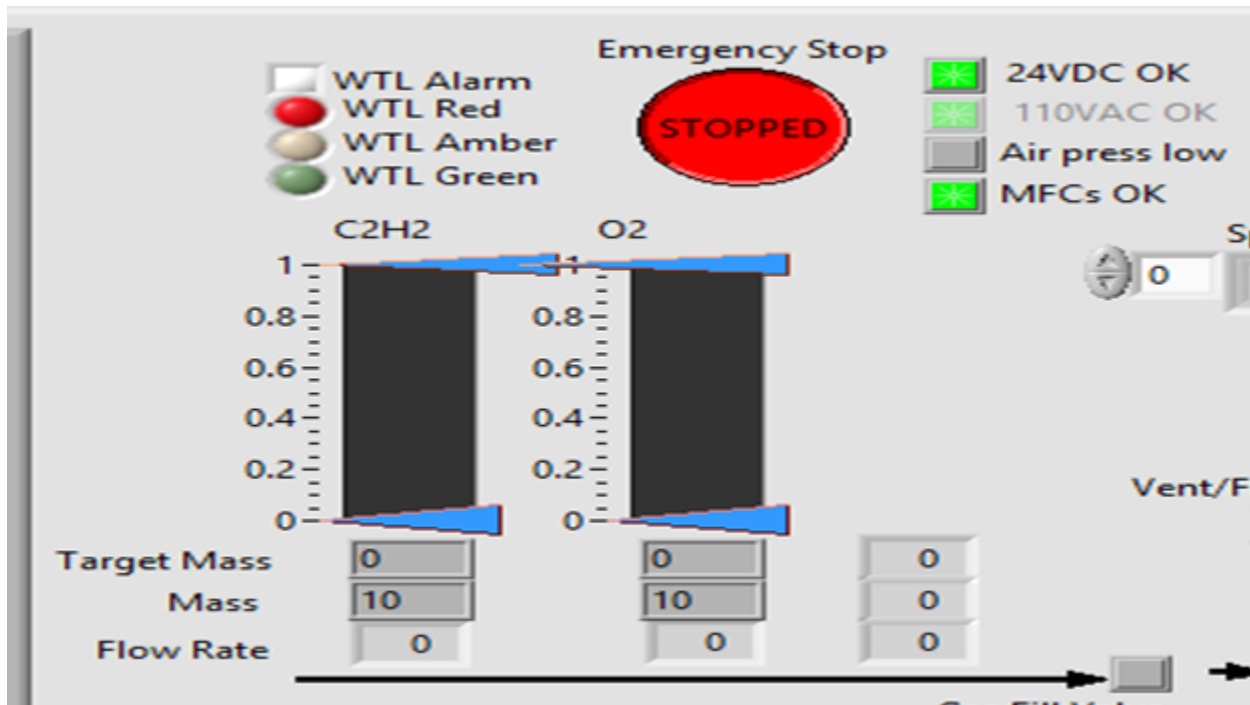


Figure 4.7: Image of the gas fill user interface. The long arrows overlap to monitor the flow rate as the gases fill the chamber.

Most affordable gaskets and o-rings are rated for either high pressure or high temperature and not both [80], leading to many breakages that cause vacuum leaks in the system and reaction gas to be vented to the blast room. The machine heating up during repeated detonations and cooling down afterward further exacerbates this issue by causing micro expansions and condensing in sensitive vacuum-sealed parts of the equipment. External temperatures of the machine generally reach 40-50 °C before further temperature increase will not occur, while the electronic valve that connects the chamber to the collection system shows no such natural asymptotic limit. A simple fan depicted in Figure 4.8 directed at the electronic valve is sufficient in maintaining temperatures under 40 °C thus improving the longevity of the gasket.

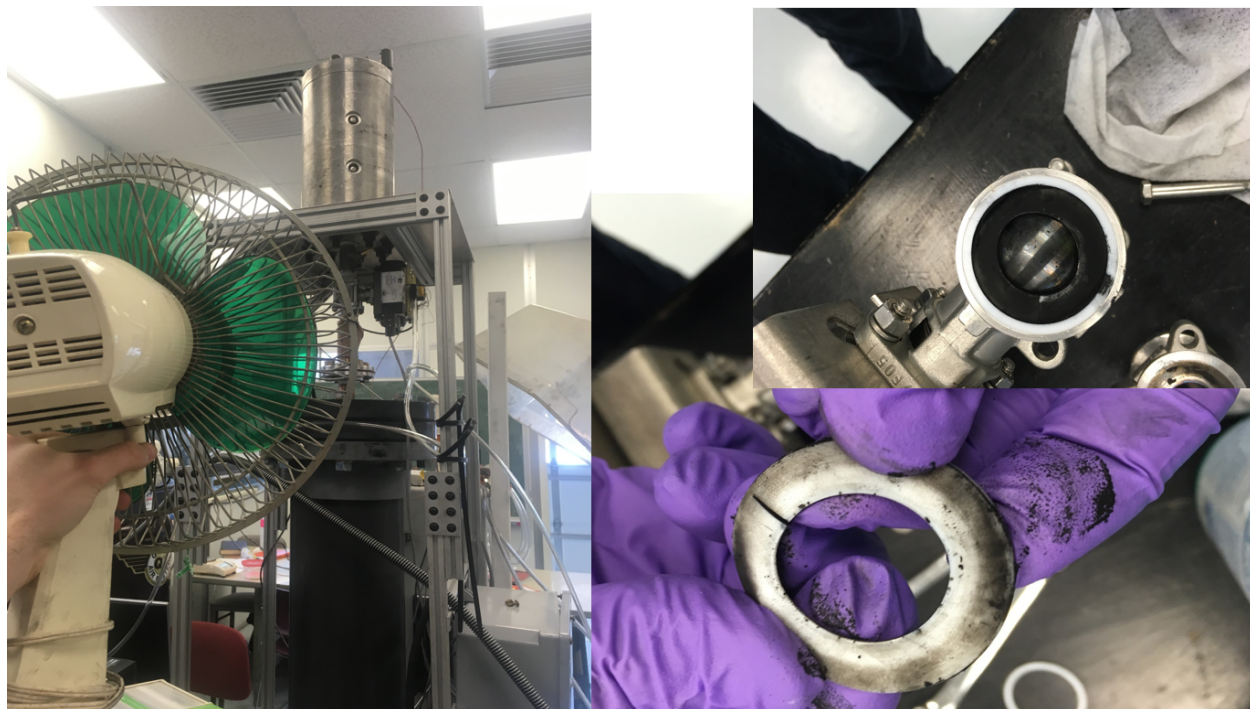


Figure 4.8: *Left: a fan directed at the valve that connects the chamber to the collection system; right: a small crack in the valve gasket responsible for leaking production gas into the blast room.*

4.4 Bulk sample comparison to single-shot sample

Producing kilograms of graphene in a quick process is only useful if the graphene retains its quality and properties. Here, characterization of the bulk graphene in comparison to the original single-shot graphene sample is presented.

4.4.1 Appearance and density

The bulk graphene sample appears as a thick black powder with dense chunks in comparison to the fluffy aerosol gel produced by single shot samples. Figure 4.5 shown earlier provides a visual comparison. Bulk graphene density is measured as 70-100 mg/mL in comparison to the single shot sample at 3-10 mg/mL as shown in 3.1. This is due to the compression effect of being held under constant vacuum during the collection process; crushing of the single-shot samples leads to the same densities.

4.4.2 Raman

Figure 4.9 shows the Raman for the bulk sample compared to the single shot sample has the same peak ratios and peak locations.

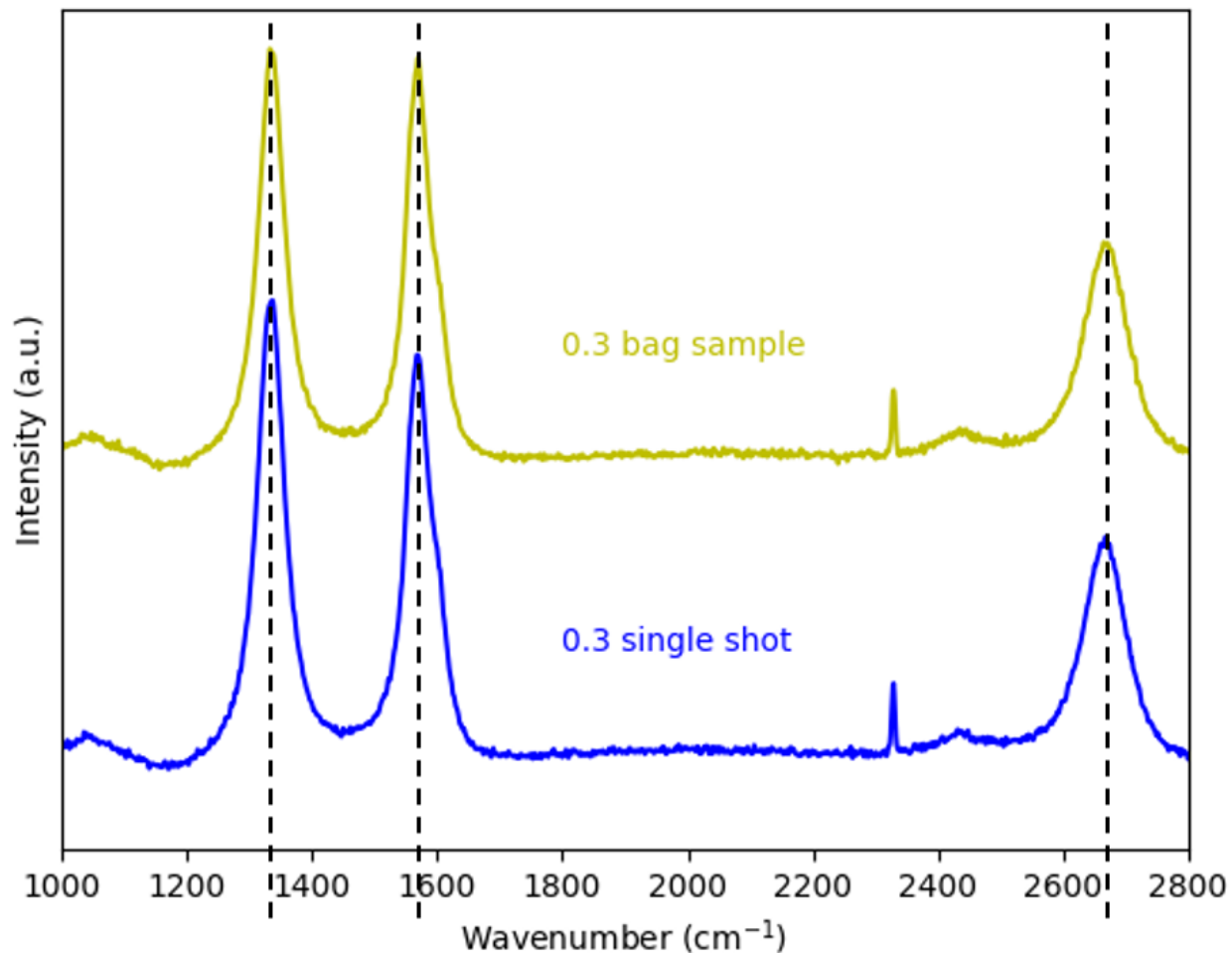


Figure 4.9: Raman of single shot 0.3 O/C sample in blue and bulk 0.3 O/C sample in yellow.

4.4.3 XRD

XRD comparison in Figure 4.10 shows the bulk sample to have the same peak turbostratic structure, FWHM, intensity, and locations as the single-shot sample. Refer to section 3.1 for the full XRD analysis.

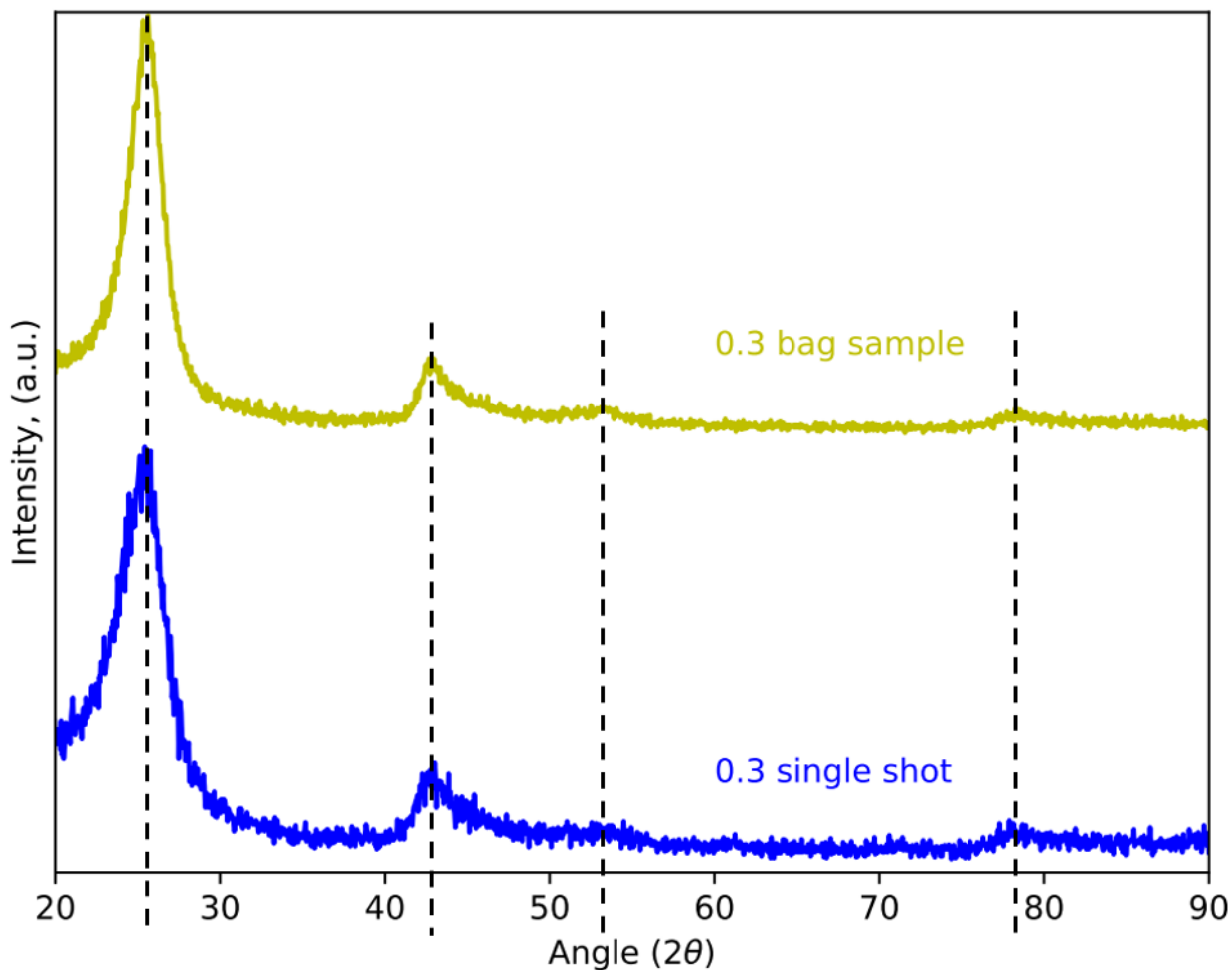


Figure 4.10: XRD of single shot 0.3 O/C sample in blue and bulk 0.3 O/C sample in yellow. The (002) peak intensity is scaled to unity for both samples.

4.4.4 BET

The SSA of the bulk sample in comparison to the single shot sample is the same within experimental error at $168\text{-}170\text{ m}^2/\text{g}$. Crushing of the single-shot sample to produce similar densities as the bulk sample provides no changes to the measured SSA.

4.4.5 TEM

TEM comparison in Figure 4.11 shows little difference in the morphology between the bulk sample and single shot sample. Both produce ramified fractal aggregates and platelet lateral

widths between 20-50 nm.

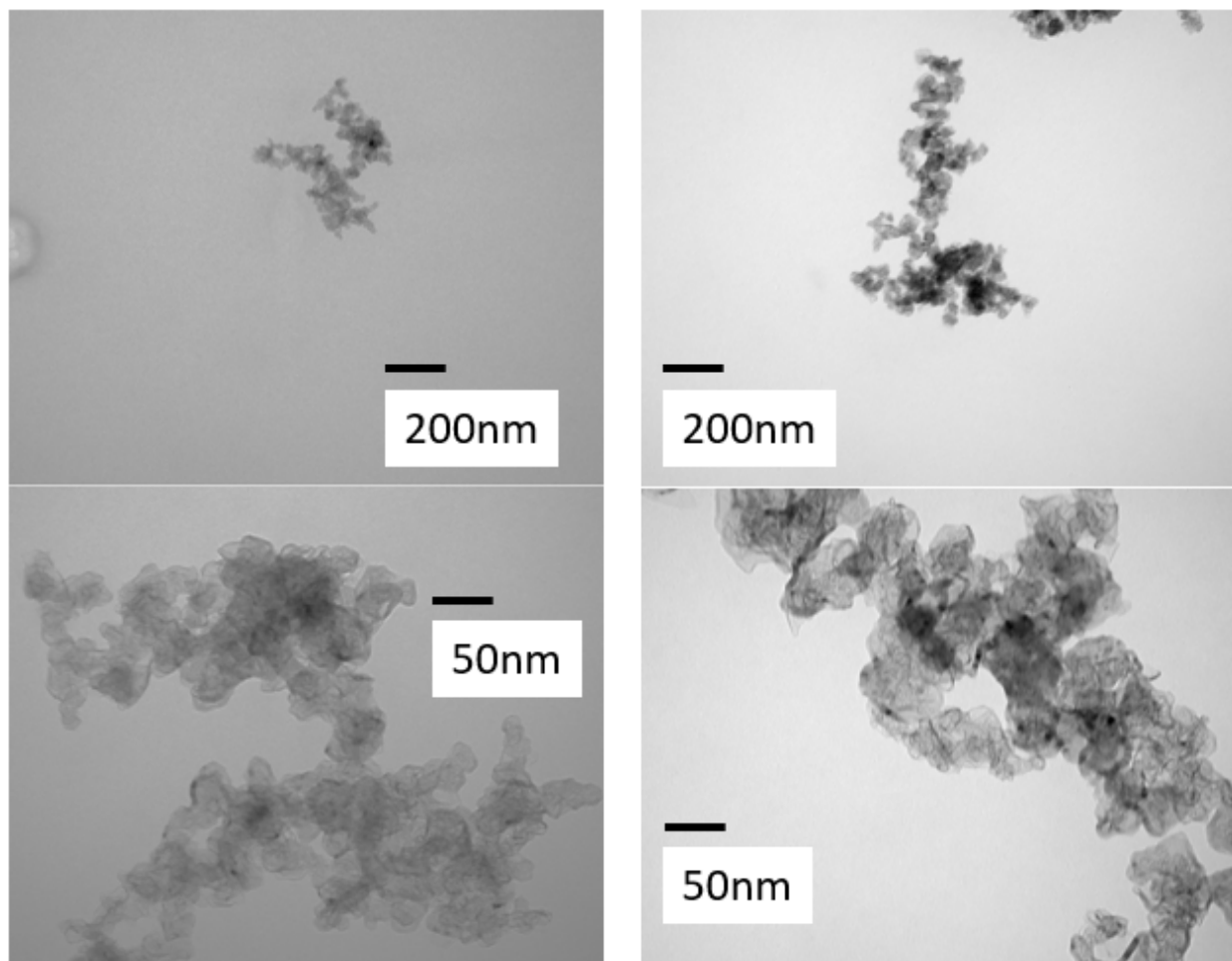


Figure 4.11: *Left: single shot 0.3 O/C sample; right: bulk 0.3 O/C sample.*

4.4.6 SEM

SEM comparison in Figure 4.12 shows little difference in the morphology between the bulk sample and single shot sample. Both produce aggregates of various sizes comprised of smaller fibrous-looking structures.

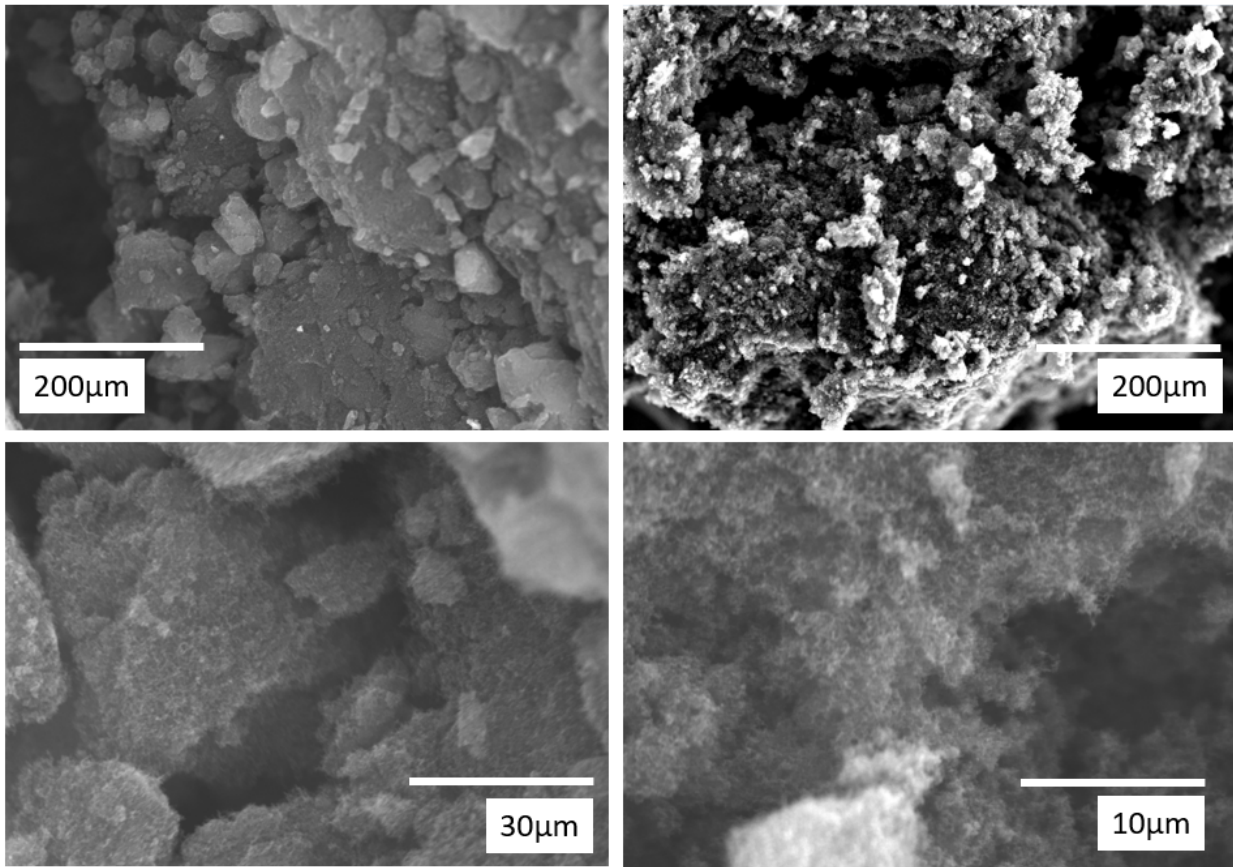


Figure 4.12: *Left: single shot 0.3 O/C sample; right: bulk 0.3 O/C sample.*

Chapter 5

Various precursor fill-mixtures

The success of acetylene-oxygen fill mixtures in producing high quality turbostratic graphene raises the possibility of using other precursor fill-mixtures to obtain similar or perhaps better results. Here, a systematic analysis various other fill-mixtures are presented.

5.1 Methane-oxygen

As a cheaply available commodity, the use of methane to produce graphene or other useful materials via detonation synthesis would help to reduce our carbon footprint [81]. All tested O/C will be > 1 due to methane's flammability limit [82].

5.1.1 Detonation data

Figure 5.1 shows the peak pressure and rise times have an inverse relationship indicative of the deflagration to detonation transition time consistent with data found in section 3.1 [53]. O/C = 1.4 was also attempted multiple times but would not detonate. Spectra was measured but found no blackbody radiation and thus temperature cannot be calculated.

Figure 5.2 shows a chart of the overpressures measured after the detonation that can be taken relative to the fill pressure. At O/C = 2.2 the resulting underpressure made gas recovery difficult; a septum installed on the gas collection port with a syringe was also

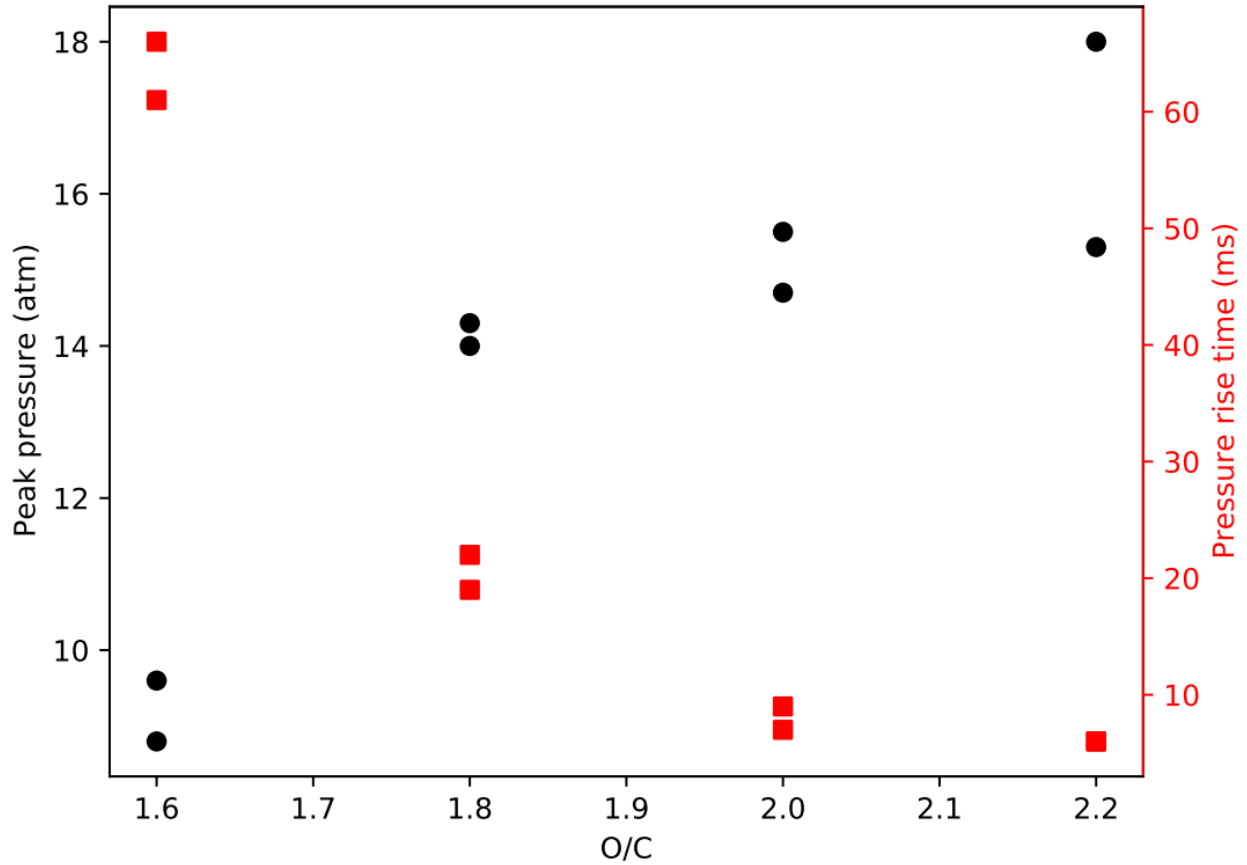


Figure 5.1: Peak pressure plotted in black circles on left axis and rise time to peak pressure plotted in red squares on right axis.

unsuccessful in recovering the gas for analysis.

$\frac{O_2}{CH_4}$	$\frac{O}{C}$	Day 1			Day 2		
		Fill Pressure (atm)	Post Explosion Pressure (atm)	Relative Over Pressure (atm)	Fill Pressure (atm)	Post Explosion Pressure (atm)	Relative Over Pressure (atm)
1.1	2.2	1.05	0.97	0.92	1.05	0.98	0.93
1	2	1.05	1.08	1.03	1.05	1.13	1.08
0.9	1.8	1.06	1.28	1.23	1.05	1.29	1.23
0.8	1.6	1.06	1.45	1.39	1.06	1.45	1.39
0.7	1.4	X	No Detonation				

Figure 5.2: Chart shows the fill pressure, measured overpressure, and relative overpressure adjusted for fill pressure for each O/C.

5.1.2 Post-detonation analysis

Opening the chamber revealed no solid carbon and instead dense gases and water droplets as detonation products. GC analysis was performed on the gases withdrawn for three of the samples in Figure 5.3. Figure 5.4 shows the chemical equation as predicted by the measured after-detonation pressures combined with the calibration of the GC analysis in 5.3.

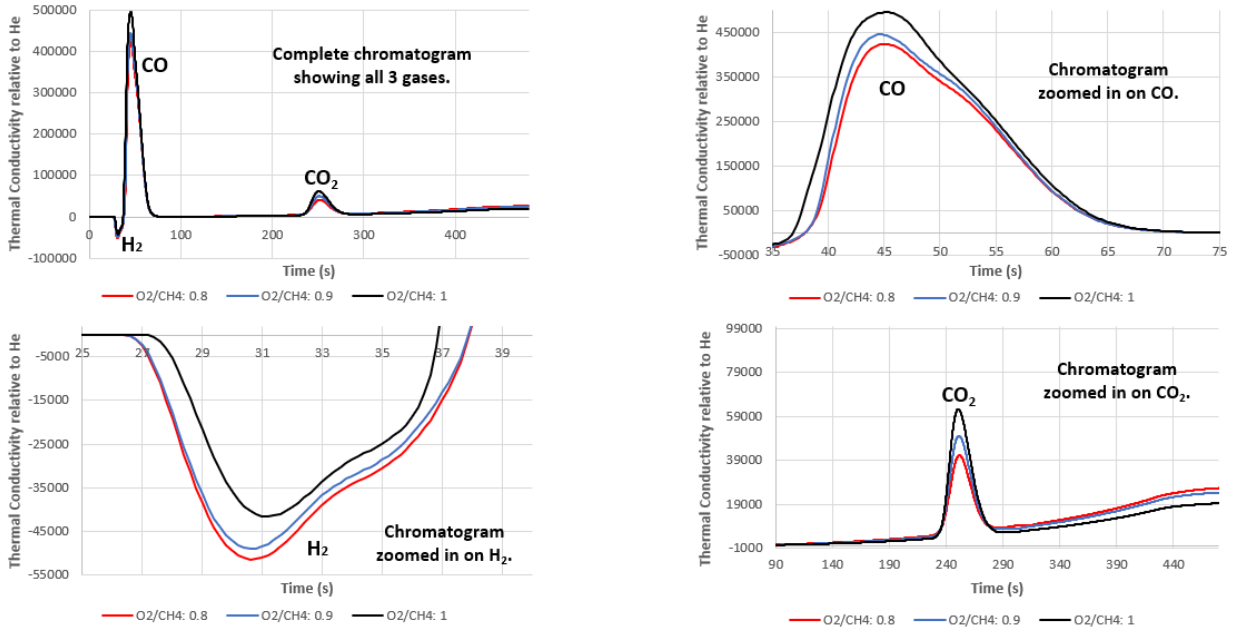


Figure 5.3: GC measurements showing the full chromatogram and closeups up the three detected peaks for $O/C = 1.6, 1.8,$ and 2.0 .

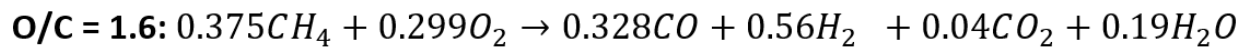


Figure 5.4: The methane-oxygen fill mixture chemical equation for all O/C .

That the final and initial moles in Figure 5.4 can be equated to the measured overpressure relative to the fill pressure indicates that a matrix of predictable gaseous products are possible for each O/C resulting in Figure 5.5.

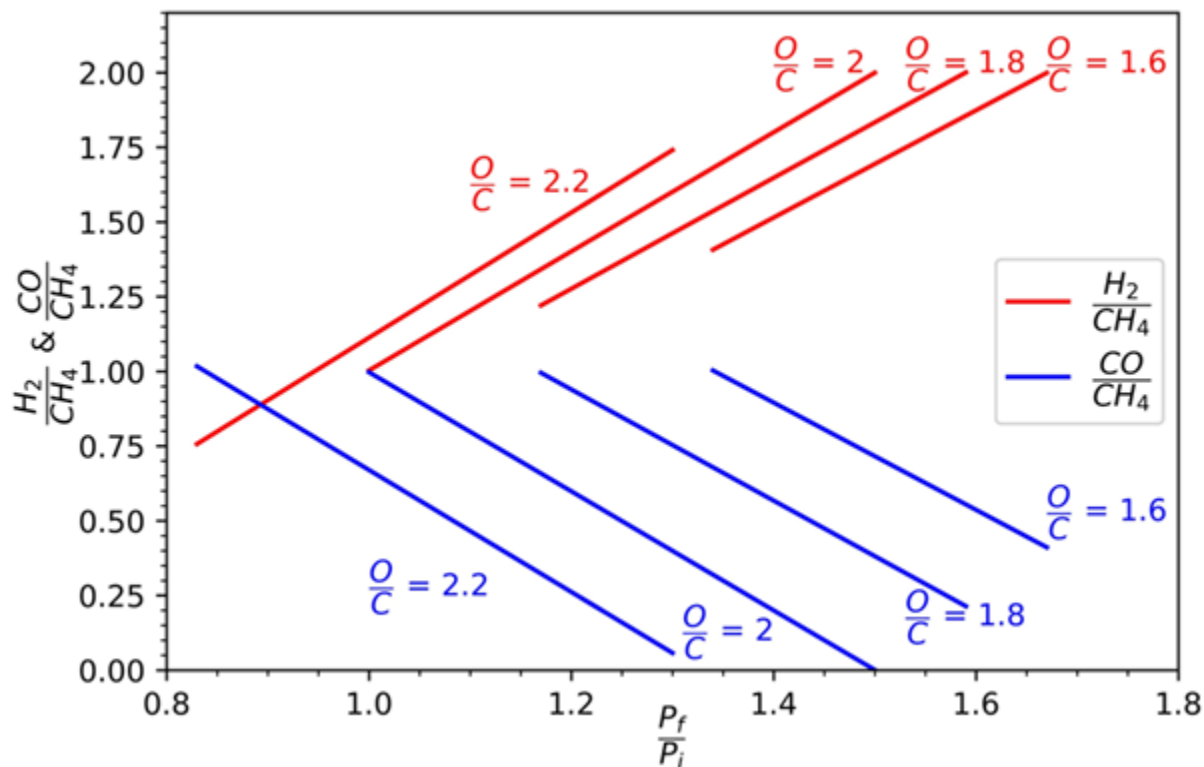


Figure 5.5: Molar hydrogen (red) and carbon monoxide (blue) products with respect to methane-fill is plotted as a function of the ratio of over pressure to fill pressure.

Though no graphene was obtained, the detonation products hydrogen and carbon monoxide are valuable industry commodities [64–72] as a product referred to as synthesis gas (syngas) [83]. Syngas is typically created using reactors that heat methane up to 800-1000 °C and produces carbon soot byproducts [84, 85]. Our technology by comparison is green with no wasted byproducts, and cheap by using a simple spark to induce the potential of the precursors to bring their own energy to react. Thus, converting methane to syngas via detonation synthesis was filed for a patent, and prototypes for mass production are under experimentation.

5.2 Ethylene-oxygen

Ethylene, also known as ethene, is a hydrocarbon with many similarities to that of acetylene [86]. Here, a rigorous analysis of ethylene-oxygen fill-mixtures to that of acetylene-oxygen

fill-mixtures is presented.

In addition to varying O/C from 0.6 to 1.0, experiments with filling to 2 atm for the 0.7 O/C sample is included. A 2 atm fill pressure may result in changes to detonation temperature and peak pressure which subsequently may affect the resulting properties and morphology of the material.

5.2.1 Pressure

Figure 5.6 plots the peak pressure and pressure rise time data as a function of O/C. As seen in sections 3.1 and 5.1 there is an inverse correlation between rise time and peak pressure, and higher O/C mixtures have quicker rise times and larger peak pressures. The 0.7 O/C 2 atm fill pressure and 0.7 O/C 1 atm fill pressure have peak pressures that range between 21-26 atm and 10-13 atm, respectively, while having the same rise times. Taking the former's fill pressure into account by ratioing P_f/P_i results in the same peak pressure data range. It is worth noting that around the 0.825 O/C mixture the peak pressure and rise time start behaving similarly to that of 0.25 O/C acetylene-oxygen fill mixtures.

Similarly, the overpressures plotted in Figure 5.7 for the 0.7 O/C 2 atm fill pressure lie in the same range to that of the 1 atm fill pressure when taking P_f/P_i into account, obeying the ideal gas law [52].

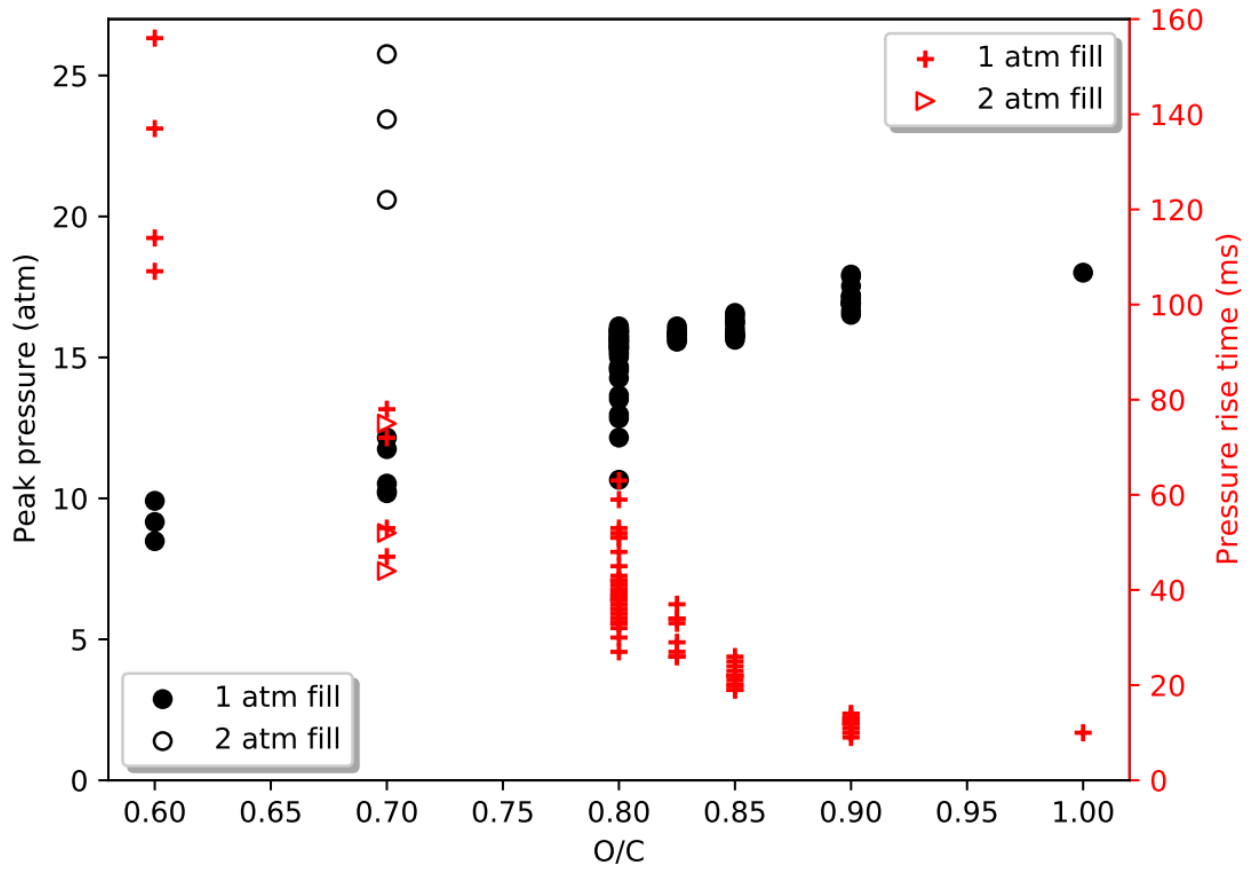


Figure 5.6: Peak pressure in black circles on the left axis and rise time to peak pressure in red pluses and triangles on the right axis are plotted versus O/C . Open circles and open triangles represent 2 atm fill data that was taken for 0.7 O/C .

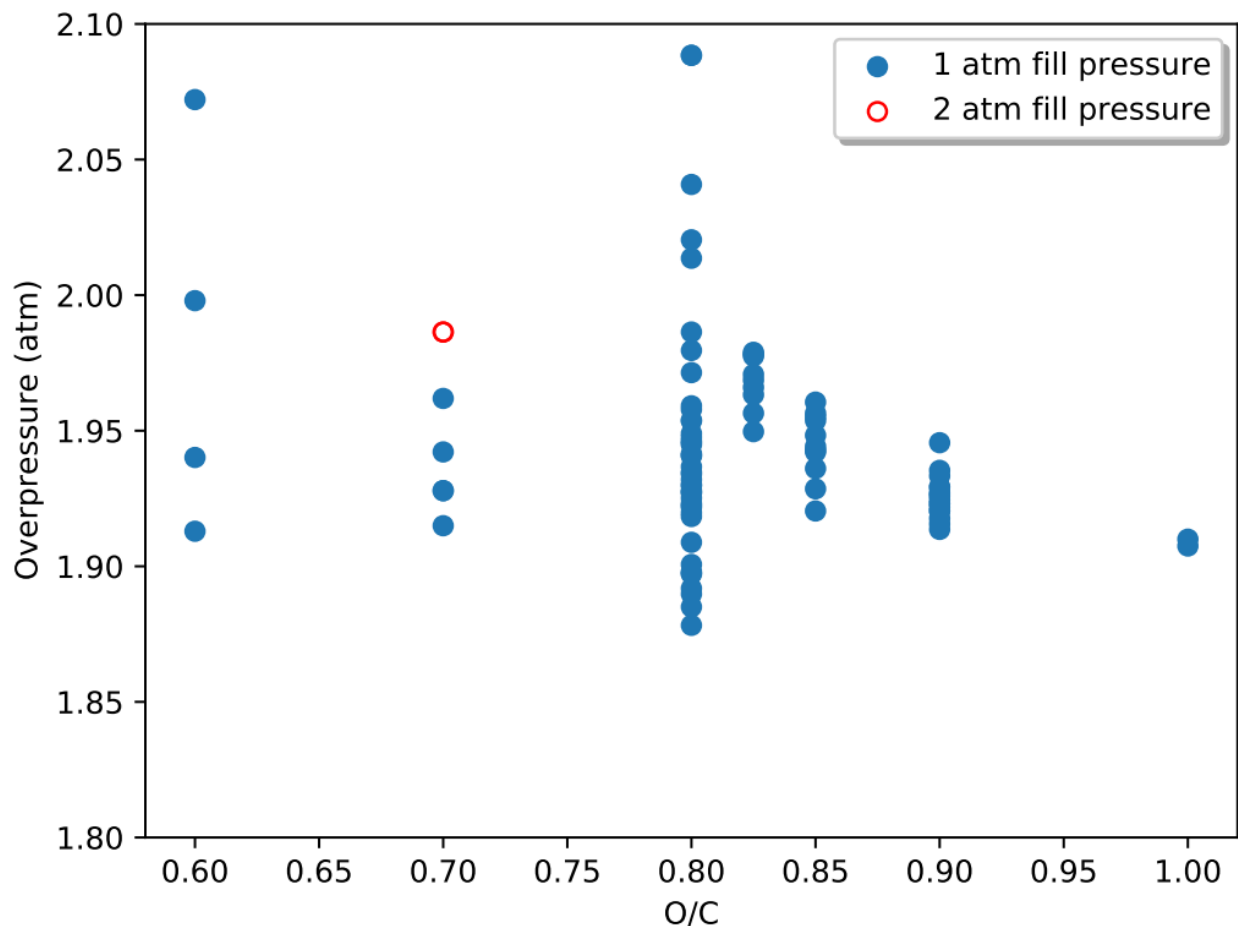


Figure 5.7: After-detonation overpressure plotted as a function of O/C. 1 atm fill pressures are plotted as blue closed circles, and 2 atm fill pressures are plotted as red open circles. All data is taken relative to fill pressure.

5.2.2 Temperature

Unlike acetylene-oxygen mixtures that had relatively constant temperature regardless of O/C (as seen in section 3.1), ethylene-oxygen mixtures show increasing temperature with increasing O/C in Figure 5.8. Ethylene-oxygen fill mixtures do not reach similar temperatures as acetylene-oxygen until 0.9 O/C. The 2 atm fill pressure at 0.7 O/C show ~ 75 K larger temperatures compared to the 1 atm fill pressure, a result that is largely consistent with pressure data in 5.2.1. Light intensity duration is also plotted versus O/C and seen to decrease with increasing O/C, although there is large deviation within the data. This

duration is correlated with peak pressure rise time (Figure 5.6) in that long rise times and durations of light intensity indicate a small degree of burning and particle formation before the sample mixture eventually detonates and quickly completes the reaction [53]. By comparison, the majority of acetylene-oxygen mixtures had a light intensity duration of 20-30 ms in Figure 3.6. The 1.0 O/C ethylene-oxygen fill mixture spectra was not a blackbody and so temperature could not be measured.

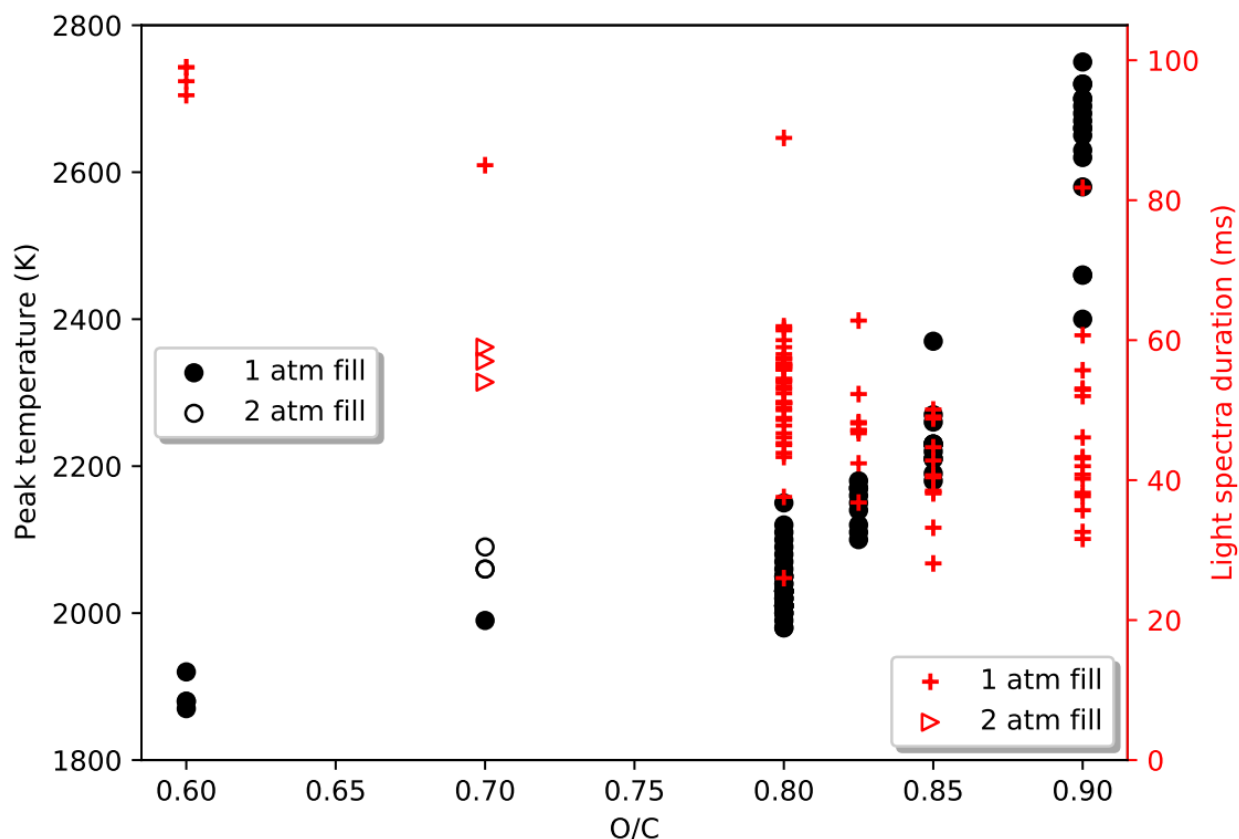


Figure 5.8: Temperature in black circles on the left axis and duration of light intensity in red pluses and triangles on the right axis are plotted versus O/C. Open circles and open triangles represent 2 atm fill data that was taken for 0.7 O/C. The 1.0 O/C mixture is omitted due to a lack of blackbody radiation.

5.2.3 Mass and yield

Figure 5.9 shows both mass and yield expectedly decrease linearly with O/C as seen in section 3.1. The 0.7 2 atm fill pressure produced twice the mass at the same yield % to that

of the 0.7 1 atm fill pressure, a result comparable to the pressures found in section 5.2.1. Blackbody radiation was not found for methane data (section 5.1.1) which forecasted zero solid carbon yield; similarly, no blackbody radiation was measured for O/C = 1.0 ethylene fill mixtures which also produced zero yield.

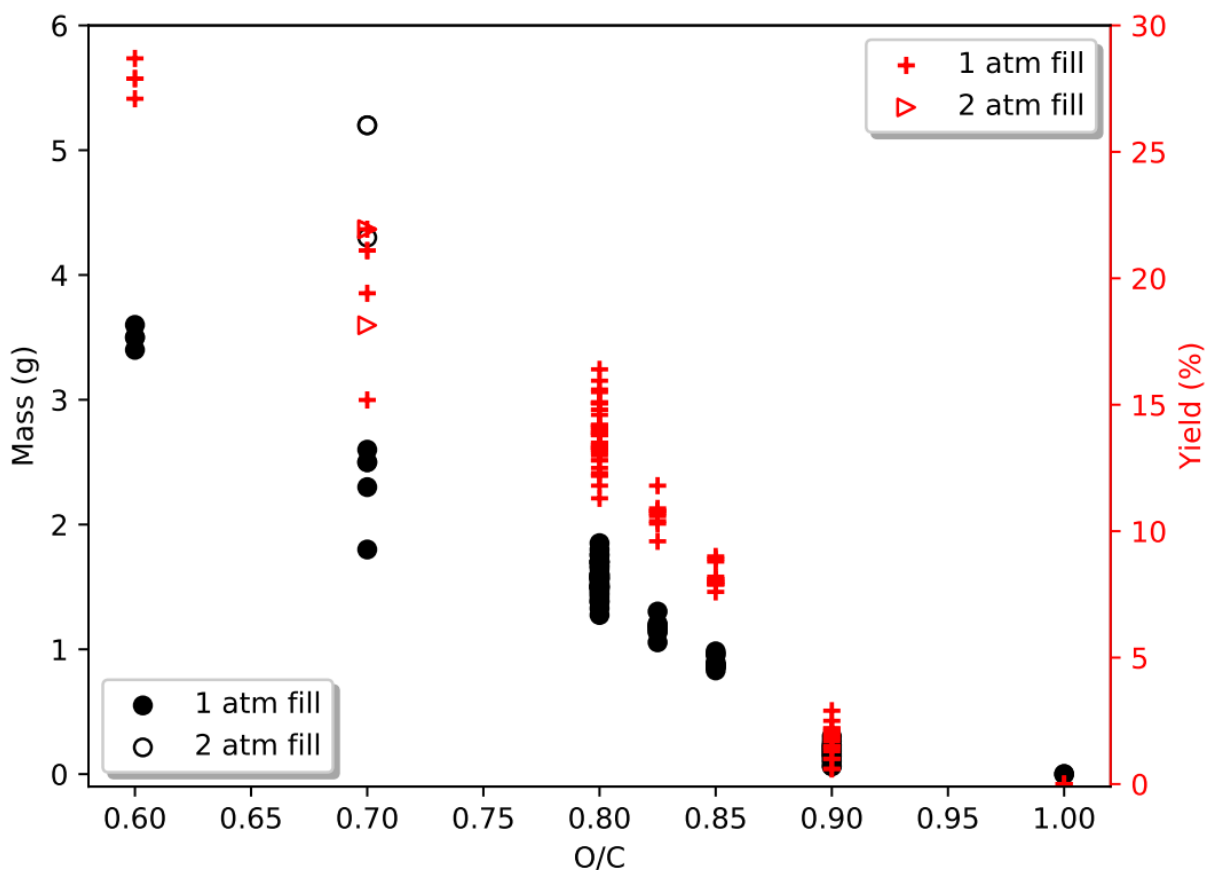


Figure 5.9: Mass in black circles on the left axis and yield in red pluses and triangles on the right axis are plotted versus O/C. Open circles and open triangles represent 2 atm fill data that was taken for 0.7 O/C.

5.2.4 Chemical equation

Figure 5.10 shows the chemical equation produced by a combination of overpressure data and GC analysis. The equations are similar to that of acetylene-oxygen fill mixtures in section 3.1, though like methane-oxygen fill mixtures water and zero carbon are produced at O/C mixtures ≥ 1 .

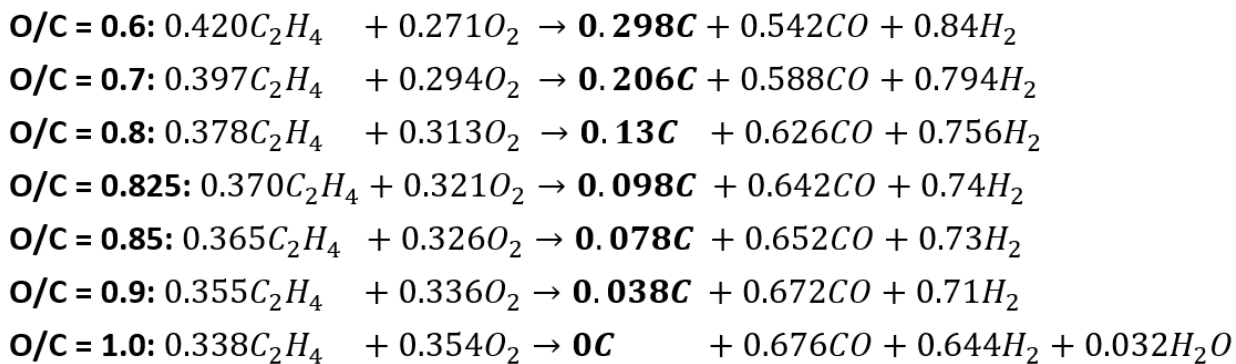


Figure 5.10: *The chemical equation in moles for ethylene-oxygen fill mixtures for all O/C. 2 atm fill pressures for 0.7 O/C are equivalent for 1 atm fill pressures when adjust for initial pressure and thus are represented by the 1 atm equation.*

5.2.5 BET

Figure 5.11 shows the SSA for the ethylene-oxygen samples increase with increasing O/C. At 164 m^2/g 0.825 O/C sample is just under the 0.3 acetylene-oxygen O/C sample at 168 m^2/g before decreasing at > 0.85 O/C. The 0.6, 0.7, 0.8, and 0.9 O/C follow a linear pattern with some variation around 0.825 and 0.85 O/C.

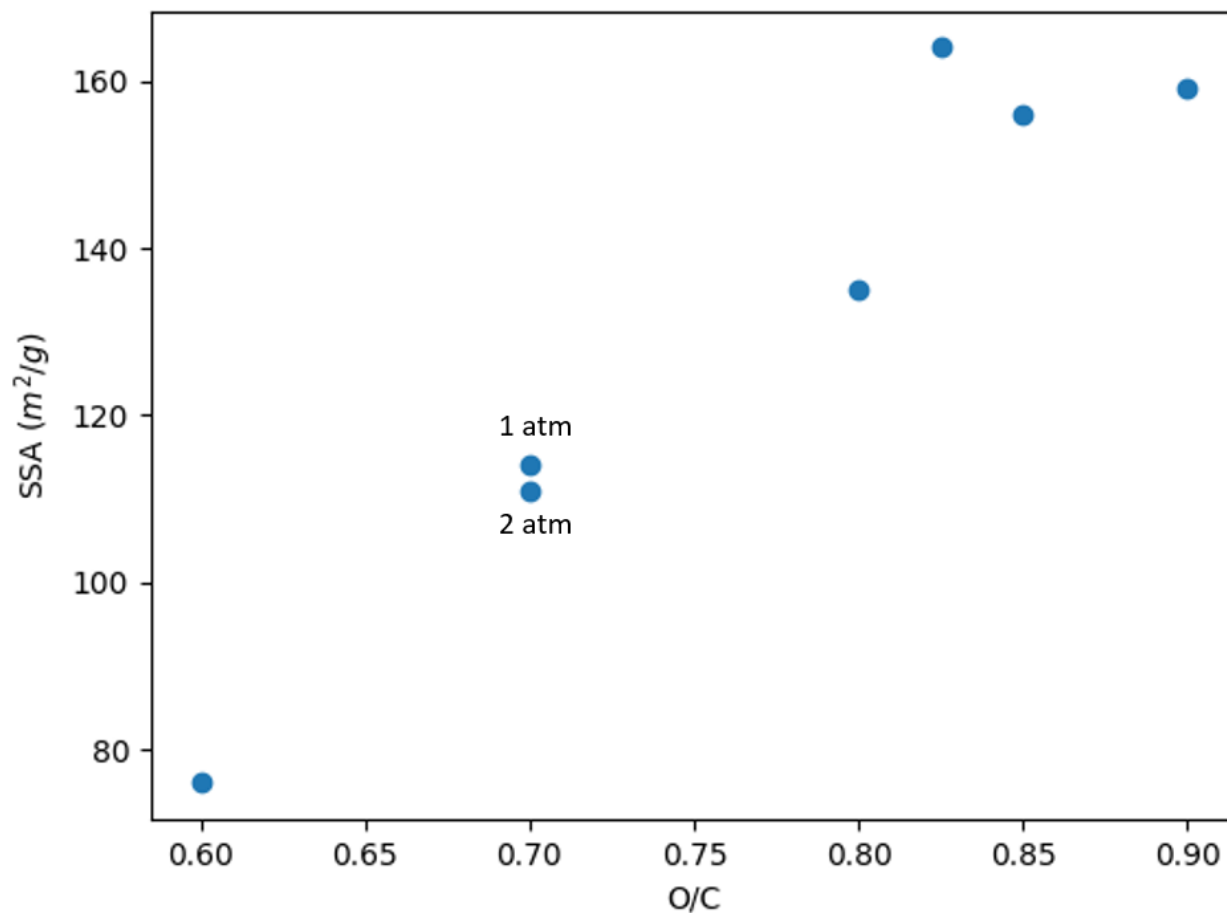


Figure 5.11: *SSA plotted versus O/C. The 2 atm and 1 atm fill pressures for 0.7 O/C are labeled.*

5.2.6 Raman

Figure 5.12 shows Raman spectra of ethylene-oxygen samples in comparison to the 0.3 O/C acetylene-oxygen mixture and graphite as well as a log plot of the 0.825 and 0.9 O/C mixtures to showcase more detail. Table 5.1 supplements Figure 5.12. The Raman indicates that all of the ethylene samples are clearly not a graphite, but become more graphitic with increasing O/C, a similar trend to the acetylene samples. Samples between 0.6 and 0.8 O/C have broad overlapping D and G peaks and small 2D peaks reminiscent to that of soot and sp^2 hybridized amorphous carbon [87]. The 2 atm sample shows minor differences to that of the 1 atm sample at 0.7 O/C in peak locations which is likely due to subtle differences in the

crystallinity of the sample [38], but overall the two samples have relatively similar Raman spectra. By $O/C = 0.825$ the ethylene samples begin to show peak locations, FWHM, and peak ratios reminiscent to that of low O/C acetylene graphene samples, with the 0.9 O/C sample showing peak locations, FWHM, and peak ratios that begin to transition to that of high O/C acetylene graphene samples [35–38, 88–90].

Though the resolution is low both log plots indicate turbostratic Raman peaks between 1800 and 2050 cm^{-1} . The 0.825 and 0.9 O/C spectra as a whole resemble low O/C and high O/C graphene, respectively, despite being more amorphous with respect to peak locations, FWHM, and peak ratios. All weak peaks signifying single layer CVD graphene are present for the ≥ 0.825 O/C samples [35–38, 88–90].

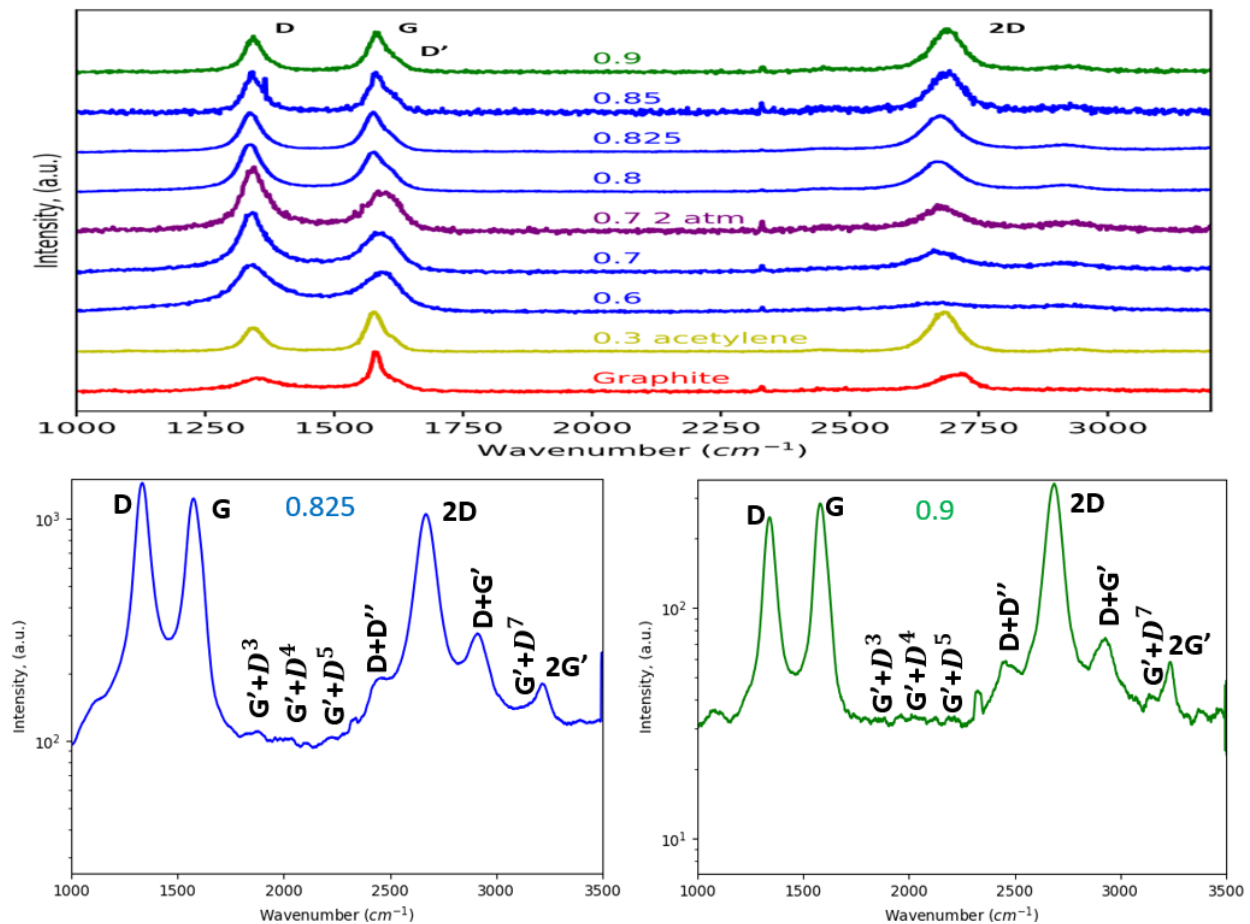


Figure 5.12: Raman spectra of ethylene samples in comparison to graphite and the 0.3 O/C acetylene sample, and spectra of the 0.825 and 0.9 O/C ethylene samples plotted on a log scale

O/C	D-peak (cm^{-1})	G-peak (cm^{-1})	2D-peak (cm^{-1})	G FWHM	2D FWHM	I_D/I_G	I_{2D}/I_G
Graphite	1355	1580	2715	27	77	0.35	0.47
0.3 acetylene	1345	1579	2683	41	65	0.72	1.05
0.6	1339	1594	2667	101	207	1.20	0.24
0.7	1340	1590	2669	79	121	1.50	0.52
0.7 2 atm	1344	1598	2669	81	91	1.60	0.69
0.8	1338	1577	2671	67	92	1.20	0.75
0.825	1336	1576	2675	52	87	0.98	0.91
0.85	1339	1582	2690	46	75	1.01	1.04
0.9	1342	1582	2690	44	70	0.90	1.10

Table 5.1: *Tabulated data of Raman spectra for the ethylene samples.*

5.2.7 XRD

XRD of ethylene-oxygen samples are compared to 0.3 O/C acetylene-oxygen and graphite in Figure 5.13. Graphite spectra are the same as used in section 3.1 and labeled accordingly [91]. All ethylene-oxygen samples have a strong (002) peak and (004), and the absence of mixed reflections (101) and (103) indicates randomly rotated graphene platelets with respect to each other (turbostratic) similar to that of acetylene-oxygen samples. Higher O/C has more visibility and greater signal-noise ratio indicating higher degrees of crystallinity [92]. There is no difference between the 1 atm and 2 atm fill pressures at 0.7 O/C. 0.6 – 0.8 O/C have (002) peak locations more similar to that of soot, becoming more graphenic with higher O/C. At $O/C \geq 0.825$ samples are similar to low O/C acetylene-oxygen samples, with 0.9 O/C ethylene-oxygen approaching the properties to that of high O/C acetylene-oxygen samples.

Table 5.2 tabulates the (002) peak location, FWHM, d-spacing, Scherrer equation τ , and predicted number of layers via the same methodology outlined in section 3.1. Increasing O/C right-shifts the (002) peak location similar to that of the acetylene-oxygen samples and is reflected in the remaining variables.

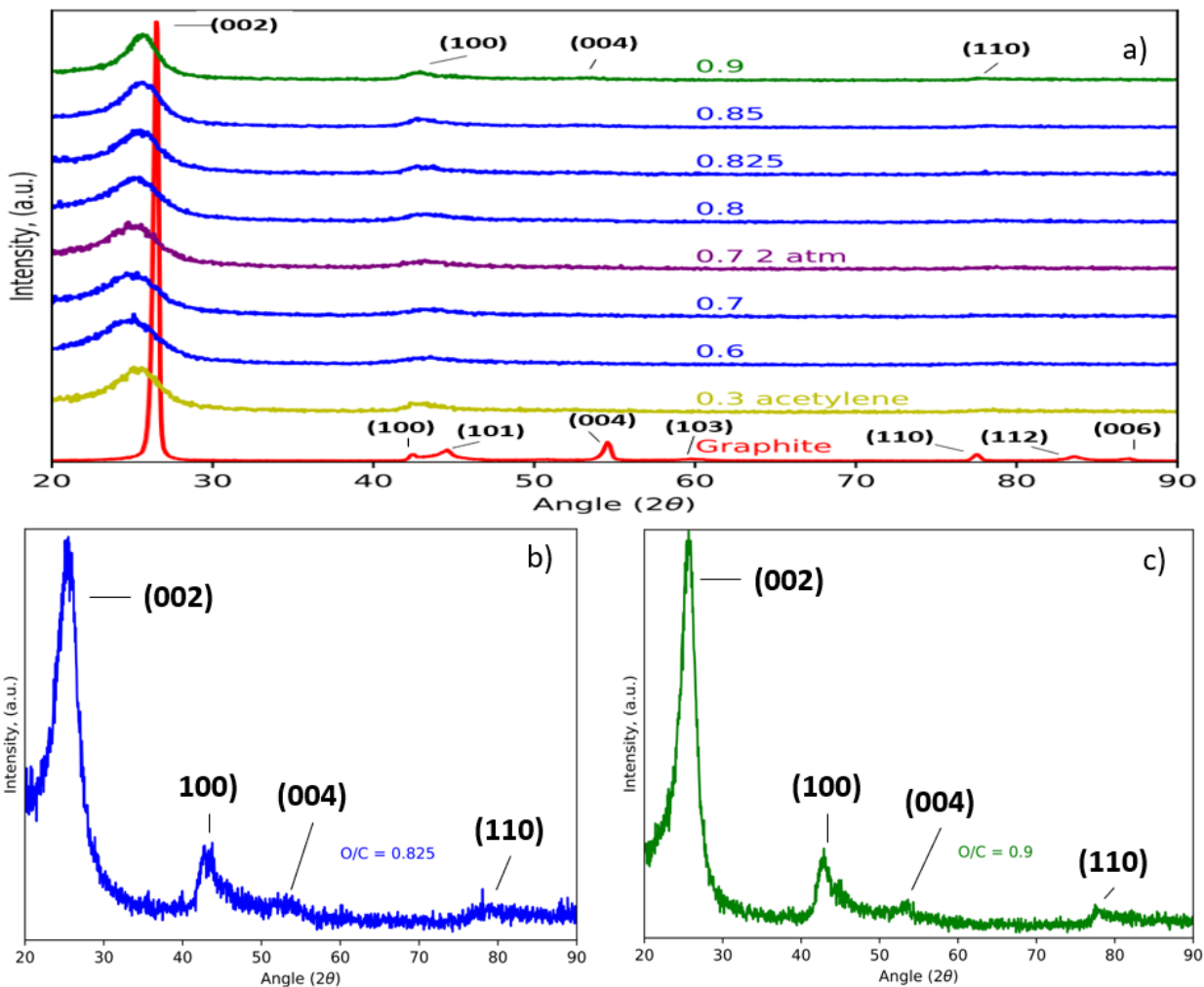


Figure 5.13: All (002) peaks are scaled to equal unity. a) XRD of ethylene-oxygen (blue) samples in comparison to the 0.3 O/C acetylene-oxygen sample (yellow) and graphite (red). The 0.9 O/C ethylene-oxygen sample is plotted in green. b) XRD spectrum of 0.825 O/C ethylene-oxygen sample. c) XRD spectrum of 0.825 O/C ethylene-oxygen sample.

O/C	(002) FWHM	(002) location (°)	d-spacing (nm)	τ (nm)	# of layers
Graphite	0.38	26.5	0.336	21.25	63.2
0.3 acetylene	3.07	25.33	0.351	2.62	7.5
0.6	6.61	25.06	0.355	1.22	3.4
0.7	3.32	25.00	0.356	2.42	6.8
0.7 2 atm	3.02	25.02	0.356	2.67	7.5
0.8	2.86	25.26	0.352	2.82	8.0
0.825	2.74	25.56	0.348	2.94	8.4
0.85	2.5	25.60	0.348	3.22	9.3
0.9	1.91	25.67	0.347	4.22	12.2

Table 5.2: *Tabulated data of XRD FWHM, location, d-spacing, Scherrer equation, and predicted number of layers.*

5.2.8 TEM

TEM images from Figure 5.14 show flake widths from 20-50 nm for all O/C. The 0.6-0.8 O/C have a spherical morphology resembling soot [93], while 0.825 and 0.85 O/C have more crystalline flake structure resembling low O/C acetylene graphene in section 3.1. O/C = 0.9 shows crystalline flake structure resembling low O/C acetylene graphene as well as larger spherical particle structure resembling that of high O/C acetylene graphene, indicating its transitional morphology between the two graphene phases. There is no clear distinction between the 1 and 2 atm fill pressure samples.

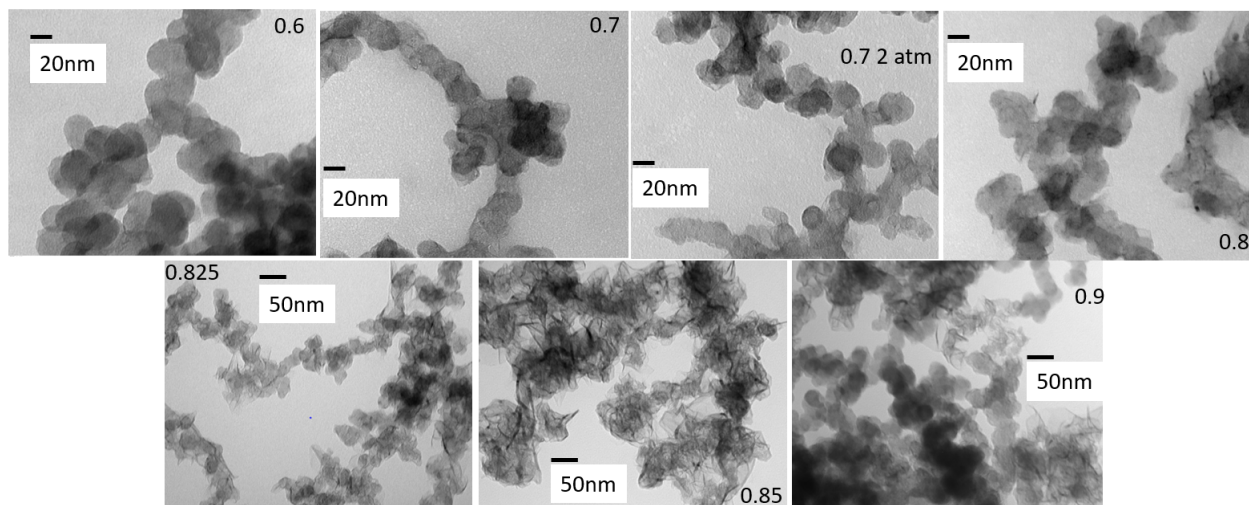


Figure 5.14: *TEM images of ethylene-oxygen samples.*

5.2.9 SEM

SEM images in Figure 5.15 were only captured for O/C 0.6 to 0.8. All O/C have a three-dimensional morphology, appearing as porous balled aggregates, perhaps fractal [32]. Each aggregate is composed of smaller fibrous structures. There is no clear distinction between the 1 and 2 atm fill pressure samples.

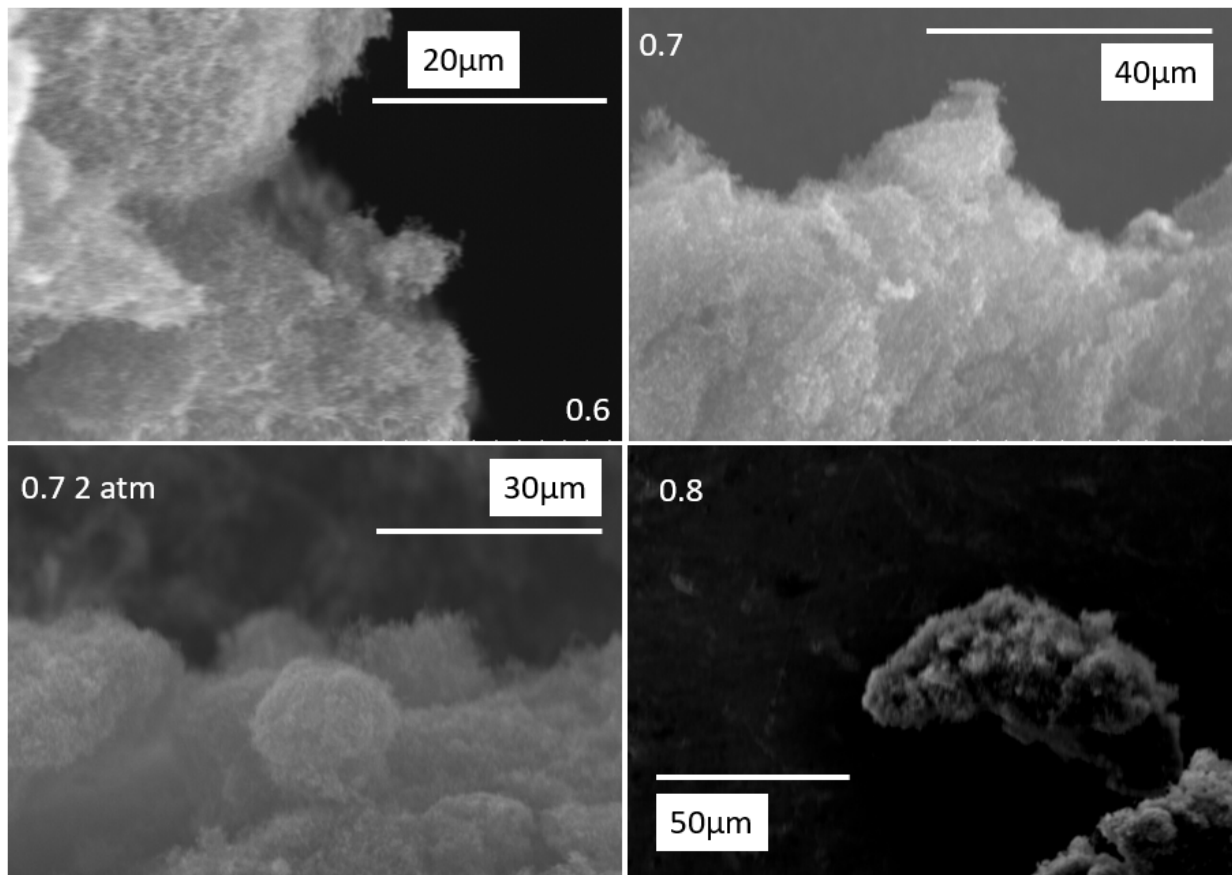


Figure 5.15: SEM images of ethylene-oxygen samples.

5.3 Acetylene-oxygen + Argon

Completion of the ethylene-oxygen sample analysis showed a transition from sooty materials to low O/C acetylene-graphene properties to high O/C acetylene-graphene properties, correlating with increasing O/C and temperature. We hypothesize that temperature is the key difference between formation of soot or graphene; by adding argon, an inert background gas that can translate in three degrees of freedom to absorb energy [52], we aim to reduce the temperature of the acetylene-oxygen mixture detonation and thus change the properties of the material, ideally creating a soot.

Keeping the 0.3 O/C acetylene-oxygen fill mixture constant, argon was included as 50%, 40%, 30%, 20%, or 10% of the total molar volume inside of the chamber. The 50% and

40% 0.3 O/C mixtures did not detonate. Keeping the 0.5 O/C acetylene-oxygen fill mixture constant, argon was included as 90%, 80%, 70%, 60%, 50%, or 30% of the total molar gas volume inside of the chamber. The 60-90% mixtures did not detonate. In both O/C, the highest listed % argon were attempted first, with the argon % being reduced after multiple detonation failure attempts. Thus a total of five acetylene-oxygen + argon samples were obtained.

5.3.1 Pressure, rise time, temperature, mass, density, and SSA

Figure 5.16 shows the peak pressure, rise time to peak pressure, temperature, collected sample mass, powder density, and SSA of the argon-added samples relative to the original 0% argon samples. Table 5.3 tabulates the same dataset. For the 0.3 sample, there are slight increases to rise time to peak pressure with increasing argon, and slight decreases to detonation peak pressure, temperature, powder density, and mass with decreasing argon. Most changes are within experimental error indicating reducing the temperature of the detonation was not enough to significantly affect the sample properties. The % yield of the collected mass is the same for all samples.

For the 0.5 sample, there is a significant increase in rise time to peak pressure and SSA with increasing argon, a significant decrease in powder density with increasing argon, and a slight decrease in peak pressure, temperature, and mass with increasing argon. Though the temperature decrease is of the same order of magnitude to that of the 0.3 O/C + argon samples, the changes in the measured properties are more distinct; furthermore, the appearance of the sample changed from that of a grey-black powder to a black fluffy aerosol gel with added argon.

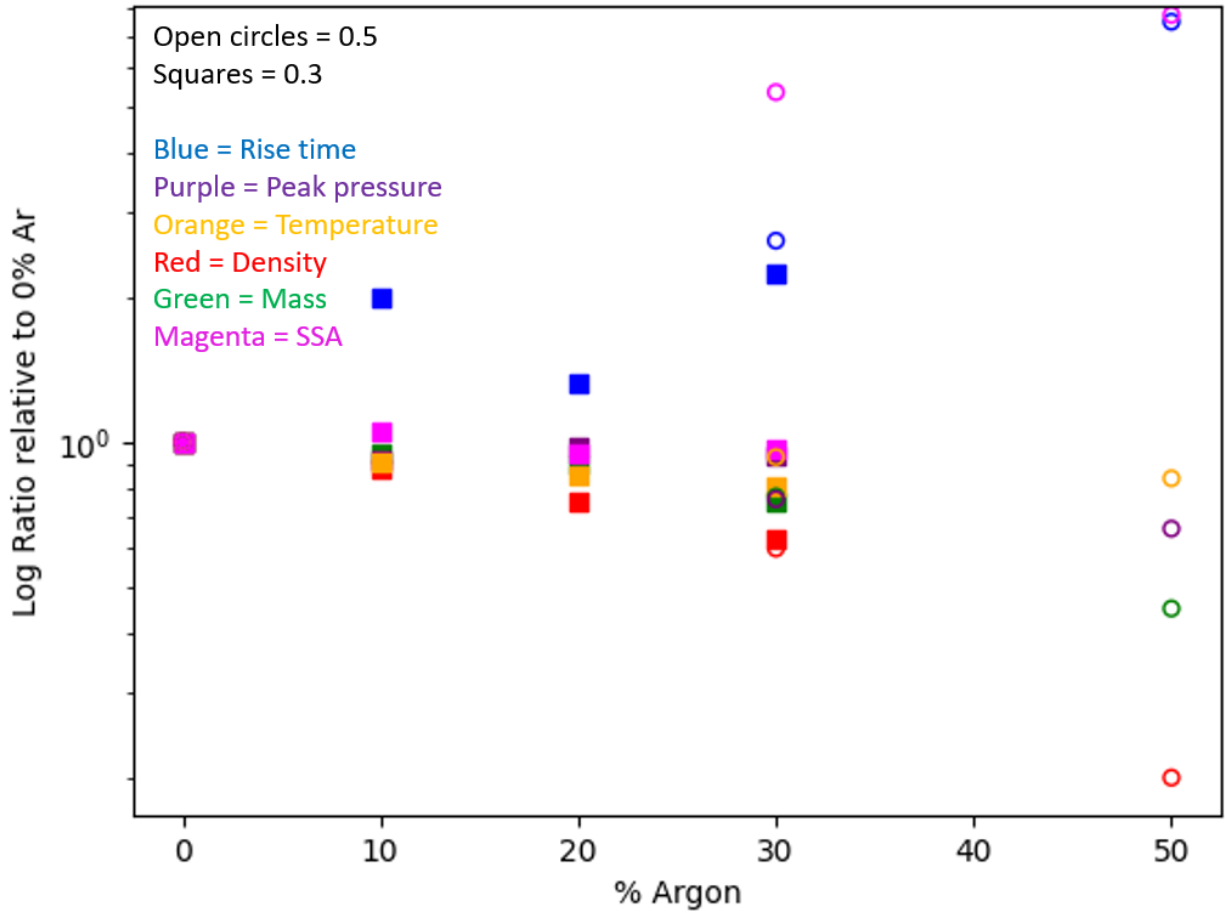


Figure 5.16: Comparison of samples with added argon to the original samples. The open circles represent the 0.5 O/C, and the squares represent the 0.3 O/C. Rise time to peak pressure is plotted in blue, the peak pressure is plotted in purple, the temperature is plotted in orange, the density is plotted in red, the mass is plotted in green, and the SSA is plotted in magenta.

O/C	% Argon	Rise time (ms)	Peak pressure (atm)	Temperature (K)	Mass (g)	Powder density (mg/mL)	SSA (m^2/g)
0.3	0	24	12.9	2550	8.14	8	169
0.3	10	48	11.9	2310	7.74	7	177
0.3	20	32	12.7	2180	7.34	6	160
0.3	30	54	12.1	2070	6.11	5	164
0.5	0	8	17.0	2550	4.84	25	20
0.5	10	21	13.0	2360	3.72	15	107
0.5	30	60	11.3	2140	2.17	5	155

Table 5.3: *Tabulated data of rise time to peak pressure, peak pressure, temperature, mass, powder density, and SSA of the acetylene+argon samples.*

5.3.2 Raman

Figure 5.17 supplemented by Table 5.4 show the Raman data for the argon samples in comparison to the original samples and graphite. The addition of argon did not appreciably change the peak locations of the D and G peaks for all samples. For the 0.3 O/C sample, adding argon induces small shifts in the 2D peak location and a larger FWHM with increasing argon of both the G and 2D peaks. The peak ratios I_D/I_G and I_{2D}/I_G increase and slightly decrease, respectively, with added argon indicating higher degrees of disorder and increased presence of amorphous carbon. For the 0.5 O/C sample, adding argon has major shifts in the 2D peak location and a larger FWHM with increasing argon of both the G and 2D peaks. The peak ratios I_D/I_G and I_{2D}/I_G both significantly increase approaching characteristics of the low O/C samples with added argon, which signifies a higher degree of disorder and increases presence of amorphous carbon [35–38, 88–90].

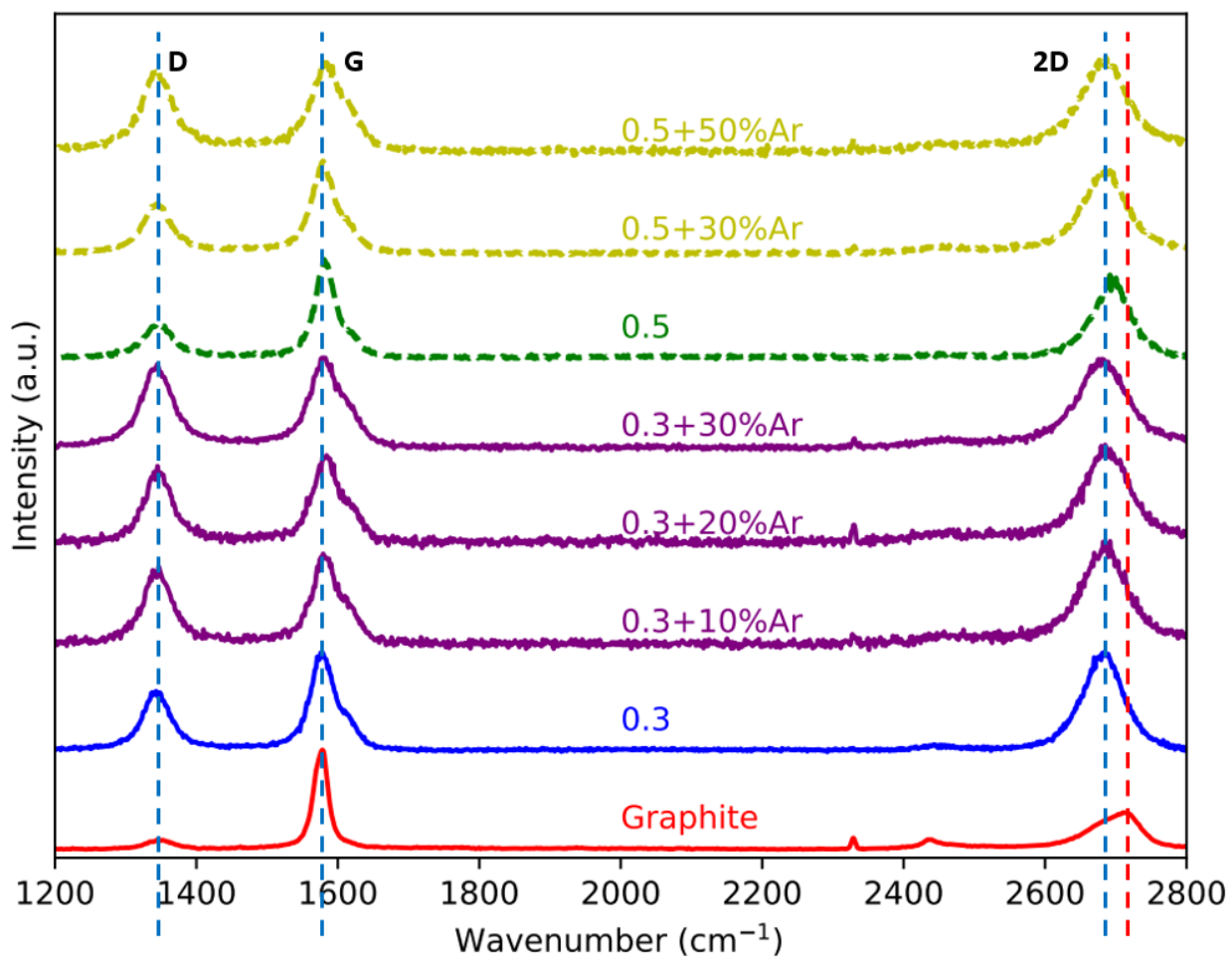


Figure 5.17: Raman comparison of samples with added argon to the original samples. The original low and high O/C are plotted in blue and green, respectively. Added argon to low and high O/C are plotted in purple and yellow, respectively. Graphite plotted in red is added for comparison. All samples are scaled such that $I_G = 1$. Three dashed blue lines are centered on the three prominent peaks of the 0.3 sample, and one dashed red line is centered on the 2D peak of the graphite sample.

O/C	% Ar	D-peak (cm^{-1})	G-peak (cm^{-1})	2D-peak (cm^{-1})	G FWHM	2D FWHM	I_D/I_G	I_{2D}/I_G
Graphite	0	1355	1580	2715	27	77	0.35	0.47
0.3	0	1345	1579	2683	41	65	0.72	1.05
0.3	10	1344	1580	2686	59	80	0.87	1.13
0.3	20	1345	1583	2686	63	84	0.90	1.11
0.3	30	1345	1580	2680	66	92	0.94	0.98
0.5	0	1346	1580	2695	33	60	0.35	0.79
0.5	30	1345	1579	2686	43	78	0.60	0.91
0.5	50	1346	1582	2683	70	80	0.95	1.10

Table 5.4: *Tabulated data of Raman spectra for the argon samples.*

5.3.3 XRD

Figure 5.18 supplemented by Table 5.5 shows the XRD of argon added to the acetylene samples. The 0.3 O/C + 10% argon sample appears slightly more crystalline than the original sample due to its higher signal to noise ratio and decreased FWHM, whereas the other argon + 0.3 O/C samples appear similar to the original sample within experimental error. Adding just 30% argon to the 0.5 O/C sample changes the original sample from high O/C to low O/C properties whereas 50% argon further shifts to even lower angles while retaining a similar FWHM to that of the low O/C sample. All samples are of graphenic nature with d-spacings above that of graphite and below that of soot [94], and show an asymmetry in plane (100) indicating turbostratic nature similar to the original sample [92].

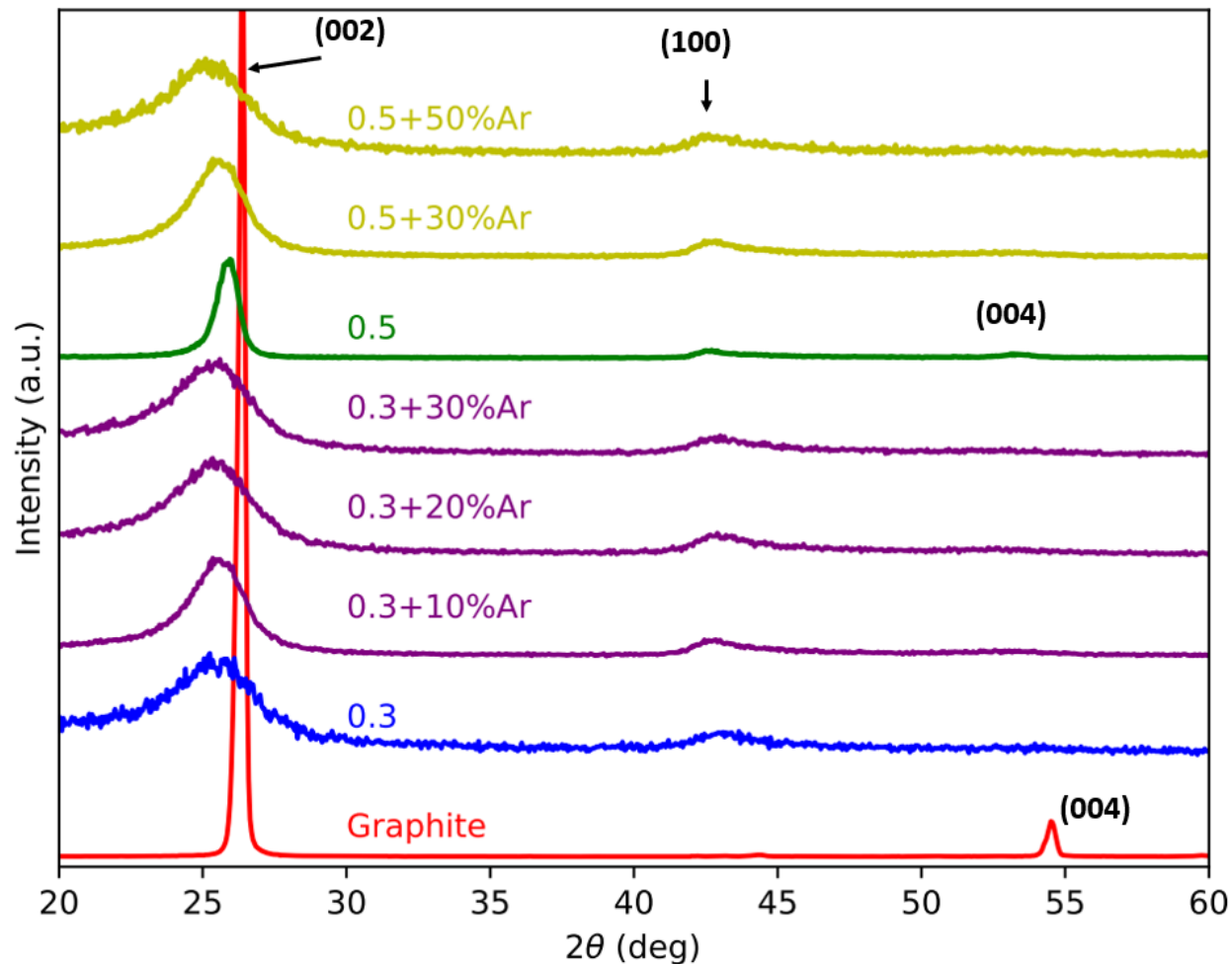


Figure 5.18: XRD of acetylene-oxygen + argon samples in comparison to acetylene-oxygen and graphite. Low and high O/C of acetylene samples are plotted in blue and green, respectively. The argon added samples of low and high O/C are plotted in purple and yellow, respectively. Graphite is plotted in red and is a different graphite powder than used previously.

O/C	% Ar	(002) FWHM	(002) location (°)	d-spacing (nm)	τ (nm)	# of layers
Graphite	0	0.28	26.4	0.336	28.83	85.8
0.3	0	2.75	25.48	0.349	2.93	8.3
0.3	10	2.08	25.48	0.349	3.87	11.1
0.3	20	2.71	25.44	0.350	2.97	8.5
0.3	30	2.66	25.48	0.349	3.03	8.7
0.5	0	0.87	25.93	0.343	9.27	27.0
0.5	30	2.08	25.48	0.349	3.87	11.1
0.5	50	2.75	25.16	0.354	2.93	8.3

Table 5.5: Tabulated data of XRD FWHM, location, d-spacing, Scherrer equation, and predicted number of layers.

5.3.4 TEM

TEM images in Figure 5.19 shows little distinction between the 0.3 O/C samples regardless of added argon content. The 0.5 O/C morphology changes drastically from spherical fractal aggregates in 0% argon to platelet structures with 30% argon to resembling the 0.3 O/C 0% argon sample with 50% argon. The particle size decreases in the 0.5 sample with increasing argon from 100 nm sized platelets to 20-50 nm sized platelets.

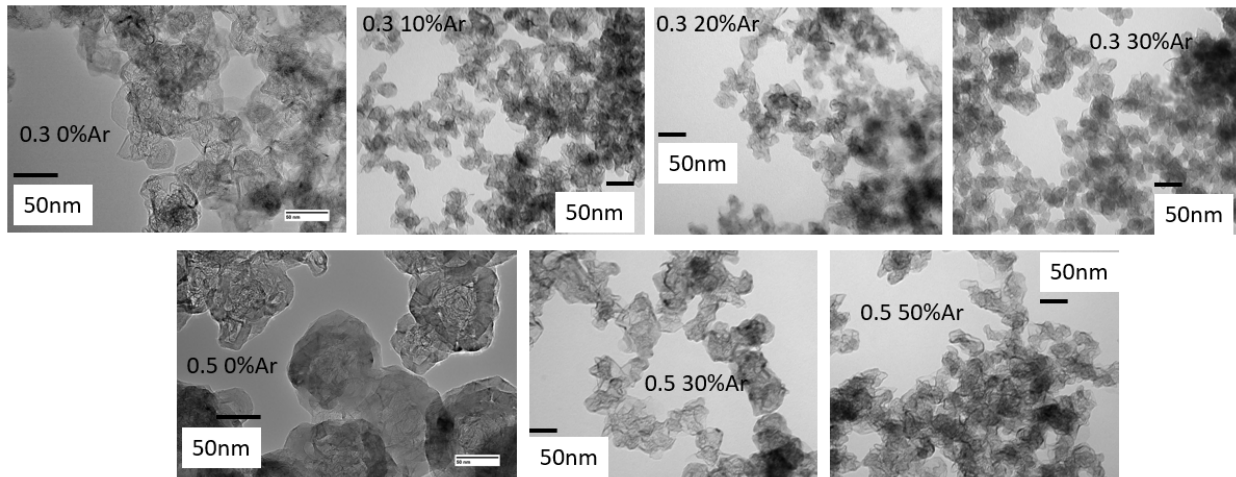


Figure 5.19: TEM images of 0% argon samples were taken at KU, and TEM images of added argon samples were taken at k-state, described in section 2.2.3.

5.4 Acetylene-oxygen + nitrogen

The success in changing the sample properties of the 0.5 O/C sample to that of a low O/C graphene material inspired experiments to reduce the temperature further in attempt to obtain a soot material. Nitrogen was chosen due to its diatomic nature allowing five degrees of freedom in which to absorb energy [52], potentially quenching temperature even more than that of argon. There is also hope that nitrogen may participate in the chemical reaction in high enough temperatures creating a N-doped graphene material [95].

5.4.1 Detonation details

30% and 50% nitrogen were added to the 0.5 O/C fill mixture of acetylene-oxygen. The 30% nitrogen sample successfully detonated at a reduced temperature of 1960 K, which is lower than that of the 50% argon sample, but the 50% nitrogen mixture would not detonate. Due to an equipment failure, pressure data was not collected. Mass collected expectedly reduced in comparison to the 0% nitrogen sample at the equivalent rate of yield. GC analysis and measured overpressure revealed no changes to the chemical reaction except with that of unburned nitrogen to imply no nitrogen-doping in the carbon.

5.4.2 Raman

Figure 5.20 shows the Raman spectra of the sample nitrogen sample retains all turbostratic peaks when plotted on a log scale as well as graphene characteristics in the strong G and 2D peaks. The D, G, and 2D peak locations have shifted from 1346, 1580, and 2695 cm^{-1} to 1342, 1581, and 2674 cm^{-1} , respectively, the FWHM of the G and 2D peak have increased from 33 and 60 cm^{-1} to 77 and 100 cm^{-1} , respectively, and the ratios I_D/I_G and I_{2D}/I_G have increased from 0.35 and 0.79 to 1.08 and 0.88, respectively. These results signify an even further shift to low O/C graphene from the original sample than that of the argon samples in section 5.3.2, correlating with continued temperature decrease of the reaction. It is worth noting that temperatures ~ 1950 K in the ethylene samples (section 5.2) turn into soots,

whereas the low temperature acetylene samples + argon and nitrogen still remain graphenes.

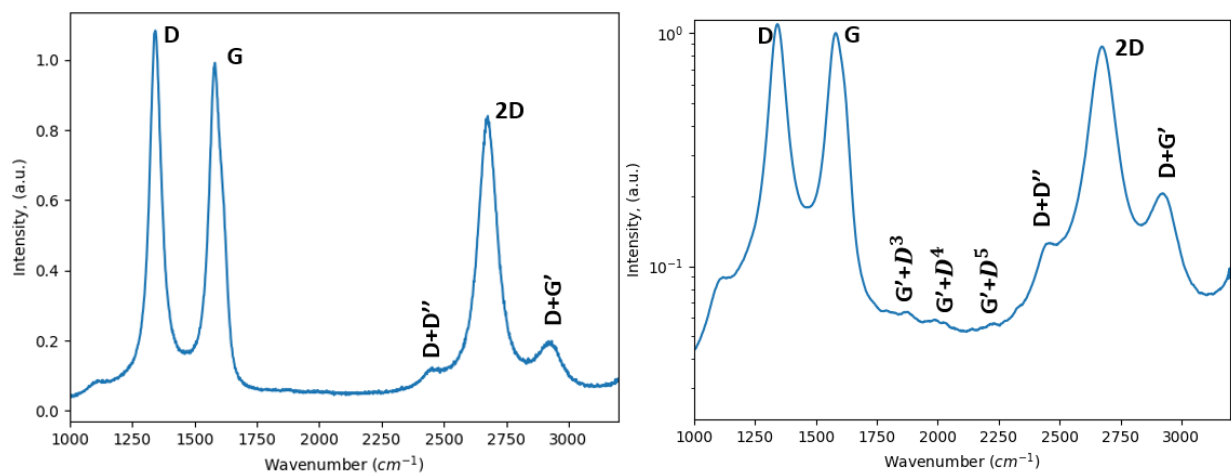


Figure 5.20: Raman spectra plotted on normal axis and log scale. The G peak intensity is scaled to unity.

5.5 Propane-oxygen

Propane is a widely available hydrocarbon that commonly used in grilling and vehicles [96]. Here, the study of various O/C of propane is presented.

5.5.1 Detonation details

No detonation pressure data was collected due to an equipment failure. The detonation temperature recorded 1830 K for the 0.9 O/C sample for a total spectra time 146 ms, but did not measure blackbody spectra for the 1.2 and 1.5 O/C samples and thus temperature could not be calculated. 1.34 g sample mass at 10 % yield was collected. 0.7 O/C was attempted but the detonation failed multiple attempts.

Figure 5.21 shows the chemical equation derived from overpressure data and GC analysis. At $O/C \geq 1.2$, no more carbon is produced and instead water begins to form in significant amounts. There is no presence of carbon dioxide.

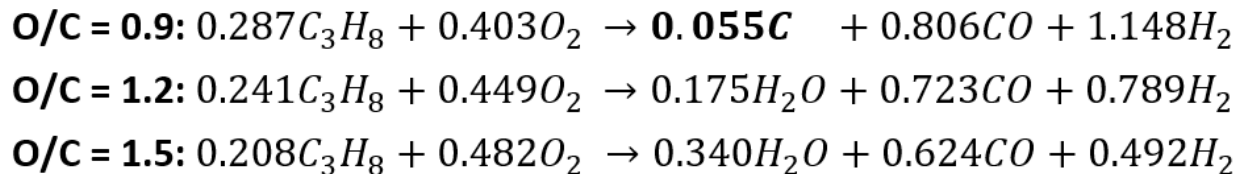


Figure 5.21: *Chemical equation of propane samples. An extra 0.0159 mol of oxygen was included in equation due to residual air left after vacuum.*

5.5.2 Raman

Figure 5.22 shows Raman spectra of the single carbon sample obtained from the propane detonations. The broad D and G peaks overlapping combined with an insignificant 2D peak distinguish the sample clearly as soot [87], with ratios I_D/I_G and I_{2D}/I_G equal to 1.04 and 0.34, respectively. Though the significance of propane to the overall picture will become clear in chapter 6, the study of propane detonations was suspended after this result.

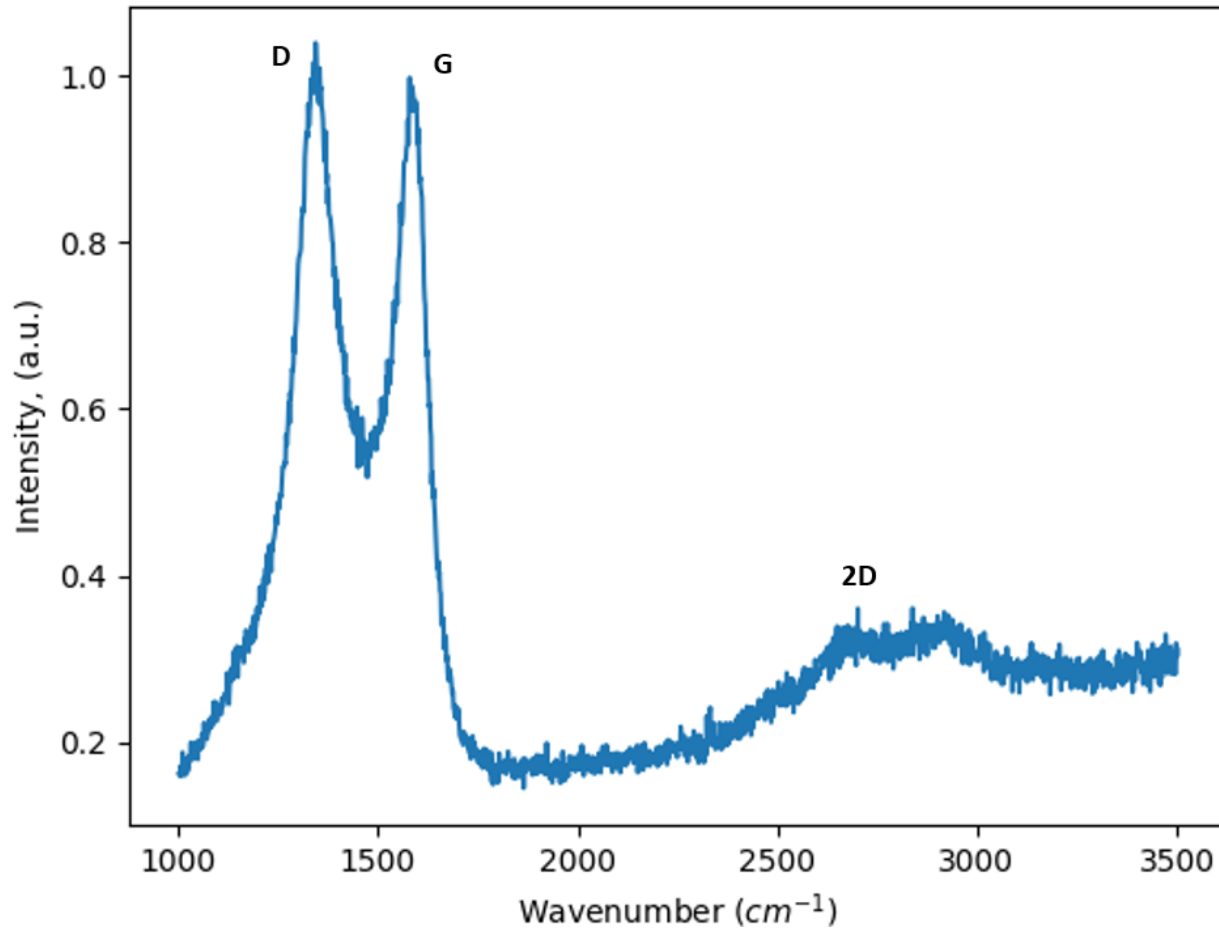


Figure 5.22: Raman spectra of the 0.9 O/C propane sample. The G peak intensity is scaled to unity.

5.6 Acetylene-oxygen via different methods

Figure 5.23 shows a new detonation chamber of volume 17.7 L and height x diameter 71.12 x 17.78 cm that has been constructed to test the effect of chamber dimensions on the carbon sample. Shock tubes, well studied in measuring detonation wave propagation, typically are of an aspect ratio 40 x 1 in length to width and have diameters on the order of a few cm, but the relatively large dimensions of the newly constructed chamber will still provide insight on the importance of reflected shock waves in the reaction [53].



Figure 5.23: *Newly constructed 17 L skinny detonation chamber.*

Furthermore, since acetylene has a flammability limit including 100% acetylene [23], an attempt to include as much acetylene as possible in the traditional 17 L chamber and fill only the spark area with a highly explosive mixture of stoichiometric acetylene-oxygen mixture was attempted. This method of ignition is referred to as a "Shock tube". The lowest O/C that the traditional procedure as outlined in section 2.1.4 has produced is 0.18 O/C, though no characterization was performed on the sample at that time and the sample has since been lost.

5.6.1 Skinny tube experiment

The 0.3 O/C acetylene-oxygen mixture was tested. Sample mass, yield, density, and appearance match results to that of the original 17 L chamber. Due to its recent construction, data collection was not yet assembled and so detonation pressure and temperature were not collected.

Figure 5.24 compare Raman and XRD as of the new chamber sample versus the original chamber sample as the simplest quality control check. Both results match, thus indicating that chamber alterations to this degree do not affect the sample characterization and properties.

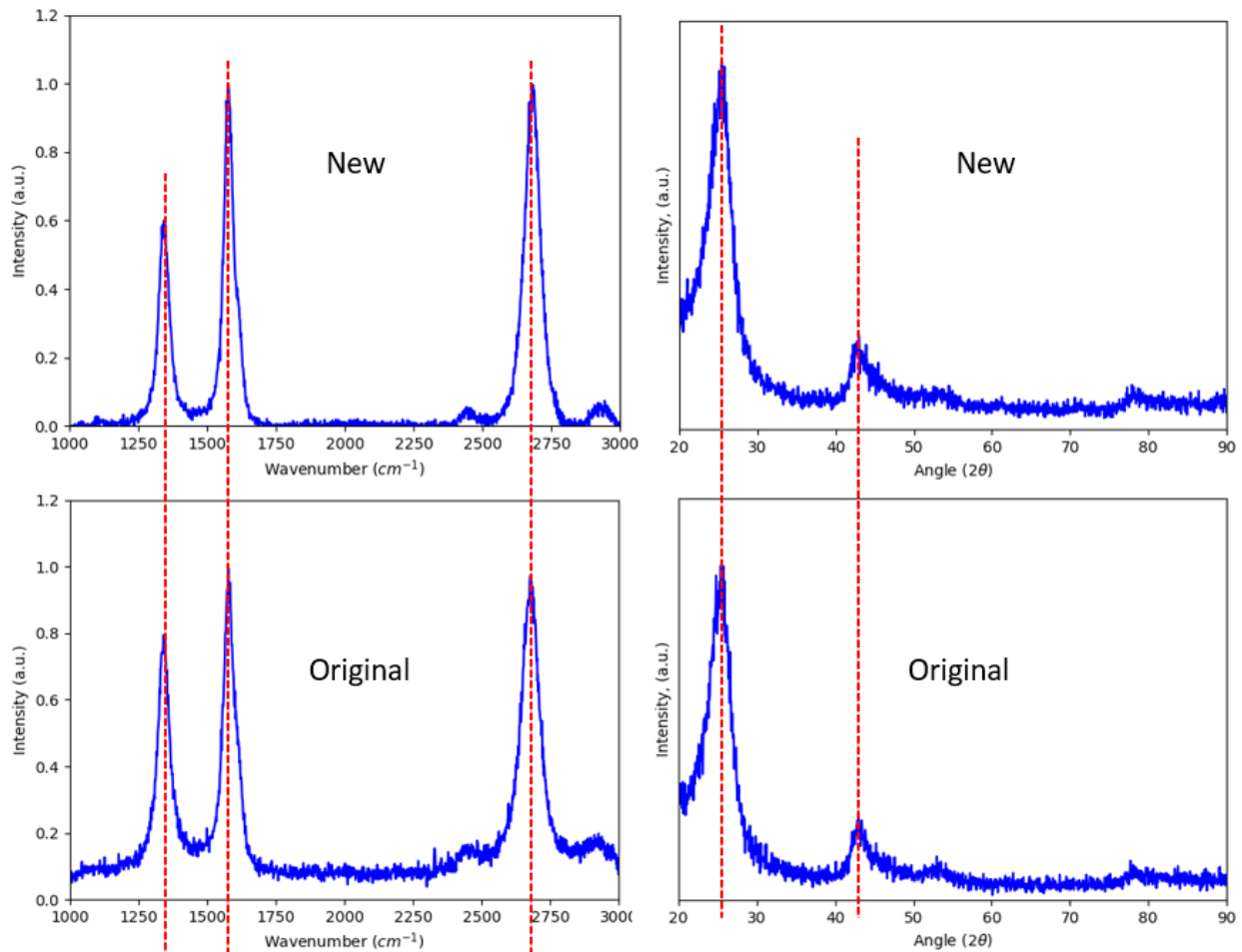


Figure 5.24: Raman spectra (left) and XRD (right) of the 0.3 O/C acetylene sample made in the new chamber (bottom) compared to the original chamber (top). The G peak intensity and (002) peak are scaled to unity.

5.6.2 Shock tube experiment

The overall O/C mixtures attempted were 2, 4, 6, and 12 % oxygen that resulted in 0.018, 0.036, 0.056, and 0.13 O/C, respectively. Only the 0.13 O/C successfully detonated. Due to an equipment failure, no detonation pressure was obtained. The spectrometer recorded a peak temperature of 1900 K. 9.999 g of sample mass was obtained at a yield of 65%, lower than expected.

Figure 5.25 shows Raman spectra of the sample obtained. The D, G, and 2D peak locations are 1340, 1575, and 2666 cm^{-1} , respectively, with G and 2G peaks' FWHM of 76

and 112 cm^{-1} , respectively, with ratios I_D/I_G and I_{2D}/I_G equal to 1.09 and 0.29, respectively. Though a 2D peak is visible, its low ratio to the G peak indicates soot [87]. The shift to lower wavenumbers of this sample from our typical acetylene samples indicate the presence of amorphous sp^2 hybridized carbon [38]. No further characterization was carried out.

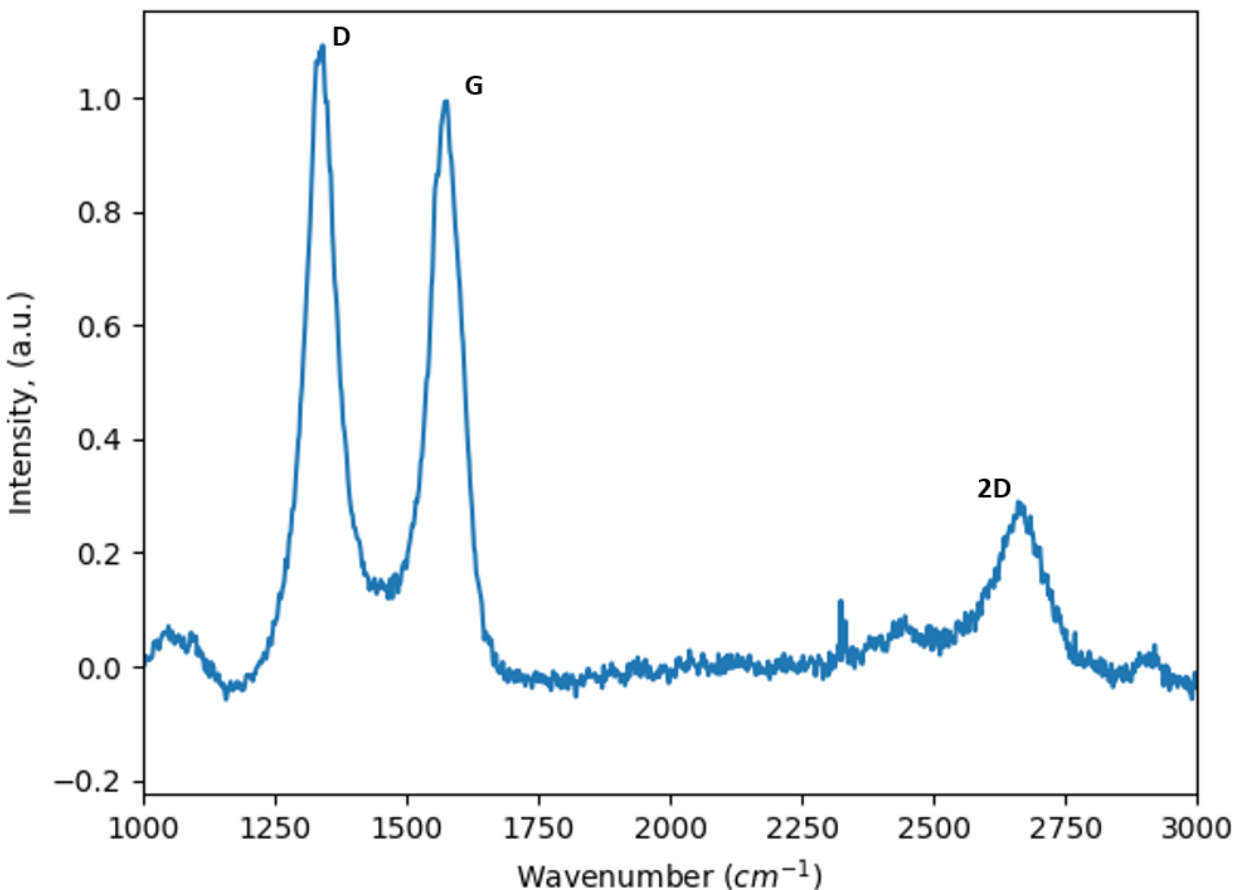


Figure 5.25: Raman spectra of the 0.13 O/C acetylene sample. The G peak intensity is scaled to unity.

5.7 Benzene, toluene, and xylenes

Though the work on these liquid precursors was carried out by Shusil Sigdel in collaboration with the author, this dissertation requires the data of benzene, toluene, and xylenes for completeness. Due to the nature of gaseous precursors, little effort is required aside from metering in calibrated mixture ratios into the chamber as outlined in section 2.1.4. For liquid

precursors to obtain an even dispersion and detonation in the chamber, however, requires either fuel injection of droplets timed to spark at the peak of dispersion or to evaporate the liquids into gases inside the chamber. For this section, we will describe the latter. Figure 5.26 depicts the 17 L chamber setup, where it is heated up to 80 °C and then vacuumed to 0.03 atm. Liquid precursors were then filled into the chamber using a syringe through a septum. Finally, after time has passed and the liquids have evaporated, oxygen is metered in to bring the chamber pressure up to 1 atm.

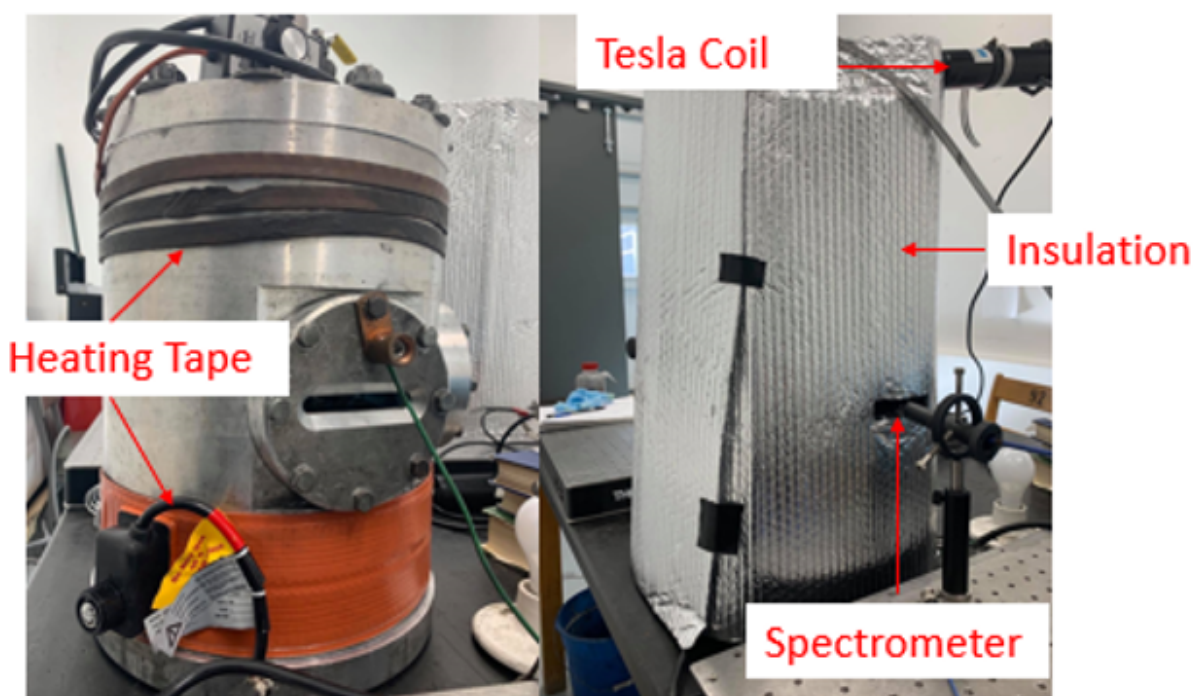


Figure 5.26: *Picture showcasing the alternate setup for liquid precursors. Left shows the heating tape to bring the chamber up to temperature, and right shows the insulation required. Figure reproduced with permission from Shusil Sigdel.*

5.7.1 Detonation data

Table 5.6 shows the available data for the liquid precursor detonations. Pressure data collection has not yet been set up for these experiments. The benzene 1.30 O/C and the toluene

1.22 and 1.37 O/C formed little collectible solid carbon and thus could not be characterized. Furthermore, they did not provide appreciable blackbody spectra so their temperatures cannot be calculated. The toluene and benzene 0.9 and 1.0 O/C, respectively, show an SSA \sim double of that seen by the acetylene and ethylene samples. Figure 5.27 shows that the samples' physical appearance largely look similar to low O/C graphene, with the exception of the 1.3 O/C xylenes sample that is a powder. The xylenes samples are also tinged slightly brown to the naked eye which is not well captured in this photograph.

Precursor	O/C	Yield (%)	Temperature (K)	SSA (m^2/g)
C_6H_6	0.80	26	2270	187
C_6H_6	0.96	7.2	2680	365
C_6H_6	1.30	0.2	no bb	n/a
C_7H_8	0.63	30.0	2090	147
C_7H_8	0.90	10.0	2410	344
C_7H_8	1.22	<0.5	no bb	n/a
C_7H_8	1.37	<0.5	no bb	n/a
C_8H_{10}	0.59	28.4	2180	32
C_8H_{10}	0.88	18.4	2160	54
C_8H_{10}	1.44	5.0	2490	32

Table 5.6: *Tabulated data of the precursor, O/C, yield, temperature, and SSA. “no bb” for temperature means no blackbody was recorded, and n/a for SSA means the measurement could not be done due to a lack of mass produced by the sample.*

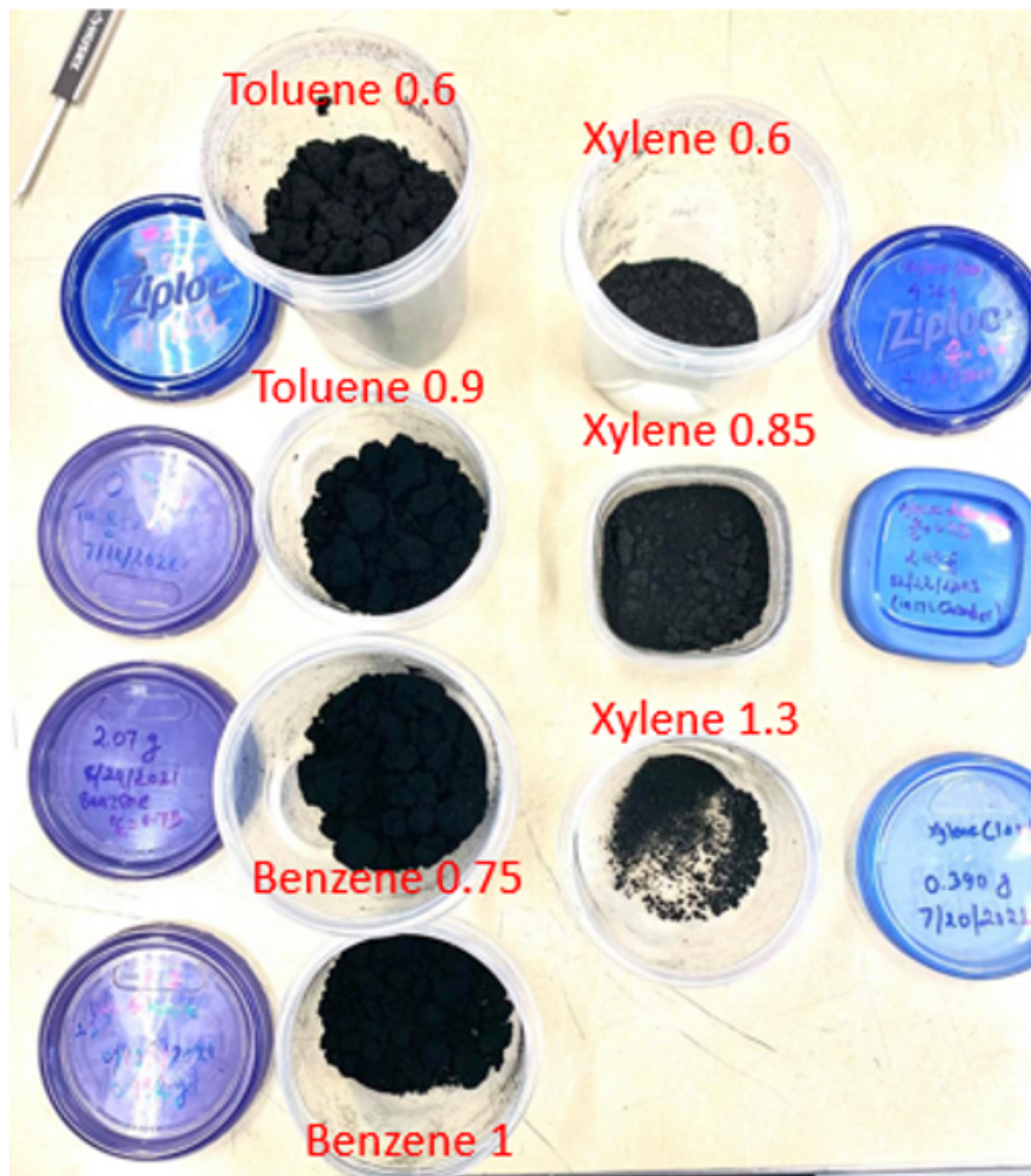


Figure 5.27: *Picture of the samples. Figure reproduced with permission from Shusil Sigdel.*

Figure 5.28 shows the results of the analysis from overpressure data, GC, and FTIR. Similar to previous experiments the reaction predominantly produces carbon, carbon monoxide, and hydrogen, alongside a larger presence of water and carbon dioxide at $O/C \geq 1.0$.

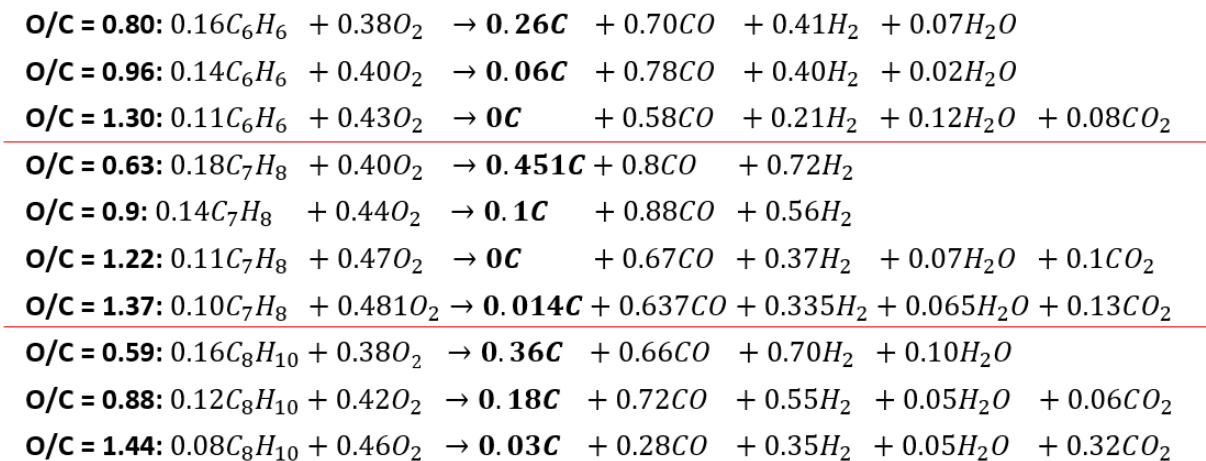


Figure 5.28: Chemical equations of the liquid precursors verified by overpressure, GC, and FTIR analysis. A thin red line separates each liquid precursor dataset.

5.7.2 Raman

Figure 5.29 and Table 5.7 show the Raman data primarily indicates soot for the liquid precursors excepting that of 1.0 O/C benzene and 0.9 O/C toluene which indicate graphene. The 0.9 O/C toluene sample has turbostratic peaks similar to our acetylene samples in 3.1, whereas the 1.0 O/C benzene sample does not clearly show such peaks. For both of these samples, the relatively low 2D peak wavenumber indicates amorphous sp^2 carbon [35–38, 88–90].

Precursor	O/C	D-peak cm^{-1}	G-peak cm^{-1}	2D-peak cm^{-1}	G FWHM	2D FWHM	I_D/I_G	I_{2D}/I_G
C_6H_6	0.80	1344	1583	2761	135	n/a	1.05	0.41
C_6H_6	0.96	1331	1579	2668	74	102	1.28	0.83
C_7H_8	0.63	1339	1586	2679	142	n/a	1.02	0.35
C_7H_8	0.90	1339	1588	2675	92	224	1.33	0.69
C_8H_{10}	0.59	1352	1586	2724	n/a	n/a	0.83	0.33
C_8H_{10}	0.88	1345	1588	2685	n/a	n/a	0.96	0.27
C_8H_{10}	1.44	1344	1590	2707	n/a	n/a	0.87	0.38

Table 5.7: Tabulated data of Raman spectra for the liquid precursor samples. “n/a” is written for samples where data doesn’t apply.

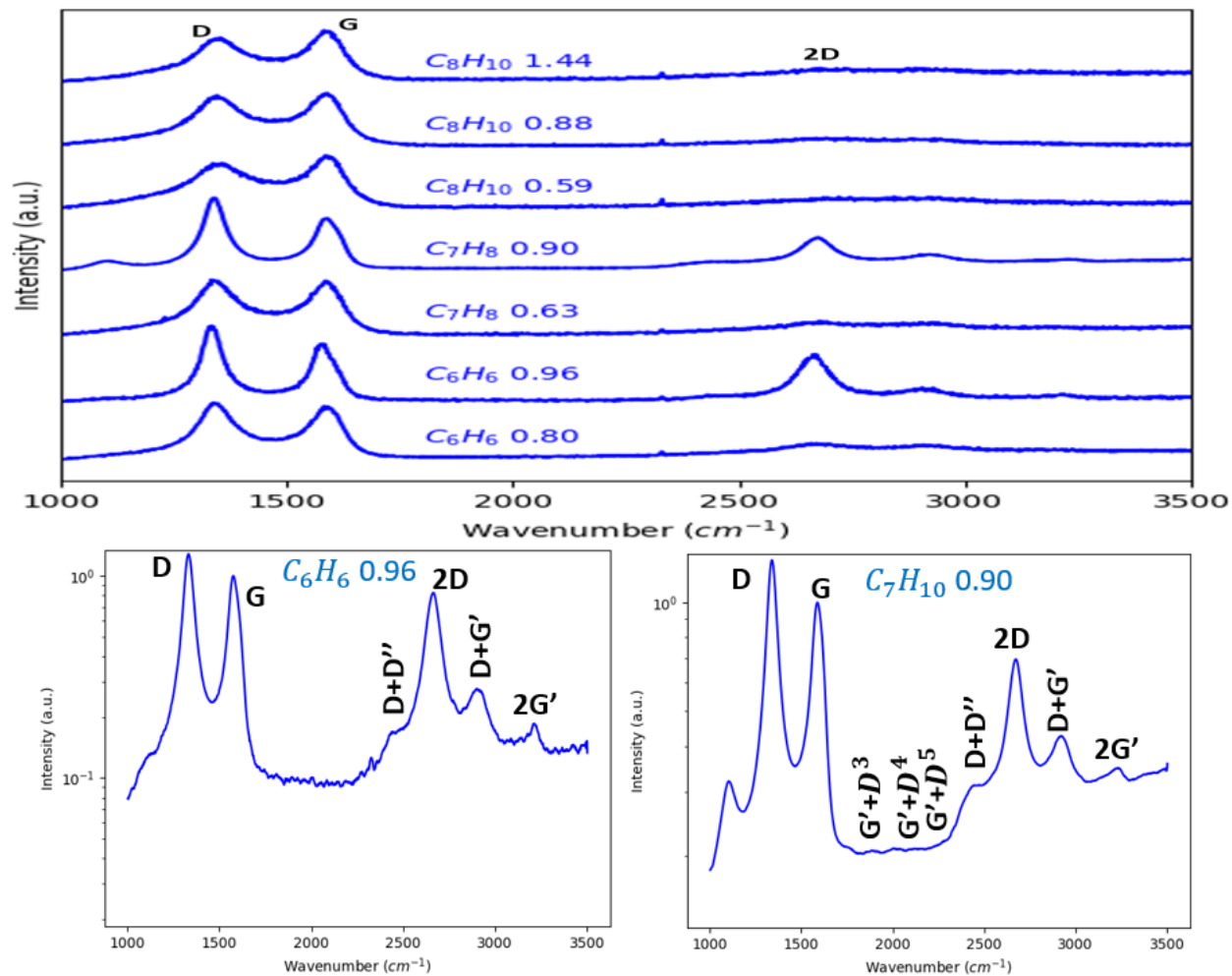


Figure 5.29: Raman spectra of all liquid precursors (top) and Raman plotted on log scale of the 1.0 O/C benzene and 0.9 O/C toluene samples (bottom).

5.7.3 XRD

Figure 5.30 supplemented by Table 5.8 shows the XRD data. The (002) peaks for all liquid samples are located $\leq 25.0^\circ$, agreeing with that of soot [94]. All samples show asymmetry classic of a 2D material at peak (100) $\sim 44^\circ$ which may suggest turbostratic layers [92], but this cannot be verified by XRD alone due to the lack of clearly distinguishable (004) and (110) peaks, perhaps because of a low signal-to-noise ratio.

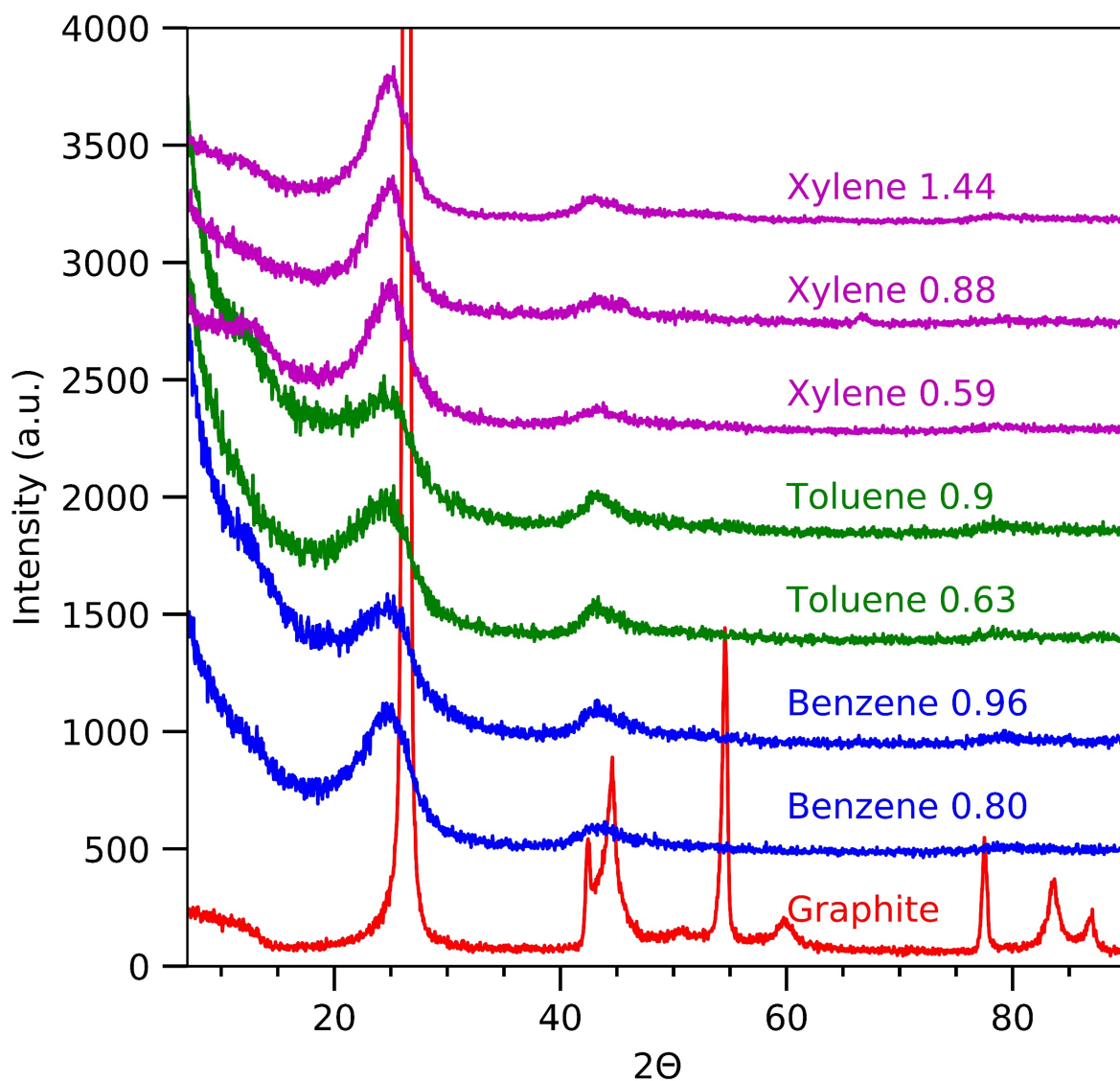


Figure 5.30: XRD spectra of benzene (blue), toluene (green), and xylene (magenta) in comparison to graphite (red). Figure reproduced with permission from Shusil Sigdel.

Precursor	O/C	(002) FWHM	(002) location (°)	d-spacing (nm)	τ (nm)	# of layers
Graphite	n/a	0.28	26.4	0.336	28.83	85.8
C_6H_6	0.80	4.2	24.6	0.362	1.91	5.5
C_6H_6	0.96	3.0	24.5	0.363	2.68	7.4
C_7H_8	0.63	4.5	24.8	0.359	1.79	5.0
C_7H_8	0.90	3.2	24.6	0.362	2.51	6.9
C_8H_{10}	0.59	3.9	24.9	0.357	2.06	5.8
C_8H_{10}	0.88	3.8	25.0	0.356	2.12	5.9
C_8H_{10}	1.44	4.0	25.0	0.356	2.01	5.7

Table 5.8: *Tabulated data of XRD FWHM, location, d-spacing, Scherrer equation, and predicted number of layers.*

5.7.4 TGA

Figure 5.31 shows TGA of the two toluene samples. Both 0.6 and 0.9 O/C are relatively stable up to 600 °C, perhaps surprising given the soot-like nature of both samples. This indicates the purity of the soot and a lack of PAH groups and volatiles on the surface of the sample [58–61].

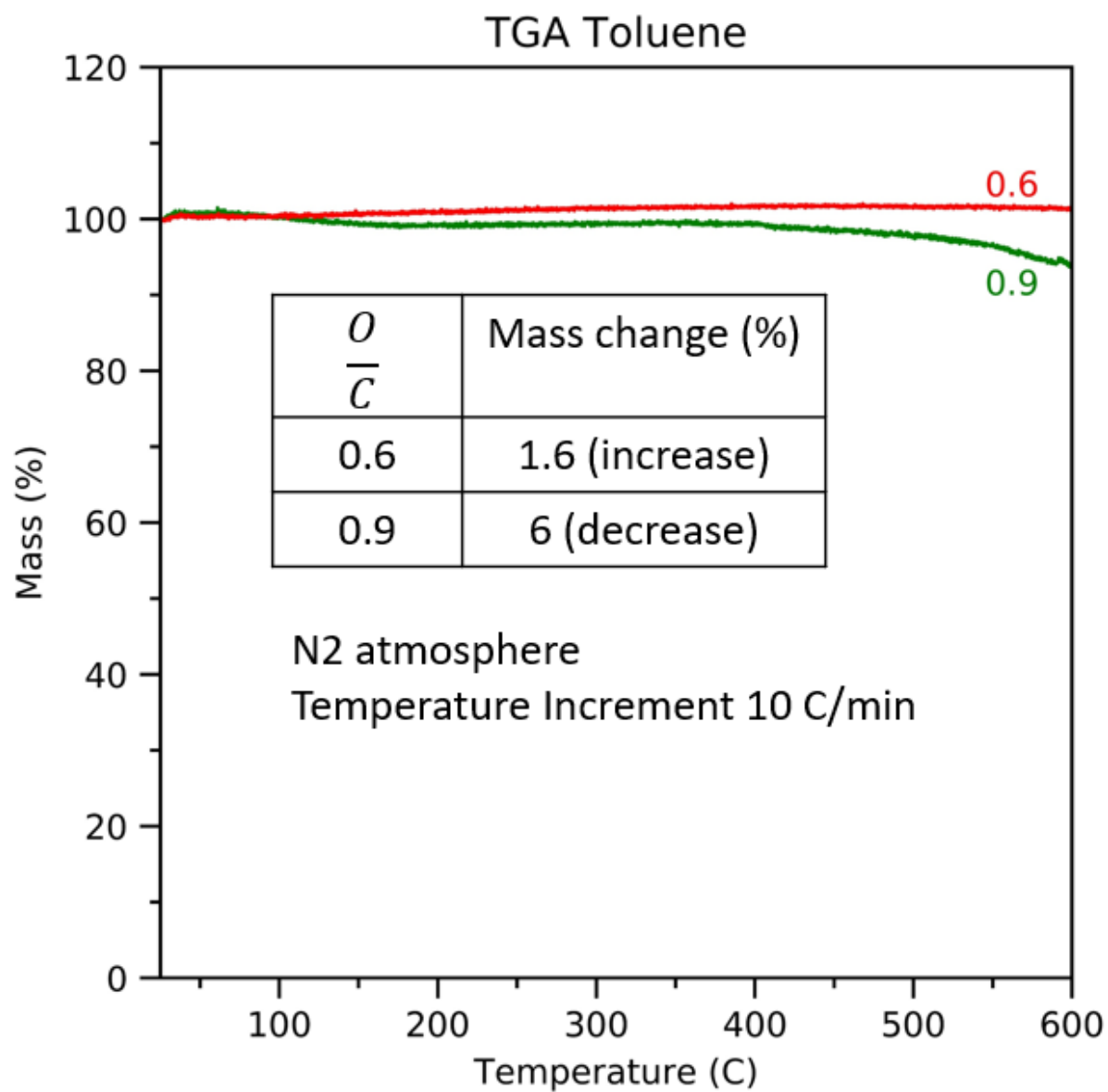


Figure 5.31: TGA of the toluene 0.6 (red) and 0.9 (green) O/C samples. Figure reproduced with permission from Shusil Sigdel.

Chapter 6

Overall trends

Characterization of the detonation products for each precursor has been presented. Here, the overall trends that occur between the different samples will be explored.

6.1 Product yields

Figure 6.1 shows the yields for each detonation product plotted versus O/C. Each color represents a precursor, and each shape represents a detonation product. Following one shape, such as the filled-in square representing hydrogen, shows the individual trend for each product across all precursors and O/C. In this example, hydrogen is near 100% yield from O/C = 0 to O/C = 1 for most precursors, and starts reducing in yield after O/C = 1. Analyzing each shape in this manner shows that each detonation product is largely similar for each precursor when plotted versus O/C. At O/C near 0, the products formed are largely solid carbon and hydrogen with a small amount of carbon monoxide. Solid carbon formation linearly decreases with increasing O/C and carbon monoxide linearly increases with increasing O/C while hydrogen gas remains constant. At O/C = 1, solid carbon formation ceases, carbon monoxide becomes relatively constant, and hydrogen gas begins to decrease with increasing O/C while water formation increases with increasing O/C. In some cases, small amounts of carbon dioxide are detected.

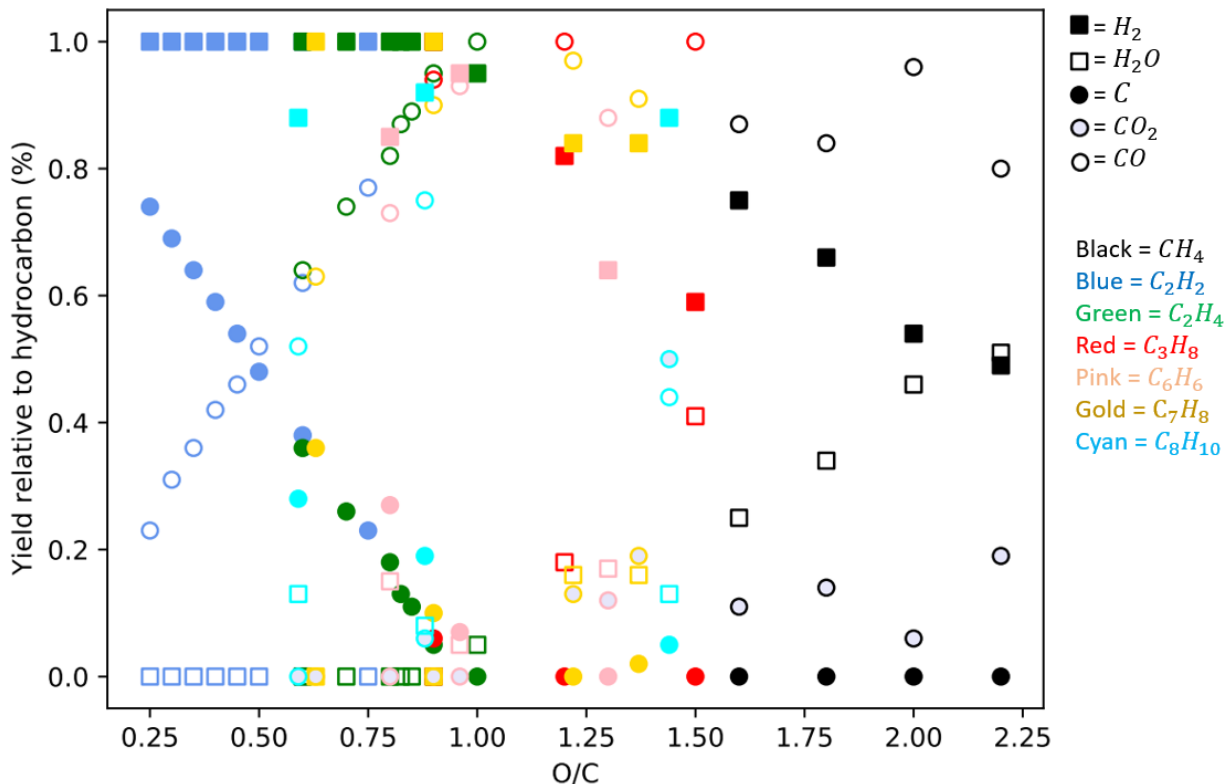


Figure 6.1: The yield of each product relative to the hydrocarbon precursor is plotted versus O/C for all precursors. Each symbol represents a different product, and each color represents a different precursor. Squares represent hydrogen, empty squares represent water, circles represent carbon, lightly-filled circles represent carbon dioxide, and empty circles represent carbon monoxide. Black represents methane, blue represents acetylene, green represents ethylene, red represents propane, pink represents benzene, gold represents toluene, and cyan represents xylenes.

From these trends we infer that the amount of carbon monoxide would remain relatively stable with increasing O/C until all hydrogen atoms are saturated with oxygen, which then prompts formation of carbon dioxide until stoichiometric mixtures are reached. Figure 6.2 shows that five of the seven of the hydrocarbon precursors reach their precursor stoichiometric mixture between O/C of 2.5 and 3.0, indicating similar yield growth rates. It must be noted that the two outliers, methane and propane, are both alkanes.

The trends derived from Figure 6.1 can be summarized in Figure 6.3. Knowing which detonation products form at any O/C for all hydrocarbon precursors cross-referenced with the flammability limits of each hydrocarbon precursor allows a prediction of what hydrocarbon precursors may be useful for making solid carbon before any experiment may begin,

though the solid carbon formed must still be distinguished between soot and graphene. It is well known that fuel-rich mixtures causes incomplete combustion to result in the formation of these products, but the exact degree of originality of Figure 6.3, specifically that of the predictable behavior of each product with O/C, is unclear in the literature [97, 98]. Note that this trend presented is specific for the context of constant volume combustions.

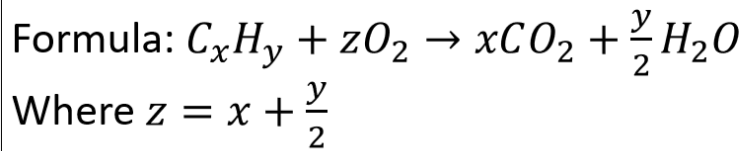
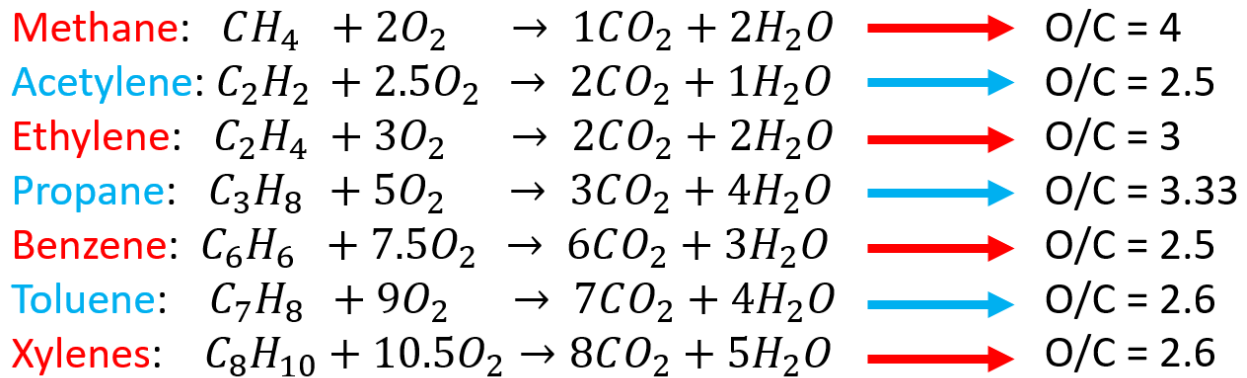


Figure 6.2: *Stoichiometric chemical equation for each hydrocarbon precursor used, and a general equation for balancing the equation.*

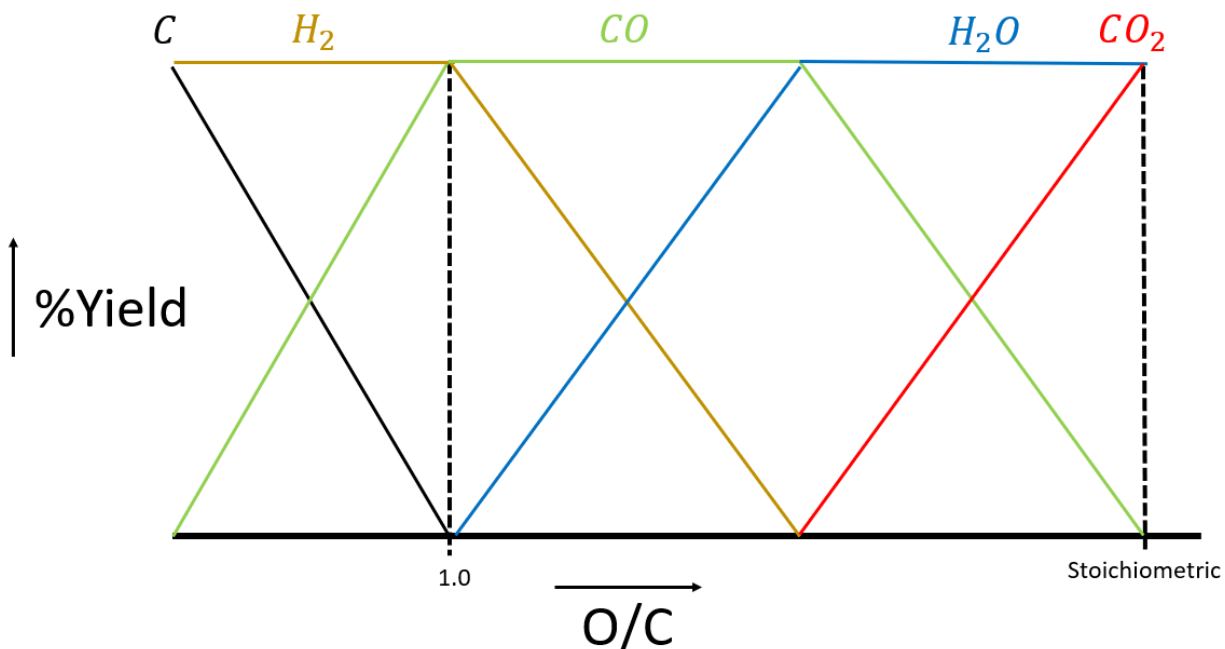


Figure 6.3: Qualitative plot summarizing the trends seen in Figure 6.1. Carbon monoxide is tracked in green, solid carbon is tracked in black, hydrogen is tracked in gold, water is tracked in blue, and carbon dioxide is tracked in red. The stoichiometric label is placed ~ 2.5 O/C, though all precursors are expected to follow this trend relative to their stoichiometric O/C.

6.2 Raman and XRD

The most clear distinction in the Raman between soot and graphite is perhaps the D-G peak overlap, in which soot has broad bands and an overlap height that is often ≥ 0.4 of the G-peak, and graphite has narrow bands resulting in zero D-G peak overlap. Figure 6.4 shows that there is some association of this overlap with the SSA. As the overlap decreases, the SSA increases until the domain of graphite is reached, in which SSA quickly decreases. The 0.5 O/C acetylene sample has an overlap ~ 0 ; adding 30% Ar increases the SSA but does not significantly effect the overlap, and adding 50% Ar greater increases the SSA and does affect the overlap to values reminiscent that of low O/C graphene. The best graphenes within each precursor have the lowest D-G peak overlap with the exception of the the acetylene precursor graphenes, in which the low O/C overlap is favorable. Though not plotted versus

O/C, there is a clear trend with D-G peak overlap and O/C within each precursor.

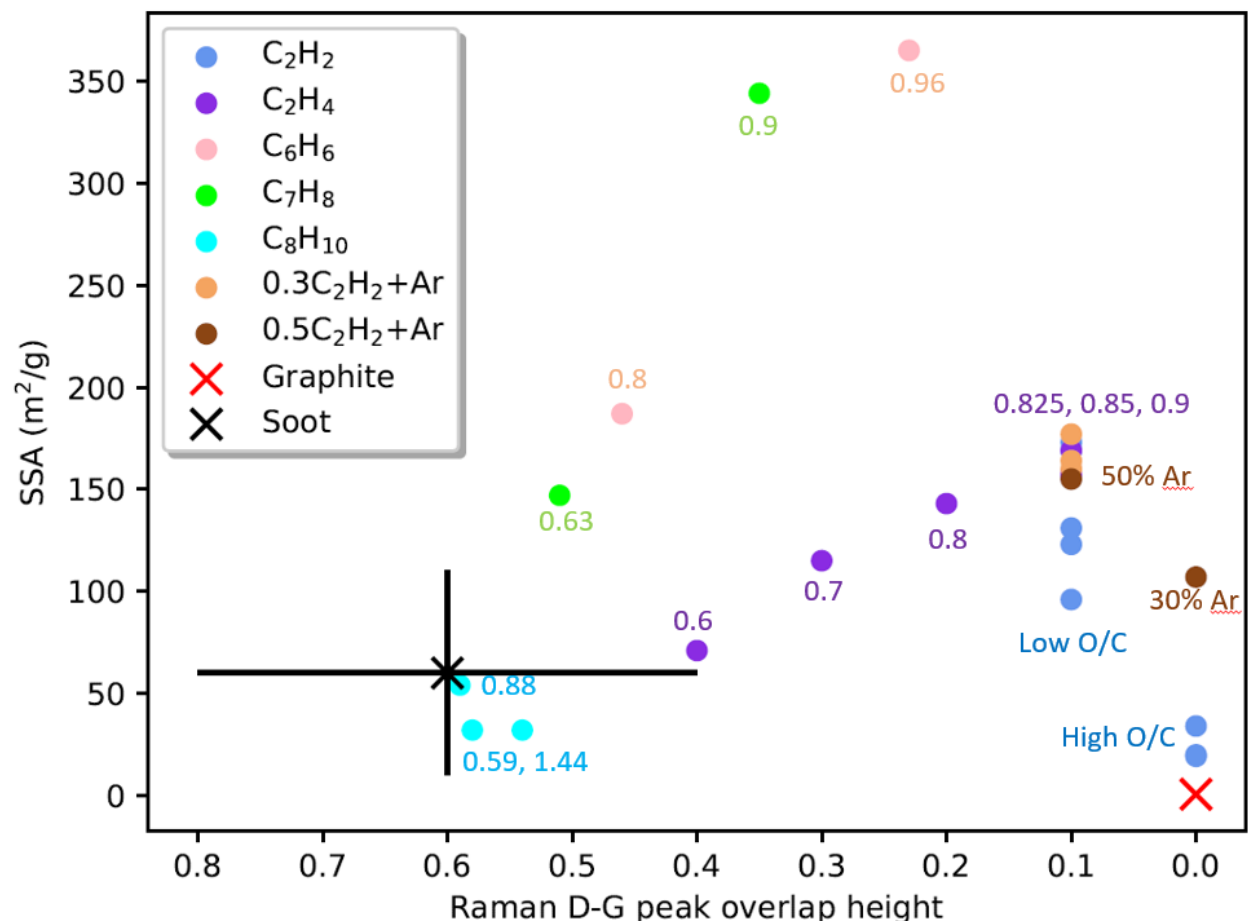


Figure 6.4: SSA is plotted versus the D-G peak overlap height relative to the G peak from the Raman. Soot has a wide variety of reported SSA and D-G peak overlap height values from the literature [1–4]. An arrow signifies the trend from low O/C to high O/C for each precursor.

Figure 6.5 shows that soot, with a near-zero 2D peak and indiscernible FWHM, is distinct from that of graphite and graphenes, both of which have a measurable FWHM and an increasing I_{2D}/I_G peak ratio the more graphenic the nature. Samples that have a higher I_{2D}/I_G peak ratio and lower 2D peak FWHM are generally interpreted as higher quality graphenes with a I_{2D}/I_G peak ratio = 2 considered pristine single-layer graphene and a I_{2D}/I_G peak ratio = 0.5 considered bilayer graphene [37]. That most of the samples have I_{2D}/I_G peak ratios above ~ 0.7 indicates the turbostratic nature of the samples [35–38, 88–90]. There is no overall trend with O/C, as lower O/C samples that are clearly distinguished

from soot have higher I_{2D}/I_G peak ratios than samples of higher O/C, and lower O/C samples with soot characteristics have lower I_{2D}/I_G peak ratios than samples of higher O/C, indicating that each precursor will have an individual O/C trend.

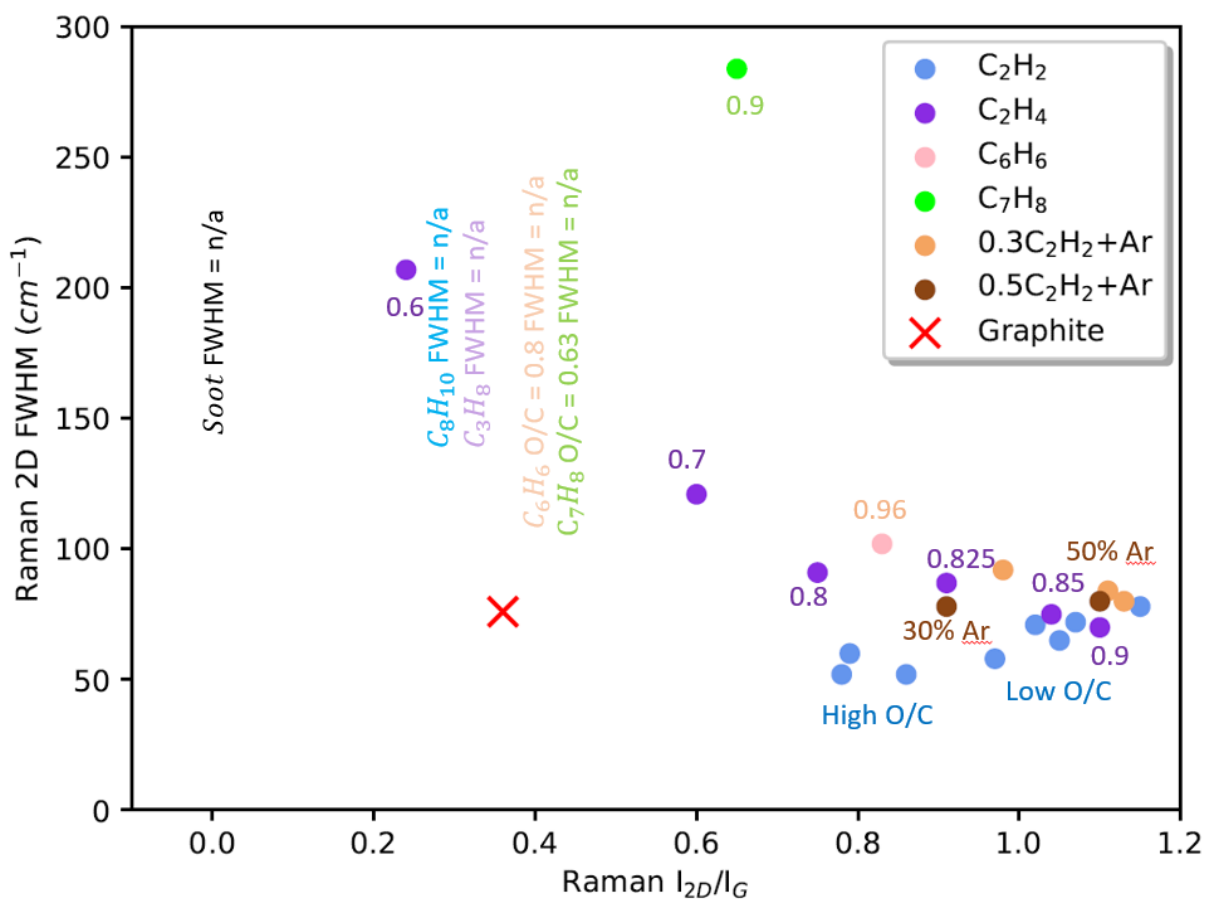


Figure 6.5: Raman 2D peak FWHM is plotted versus the Raman I_{2D}/I_G peak ratio. Samples with wide or zero 2D peaks have an indiscernible FWHM. Soot has a known absence of a 2D peak [2–4].

Figure 6.6 indicates the relative crystallinity of the sample, with low defects and crystalline structures having lower I_D/I_G peak ratios approaching that of graphite as well as a narrower G peak that does not overlap with the D peak. The samples generally follow the trend that higher O/C has lower defect and more crystalline structure, with lower O/C samples more amorphous and approaching that of soot-like characteristics [35–38, 88–90].

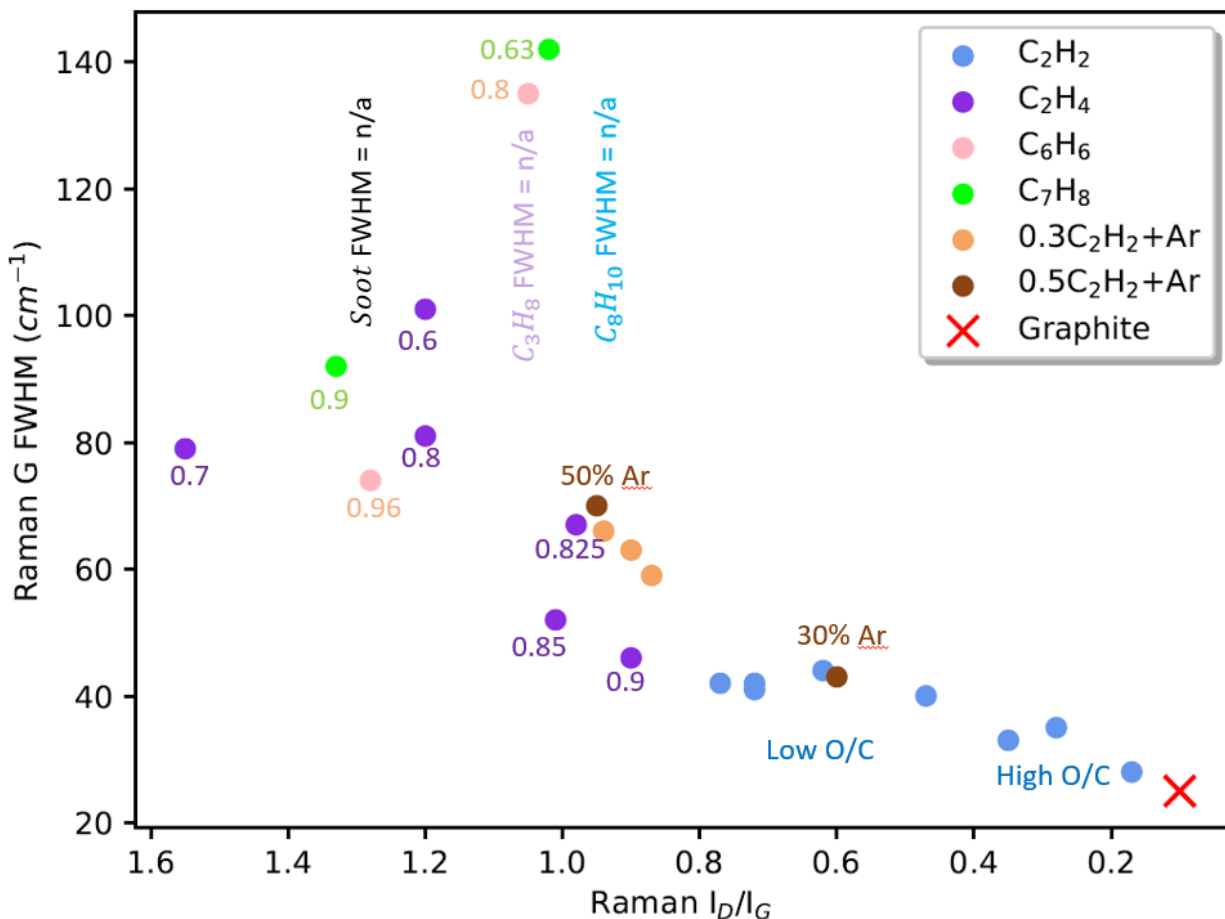


Figure 6.6: Raman G peak FWHM is plotted versus the Raman I_D/I_G peak ratio. Samples with D-G peak overlaps of ≥ 0.5 have an indiscernible FWHM but measurable I_D/I_G . Soot has a known high D-G peak overlap and broad range of possible I_D/I_G peak ratios [2–4].

Figure 6.7 shows that XRD (002) FWHM and d.spacing generally decrease with O/C, indicating more crystalline/graphitic structure and layering. XRD generally shows all samples as graphenic to varying degrees, and does not show sootlike characteristics unless both the d.spacing and FWHM lie in the range of soot. Here some samples show either FWHM or d.spacing in the range of soot, but not both [2, 5, 92, 94].

soot < *graphite* < *graphene*. Thus these three phases cannot be distinguished on a single scale, and a multidimensional diagram is required.

We choose two functions for the purpose of developing a phase diagram: $\phi(x)$ for the x-axis, and $\Gamma(y)$ for the y-axis. $\phi(x)$ measurements will be described by each measurement that has values in the order of *graphite* < *graphene* < *soot*, and $\Gamma(y)$ will be described by each term that has values in the order of *soot* < *graphite* < *graphene*. Thus $\phi(x)$ will describe the material relative to the limits of graphite and soot, and $\Gamma(y)$ will describe the material relative to the limits of soot and graphene. The instrument measurements that fit these parameters are the Raman I_{2D}/I_G peak ratio for $\Gamma(y)$, and the Raman I_D/I_G peak ratio, Raman D-G peak overlap relative to G-peak ratio, and the XRD d-spacing for $\phi(x)$. Each of these measurements will be weighted equally in the equation.

$\Gamma(y)$ and $\phi(x)$ will be normalized such that soot is located at (1,0), graphite is located at ($\sim 0, \sim 0.2$), and single-layer graphene (SLG) is located at ($\sim 0.1, 1$). Graphite values were chosen based on the measured graphite comparison in Chapter 5, where graphite d-spacing = 0.337 nm, $I_D/I_G = 0$, the D-G overlap = 0, and $I_{2D}/I_G \leq 0.36$. Soot values were chosen based on the minimum of the XRD and Raman measurements in the literature [2–5], where soot d-spacing ≥ 0.36 nm, $I_D/I_G \geq 1.2$, the D-G overlap ≥ 0.6 , and $I_{2D}/I_G = 0$. Single-layer graphene (SLG) and bi-layer graphene (BLG) have XRD [99, 100] and Raman [36, 37, 99] values determined by the literature, where SLG and BLG d-spacing = 0.345 nm and 0.345 nm (SLG does not have layers and so this parameter is instead the van der Waals thickness), respectively, $I_D/I_G = 0$ and 1, respectively, the D-G overlap = 0 and 0.1, respectively and $I_{2D}/I_G = 2$ and 0, respectively.

Our functions thus become

$$\phi(x) = \frac{1}{3} \left[\frac{(x_{d.sp} - (d.sp)_{ite})}{((d.sp)_s - (d.sp)_{ite})} + \frac{(x_{D-G} - (D-G)_{ite})}{((D-G)_s - (D-G)_{ite})} + \frac{(x_{I_D/I_G} - (I_D/I_G)_{ite})}{((I_D/I_G)_s - (I_D/I_G)_{ite})} \right] \quad (6.1)$$

$$\Gamma(y) = \frac{(y_{I_{2D}/I_G} - (I_{2D}/I_G)_s)}{((I_{2D}/I_G)_{SLG} - (I_{2D}/I_G)_s)} \quad (6.2)$$

where s = soot, ite = graphite, d.sp = XRD d-spacing, SLG = single layer graphene, D-G

= D-G Raman peak overlap relative to G-peak ratio, I_{2D}/I_G = Raman 2D/G peak intensity ratio, and I_D/I_G = Raman D/G peak intensity ratio.

These equations are by no means the graphene standard as they do not include other important parameters such as turbostraticity and X-Ray Photoelectron spectroscopy (XPS), the latter of which has not been measured in this dissertation due to lack of instrument availability. Furthermore, "perfect" SLG and BLG have zero Raman-D peak which significantly decreases these terms to lower $\phi(x)$ due to the absence of terms 2 and 3 in Eq. (6.1), but in the literature such perfect graphene is rarely seen [35–38, 88, 89, 99]. Due to this, SLG and BLG could also be located at $\phi(x) > 0.2$. All parameters are weighted equally in Eqs (6.1) and (6.2), though in reality it is not so quantitatively clear as to what parameters should have more weight. Other carbon allotropes, such as diamond and carbon-nanotubes, are not discussed. Finally, a wide range of XRD and Raman results can be accepted particularly for soot, but also graphite, SLG, and BLG, and so choosing values requires sufficient investigation and will be reflected in their error bars.

Plotting $\Gamma(y)$ versus $\phi(x)$ results in Figure 6.8, a diagram that indicates the phase of the material. The three corners represent the purest forms of each phase - soot, graphite, and SLG - as measured in this dissertation or as referred to by the literature. A wide error bar is given for soot due to its many possible XRD and Raman measurements, as discussed above. Smaller error bars are given to SLG and BLG for their possible Raman d-peak measurements. All of our detonation samples have been given 5% error bars. Dot-dash boundaries have been drawn between SLG and Graphite, and between SLG and soot, to signify the resemblance of each sample to these phases. A dash boundary has been drawn between graphite and soot to indicate that all samples in this region are clearly neither of these soot or graphite. Three zones have been identified: zone 1, zone 2, and zone 3. Samples in zone 1 have properties most resembling that of soot, with the exception of the 0.9 and 0.96 O/C toluene and benzene samples, respectively, which have graphenic properties. Zone 2 samples have the "best" graphenic properties that we have referred to as "low O/C graphene" throughout this work. Zone 3 samples are graphenes with increasingly graphitic properties and have been referred to as "high O/C graphene" throughout this work.

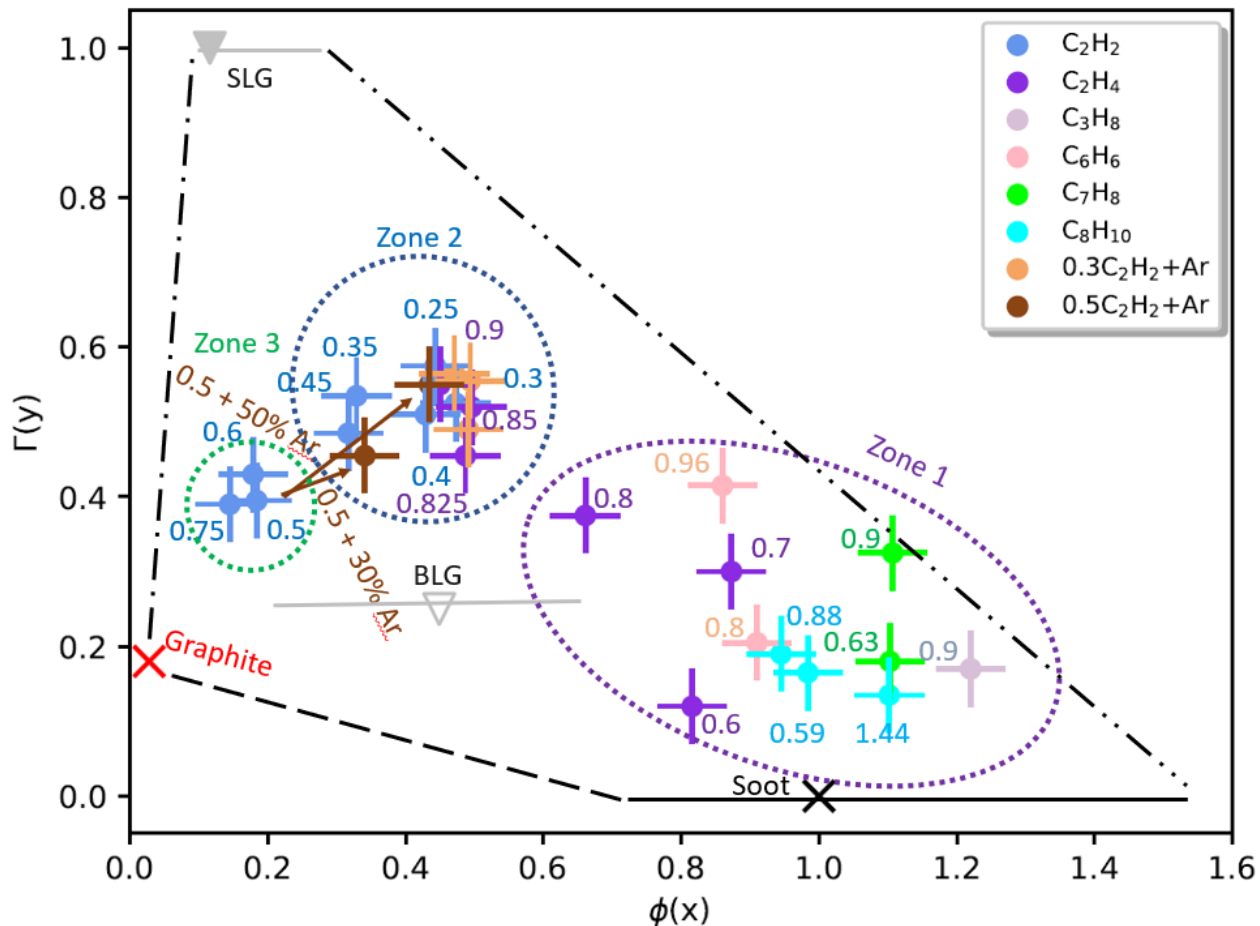


Figure 6.8: $\Gamma(y)$ is plotted versus $\phi(x)$ for all samples, literature values of SLG, BLG, soot, and measured graphite. The large error bar on soot signifies the large range of accepted soot values in the literature.

What Figure 6.8 indicates is that the samples with the most graphenic properties are clustered in the range $\phi(x) = 0.4 - 0.5$ in zone 2, with more sootlike characteristics at higher $\phi(x)$ in zone 3 and more graphitic characteristics at lower $\phi(x)$ in zone 3. Zone 2 not only indicates the best Raman and XRD measurements within each O/C, but also coincidentally correlates with the highest SSA within each precursor, which is not plotted. Remarkably, O/C within each precursor trends from soot-like characteristics to graphene-like characteristics at with increasing O/C as indicated by increasing $\Gamma(y)$ and decreasing $\phi(x)$ in zone 3, and finally trends towards that of more graphitic characteristics with decreasing $\Gamma(y)$ and $\phi(x)$ with increasing O/C for the acetylene and ethylene samples in zones 2 and 3. This suggests that the best graphenes are the minimum O/C of each precursor necessary to

clearly distinguish the detonation graphene from that of soot, a similar result found by Lei et al. in a simulation study of our method [63].

Lei et al. begin by suggesting that detonating pure acetylene will follow the known acetylene pyrolysis route in the literature [101], where the growth of PAHs and hydrocarbon species are expected (i.e. soot). The presence of a little oxygen favorably regulates hexagonal acetylene growth mechanisms over other carbon ring formations (pentagonal, heptagonal, etc.) during the growth process. Excess oxygen, however, prevents the growth of carbon rings and instead forms carbon oxides. The simulation in Lei et al. find the best acetylene-oxygen graphene at $O/C = 0.1$, where at $O/C \geq 0.2$ oxygen already plays a role in hindering the growth of carbon rings resulting in little-to-no graphene production [63]. While Lei et al. acknowledge the simulation has its own limitations, the conclusions are parallel to our own results: until enough oxygen is present in the reaction, soot is formed, followed by the "best" graphene, followed by reduced graphene properties and yield.

6.4 Temperature and Pressure

Figure 6.9 shows the temperature plotted versus pressure data. There we see the data for soot and graphene to be intermingled due to the presence of the argon-added samples. This can perhaps be explained due to the fact that measuring the total temperature and pressure of the argon-added reactions is misleading: we hypothesize that the oxygen-acetylene reaction should release the same energy and thus temperature and pressure regardless of whether there is argon or not, but the presence of argon dampens the resulting wave's kinetic energy. This then results in lower instrument temperature and pressure measurements. Bypassing the argon mixtures measurements results in a region of temperature circa 2200 K and pressure circa 13 atm that distinguishes graphene from soot.

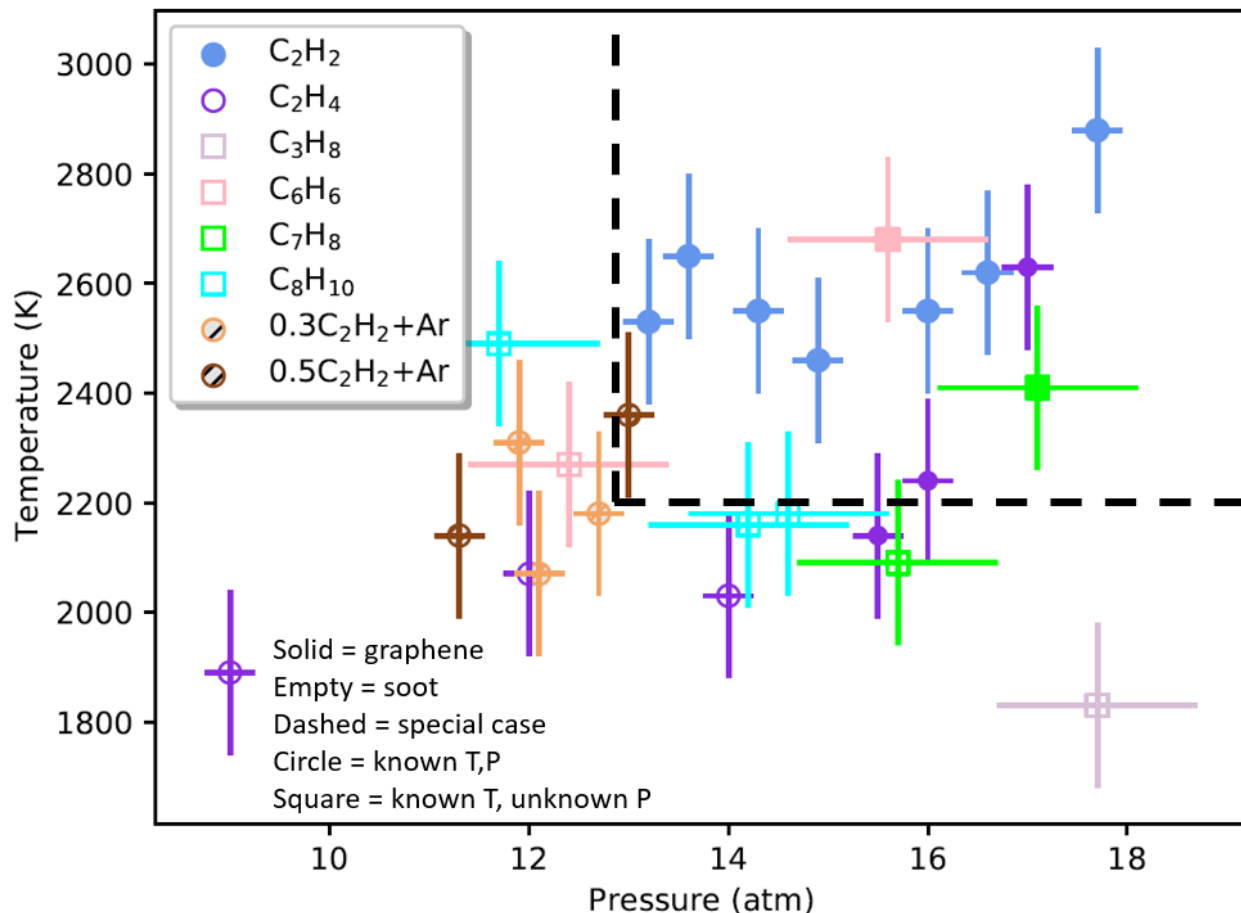


Figure 6.9: Temperature is plotted versus pressure for all precursors. Solid points represent graphene characterization and empty points represent soot characterization. Circle points have known values of both temperature and pressure, and square points have known values of temperature but calculated pressure via ideal gas law. A larger x-axis error-bar is given for square points for this reason. The dashed circles labeled "special case" are the graphenes from the argon samples whose temperature and pressure values are considered incorrect. A square is drawn in dashed lines to indicate a likely boundary between the soot samples and the graphene samples.

Figure 6.10 is based on Figure 6.9 and the hypothesis that the argon-added samples have misleading temperature and pressure data, resulting in their omission. This result shows the estimation of necessary temperature and pressure conditions to obtain a graphene rather than a soot during the detonation. The boundaries drawn indicate a minimum temperature and pressure of 2300 ± 150 K and 13 ± 1 atm, respectively, to make a graphene. Further data will elicit a reduced error in the required measurements.

The most critical step in the chemical reaction phase is the initial reaction of the pre-

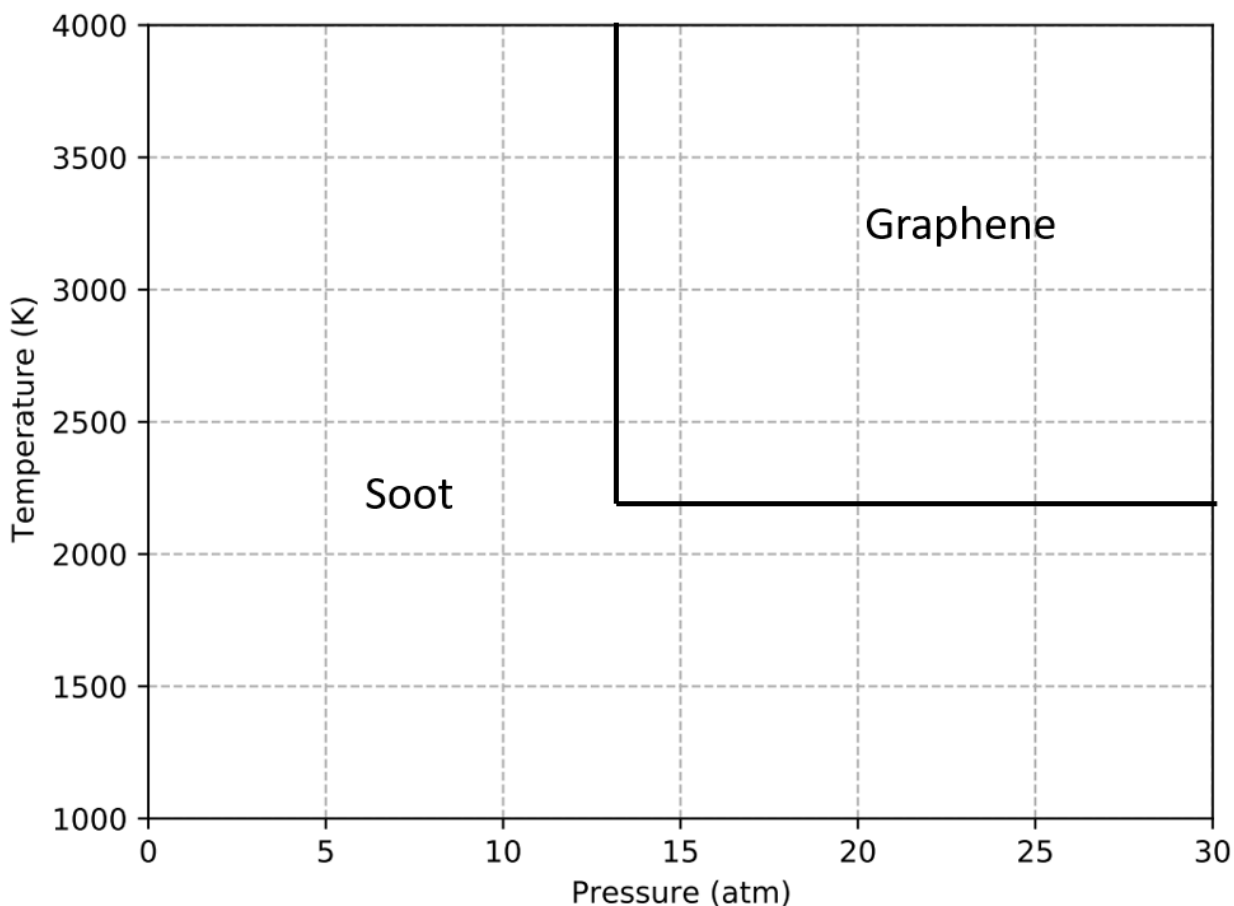


Figure 6.10: *Temperature is plotted versus pressure with a boundary between graphene and soot drawn.*

cursors based on their potential energy, whereas the kinetic energy of the reaction largely serves to propagate and then initiate the reaction. That the morphology of the 0.5 O/C + argon samples changed from high O/C properties to that of low O/C properties is likely due to the reduced reaction density of the sample (i.e. dilution) in the presence of argon. This creates longer reaction times that likely affects the gelation process [18, 32, 33]. Meanwhile the 0.3 O/C + argon remains relatively unchanged despite the measured changes in temperature. Both of these results indicate that a chemical potential threshold above the minimum ignition energy required to begin the reaction exists in which significant graphitization and aggregation kinetics occur. Beginning with reactions at the lowest possible energy, a soot is formed; increasing the energy in the reaction forms more graphitic properties as evidenced by the morphology changes in heat treatment of carbon black, where Kim et al. claim that

soft carbon can be graphitized at ~ 2700 K [102]. Eventually, a threshold of high enough temperature and pressure is reached where low O/C graphene properties are distinguished, and further temperature and pressure increases will eventually reach a threshold to form high O/C graphene properties.

These results correlate with pressure rise times across all O/C for the acetylene and ethylene samples, where soot-like properties are seen with pressure rise times ≥ 60 ms, the best graphene-like properties (i.e. "low O/C") are seen with pressure rise times between 10 - 60 ms, and more graphitic (i.e. "high O/C") properties are seen with pressure rise times ≤ 10 ms. This correlation may perhaps indicate how strongly (and thus, quickly) oxygen reacts with the precursor via how quickly carbon oxides are formed relative to carbon ring growth as discussed at the end of the previous section [63].

6.5 The graphene model

Figures 6.3 and 6.10 combine to form an empirical model that may predict whether a hydrocarbon precursor is capable of producing graphene before any experiment is conducted. First, the flammability limits of the hydrocarbon must be converted to O/C; any hydrocarbon that is capable of burning at $O/C \leq 1$ may produce solid carbon. The predicted chemical reaction in full can also be obtained from Figure 6.3 based on the O/C chosen, from which the number of moles can be predicted. Second, if the calculated temperature and pressure of the reaction are high enough per Figure 6.10, the resulting solid carbon may be characterized as graphene. Chemistry software capable of calculating the temperature of the reaction is currently being explored during the writing of this dissertation. If a software is able to predict the temperature within reasonable error, then the calculated temperature and predicted number of moles can be used via the ideal gas law [52] to calculate pressure.

It is also conceivable that detonation pressure is an aspect of the chemical reaction number of moles that form during the explosion, and that only minimum temperature conditions are required to form a graphene. However, given that heavy compression is required to turn carbon into diamond [103] and that high temperature (> 3000 K) at constant pressure

reactions of oxygen-acetylene torches are common yet yield no graphene [104], the author contends that pressure also plays a role in shaping the morphology of the reaction.

6.5.1 The thermodynamic argument of graphene formation

This section will use the First Law of thermodynamics to present an argument using temperature as a mechanism of graphene formation.

The First Law of thermodynamics

$$Q = \Delta U + p\Delta V \quad (6.3)$$

and the ideal gas law

$$p\Delta V = nR\Delta T \quad (6.4)$$

thus become

$$Q = \Delta U + nR\Delta T \quad (6.5)$$

Consider the chamber after release of the chemical energy to create heat, Q , but before the gases condense to solids. The internal energy U of an ideal gas is determined solely by its temperature. It depends on translational, rotational and sometimes vibrational degrees of freedom for the molecule. This energy changes with temperature. Thus, we have:

$$\textit{Monotonic gases} : \Delta U = n(3/2)R\Delta T \quad (6.6)$$

$$\textit{Diatomic gases} : \Delta U = n(5/2)R\Delta T \quad (6.7)$$

$$\textit{Diatomic gases at high } T \textit{ with a vibrational degree of freedom} : \Delta U = n(7/2)R\Delta T \quad (6.8)$$

$$\textit{In general, gases have} : \Delta U = nCR\Delta T \textit{ where } CR \textit{ is the molar heat capacity.} \quad (6.9)$$

The chemical reaction in the chamber generates the heat Q . It depends on the bond energies of the reactants and products in a complex manner that we do not understand yet.

In an open flame, i.e. a flame at constant p, the First Law (Eq. 6.5) is

$$Q = \Delta U + nR\Delta T = n(C + 1)R\Delta T \quad (6.10)$$

For a given reaction, Q is determined. With a Q, we solve the First Law (Eq. 6.10) for ΔT_p , the temperature change induced by the reaction at constant pressure

$$T_p = Q/(n(C + 1)R) \quad (6.11)$$

In a closed container, the volume is constant. Then the First Law (Eq. 6.3) is

$$Q = \Delta U = nCR\Delta T \quad (6.12)$$

Now solving (Eq. 6.12) for ΔT_V , the temperature change induced by the reaction at constant volume, we find

$$T_V = Q/(nCR) \quad (6.13)$$

The ratios of Eqs. (6.13) and (6.11) is

$$\Delta T_V/\Delta T_p = (C + 1)/C \quad (6.14)$$

Note that $T_V > T_p$.

As an example, for a diatomic gas, Eq. (6.7) holds with $C = 5/2$. Then (6.14) yields

$$\Delta T_V/\Delta T_p = (C + 1)/C = 7/5 \quad (6.15)$$

Now, suppose an open, sooting, C_2H_2 flame has a $T = 2000$ K; this is T_p . Room $T = 300$ K, so $\Delta T_p = 2000 - 300 = 1700$ K. By Eq. (6.15), in the chamber with the same conditions, $\Delta T_V = 1700*(7/5) = 2380$ K. Then $T_V = 2380 + 300 = 2680$ K in the chamber.

The constant volume chamber takes no work, $p\Delta V$ energy away from the heat release of

the chemical combustion reaction, hence causes a higher temperature than an open flame. At this higher temperature, the amorphous soot (soft carbon) formed is converted (graphitized) to graphene. Both Kim et al. and Jurkiewicz et al. show evidence of soft carbon being graphitized at high T [102, 105]. Thus, we propose that graphene is obtained as a result of the graphitization of soot due to the increased temperature and pressure conditions of a closed volume environment.

6.5.2 Aerosol gelation revisited

In the journal submission in section 3.1, aerosol gelation was postulated as the possible mechanism for differentiating low versus high O/C acetylene-oxygen fill mixture graphene properties. Though we now argue that temperature plays the key role in graphitization of soft carbon, aerosol gelation is still relevant as our samples are often aerosol gels.

For acetylene graphene, lateral flake size and thus gel time increased with increasing O/C, which resulted in more layered carbon compared to smaller lateral flake sizes and thus shorter gel times and less layering at lower O/C ratios. Many properties of low versus high O/C graphene can be explained due to the difference in lateral flake size and layering. For example, the SSA will decrease with more layers, and wider flakes with more layers will have fewer edge sites resulting in a smaller D-peak in the Raman. Considering this flake size difference and our hypothesis that temperature is the key formation mechanism, these together indicate there is a correlation between temperature and later flake size, and thus temperature and the gelation process.

The problem is that the acetylene graphene data shows 2550 ± 100 K regardless of O/C, which may be due to user error or the spectrometer's inability to consistently capture peak temperatures. However, the ethylene data, of which there is more than 3x the amount of data for, shows a consistent increase in temperature with increasing O/C. Before the relationship between aerosol gelation and temperature can be fully understood, the acetylene graphene temperature dilemma must be resolved.

6.6 Conclusion

A systematic study on the formation and characterization of detonation carbon using various hydrocarbon precursors has been presented. All precursors share similar trends in product yields with the requirement of oxygen/carbon ratio (O/C) ≤ 1.0 to produce solid carbon, and the detonation data indicating that a minimum temperature and pressure of 2300 ± 150 K and 13 ± 1 atm, respectively, are both required to produce solid carbon with graphene morphology. These two results form a theoretical model that can be used to predict whether the reaction will form a soot or a graphene before the experiment takes place. Characterizations such as Raman, XRD, TEM, etc. are used to systematically distinguish the solid carbon produced between soot, graphene, and graphite. The resulting graphene product is a turbostratic nanoscale graphene with 5-30 layers depending on the O/C ratio and precursor, and can be industrially scaled up to produce kg/day quantities at low cost. Differing O/C ratios produce graphenes with different properties that we call low O/C and high O/C graphene. Syngas is also produced as a byproduct for O/C mixtures ≤ 1.0 , and there are low-to-zero solid carbon yields for O/C mixtures > 1.0 which instead produce carbon monoxide and hydrogen, an appealing industry reaction in the process of being scaled up.

Bibliography

- [1] F.-X. Ouf, S. Bourrous, C. Vallières, J. Yon, and L. Lintis. Specific surface area of combustion emitted particles: Impact of primary particle diameter and organic content. *Journal of Aerosol Science*, 137:105436, 2019. ISSN 0021-8502. doi: <https://doi.org/10.1016/j.jaerosci.2019.105436>. URL <https://www.sciencedirect.com/science/article/pii/S0021850219305324>.
- [2] A. Sadezky, H. Muckenhuber, H. Grothe, R. Niessner, and U. Pöschl. Raman microspectroscopy of soot and related carbonaceous materials: Spectral analysis and structural information. *Carbon*, 43(8):1731–1742, 2005. ISSN 0008-6223. doi: <https://doi.org/10.1016/j.carbon.2005.02.018>. URL <https://www.sciencedirect.com/science/article/pii/S0008622305001247>.
- [3] Mario Commodo, Peter H. Joo, Gianluigi De Falco, Patrizia Minutolo, Andrea D’Anna, and Ömer L. Gülder. Raman spectroscopy of soot sampled in high-pressure diffusion flames. *Energy and Fuels*, 31(9):10158–10164, 2017. doi: 10.1021/acs.energyfuels.7b01674.
- [4] Markus Knauer, Manfred E. Schuster, Dangsheng Su, Robert Schlögl, Reinhard Niessner, and Natalia P. Ivleva. Soot structure and reactivity analysis by raman microspectroscopy, temperature-programmed oxidation, and high-resolution transmission electron microscopy. *The Journal of Physical Chemistry A*, 113(50):13871–13880, 2009. doi: 10.1021/jp905639d. URL <https://doi.org/10.1021/jp905639d>. PMID: 19899796.
- [5] Vikrant Sahu, Shashank Shekhar, Preety Ahuja, Govind Gupta, Sushil Singh, Raj Sharma, and Gurmeet Singh. Synthesis of hydrophilic carbon black; role of hydrophilic-

- ity in maintaining the hydration level and protonic conduction. *RSC Adv.*, 3:3917–3924, 02 2013. doi: 10.1039/C3RA23136D.
- [6] A. K. Geim. Graphene: Status and prospects. *Science*, 324(5934):1530–1534, 2009. doi: 10.1126/science.1158877. URL <https://www.science.org/doi/abs/10.1126/science.1158877>.
- [7] Mikhail I. Katsnelson. Graphene: carbon in two dimensions. *Materials Today*, 10(1):20–27, 2007. ISSN 1369-7021. doi: [https://doi.org/10.1016/S1369-7021\(06\)71788-6](https://doi.org/10.1016/S1369-7021(06)71788-6). URL <https://www.sciencedirect.com/science/article/pii/S1369702106717886>.
- [8] Rod Ruoff. Calling all chemists. *Nature Nanotechnology*, 3(1):10–11, 2008. doi: 10.1038/nnano.2007.432.
- [9] A. K. Geim and K. S. Novoselov. The rise of graphene. *Nature Materials*, 6(3):183–191, 2007. doi: 10.1038/nmat1849.
- [10] K. Novoselov, A. Geim, S. Morozov, Da Jiang, Yanshui Zhang, S. Dubonos, Irina Grigorieva, and A. Firsov. Electric field effect in atomically thin carbon films. *Nat. Mater.*, 6, 01 2004.
- [11] Sungjin Park and Rodney Ruoff. Chemical methods for the production of graphenes. *Nature nanotechnology*, 5:309, 04 2010. doi: 10.1038/nnano.2010.69.
- [12] Sungjin Park, Jinho An, Inhwa Jung, Richard Piner, Sung Jin An, Xuesong Li, Aruna Velamakanni, and Rodney Ruoff. Colloidal suspensions of highly reduced graphene oxide in a wide variety of organic solvents. *Nano letters*, 9:1593–7, 05 2009. doi: 10.1021/nl803798y.
- [13] Cristina Navarro, Thomas Weitz, Alexander Bittner, Matteo Scolari, Alf Mews, Marko Burghard, and Klaus Kern. Electronic transport properties of individual chemically reduced graphene oxide sheets. *Nano letters*, 9, 05 2009. doi: 10.1021/nl901209z.

- [14] Alexander Green and Mark Hersam. Solution phase production of graphene with controlled thickness via density differentiation. *Nano letters*, 9:4031–6, 09 2009. doi: 10.1021/nl902200b.
- [15] Anne Charrier, A. Coati, Tatiana Argunova, Franck Thibaudau, Yves Garreau, Pinchaux, Forbeaux, Debever, Sauvage-Simkin, and Jean-Marc Themlin. Solid-state decomposition of silicon carbide for growing ultra-thin heteroepitaxial graphite films. *Journal of Applied Physics*, 92:2479, 09 2002. doi: 10.1063/1.1498962.
- [16] Claire Berger, Zhimin Song, Xuebin Li, Xiaosong Wu, Nate Brown, Cécile Naud, Didier Mayou, Tianbo Li, Joanna Hass, Alexei Marchenkov, E. Conrad, Phillip First, and Walt Heer. Electronic confinement and coherence in patterned epitaxial graphene. *Science (New York, N.Y.)*, 312:1191–6, 06 2006.
- [17] Colin Hong An Wong, Zdeněk Sofer, Marie Kubešová, Jan Kučera, Stanislava Matějková, and Martin Pumera. Synthetic routes contaminate graphene materials with a whole spectrum of unanticipated metallic elements. *Proceedings of the National Academy of Sciences*, 111(38):13774–13779, 2014. ISSN 0027-8424. doi: 10.1073/pnas.1413389111. URL <https://www.pnas.org/content/111/38/13774>.
- [18] Rajan Dhaubhadel, Amitabha Chakrabarti, and Christopher Sorensen. Ultra low density materials synthesized via an aerosol gelation process. 01 2007.
- [19] Arjun Nepal, Gajendra Singh, Bret Flanders, and C Sorensen. One-step synthesis of graphene via catalyst-free gas-phase hydrocarbon detonation. *Nanotechnology*, 24:245602, 05 2013. doi: 10.1088/0957-4484/24/24/245602.
- [20] Anand P. S. Gaur, Wenjun Xiang, Arjun Nepal, Justin P. Wright, Pingping Chen, Thiba Nagaraja, Shusil Sigdel, Brice LaCroix, Christopher M. Sorensen, and Suprem R. Das. Graphene aerosol gel ink for printing micro-supercapacitors. *ACS Applied Energy Materials*, 4(8):7632–7641, 2021. doi: 10.1021/acsaem.1c00919. URL <https://doi.org/10.1021/acsaem.1c00919>.

- [21] Young Kim, Sanghoon Lee, Peter Pikhitsa, and Mansoo Choi. Laser induced transition from soot generation to shell shaped carbon nanoparticles in an acetylene flow: Aerosol characterization. *Journal of Mechanical Science and Technology*, 22:134–140, 01 2008. doi: 10.1007/s12206-007-1016-7.
- [22] Duy Luong, Ksenia Bets, Wala Algozeeb, Michael Stanford, Carter Kittrell, Weiyin Chen, Rodrigo Salvatierra, Muqing Ren, Emily McHugh, Paul Advincula, Zhe Wang, Mahesh Bhatt, Hua Guo, Vladimir Mancevski, Rouzbeh Shahsavari, Boris Yakobson, and James Tour. Gram-scale bottom-up flash graphene synthesis. *Nature*, 577, 01 2020. doi: 10.1038/s41586-020-1938-0.
- [23] URL <https://chemicalsafety.com/sds-search/>.
- [24] Department of labor logo united statesdepartment of labor, . URL <https://www.osha.gov/laws-regs/regulations/standardnumber/1910/1910.132>.
- [25] Department of labor logo united statesdepartment of labor, . URL <https://www.osha.gov/hazcom>.
- [26] Vanesa Sanchez, Ashish Jachak, Robert Hurt, and Agnes Kane. Biological interactions of graphene-family nanomaterials: An interdisciplinary review. *Chemical research in toxicology*, 25:15–34, 09 2011. doi: 10.1021/tx200339h.
- [27] Rickard Arvidsson, Max Boholm, Mikael Johansson, and Monica Montoya. “just carbon”: Ideas about graphene risks by graphene researchers and innovation advisors. *NanoEthics*, 12, 12 2018. doi: 10.1007/s11569-018-0324-y.
- [28] Tanveer Tabish, Zahid Pranjol, Farhat Jabeen, Trefa Abdullah, Asif Latif, Adeel Khalid, Muhammad Ali, Hasan Hayat, Paul Winyard, Jacqueline Whatmore, and Shaowei Zhang. Investigation into the toxic effects of graphene nanopores on lung cancer cells and biological tissues. *Materials Today*, 12:389–401, 07 2018. doi: 10.1016/j.apmt.2018.07.005.

- [29] Yuri Volkov, Jennifer McIntyre, and Adriele Prina-Mello. Graphene toxicity as a double-edged sword of risks and exploitable opportunities: A critical analysis of the most recent trends and developments. *2D Materials*, 4, 12 2016. doi: 10.1088/2053-1583/aa5476.
- [30] Anja Schinwald, Fiona Murphy, Alan Jones, William MacNee, and Ken Donaldson. Graphene-based nanoplatelets: A new risk to the respiratory system as a consequence of their unusual aerodynamic properties. *ACS nano*, 6:736–46, 12 2011. doi: 10.1021/nn204229f.
- [31] Peter Hoet, Irene Brüske, and Volodymyr Salata. Nps – known and unknown health risks. *Journal of nanobiotechnology*, 2:12, 01 2005. doi: 10.1186/1477-3155-2-12.
- [32] Rajan Dhaubhadel, Corey Gerving, Amitabha Chakrabarti, and Christopher Sorensen. Aerosol gelation: Synthesis of a novel, lightweight, high specific surface area material. *Aerosol Science and Technology*, 41:804–810, 08 2007. doi: 10.1080/02786820701466291.
- [33] C. M. Sorensen and A. Chakrabarti. The sol to gel transition in irreversible particulate systems. *Soft Matter*, 7(6):2284–2296, 2011. doi: 10.1039/c0sm00228c.
- [34] What is raman spectroscopy and why is it useful?, Oct 2020. URL <https://www.princetoninstruments.com/learn/raman/introduction-to-raman-spectroscopy>.
- [35] AC Ferrari, J. Meyer, Vittorio Scardaci, C Casiraghi, Michele Lazzeri, Francesco Mauri, S Piscanec, Dingde Jiang, K Novoselov, Siegmund Roth, and AK Geim. Raman spectrum of graphene and graphene layers. *Physical review letters*, 97:187401, 12 2006.
- [36] I Calizo, Alexander Balandin, Wenzhong Bao, Feng Miao, and Jeanie Lau. Temperature dependence of the raman spectra of graphene and graphene multilayers. *Nano letters*, 7:2645–9, 10 2007. doi: 10.1021/nl071033g.

- [37] Mark Wall. Raman spectroscopy optimizes graphene characterization. *Advanced Materials and Processes*, 170:35–38, 04 2012.
- [38] Andrea Ferrari. Raman spectroscopy of graphene and graphite: Disorder, electron-phonon coupling, doping and nonadiabatic effects. *Solid State Communications*, 143: 47–57, 07 2007. doi: 10.1016/j.ssc.2007.03.052.
- [39] X-ray diffraction, 2021. URL <https://www.jove.com/v/10446/x-ray-diffraction>.
- [40] David B. Williams and C. Barry. Carter. *Transmission electron microscopy: a textbook for materials science*. Springer, 2009.
- [41] Matthias Thommes, Katsumi Kaneko, Alexander V. Neimark, James P. Olivier, Francisco Rodriguez-Reinoso, Jean Rouquerol, and Kenneth S.W. Sing. Physisorption of gases, with special reference to the evaluation of surface area and pore size distribution (iupac technical report). *Pure and Applied Chemistry*, 87(9-10):1051–1069, 2015. doi: doi:10.1515/pac-2014-1117. URL <https://doi.org/10.1515/pac-2014-1117>.
- [42] Matthias Thommes, Katie Cychosz, and Alexander Neimark. *Advanced Physical Adsorption Characterization of Nanoporous Carbons*, pages 107–145. 12 2012. ISBN 9780080977447. doi: 10.1016/B978-0-08-097744-7.00004-1.
- [43] Susan Swapp. Scanning electron microscopy (sem), May 2017. URL https://serc.carleton.edu/research_education/geochemsheets/techniques/SEM.html.
- [44] Diane Turner. Gas chromatography, how a gas chromatography machine works, how to read a chromatograph and gcxgc. URL <https://www.technologynetworks.com/analysis/articles/gas-chromatography-how-a-gas-chromatography-machine-works-how-to-read-a-chromatogr>
- [45] Ftir spectroscopy basics: Thermo fisher scientific, us, . URL <https://www.thermofisher.com/us/en/home/industrial/spectroscopy-elemental-isotope-analysis/>

[spectroscopy-elemental-isotope-analysis-learning-center/
molecular-spectroscopy-information/ftir-information/ftir-basics.html](https://www.mt.com/us/en/home/applications/Laboratory_weighing/chnso_elemental_analysis.html).

- [46] Zeta potential :: Anton paar wiki, . URL <https://wiki.anton-paar.com/us-en/zeta-potential/>.
- [47] G. Binnig, C. F. Quate, and Ch. Gerber. Atomic force microscope. *Physical Review Letters*, 56(9):930–933, 1986. doi: 10.1103/physrevlett.56.930.
- [48] Mettler-Toledo International Inc. all rights reserved. Chnso elemental analysis - sample preparation, Dec 2019. URL https://www.mt.com/us/en/home/applications/Laboratory_weighing/chnso_elemental_analysis.html.
- [49] Nooshin Saadatkhah, Adrián Carillo Garcia, Sarah Ackermann, Philippe Leclerc, Mohammad Latifi, Said Samih, Gregory S. Patience, and Jamal Chaouki. Experimental methods in chemical engineering: Thermogravimetric analysis—tga. *The Canadian Journal of Chemical Engineering*, 98(1):34–43, 2019. doi: 10.1002/cjce.23673.
- [50] Sonication: Definition, working principle, applications and methods, May 2021. URL <https://byjus.com/physics/sonication/>.
- [51] Timothy H. Boyer. Derivation of the blackbody radiation spectrum without quantum assumptions. *Phys. Rev.*, 182:1374–1383, Jun 1969. doi: 10.1103/PhysRev.182.1374. URL <https://link.aps.org/doi/10.1103/PhysRev.182.1374>.
- [52] Charles Kittel and Kromer Herbert. *Thermal physics*. Freeman, 1980.
- [53] Irvin Glassman and Richard A. Yetter. *Preface*, page 794. Academic Press, Burlington, Jan 2008. ISBN 978-0-12-088573-2. URL <http://www.sciencedirect.com/science/article/pii/B9780120885732000130>.
- [54] Elaine S. Oran and Vadim N. Gamezo. Origins of the deflagration-to-detonation transition in gas-phase combustion. *Combustion and Flame*, 148(1-2):4–47, 2007. doi: 10.1016/j.combustflame.2006.07.010.

- [55] M.a. Liberman, M.f. Ivanov, A.d. Kiverin, M.s. Kuznetsov, A.a. Chukalovsky, and T.v. Rakhimova. Deflagration-to-detonation transition in highly reactive combustible mixtures. *Acta Astronautica*, 67(7-8):688–701, 2010. doi: 10.1016/j.actaastro.2010.05.024.
- [56] Takahiro Matsumoto, Tomoaki Koizumi, Yasuyuki Kawakami, Koichi Okamoto, and Makoto Tomita. Perfect blackbody radiation from a graphene nanostructure with application to high-temperature spectral emissivity measurements. *Opt. Express*, 21(25):30964–30974, Dec 2013. doi: 10.1364/OE.21.030964. URL <http://www.osapublishing.org/oe/abstract.cfm?URI=oe-21-25-30964>.
- [57] S Galal Yousef, P Sperfeld, and J Metzdorf. Measurement and calculation of the emissivity of a high-temperature black body. *Metrologia*, 37(5):365–368, oct 2000. doi: 10.1088/0026-1394/37/5/4. URL <https://doi.org/10.1088/0026-1394/37/5/4>.
- [58] R.M. Morris. Effect of particle size and temperature on volatiles produced from coal by slow pyrolysis. *Fuel*, 69(6):776–779, 1990. ISSN 0016-2361. doi: [https://doi.org/10.1016/0016-2361\(90\)90045-R](https://doi.org/10.1016/0016-2361(90)90045-R). URL <https://www.sciencedirect.com/science/article/pii/001623619090045R>.
- [59] Lei Shi, Qingya Liu, Xiaojin Guo, Weize Wu, and Zhenyu Liu. Pyrolysis behavior and bonding information of coal — a tga study. *Fuel Processing Technology*, 108:125–132, 2013. ISSN 0378-3820. doi: <https://doi.org/10.1016/j.fuproc.2012.06.023>. URL <https://www.sciencedirect.com/science/article/pii/S0378382012002457>. Special Issue of APCRE11.
- [60] Didem N. Inceoğlu, İsmail Özbay, and Aykan Karademir. Voc and pah characterization of petroleum coke at maximum thermal decomposition temperature. *Energy Sources, Part A: Recovery, Utilization, and Environmental Effects*, 41(11):1305–1314, 2019. doi: 10.1080/15567036.2018.1548509. URL <https://doi.org/10.1080/15567036.2018.1548509>.

- [61] Adeola Akeem Akinpelu, Md Eaqub Ali, Mohd Rafie Johan, R. Saidur, Zaira Zaman Chowdhury, Ahsan Mushir Shemsi, and Tawfik A. Saleh. Effect of the oxidation process on the molecular interaction of polyaromatic hydrocarbons (pah) with carbon nanotubes: Adsorption kinetic and isotherm study. *Journal of Molecular Liquids*, 289:111107, 2019. ISSN 0167-7322. doi: <https://doi.org/10.1016/j.molliq.2019.111107>. URL <https://www.sciencedirect.com/science/article/pii/S0167732219311857>.
- [62] K. H. Kangasniemi, D. A. Condit, and T. D. Jarvi. Characterization of vulcan electrochemically oxidized under simulated pem fuel cell conditions. *Journal of The Electrochemical Society*, 151(4), 2004. doi: 10.1149/1.1649756.
- [63] Tingyu Lei, Wenping Guo, Qingya Liu, Haijun Jiao, Dong-Bo Cao, Botao Teng, Yong-Wang Li, Xingchen Liu, and Xiao-Dong Wen. Mechanism of graphene formation via detonation synthesis: A dftb nanoreactor approach. *Journal of chemical theory and computation*, 15, 05 2019. doi: 10.1021/acs.jctc.9b00158.
- [64] U.s. energy information administration - eia - independent statistics and analysis, Jan 2021. URL <https://www.eia.gov/energyexplained/hydrogen/use-of-hydrogen.php>.
- [65] Annual reports, Sep 2021. URL <https://www.ieahydrogen.org/annual-reports/>.
- [66] Andy Brown, Jul 2019. URL <https://www.thechemicalengineer.com/features/uses-of-hydrogen-in-industry/>.
- [67] J P Mesguen, J Bidon, and L Lelong. Uses of hydrogen, Mar 2020. URL <https://energies.airliquide.com/resources-planet-hydrogen/uses-hydrogen>.
- [68] Sunita Satyapal. Hydrogen: A clean, flexible energy carrier, Feb 2021. URL <https://www.energy.gov/eere/articles/hydrogen-clean-flexible-energy-carrier>.
- [69] URL <https://www.agpgas.com/rare-specialty-gases/carbon-monoxide/>.

- [70] Alla Katsnelson. Carbon monoxide can be deadly. but researchers want to use it for good, Nov 2019. URL <https://cen.acs.org/pharmaceuticals/drug-development/Carbon-monoxide-deadly-researchers-want/97/i45>.
- [71] URL https://www.linde-gas.com/en/products_and_supply/packaged_chemicals/product_range/carbon_monoxide.html.
- [72] Melissa Knauert, Sandeep Vangala, Maria Haslip, and Patty J. Lee. Therapeutic applications of carbon monoxide. *Oxidative Medicine and Cellular Longevity*, 2013: 1–11, 2013. doi: 10.1155/2013/360815.
- [73] Stephen Corkill, Christopher Sorensen, Justin P. Wright, Arjun Nepal, and Stefan Bossmann. Device and process for mass production of particulate materials. 06 2021.
- [74] Katherine Swift. Can epoxy resin be used on glass? - resin and glass, May 2021. URL <https://www.resinobsession.com/resin-frequently-asked-questions/can-epoxy-resin-be-used-on-glass-resin-and-glass/>.
- [75] Stéphane Pérès Jean Tiberghien. Tibtech innovations. URL <https://www.tibtech.com/conductivite>.
- [76] Griffiths. *Introduction to Electrodynamics*. Cambridge University Press, 2017.
- [77] John David Jackson. *Classical electrodynamics*. Wiley, 2021.
- [78] John L. Cooper and Hiroshi Sakai. Aramid fiber kevlar® and its applications. *Seni Gakkaishi*, 43(4), 1987. doi: 10.2115/fiber.43.4.p125.
- [79] Amanda Gronot. Is pure o2 flammable?, May 2021. URL <https://sciencing.com/pure-o2-flammable-7804267.html>.
- [80] Carr. URL <https://www.mcmaster.com/>.
- [81] Importance of methane, . URL <https://www.epa.gov/gmi/importance-methane>.

- [82] Gases - explosion and flammability concentration limits, . URL https://www.engineeringtoolbox.com/explosive-concentration-limits-d_423.html.
- [83] A greener, simpler way to create syngas, Jan 2020. URL <https://samueli.ucla.edu/a-greener-simpler-way-to-create-syngas/>.
- [84] Raghda Ahmed El-Nagar and Alaa Ali Ghanem. Syngas production, properties, and its importance, Nov 2019. URL <https://www.intechopen.com/chapters/69842>.
- [85] Chunshan Song. Introduction to hydrogen and syngas production and purification technologies. *Hydrogen and Syngas Production and Purification Technologies*, page 1–13, 2009. doi: 10.1002/9780470561256.ch1.
- [86] Francis A Carey. Ethylene. URL <https://www.britannica.com/science/ethylene>.
- [87] Ramya A V, Jerin John, and Manoj Balachandran. Raman spectroscopy investigation of camphor soot: Spectral analysis and structural information. *International journal of electrochemical science*, 8:9421–9428, 07 2013.
- [88] Eric J. Heller, Yuan Yang, Lucas Kocia, Wei Chen, Shiang Fang, Mario Borunda, and Efthimios Kaxiras. Theory of graphene raman scattering. *ACS Nano*, 10:2803, 2016. URL <http://pubs.acs.org/doi/abs/10.1021/acsnano.5b07676>.
- [89] Joseph A. Garlow, Lawrence K. Barrett, Lijun Wu, Kim Kisslinger, Yimei Zhu, and Javier F. Pulecio. Large-area growth of turbostratic graphene on ni(111) via physical vapor deposition. *Scientific Reports*, 6(1), 2016. doi: 10.1038/srep19804.
- [90] Jiang-Bin Wu, Miao-Ling Lin, Xin Cong, He-Nan Liu, and Ping-Heng Tan. Raman spectroscopy of graphene-based materials and its applications in related devices. *Chem. Soc. Rev.*, 47:1822–1873, 2018. doi: 10.1039/C6CS00915H. URL <http://dx.doi.org/10.1039/C6CS00915H>.
- [91] R. W. G. Wyckoff. *Crystal structures*. John Wiley and Sons, 1965.

- [92] Cameron F. Holder and Raymond E. Schaak. Tutorial on powder x-ray diffraction for characterizing nanoscale materials. *ACS Nano*, 13(7):7359–7365, 2019. doi: 10.1021/acsnano.9b05157.
- [93] Karolina Jurkiewicz, Mirosława Pawlyta, and Andrzej Burian. Structure of carbon materials explored by local transmission electron microscopy and global powder diffraction probes. *C*, 4(4), 2018. ISSN 2311-5629. doi: 10.3390/c4040068. URL <https://www.mdpi.com/2311-5629/4/4/68>.
- [94] Joseph C. Scanlon and Lawrence B. Ebert. X-ray diffraction study of fullerene soot. *The Journal of Physical Chemistry*, 97(28):7138–7140, 1993. doi: 10.1021/j100130a004.
- [95] George E. Moore and Howard H. Hansen. Direct observation of the thermal dissociation of molecular nitrogen. *The Journal of Chemical Physics*, 54(1):399–404, 1971. doi: 10.1063/1.1674621.
- [96] Propane fuel basics. URL https://afdc.energy.gov/fuels/propane_basics.html.
- [97] Combustion, Oct 2021. URL https://en.wikipedia.org/wiki/Combustion#cite_note-ExoCalc-13.
- [98] Jim Clark. Complete vs. incomplete combustion of alkanes, Nov 2020. URL [https://chem.libretexts.org/Bookshelves/Organic_Chemistry/Supplemental_Modules_\(Organic_Chemistry\)/Alkanes/Reactivity_of_Alkanes/Complete_vs._Incomplete_Combustion_of_Alkanes](https://chem.libretexts.org/Bookshelves/Organic_Chemistry/Supplemental_Modules_(Organic_Chemistry)/Alkanes/Reactivity_of_Alkanes/Complete_vs._Incomplete_Combustion_of_Alkanes).
- [99] Pavel V. Bakharev, Ming Huang, Manav Saxena, Suk Woo Lee, Se Hun Joo, Sung O Park, Jichen Dong, Dulce C. Camacho-Mojica, Sunghwan Jin, Youngwoo Kwon, and et al. Chemically induced transformation of chemical vapour deposition grown bilayer graphene into fluorinated single-layer diamond. *Nature Nanotechnology*, 15(1):59–66, 2019. doi: 10.1038/s41565-019-0582-z.
- [100] Peter Rickhaus, Ming-Hao Liu, Marcin Kurpas, Annika Kurzmann, Yongjin Lee, Hiske Overweg, Marius Eich, Riccardo Pisoni, Takashi Taniguchi, Kenji Watanabe, Klaus

- Richter, Klaus Ensslin, and Thomas Ihn. The electronic thickness of graphene. *Science Advances*, 6(11):eaay8409, 2020. doi: 10.1126/sciadv.aay8409. URL <https://www.science.org/doi/abs/10.1126/sciadv.aay8409>.
- [101] K. Johansson, M. Head-Gordon, P. Schrader, K. Wilson, and H. Michelsen. Resonance-stabilized hydrocarbon-radical chain reactions may explain soot inception and growth. *Science*, 361:997–1000, 09 2018. doi: 10.1126/science.aat3417.
- [102] Kim Min Il, Jong Cho, Jin Hwang, Byong Bai, and Ji Im. Correction to: Preparation of high-crystallinity synthetic graphite from hard carbon-based carbon black. *Applied Physics A*, 127, 05 2021. doi: 10.1007/s00339-021-04471-3.
- [103] Hobart M King. How do diamonds form? URL <https://geology.com/articles/diamonds-from-coal/>.
- [104] Acetylene. URL <https://ilmoproducts.com/industries-served/welding-cutting/gases-their-applications/acetylene/>.
- [105] Karolina Jurkiewicz, Mirosława Pawlyta, and Andrzej Burian. Structure of carbon materials explored by local transmission electron microscopy and global powder diffraction probes. *C*, 4(4):68, 2018. doi: 10.3390/c4040068.